Publicly Accessible Penn Dissertations

2016

Reconfigurable Periodic Porous Membranes & Nanoparticle Assemblies

Gaoxiang Wu
University of Pennsylvania, wugao@seas.upenn.edu

Reconfigurable Periodic Porous Membranes & Nanoparticle Assemblies

Abstract

The thesis here will cover two parts of my research. The focus of the first part of the thesis will be using responsive hydrogel materials to manipulate the pattern transformation at microscale (Chapter 3-5), and meanwhile using the finite element method (FEM) to guide new designs of the periodic porous structures that can undergo controlled pattern transformation processes (Chapter 6). In beginning, I design fabrication methods of micro-structures from responsive hydrogel materials via micro-/nano- imprinting. The responsiveness of the hydrogels is introduced by incorporating responsive monomers into the hydrogel precursors. Here, the responsiveness of the hydrogel leads to the tunable swelling ratio of the hydrogel under external stimuli, e.g. pH, temperature, and variation of humidity, so that the imprinted nano-/micro-structures can be dynamically controlled. Later, upon using FEM simulation, we design and experimentally test the deformation and mechanical properties of the periodic porous membranes based on different collapsing modes of kagome lattices. The experiments are performed at macroscopic scale taking advantage of powerful 3D printing prototyping. As the deformation phenomenon is scale independent, the observed phenomenon is applicable to predict the deformation of the micro-structures.

In the second part of the thesis, we investigate two colloidal assembly systems. First (Chapter 7-8), we utilize the new form of silica nanoparticles with chain-like morphology to generate sharp nanostructures on the coating surface that minimize the contact between liquid and solid phase, and thus improve dramatically the water repellency on the coating surfaces. The stability test of the superhydrophobicity against hydrodynamic/hydrostatic pressure, low surface tension liquid, and vapor phase condensation, are also investigated for a complete interpretation of the wetting behavior. Secondly (Chapter 9), I design colloidal suspensions matching the inter-particle interactions with those used in theoretical study of colloidal assembly within the confined the space. The beauty of the system is that the colloidal suspension can be cross-linked and lock the assembled structures, so that the assembled structure can be observed under electron microscope and compare to theory and simulation. So far, a good consistence has been observed, indicating a validated design of the systems.

Degree Type
Dissertation

Degree Name
Doctor of Philosophy (PhD)

Graduate Group
Materials Science & Engineering

First Advisor
Shu Yang

Keywords
Assembly, Nano-imprinting, Nanoparticles, Pattern transformation, Wetting behavior

Subject Categories
Mechanics of Materials

RECONFIGURABLE PERIODIC POROUS MEMBRANES & NANOPARTICLE ASSEMBLIES

Gaoxiang Wu

A DISSERTATION

in

Materials Science and Engineering

Presented to the Faculties of the University of Pennsylvania

in

Partial Fulfillment of the Requirements for the

Degree of Doctor of Philosophy

2016

Supervisor of Dissertation

_____

Shu Yang, Professor, Materials Science and Engineering

Graduate Group Chairperson

_____

Dave Srolovitz, Professor, Materials Science and Engineering

Dissertation Committee

Christopher B. Murray, Professor, Materials Science and Engineering

Russell Composto, Professor, Materials Science and Engineering

Daeyeon Lee, Professor of Chemical and Biomolecular Engineering

ACKNOWLEDGEMENT

ABSTRACT

RECONFIGURABLE PERIODIC POROUS MEMBRANES &

NANOPARTICLE ASSEMBLIES

Gaoxiang Wu

Shu Yang

The thesis here will cover two parts of my research. The focus of the first part of the thesis will be using responsive hydrogel materials to manipulate the pattern transformation at microscale (Chapter 3-5), and meanwhile using the finite element method (FEM) to guide new designs of the periodic porous structures that can undergo controlled pattern transformation processes (Chapter 6). In beginning, I design fabrication methods of micro-structures from responsive hydrogel materials via micro-/nano- imprinting. The responsiveness of the hydrogels is introduced by incorporating responsive monomers into the hydrogel precursors. Here, the responsiveness of the hydrogel leads to the tunable swelling ratio of the hydrogel under external stimuli, e.g. pH, temperature, and variation of humidity, so that the imprinted nano-/micro-structures can be dynamically controlled. Later, upon using FEM simulation, we design and experimentally test the deformation and mechanical properties of the periodic porous membranes based on different collapsing modes of kagome lattices. The experiments are performed at macroscopic scale taking advantage of powerful 3D printing prototyping. As the deformation phenomenon is scale independent, the observed phenomenon is applicable to predict the deformation of the micro-structures.

In the second part of the thesis, we investigate two colloidal assembly systems. First (Chapter 7-8), we utilize the new form of silica nanoparticles with chain-like

morphology to generate sharp nanostructures on the coating surface that minimize the contact between liquid and solid phase, and thus improve dramatically the water repellency on the coating surfaces. The stability test of the superhydrophobicity against hydrodynamic/hydrostatic pressure, low surface tension liquid, and vapor phase condensation, are also investigated for a complete interpretation of the wetting behavior. Secondly (Chapter 9), I design colloidal suspensions matching the inter-particle interactions with those used in theoretical study of colloidal assembly within the confined the space. The beauty of the system is that the colloidal suspension can be cross-linked and lock the assembled structures, so that the assembled structure can be observed under electron microscope and compare to theory and simulation. So far, a good consistence has been observed, indicating a validated design of the systems.

Table of Contents

List of Tables

List of Figures

Chapter 1: Reconfigurable Surfaces via Pattern Transformation of Periodic Porous Membranes

1.0 Overview

Materials that undergo dramatic shape changes in response to external stimuli offer unique opportunities for the design of responsive and reconfigurable devices. Conventionally, reconfigurable or foldable macroscopic structures (*e.g.* camera tripods, foldable satellite solar panels, umbrella, and furniture) have been fabricated from rigid components connected by mechanical joints.[1, 2] Nature, on the other hand, provides many examples of how organisms generate actuation from adaptive soft materials or structures via a large variety of chemical-mechano responses. For example, venus flytraps open and close to catch preys via osmotic pressure induced buckling of the leaf structures,[3] squids dynamically change the skin color via mechanical expansion and contraction of the pigment-filled sacks,[4] and mimosa leaves fold via pressure sensing and osmotic pressure induced motion when being touched. There have been increasing interests to applying these natural design principles to design a new class of soft materials that can reconfigure the shape and structural symmetry in response to external stimuli (*e.g.* pH, mechanical forces, temperature, electric field, and light) for potential applications including 3D morphing,[5-7] sensing, miniaturized devices,[8-10] micro-actuation,[5, 10-12] tunable optics,[13, 14] microfluidic devices,[15] and drug delivery.[16]

Artificial materials with periodic structures at different length scales, so called metamaterials, offer exciting new directions in fields such as optics,[17] biology,[18] acoustics,[19] and surface science[20] since their properties rely on their structure arrangement rather than compositions. When these structures are changed in response to external stimuli, their properties can be varied significantly. Therefore, they are of

great interests in design of sensing materials,[17] micro-actuation,[8] colorful display,[21] and smart responsive surface.[22]

Despite all these developments, limitations remain. First, the switching of many physical properties of materials is related to micro- to nanoscale pattern changes (*e.g.* submicron to micron scale). [23] However, to induce a well-controlled and homogenous structural change micro- to nanoscale is challenging. Second, the triggering mechanism of existing reconfiguration periodic structures is mostly based on affine actuation, leading to a narrow range of tunable properties. In this chapter, I will first review the basic concepts of pattern transformation of periodic porous membranes in Section 1.1. As most of the structural mechanics study is guided by kinematic and/or periodic truss models of lattices, in Section 1.2 I will discuss how the models are incorporated in pattern transformation study, in particular, the kinematic model of kagome lattices. I will also review the actuation mechanisms from various hydrogel materials in response to different external stimuli (session 1.3). After that, I will review the studied pattern transformation system (session 1.4).

1.1 Buckling Induced Pattern Transformation of Soft Materials

1.1.1 Buckling of an Elastic Beam

A classic example of buckling instability is a slender beam subjecting to an axial load. [24] The deformation of the beam is initially along the axial direction of the beam due to the elasticity of its materials. However, such a state can become unstable above a critical load leading to a "buckling" failure. Upon buckling, bending deformation of the beam becomes more energetically favored to release the axial compression. For a simple supported ideal beam, the lowest critical load (P_1) can be obtained by solving differential equations describing the bending and elasticity of the beam. The tendency of the buckling deformation can also be derived from the

differential equation, *i.e.* wave-function having different eigenvalues. The solution with the lowest eigenvalue corresponds to most preferably deformed state with lowest elastic energy increment during the post-buckling process.

$$P_1 = \frac{\pi^2 EI}{l^2} \qquad (1.1)$$

where l is the total length of the beam, E is the elastic modulus, and I is the area moment of inertia of the cross-section of the beam.

1.1.2 Buckling of Periodic Structures

Similarly, periodic buckling process of structures (*e.g.* periodic lattice of beams) can be solved from matrix of differential equations defined by the elastic nature of beams and boundary conditions to the lattice (e.g. force/displacement of the beams in the lattice).[24] Again, the most preferable deformation mode is the solution of the differential equation having the lowest eigenvalue. In Fig. 1.1, we show an example of the predicted buckling structures from a slab in building design. The established theory of periodic buckling behavior can be traced back to late 1800s, when periodic truss design started to be extensively used in architecture, e.g. Eiffel tower, and internal truss of Lady Liberty.[24] The purpose is to design periodic truss structures to avoid buckling induced failure that is found to significantly reduce the mechanical stability of the building.
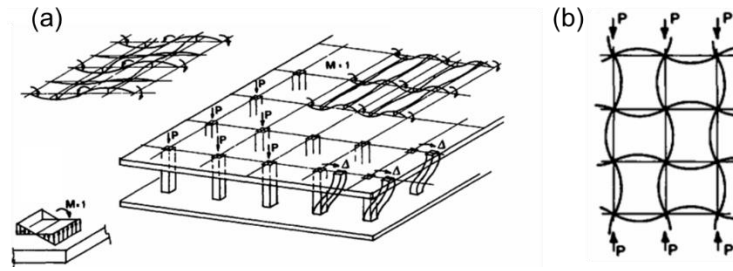
Figure 1.1 (a) Buckling analysis of in slab building; (b) Predicted lowest eigenvalue mode for buckling of the periodic structures in the design.[24]

1.1.3 Buckling Induced Pattern Transformation

Periodic buckling of porous membranes was first shown by Mullin, *et al*.[25] to undergo pattern transformation that simultaneously alters the lattice symmetry, pore size, shape, and filling fraction homogeneously over a large area and in multiple lengthscales.[19, 23, 26-31] More importantly, the trigger of the whole process requires a relatively small external perturbation, *e.g.* less than 10% uniaxial compressive strain (see Fig. 1.2).[23] Here, undergo uniaxial compression, the inter-pore ligaments undergo buckling induced bending. The low elastic energy from of the buckling structure in this case can be predicted by finite element methods (FEM), corresponding to an array of buckled elliptical pores with mutually orthogonal elliptical pores. Thus, the buckling instability induces reversible and repeatable switching between such two phases.
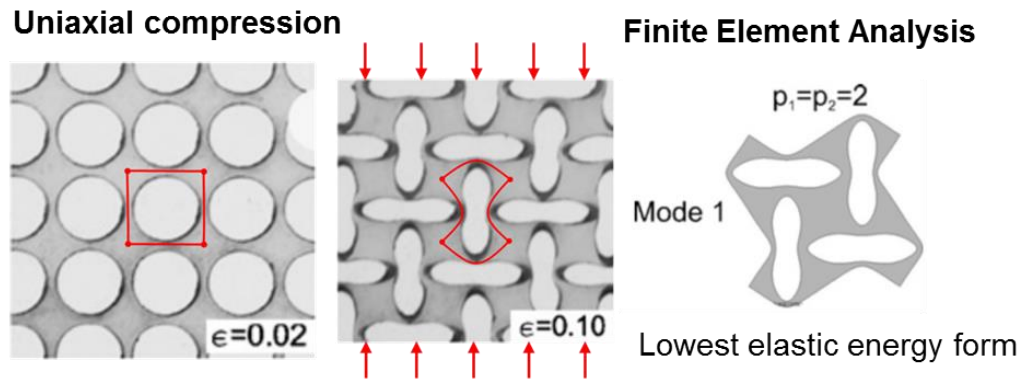
Figure 1.2 Example of pattern transformation occurred under uniaxial compression of a square array of porous membrane made of silicone rubber.[23]

1.2 Kinematic Model for Design of Periodic Lattices

In structural mechanics, the effective macroscopic properties of a periodic porous membrane are closely related to the structural performance of the pin-jointed parent structure or kinematic model of the structures.[32-35] Although the practical lattices made of soft materials are neither pin-jointed nor rigid-jointed, kinematic model gives useful insights in their deformations in a simplistic manner compared to other available tools,[24] e.g. FEM simulation and beam buckling analysis.

1.2.1 Kinematic Model in Pattern Transformation of Lattices

Traced back to the emergence of the structural mechanics, kinematic model with pin jointed truss was used to evaluate the stability of the lattice structures. When the bar connectivity of the pin-joints is sufficiently low, the pin-jointed truss collapses by non-extensional mechanism (*i. e*., floppy mode); the rigid-jointed version deforms by bending of the bars and rotation of the joints.[33, 36] Such structures were considered non-stable against the external load, since the lattice yields at a much lower stress due to the bending at weak joints rather than mechanical yielding of the bulk

materials. In the case of pattern transformation, however, such unique "floppy mode" of pin-jointed lattice has been demonstrated as an effective tool for designing 2D periodic soft materials with diverse pattern transformation behaviors. Bertoldi, *et al.* have estabilished a criteria using thin-ligment elastomer to replace the joints in the kinematic model.[37] Since the bending modulus of the thin ligaments is significantly lower compared to that of the bulk, the structure can undergo pattern transformation in a well-defined manner demonstrated in the kinematic model. In Fig. 1.3 and 1.4, we show both kinematic model (Fig. 1.3) and experimental observation vs. FEM simulation of pattern transformation of various periodic porous structures at different stain levels.
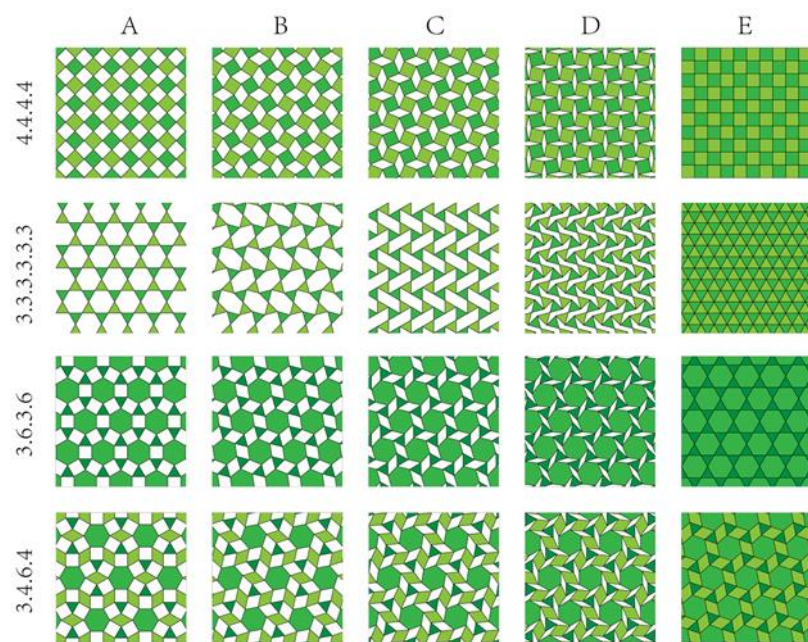
Figure 1.3 Folding mechanism described by kinematic models.[37]
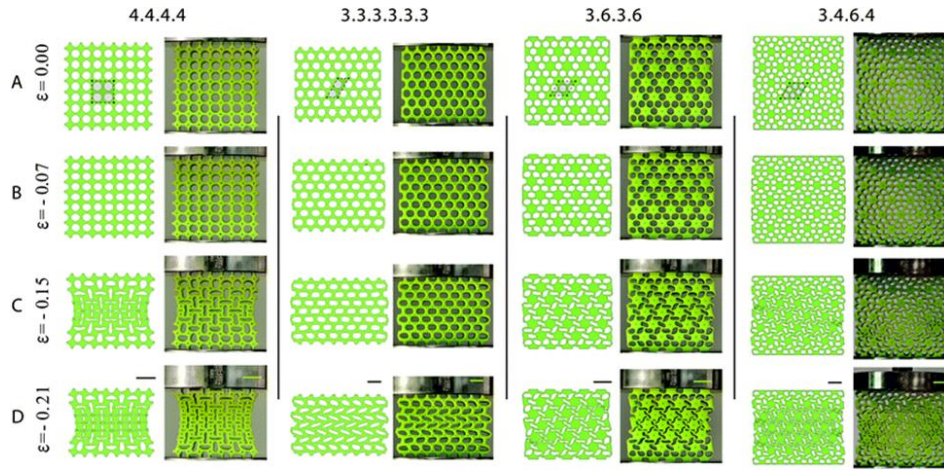
Figure 1.4 Experimental observation of the deformation of periodic porous structures (right) and the corresponding and FEM simulation (left) at different strains.[37]

1.2.2 Kagome Lattices

Among various two-dimensional (2D) lattices that undergo periodic collapse mechanisms,[33] the kagome lattices (also referred as trihexagonal tiling) and related lattices offer many desirable transport and elastic properties, heat-dissipation characteristics, and large photonic bandgaps.[38-40] The twisted kagome lattices exhibit isotropic elasticity with a vanishing bulk modulus. More importantly, kagome lattices of N lattice sites can have an order of $N^{1/2}$ "floppy" modes of lattice distortion under free boundary conditions, that is, they have $N^{1/2}$ modes of low-energy deformations of the structures via rotation of neighboring "rigid" structural units (here triangles) against each other without distorting the triangles. Correspondingly, kagome lattices could exhibit the maximal negative Poisson's ratio of −1.[36]

Different from previous studies in pattern transformation, which often involves circular hole arrays, upon deformation, the lattice undergoes relative rotation of neighboring triangles. we refer latter as "*twisted kagome lattices*". Theoretically, there

7

are an infinite number of degenerate modes of twisted kagome lattices if the hinges are perfectly free for rotation.[33] However, here we are particularly interested in two *"collapsing modes"* that involve the lattice transformation into new periodic structures. Meanwhile, the final collapsed states have structures, consisting of close-packed triangular unit, which offers maximum area shrinkage up to 75% (see Fig. 1.3). These collapsing modes are characterized by a single angle α specifying the direction of kagome triangles relative to the x-axis, or $\alpha = \frac{120° - \theta}{2}$, where θ is the angle between two edges of interconnected triangular units. In both cases, as α is increased from 0° (fully extended state) to 60° (fully compacted state), the lattice contracts in all directions by a factor of cos (α), and the area of the lattice decrease by a factor of $\cos^2(\alpha)$. These large deformations in response to relatively small external perturbations are highly attractive deformations that have been found to modify not only mechanical properties but also photon/phonon dispersion relations and bandgaps.
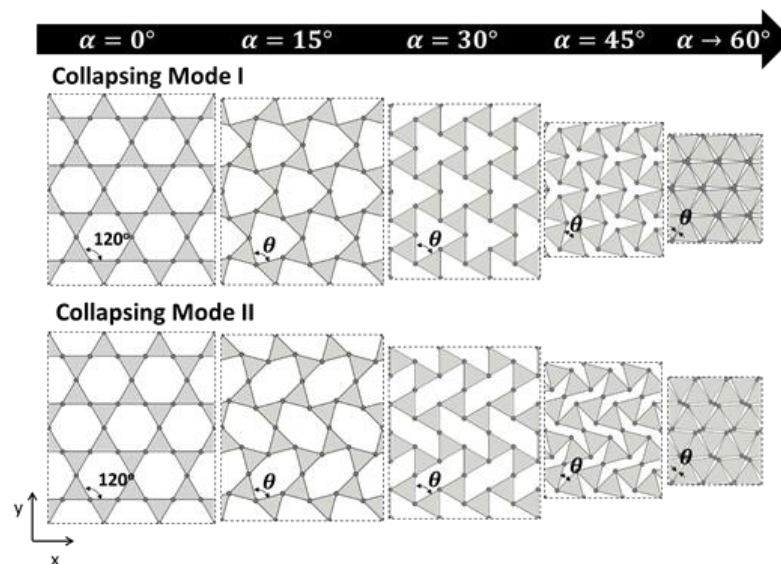
Figure 1.5 Schematics showing the periodic truss model of the kagome lattice and the corresponding two collapsing modes. With the increase of the twisting angle α from 0° to 60° degrees, the lattice reaches fully compacted configuration.

1.3 Swelling/Actuation of Hydrogels

Hydrogels are crosslinked materials that have hydrophilic polymer network and absorbs large amount of water without dissolving.[41] Responsive hydrogels can exhibit dramatic volume change in response to a large number of external stimuli such as temperature, electrical voltage, pH, ionic strength, and concentration of organic compounds.[42] In this session, we will review the mechanism of swelling and common responsive hydrogels.
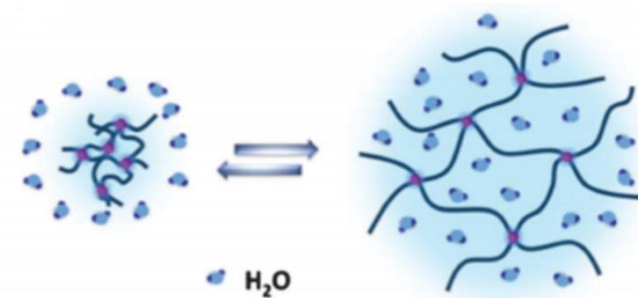
Figure 1.6 Illustration of swelling of the hydrogel network.[43]

1.3.1 Homogenous Swelling of Hydrogels

In general, swelling of the hydrogel means an increase in volume of the hydrogel by uptake of water surrounding the network. The degree of the swelling refers to the amount of water that the gel can absorb to reach the equilibrium state. In the model developed by Flory and Rehner,[44] and Brannon-Peppas and Peppas,[45] three terms of osmotic pressures are involved in the swelling equilibrium of the hydrogel: (1) mixing term π_M – the osmotic pressure due to mixing of the hydrogel network with the solvent molecules; (2) Elastic term π_{el} – the osmotic pressure due to the deforming of the polymer networks during the swelling process, and (3) Ionic term π_{ion} – osmotic pressure due to the dilution of ions concentrated inside the hydrogel network. In the

9

classical theory, the first two terms of free energy π_M and π_{el} are given by the Flory-Huggins lattice model and the classical Gaussian network model[44], respectively:

$$\pi_M = -\frac{RT}{V_S}\left[\ln\left(1 - \frac{V_0}{V}\right) + \frac{V_0}{V} + \chi\left(\frac{V_0}{V}\right)^2\right] \tag{1.4}$$

$$\pi_{el} = -\frac{RT v_{eff}}{V_m}\left[\left(\frac{V_m}{V}\right)^{\frac{1}{3}} - \frac{\frac{1}{2}V_m}{V}\right] \quad \text{Affine model} \tag{1.5}$$

$$\pi_{el} = -\frac{RT v_{eff}}{2V_m}\left(\frac{V_m}{V}\right)^{\frac{1}{3}} \quad \text{Free phantom model} \tag{1.6}$$

where tR, χ and T are the gas constant, the polymer-solvent interaction parameter, and the temperature, respectively. v_{eff} is the effective crosslinking density. V_0, V, and V_m, are the volume of the hydrogel in the dry, swollen, and fully relaxed states, respectively.

If the polymer-chain segments within the hydrogel network contain ionizable groups, the swelling force has been observed to be greatly enhanced as a result of the immobilized charge groups attached to the polymer chains.[46] This extra swelling force is often treated as the osmotic pressure across the semipermeable membrane: excessive amount of charge groups trapped inside the hydrogel network build up a negative osmotic pressure that makes the gel absorb excessive solvent from the external solution. Given that the ions in the solution are dilute, the extra swelling pressure due to the trapped ions becomes

$$\pi_{ion} = RT \sum_x (c_x - c_x^*) \tag{1.7}$$

where c_x and c_x^* are the concentration of charge groups inside and outside the hydrogel. The concentration difference of the charged groups inside and outside of the hydrogel is governed by the Donnan potential at the hydrogel-solvent interface. At equilibrium

state, the sum of the osmotic pressure vanishes, indicating a free of stress condition on the homogeneously swollen hydrogels.

1.3.2 Inhomogeneous Swelling of Hydrogels

Unlike homogenous swelling of the gel, where only volume of the polymer gel changes, inhomogeous swelling of the hydrogel can generate actuation due to unevenly distributed volume expansion of the materials. Inhomogeneous state of swelling equilibrium occurs when the network itself is in modulated (e.g. gradient crosslinking density[6, 47] and chemical composition[48]), or when network is subjected to anisotropic mechanical load or geometric constraint (e.g. confined swelling [15, 49-52]). Here, swelling can induce cavitation,[53] delamination,[54] creasing,[55, 56] and other forms of instability upon confinement to substrate.[57] Inhomogeous swelling can also be found on structural actuation of free-standing polymer films. In this case, the actuation can be simple swelling[58, 59] and bending,[49] and/or more complex folding and buckling.[6, 47]

On patterned substrates, the degree of swelling can be transduced into delicately controlled mechanical actuation in micro-scale. We and other have shown that swelling of elastomers and crosslinked photoresists can induce interesting pattern transformation on both hexagonal pore arrays and square pore arrays.[19, 26, 60] In microfluidic channel, microfluidic device, the micro-patterned responsive hydrogels can be used as valves to turn on and off the liquid flow. Micro-structured protein hydrogels fabricated by multi-photon polymerization are demonstrated for actuation for investigating dynamic tissue engineering.[61] By incorporating non-swollen components, the micro-patterned hydrogel films can be actuated to form complex origami structures.[62]

The inhomogenous hydrogel swelling has been widely used in applications, including artificial muscles,[63, 64] foldable structures,[64] micro-robotics,[62] adapted lens,[13] and chemo-mechano[8, 65] or chemo-optical sensors.[17, 59, 66, 67] Meanwhile, micro-patterned hydrogel offers model systems to study complex swelling of other polymer system, e.g. rubber in organic solvent,[68] and photoresist deformation during fabrication process.[69, 70] due to the well-controlled swelling, simplicity, and biocompatibility. Swelling instability has been observed during the growth of biological systems, which can explain the formation of unique morphologies on surfaces such as fruits and leaves.[71]

1.3.3 Swelling of pH and Thermal Responsive Copolymer Hydrogels

Stimuli-responsiveness of hydrogels is often related to the volume phase transitions triggered by external environmental change. This process is reversible and also known as swelling-deswelling transition.[43] The volume phase transition can be triggered by a variety of stimuli that altering the equilibrium among the ionic osmotic pressure, network elasticity, and enthalpy of mixing in the polymer network. In my study, we created hydrogels from poly(2-hydroxyethyl methacrylate) (PHEMA), poly(acrylic acid) (PAA), and poly(N-isopropyl acrylamide) (PNIPAM) (Fig. 1.7).
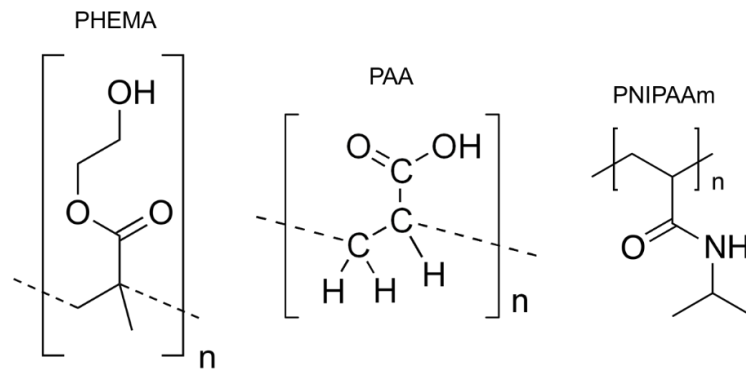
Figure 1.7 Chemical structures of hydrophilic polymers, PHEMA, PAA, and PNIPAAm.

PHEMA has been widely utilized in fabrication of micro-structured hydrogels due to its mechanical integrity at both dry and wet states.[31] In the dry state, PHEMA has T_g ~ 100 °C and Young's modulus ~ 1-3 GPa.[72] After immersing in the aqueous environment, the polymer network quickly absorb water and become hydrogels.

PAA is pH responsive due to ionization of polymer chain at different pH. At pH > pK_a of the acylic acid (~ 4.3), the polymer chains are fully deprotonated, and the PAA based hydrogels become ionic[73]; volume increases significant due to the osmotic pressure driven by the ionic strength difference within the hydrogel and external aqueous environments. When pH is smaller than pK_a of the acrylic acid, the PAA based hydrogel becomes non-ionic and the swelling ratio decreases.

The PNIPAAm hydrogel has a sharp volume phase transition near ~33°C.[43] This effect is due to the chain transformation from a coiled (swollen) to globular (collapsed) state above the lower critical solution temperature (LCST) of the hydrogel.[73] Below LCST, the network swells due to the favored interactions between the PNIPAAm

chains and water molecules. Above LCST, PNIPAAm chains become hydrophobic and phase separate from water, thus, the hydrogel collapses, expels water.

1.4 Pattern Transformation with Different Structures and Mechanisms

To harvest buckling instability in two-dimensional (2D) porous membranes with other periodic hole array, we and others have investigated a wide variety of materials systems with different geometries.

1.4.1 Pattern Transformation of Porous Membranes with Different Geometries

The homogenously collapsed void space within the cellular solid structure can result in significant compaction and alteration of mechanical property of the lattice materials.[29, 37] The engineered pore size, shape,[28] [29] and arrangement[37] of the cellular solid has been found to strongly affect the compaction behavior and mechanical property alteration. Bertoldi *et al*. have demonstrated that above the buckling threshold, periodic porous membrane undergoes a dramatic transition in elastic modulus and Possion's ratio.[28] In particular, the negative Poisson's ratio behavior can be triggered upon the buckling of the entire structures, offering a unique mechanical response of the materials. Meanwhile, the refined cellular solid structures have demonstrated up to 40% volume shrinkage under a modest stress[29] and the possibility of forming of chiral patterns [37] have been later demonstrated by varying the pore shape and location. These unique compaction behaviors will be of interests for applications including mechanical metamaterials[28] and foldable or deployable devices. As mentioned in the Sections 1.1-1.2, porous membranes undergoing pattern transformation can be designed by considering kinematic models. The mechanical responses of the membranes as a result of pattern transformation are also investigated

in macroscopic scale due to the easy actuation and characterization of the deformation. The pattern transformation behavior was found strongly dependent on the pore size, shape, and geometry. The related research is reviewed as follows.

Effect of Pore size. Bertolding *et al*. investigate the effects of porosity to the pattern transformation, which suggests that pattern transformation only occurs at a porosity above a certain threshold.[28] For example, for square arrays of circular pores the pattern transformation under uniaxial compression only occur at porosity above 34%. For porosity lower than 34%, the collapsing behavior is dominated by macroscopic structural change, *i.e*. formation of the collapsing band in the cellular structures (see Fig. 1-8 a). Meanwhile, the porosity of the structure strongly affects uniaxial compression strain that triggers buckling instability: the critical strain increases as the porosity of cellular structure decreases (see Fig. 1-8 b). Similar effects were also demonstrated on other type of lattices, including examples shown in Fig. 1.4.[37]
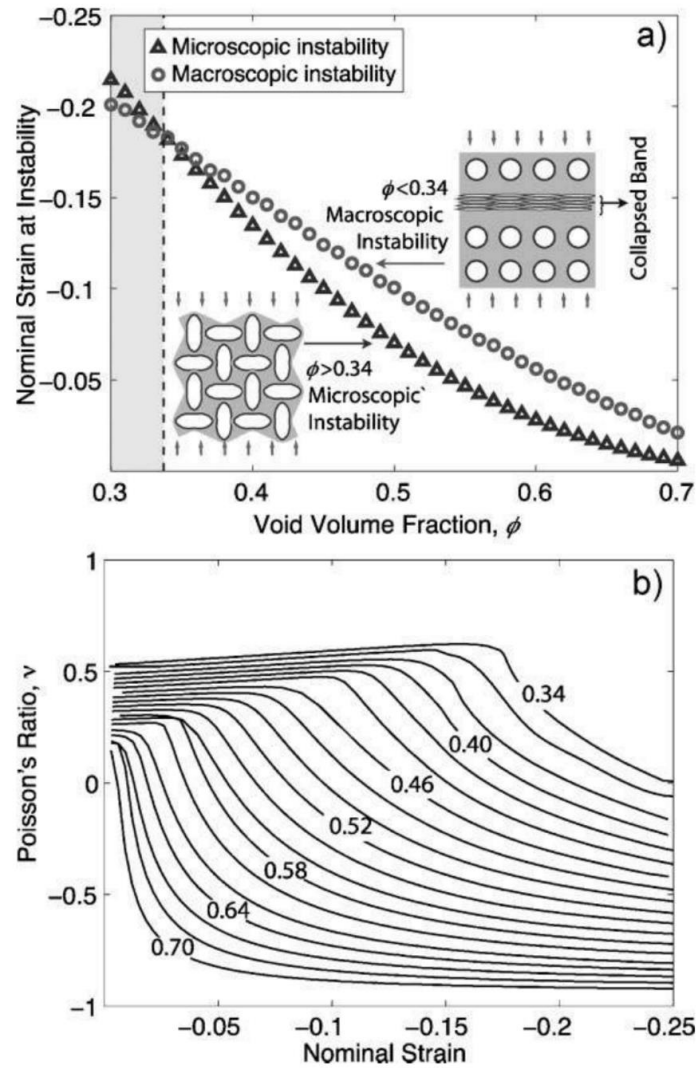
Figure 1.8 effects of pore filling fraction on the pattern transformation of periodic porous membranes. (a) shows the two types of collapsing mechanism: microscopic instability vs. macroscopic instability at porosity > 0.34 and porosity < 0.34, respectively. (b) Variation of Poisson's ratio upon changing of the porosity. The transition from positive to negative Poisson's ratio indicating the occurrence of pattern transformation.[28]

Effect of Pore shape. Overvelde *et al*. investigated the effects of pore shape by computer analysis and experiments, known as shape and topology optimization, in

comparison to experiments to investigate a spectra of porous structures that undergo pattern transformations.[29] The hole shape is found to provide a convenient parameter to control the pattern transformation: attractive features of soft porous systems, such as their compaction (quantified as change of structure planar area divided by original area) and negative Poisson's ratio effects were found strongly affected by the different shape of punctuated pores on the elastomeric membranes. Compared to square arrays of circular pores, structure B can be compacted with higher compacting ratio; and structure C instead of deformed microscopically, the structure buckled macroscopically due to the pore shape change.
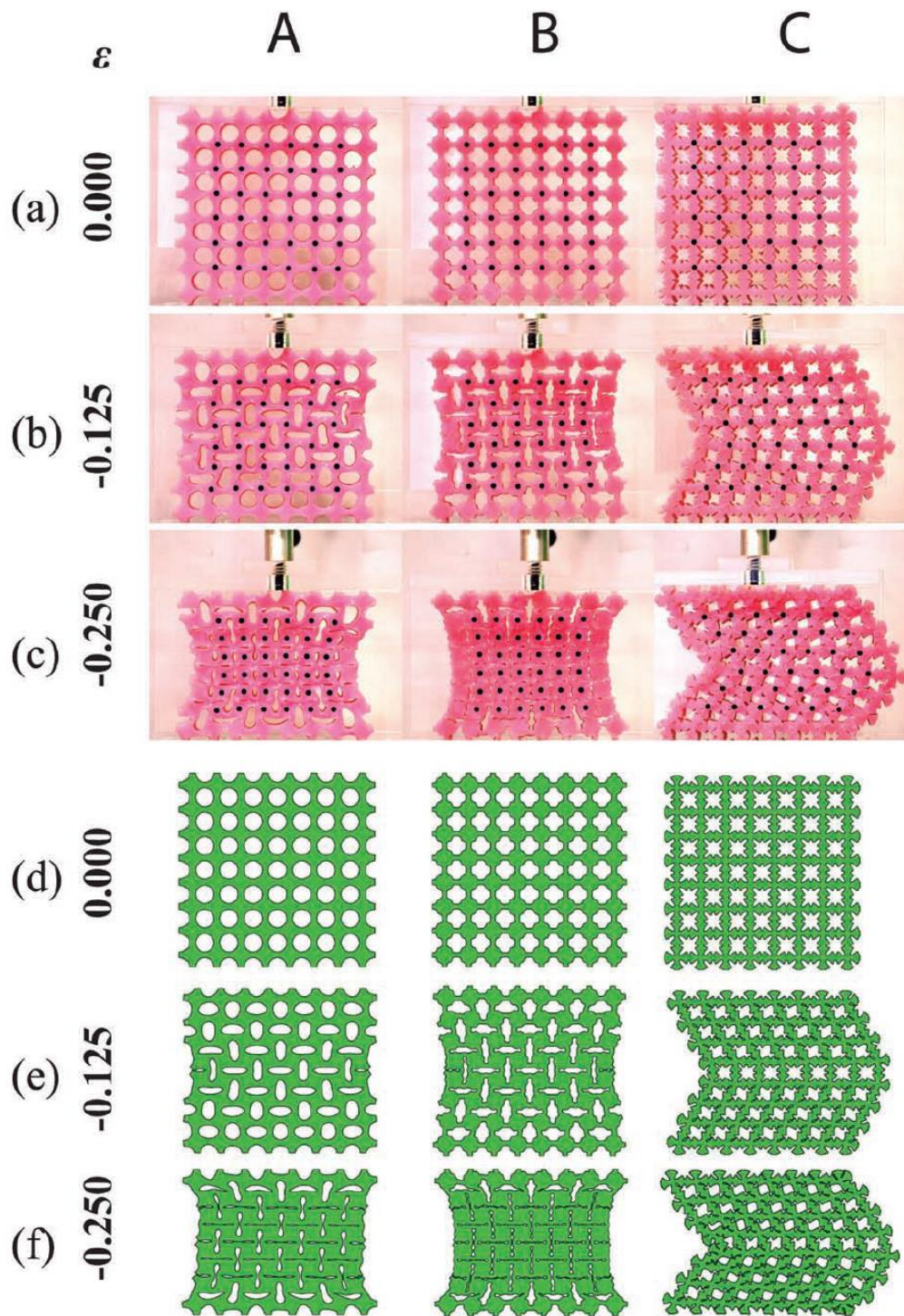
Figure 1.9 Variation of mechanical response at varied pore shapes. Here, A, B, and C have the same porosity but different shapes of pores. structure C was found to have macroscopic buckling effects that is different from structure A and B.[29] The numbers indicate the nominal strain applied to the structures.

Effect of Pore Distribution. By considering geometric constraints on the different kinematic models of collapsing (see Fig. 1.2 to 1.3), Shim *et al.* have also identified possible periodic distributions of uniform circular holes where mechanical instability can trigger pattern transformation between expanded (*e.g.* circular holes) and compacted (ellipse slits) states. In all of these structures, buckling instability is found to induce large negative values of incremental Poisson's ratio, and in two of them also the formation of chiral patterns via symmetry breaking process that was not previously observed.

Effect of application of the load: The buckling instability can be affected by the boundary conditions applied to the structures. For example, on a kagome lattice based porous membrane (see Section 1.2.2), due to large variety of collapsing modes prescribed by the kinematic model, the path way of deformation can be easily varied upon different applied boundary conditions. Sicong *et al.*[74] have demonstrated that for a kagome lattice based porous membrane, by varying the loading condition to the porous materials, different pattern transformed structures can be obtained (Fig. 1.10). As we can see in Fig. 1.10, the applied forces are guided by extra elements embedded in the compression tests, it was clear that after transformation, the new structures are completely different from each other at varying loading conditions. In their study, this unique transformation behavior has been used as tunable template for direct the propagation of elastic waves.
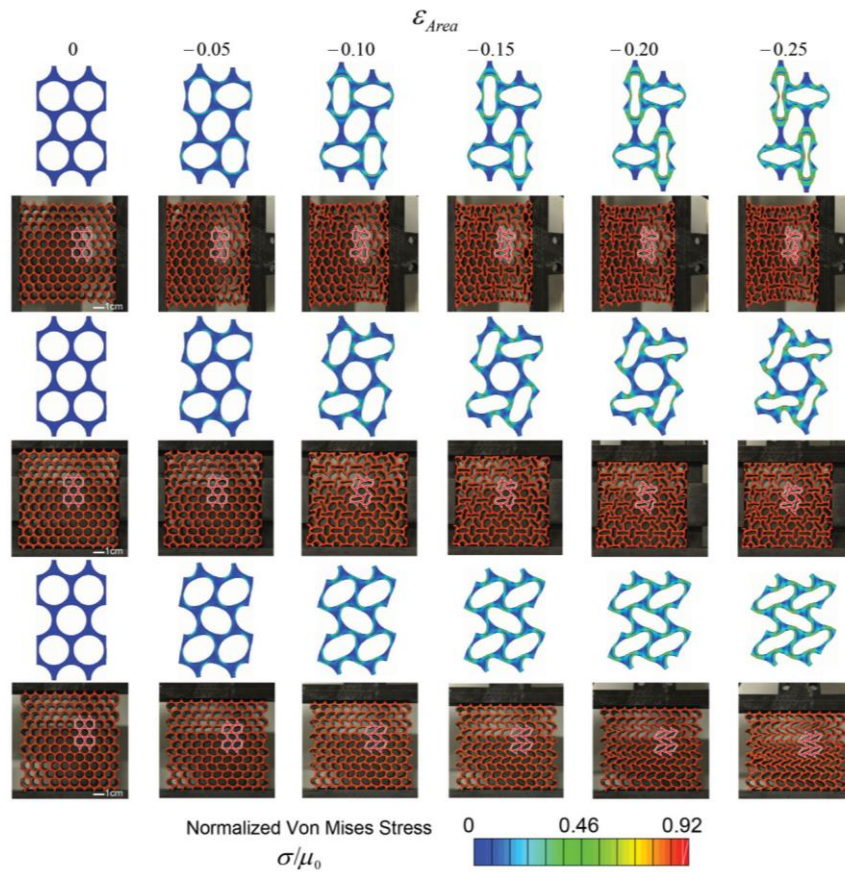
Figure 1.10 The varied paths of transformation upon structural deformation triggered by different external stress fields.[74]

1.4.2 Pattern Transformation at (sub)Micron-scale in Different Material Systems

Triggering the pattern transformation at micro-scale requires driving forces that uniformly applied to the individual repeating units on the periodic structures. The process can be initiated by mechanical forces,[75] osmotic pressure, [60] and capillary force[31]. Meanwhile, to realize the reversible switching behavior for demanding of fabricating practical device, it requires both mechanism of locking the transformation pattern and mechanisms of the recovery process that allow the periodic pattern to be reusable. So far the pattern transformation has been triggered

in multiple materials systems. Here, the transformation mechanisms are categorized by driving forces and materials, and reviewed as following.

Swelling induced pattern transformation. Zhang *et al*.[60] first demonstrated the pattern transformation in nanoscale in poly(dimethylsiloxane) (PDMS, Fig. 1.11 a) membranes patterned with periodic pore arrays (*e.g*. pore diameter of 1 μm and periodicity of 2 μm). When exposed to an organic solvent, such as toluene, PDMS swell by as much as 130% in volume. The swelling can induce negative osmotic pressure, triggering buckling instability; the circular pores snap shut to relieve the stress much like the joints in railways and bridges expand and contract to maintain structural integrity in response to changes in moisture and temperature. Here, the elastomeric behavior of the PDMS allows the recovery of transformed pattern back to the initial state after removal of the solvent. Meanwhile, by suspending functional nanoparticles in the solvent, faithfully printed the emergent patterns onto flat and curved substrates was achieved (Fig. 1.11 b). It is worth noting that due to the pattern transformation, the imprinted pattern can have much smaller dimension compared to the initial pattern on the PDMS, providing new nanofabrication techniques with pattern transformed imprinting.[60] This elastic instability in terms of elastically interacting "dislocation dipoles" was found to provide extreme useful tool of predicting the transformed patterns, and thus allows us manipulate the structural details of the membrane to tailor the elastic distortions and generate a variety of nanostructures.

Figure 1.11 Procedure of swelling induced pattern transformation on PDMS membrane. (a) Chemical structures of PDMS and toluene; (b) Triggering process of pattern transformation; (c) from left to right: pattern before, pattern after pattern transformation, and imprinted nanoparticles on the substrate. [60]

Due to the elastic nature, the transformed pattern of PDMS cannot be locked. Jang *et al*.[19] latter utilize solvent induced shape memory effects in hexagonal pore arrays made from photocrosslinked SU-8 photoresist (pore diameter of 410 nm and periodicity of 610 nm), which swells in a good solvent. Upon exposing a poor solvent, polymer chains collapse from the solvent, quickly raising the T_g of the polymer network to lock the deformed structure. In turn, the authors demonstrated switching of phononic band gap properties.

(a) (b)

Figure 1.12 (a) Chemical structure of SU8 photoresist. (b) SEM images of the structure before and after swelling induced pattern transformation (locked by freezing with non-favored solvents); the bottom shows the schematics of pattern transformation and recovery process.[19]

Nevertheless, to trigger the recovery of the transformed pattern, the membranes have to be exposed to the organic solvent to induce the relaxation of the polymer chains in the photoresist network, which may not be desirable for many applications.

Shape Memory Effects with Mechanical Compression. To further improve the switching properties, Li *et al.*[75] patterned hexagonal arrays of pores from epoxy shape memory polymers (SMPs) with diameter 1.2 μm and periodicity of 2.5 μm. As an characteristics of SMPs, the temporary shape of the materials after deformation can be locked upon cooling while the original shape can be memorized upon heating above, *e.g.* glassy transition temperature (T_g) or melting temperature (T_m) to release the stored elastic energy. When hot-pressed at temperature higher than the transition temperature, the circular holes were deformed to an array of elliptical slits (with

width of tens of nanometers). Further compression leads to a flatten surface, therefore, switching the membrane with diffraction color to a transparent film. The deformed pattern and the resulting color change can be fixed at room temperature, both of which could be recovered upon reheating due to the shape memory effects. Using finite element analyses, we further modeled the pattern transformation and recovery processes. The deformation, the cooling step, and the complete recovery of the microstructure is found corroborated well with experimental observations.
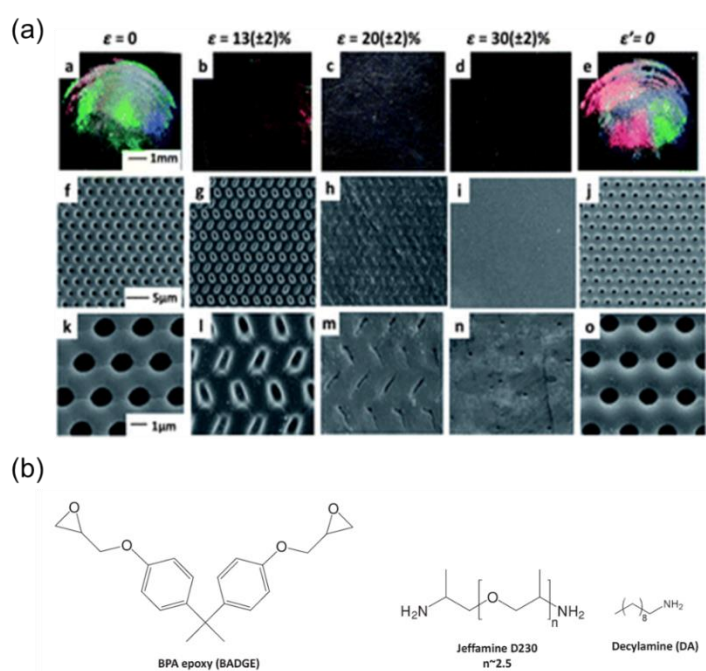
Figure 1.12 (a) The deformation and optical effects of porous membrane patterned with hexagonal arrays of pores at different loading strain. (b) The chemical composition of the shape memory polymers used for making the membrane. [75]

Polymerization Induced Pattern Transformation, Singamaneni *et al.* [26, 27] observed pattern transformation when polymerizing acrylic acid monomers within periodic pore arrays (380 nm diameter and 830 nm periodicity) made of SU-8

photoresists. The driving force was identified as the compressive stress induced by the volume shrinkage of the crosslinked PAA at the wall of the nano-pores (Fig. 1-11). pattern transformation at local regions could be induced by micro-patterning.[27]
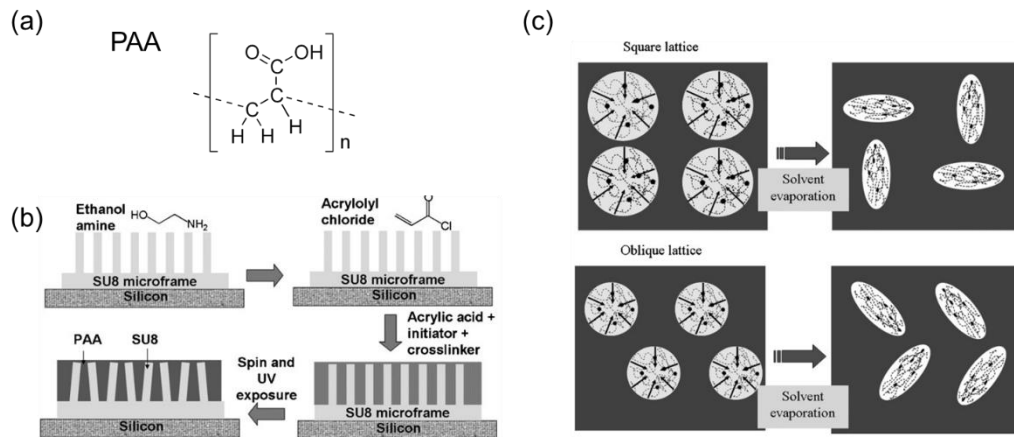
Figure 1.13 (a) Chemical structure of PAA. (b-c) Schematics showing the procedures of inducing pattern transformation on SU-8 membrane and its mechanism.[27]

Capillary Force Induced Pattern Transformation. More recently, we investigated PHMA hydrogel (Fig. 1-14 a) in pattern transformation. The membrane consists of square arrays of pores with diameter of 1 μm and periodicity of 2 μm. Zhu *et al.*[31] did not observe swelling induced pattern transformation when immersing the hydrogel membrane into water (Fig. 1-14 b) due to the lower degree of swelling of the hydrogel materials. Instead, the pattern transformation occurs upon the drying process triggered by the capillarity during the water evaporation. Here, the water meniscus breaks on top of the micro-pores that induces sufficient contraction force buckle the microspores (Fig, 1.14 c). The transformed pattern is locked due to the increased T_g of polymer upon drying (see Fig. 1.14 b-c).
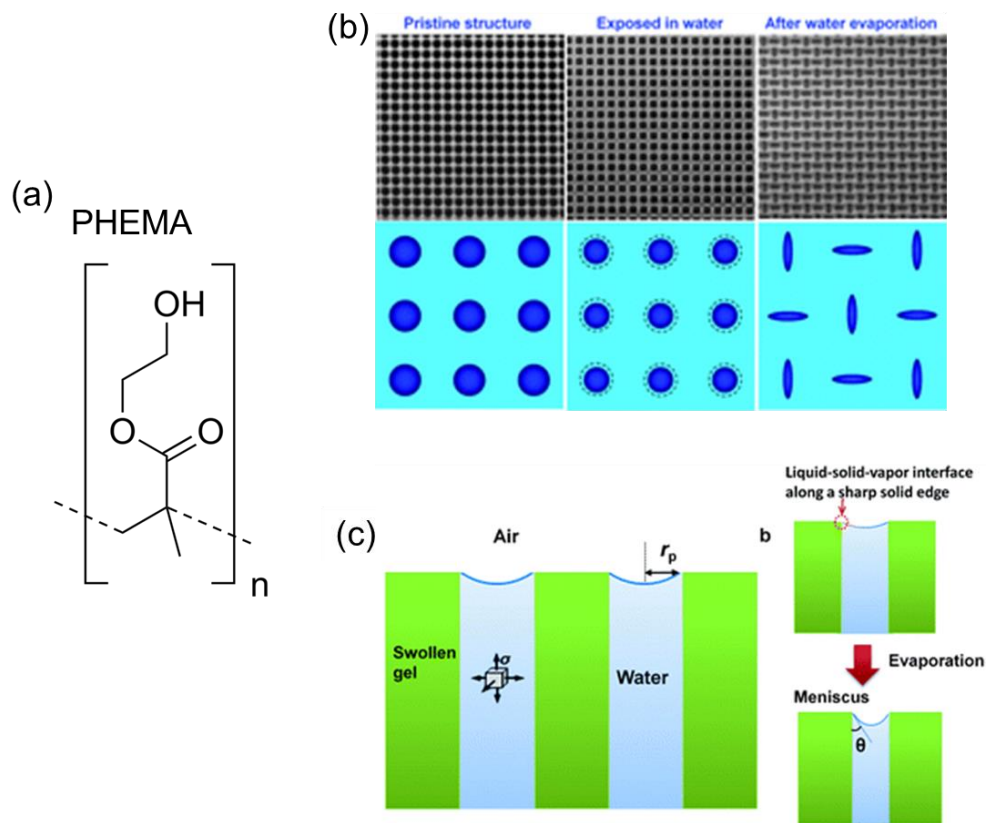
Figure 1.14 (a) Chemical structure of PHEMA. (b) The hydrogel membrane at different conditions: dry, wet, and re-dried state. (c) Illustration of the capillary force exerted on a drying PHEMA hydrogel membrane to induce the bucking closure of the hydrogel micro-pores.[31]

1.5 References

1. Kovács, F., et al., *A class of expandable polyhedral structures.* International Journal of Solids and Structures, 2004. **41**(3–4): p. 1119-1137.

2. Agrawal, S.K., M. Yim, and S. Kumar, *Polyhedral Single Degree-of-freedom Expanding Structures: Design and Prototypes.* Journal of Mechanical Design, 2002. **124**(3): p. 473-478.

3. Forterre, Y., et al., *How the Venus flytrap snaps.* Nature, 2005. **433**(7024): p. 421-425.

4. Sutherland, R.L., et al., *Cephalopod coloration model. II. Multiple layer skin effects.* Journal of the Optical Society of America A, 2008. **25**(8): p. 2044-2054.

5. Wu, Z.L., et al., *Three-dimensional shape transformations of hydrogel sheets induced by small-scale modulation of internal stresses.* Nat Commun, 2013. **4**: p. 1586.

6. Kim, J., et al., *Designing Responsive Buckled Surfaces by Halftone Gel Lithography.* Science, 2012. **335**(6073): p. 1201-1205.

7. Liu, D., et al., *Single-composition three-dimensionally morphing hydrogels.* Soft Matter, 2013. **9**(2): p. 588-596.

8. He, X., et al., *Synthetic homeostatic materials with chemo-mechano-chemical self-regulation.* Nature, 2012. **487**(7406): p. 214-218.

9. Sidorenko, A., et al., *Reversible Switching of Hydrogel-Actuated Nanostructures into Complex Micropatterns.* Science, 2007. **315**(5811): p. 487-490.

10. van Oosten, C.L., C.W.M. Bastiaansen, and D.J. Broer, *Printed artificial cilia*

from liquid-crystal network actuators modularly driven by light. Nat Mater, 2009. **8**(8): p. 677-682.

11. Glazer, P.J., et al., *Multi-Stimuli Responsive Hydrogel Cilia.* Adv. Funct. Mater., 2013: p. n/a-n/a.

12. le Digabel, J., et al., *Magnetic micropillars as a tool to govern substrate deformations.* Lab Chip, 2011. **11**(15): p. 2630-2636.

13. Dong, L., et al., *Adaptive liquid microlenses activated by stimuli-responsive hydrogels.* Nature, 2006. **442**(7102): p. 551-554.

14. Shimamoto, N., et al., *Nanopattern Fabrication of Gold on Hydrogels and Application to Tunable Photonic Crystal.* Adv. Mater., 2012. **24**(38): p. 5243-5248.

15. Beebe, D.J., et al., *Functional hydrogel structures for autonomous flow control inside microfluidic channels.* Nature, 2000. **404**(6778): p. 588-590.

16. Ehrick, J.D., et al., *Genetically engineered protein in hydrogels tailors stimuli-responsive characteristics.* Nat. Mater., 2005. **4**(4): p. 298-302.

17. Lee, Y.J. and P.V. Braun, *Tunable Inverse Opal Hydrogel pH Sensors.* Advanced Materials, 2003. **15**(7-8): p. 563-566.

18. Luo, Y. and M.S. Shoichet, *A photolabile hydrogel for guided three-dimensional cell growth and migration.* Nat Mater, 2004. **3**(4): p. 249-253.

19. Jang, J.-H., et al., *Combining Pattern Instability and Shape-Memory Hysteresis for Phononic Switching.* Nano Letters, 2009. **9**(5): p. 2113-2119.

20. Chu, K.-H., R. Xiao, and E.N. Wang, *Uni-directional liquid spreading on asymmetric nanostructured surfaces.* Nat Mater, 2010. **9**(5): p. 413-417.

21.   Arsenault, A.C., et al., *Photonic-crystal full-colour displays.* Nat Photon, 2007. **1**(8): p. 468-472.

22.   Kim, J., J. Yoon, and R.C. Hayward, *Dynamic display of biomolecular patterns through an elastic creasing instability of stimuli-responsive hydrogels.* Nat Mater, 2010. **9**(2): p. 159-164.

23.   Bertoldi, K., et al., *Mechanics of deformation-triggered pattern transformations and superelastic behavior in periodic elastomeric structures.* Journal of the Mechanics and Physics of Solids, 2008. **56**(8): p. 2642-2668.

24.   Zdebek P.Bazant, L.C., *Stability of structures elastic, inelastic, fracture, and damage theories*. The Oxford engineering science seriers. 1991, New York Oxford: Oxford University Press.

25.   Mullin, T., et al., *Pattern Transformation Triggered by Deformation.* Physical Review Letters, 2007. **99**(8): p. 084301.

26.   Singamaneni, S., et al., *Instabilities and Pattern Transformation in Periodic, Porous Elastoplastic Solid Coatings.* ACS Applied Materials & Interfaces, 2008. **1**(1): p. 42-47.

27.   Singamaneni, S., et al., *Bifurcated Mechanical Behavior of Deformed Periodic Porous Solids.* Advanced Functional Materials, 2009. **19**(9): p. 1426-1436.

28.   Bertoldi, K., et al., *Negative Poisson's Ratio Behavior Induced by an Elastic Instability.* Advanced Materials, 2010. **22**(3): p. 361-366.

29.   Overvelde, J.T.B., S. Shan, and K. Bertoldi, *Compaction Through Buckling in 2D Periodic, Soft and Porous Structures: Effect of Pore Shape.* Advanced Materials, 2012. **24**(17): p. 2337-2342.

30.   Zhu, X.L., et al., *Two-Dimensional Photonic Crystals with Anisotropic Unit*

Cells Imprinted from Poly(dimethylsiloxane) Membranes Under Elastic Deformation. Appl. Phys. Lett., 2008. **93**(16): p. 161911.

31. Zhu, X., et al., *Capillarity induced instability in responsive hydrogel membranes with periodic hole array.* Soft Matter, 2012. **8**(31): p. 8088-8093.

32. Grima, J.N., et al., *On the auxetic properties of generic rotating rigid triangles.* Proceedings of the Royal Society A: Mathematical, Physical and Engineering Science, 2012. **468**(2139): p. 810-830.

33. Hutchinson, R.G. and N.A. Fleck, *The structural performance of the periodic truss.* Journal of the Mechanics and Physics of Solids, 2006. **54**(4): p. 756-782.

34. Tantikom, K., Y. Suwa, and T. Aizawa, *In-Plane Compression Response of Regularly Cell-Structured Materials.* MATERIALS TRANSACTIONS, 2004. **45**(2): p. 509-515.

35. Gibson, L.J. and M.F. Ashby, *Cellular Solids: Structure and Properties*. 1997: Cambridge University Press.

36. Sun, K., et al., *Surface phonons, elastic response, and conformal invariance in twisted kagome lattices.* Proceedings of the National Academy of Sciences, 2012. **109**(31): p. 12369-12374.

37. Shim, J., et al., *Harnessing instabilities for design of soft reconfigurable auxetic/chiral materials.* Soft Matter, 2013.

38. Jang, D., et al., *Fabrication and deformation of three-dimensional hollow ceramic nanostructures.* Nat Mater, 2013. **advance online publication**.

39. Russell, P., *Photonic Crystal Fibers.* Science, 2003. **299**(5605): p. 358-362.

40. Zhang, Z., S. Liu, and Z. Tang, *Crashworthiness investigation of kagome*

honeycomb sandwich cylindrical column under axial crushing loads. Thin-Walled Structures, 2010. **48**(1): p. 9-18.

41.   Peppas, N.A., et al., *Hydrogels in biology and medicine: From molecular principles to bionanotechnology.* Adv. Mater., 2006. **18**(11): p. 1345-1360.

42.   Gerlach, G.A., Karl-Friedrich, *Hydrogel Sensors and Actuators.* Springer Series on Chemical Sensors and Biosensors, Vol. 6. 2010: Springer.

43.   Peppas, N.A., et al., *Hydrogels in Biology and Medicine: From Molecular Principles to Bionanotechnology.* Advanced Materials, 2006. **18**(11): p. 1345-1360.

44.   Flory, P., J, *Principle of Polymer Chemistry.* 1953, New York: Cornell University Press: Ithaca.

45.   Brannon-Peppas, L. and N.A. Peppas, *Equilibrium swelling behavior of pH-sensitive hydrogels.* Chemical Engineering Science, 1991. **46**(9ab06519-a550-befb-c700-05865ceb8ae2): p. 715-1437.

46.   Ricka, J. and T. Tanaka, *Swelling of ionic gels: quantitative performance of the Donnan theory.* Macromolecules, 1984. **17**(12): p. 2916-2921.

47.   Klein, Y., E. Efrati, and E. Sharon, *Shaping of Elastic Sheets by Prescription of Non-Euclidean Metrics.* Science, 2007. **315**(5815): p. 1116-1120.

48.   Yoon, J., et al., *Local Switching of Chemical Patterns through Light-Triggered Unfolding of Creased Hydrogel Surfaces.* Angewandte Chemie International Edition, 2012. **51**(29): p. 7146-7149.

49.   Stoychev, G., et al., *Hierarchical Multi-Step Folding of Polymer Bilayers.* Advanced Functional Materials, 2013. **23**(18): p. 2295-2300.

50.   Kolodziej, C.M. and H.D. Maynard, *Shape-Shifting Micro- and Nanopatterns Controlled by Temperature.* Journal of the American Chemical Society, 2012. **134**(30): p. 12386-12389.

51.   Shim, T.S., et al., *Controlled Origami Folding of Hydrogel Bilayers with Sustained Reversibility for Robust Microcarriers.* Angewandte Chemie International Edition, 2012. **51**(6): p. 1420-1423.

52.   Qu, J.B., et al., *A pH-Responsive Gating Membrane System with Pumping Effects for Improved Controlled Release.* Advanced Functional Materials, 2006. **16**(14): p. 1865-1872.

53.   Wu, G., Y. Xia, and S. Yang, *Buckling, symmetry breaking, and cavitation in periodically micro-structured hydrogel membranes.* Soft Matter, 2014. **10**(9): p. 1392-1399.

54.   Singamaneni, S., M.E. McConney, and V.V. Tsukruk, *Swelling-Induced Folding in Confined Nanoscale Responsive Polymer Gels.* ACS Nano, 2010. **4**(4): p. 2327-2337.

55.   Cai, S., et al., *Osmotic collapse of a void in an elastomer: breathing, buckling and creasing.* Soft Matter, 2010. **6**(22): p. 5770-5777.

56.   Yoon, J., et al., *Poroelastic swelling kinetics of thin hydrogel layers: comparison of theory and experiment.* Soft Matter, 2010. **6**(23): p. 6004-6012.

57.   Hong, W., Z. Liu, and Z. Suo, *Inhomogeneous swelling of a gel in equilibrium with a solvent and mechanical load.* International Journal of Solids and Structures, 2009. **46**(17): p. 3282-3289.

58.   Gupta, S., et al., *Poly(N-isopropyl acrylamide)−Gold Nanoassemblies on Macroscopic Surfaces: Fabrication, Characterization, and Application.*

Chemistry of Materials, 2009. **22**(2): p. 504-509.

59. Shimamoto, N., et al., *Nanopattern Fabrication of Gold on Hydrogels and Application to Tunable Photonic Crystal.* Advanced Materials, 2012. **24**(38): p. 5243-5248.

60. Zhang, Y., et al., *One-Step Nanoscale Assembly of Complex Structures via Harnessing of an Elastic Instability.* Nano Letters, 2008. **8**(4): p. 1192-1196.

61. Kaehr, B. and J.B. Shear, *Multiphoton fabrication of chemically responsive protein hydrogels for microactuation.* Proceedings of the National Academy of Sciences, 2008. **105**(26): p. 8850-8854.

62. Na, J.-H., et al., *Programming Reversibly Self-Folding Origami with Micropatterned Photo-Crosslinkable Polymer Trilayers.* Advanced Materials, 2015. **27**(1): p. 79-85.

63. Palleau, E., et al., *Reversible patterning and actuation of hydrogels by electrically assisted ionoprinting.* Nat Commun, 2013. **4**.

64. Mao, Y., et al., *Sequential Self-Folding Structures by 3D Printed Digital Shape Memory Polymers.* Scientific Reports, 2015. **5**: p. 13616.

65. Glazer, P.J., et al., *Multi-Stimuli Responsive Hydrogel Cilia.* Advanced Functional Materials, 2013: p. n/a-n/a.

66. Hu, X., et al., *Ultrasensitive Specific Stimulant Assay Based on Molecularly Imprinted Photonic Hydrogels.* Advanced Functional Materials, 2008. **18**(4): p. 575-583.

67. Kozlovskaya, V., et al., *Ultrathin Layer-by-Layer Hydrogels with Incorporated Gold Nanorods as pH-Sensitive Optical Materials.* Chemistry of Materials, 2008. **20**(24): p. 7474-7485.

68.   Hong, W., et al., *A theory of coupled diffusion and large deformation in polymeric gels.* Journal of the Mechanics and Physics of Solids, 2008. **56**(5): p. 1779-1793.

69.   Jiang, C., et al., *Complex Buckling Instability Patterns of Nanomembranes with Encapsulated Gold Nanoparticle Arrays.* Nano Letters, 2006. **6**(10): p. 2254-2259.

70.   Chen, C.-M., J.C. Reed, and S. Yang, *Guided wrinkling in swollen, pre-patterned photoresist thin films with a crosslinking gradient.* Soft Matter, 2013. **9**(46): p. 11007-11013.

71.   Wheeler, T.D. and A.D. Stroock, *The transpiration of water at negative pressures in a synthetic tree.* Nature, 2008. **455**(7210): p. 208-212.

72.   Guvendiren, M., S. Yang, and J.A. Burdick, *Swelling-Induced Surface Patterns in Hydrogels with Gradient Crosslinking Density.* Advanced Functional Materials, 2009. **19**(19): p. 3038-3045.

73.   Chen, G.H. and A.S. Hoffman, *GRAFT-COPOLYMERS THAT EXHIBIT TEMPERATURE-INDUCED PHASE-TRANSITIONS OVER A WIDE-RANGE OF PH.* Nature, 1995. **373**(6509): p. 49-52.

74.   Shan, S., et al., *Harnessing Multiple Folding Mechanisms in Soft Periodic Structures for Tunable Control of Elastic Waves.* Advanced Functional Materials, 2014. **24**(31): p. 4935-4942.

75.   Li, J., et al., *Switching periodic membranes via pattern transformation and shape memory effect.* Soft Matter, 2012. **8**(40): p. 10322-10328.

Chapter 2: Self-Assembly of Nanoparticles

2.0 Introduction

Self-assembly of nanoparticles dictated by the interactions between the constituents and the external conditions (temperature, pressure or the chemical composition of the solution)[1] plays an important role in scaling up the fabrication of functional materials for potential applications, including coatings,[2-5] energy storage,[6, 7] materials mechanical property enhancement,[8] sensing/actuation,[9] and electronics.[9]

For applications of nanoparticle assemblies over a large area, it is important that both the synthesis and assembly of nanoparticles should be simple, versatile, and at low cost. Meanwhile, to precisely control the assembled structures, which often involves more complex systems in a small area, it requires careful control of the particle size, shape, and inter-particle interactions to achieve the final morphology.[10] In this part of my thesis, I will review: (1) superhydrophobic coating obtained from nanoparticle assemblies, and (2) physical confinement of nanoparticles to investigate packing of colloidal particles and related morphologies.

2.1 Nanoparticle Synthesis and Morphology Control

In general, the nanoparticles can be characterized by their size, shape, and chemistry, including polymers,[11] ceramics,[12] metal oxide,[13] metal,[14, 15] and semiconductors.[15] Their synthesis typically involves top-down and bottom-up methods.[1] In top-down approaches, the bulk materials are physically broken into pieces in nanoscale by, e.g. grinding, milling and ultrasound, nanolithography, and mechanical alloying.[16] Particles obtained by methods such as milling and ultrasound are often not uniform in size, but higher quantity and lower cost due to absence of chemical reactions.[16] They can also be patterned by lithography techniques, offering

precisely controlled size and shape.[17] nanoparticles can also be synthesized in the bottom-up manner, where the particles are formed from seeds or precursors. For example, in liquid phase synthesis, nanoparticles can be generated from processes, including chemical reduction, spray drying, electrospinning, so-gel reaction, co-precipitation, and hydrolysis.[16] To control particle size and shape from molecular assembly, it requires control of surface energy, selective growth on different crystal planes , and/or the molecular templates (e.g. surfactants).[18] Thus, the available morphology of the particles is typically limited. nanoparticles can also be prepared in the solid phase via, *e.g.* chemical vapor deposition, flame, thermal decomposition.[16]

2.1.1 Silica Nanoparticle Synthesis

Silica nanoparticles has been studied extensively in research and industrial applications due to their abundance on earth, low cost, easy to synthesize, and commercially available with well-controlled size and surface chemistry.[19] These nanoparticles have been widely used as fillers in engineering composite, coatings, structural color, fluorescent tracer, and carrier for catalytic substances.[20]

Sol-gel synthesis is the most widely used approach to produce pure silica particles with controlled size, size distribution and morphology ranging from 10 nm to a few microns.[20] I will review two processes of synthesizing anisotropic silica particles: using amino-acid as catalyst in sol-gel chemistry for generating both spherical and non-spherical particles and surfactant template assisted growth of rod-like silica nanoparticles.

2.1.1.1 So-gel Methods for Spherical Nanoparticles

For decades, the sol-gel process is widely applied to produce silica, glass, and ceramic materials at mild conditions. The process involves hydrolysis and condensation of silicon alkoxide (i.e. $Si(OR)_4$) such as tetraethylorthosilicate (TEOS) or inorganic salts such as sodium silicate (Na_2SiO_3) in the presence of mineral acid (e.g. HCl) or base.[21] In brief (see Fig. 2.1), the hydrolysis of TEOS molecules generates silanol groups. The condensation reactions between the silanol groups or between silanol groups and ethoxy groups lead to formation of siloxane bridges (Si–O–Si) that form silica. After nucleation, silica seeds grow into particles of different sizes. Two growth mechanisms are proposed in literature, including monomer addition and controlled aggregation [12]. The monomer addition model suggests that, after an initial burst of nucleation, the particle growth occurs through the addition of hydrolyzed monomers, the (primary) particle.[21] the aggregation model, however, argues that the nucleation occurs continuously throughout the reaction and the resulting nuclei (primary particles) will aggregate together to form dimmer, trimmer, and larger particles (secondary particles).[21] Both models lead to the formation of either spherical particles or gel network depending on the reaction conditions.
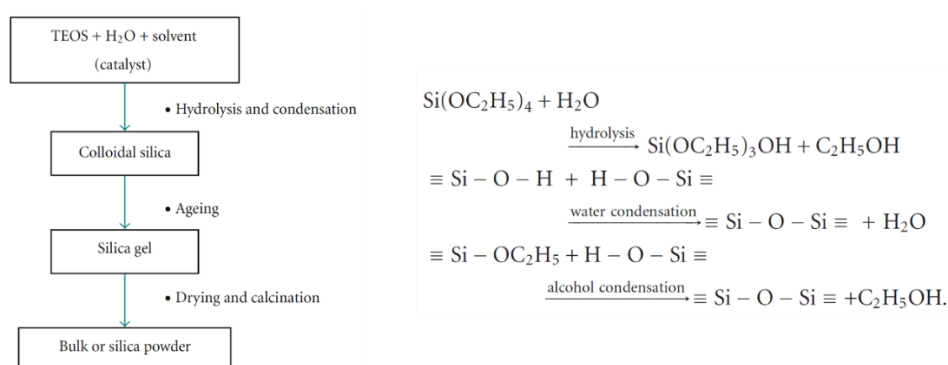
Figure 2.1. The schematics of silica sol-gel reaction and the hydrolysis/condensation chemical reactions occur during the synthesis.[20]

Stöber chemistry has been notified as the most adopted sol-gel methods for synthesizing silica particles ranging from 100 to 2000 nm in diameter.[12] It involves the use of aqueous alcohol solutions of silica alkoxides in the presence of ammonia as catalyst (basic condition) are used as major reaction ingredient. the synthesized silica particles can be used as seeds for further growth of larger with accurately controlled size and mono-dispersity, also known as modified Stöber growth methods.[12]

In 2006, Yokoi *et al*.[22] developed a simple yet novel liquid phase method to prepare uniform-sized silica nanospheres (SNSs) with size as small as 10's nm. The SNSs were synthesized through hydrolysis and condensation reactions of TEOS in the heterogeneous phase system containing TEOS as oil phase, and water phase consists of basic amino acids such as lysine and arginine under weakly basic conditions (pH 9-10). The major difference between this reaction and Stöber method is that the hydrolysis and condensation reaction occurs at the interface between the oil and water phases.[23] After the reaction, uniform-sized SNSs can be obtained and dispersed in homogeneous solutions without precipitation due to the strong negative surface charge. More recently, Hartlen *et al*.[23] reported the synthesis of monodispersed silica nanoparticles with controllable size from 10 nm to 100 nm. Despite these successes, the formation mechanism of the silica spheres and the role of the basic amino acid have not been fully understood. Tsapatsis and co-workers reported the preparation of silica nanospheres with a size of 5 nm by addition of TEOS to an unbuffered, aqueous solution of lysine and a few other types of amino acids (e.g. L-arginine).[24]

2.1.1.2 Anisotropic Silica Particles Synthesis

Amino-acid Induced Formation of Chain-like Nanoparticles. More interestingly, it was found that in the presence of amino acid (*e.g*. L-Arginine), seed nanoparticles with size ~ 20 nm, and ethanol water mixture, the seed nanoparticles can assemble into chain-like morphology due to the partially screened electrostatic repulsion, and reduced dielectric constant of the solvent.[25, 26] Followed by growth of addition silica layer to fix the shape of the particle assembly, the anisotropic chain-like silica particles (CNPs) can be synthesized. Ethanol and L-arginine (Arg) components in the reaction mixture are used to modify the dielectric constant and ionic strength of the reaction media, by which seed assembly is controlled. In addition to CNPs with wormlike structures, different kinds of NPs (bimodal spherical NPs, monodisperse spherical NPs, and particle network) have also been obtained by changing the concentrations of ethanol and Arg. The length, thickness, or both of CNPs are controlled systematically by varying the concentrations of Arg, seed NPs, and TEOS. Other alcoholic cosolvents, such as methanol, 1-propanol, 2-propanol, and t-butanol, are also effective to give CNPs when the dielectric constant of the alcohol-water mixed media is properly adjusted, showing the versatility of the present method.

Surfactant Templated Silica Nanorods. The silica rods were also reported to be synthesized by using a simple one-pot method: ethanol, water, sodium citrate, and ammonia were added to a solution of polyvinylpyrrolidone (PVP) in pentanol.[25] Upon further addition of TEOS, silica rods started to grow. It was found that the synthesized rods had one flat end and one rounded end, i.e. the rods are bullet shaped. The rods generally have a fixed diameter of 200-300 nm and a length varied from 300 nm to 3 μm (aspect ratios = length/diameter from 1 to ~10), depending on the

concentrations of reagents employed. The rod-like particles in general are highly monodisperse with density similar for spherical colloidal silica previously mentioned.

It is suggested that growth of nanorods first involves the formation of droplets composed of the precursor emulsions (see Fig. 2.2). In the second step, silica nucleus is formed on the surface the emulsion droplet initiated by the addition of the silica precursor TEOS. The hydrolyzed TEOS is only supplied from within the droplet and grows onto the existing nucleus rather than nucleating elsewhere. Due to this effect, the nucleus grows in one direction to form asymmetric rod-like particles.
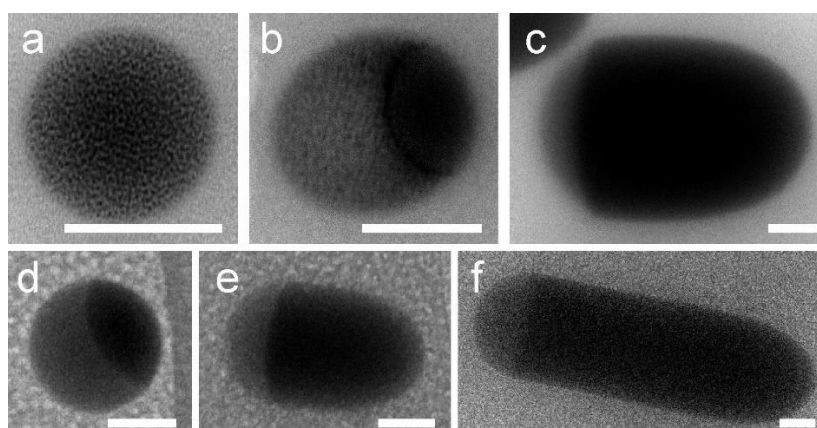
Figure 2.2. TEM images of the rods with emulsion droplets attached during growth after respectively 0, 30, and 180 min. (D-F). Scale bars are 100 nm. The images indicate a asymmetric growth of the particle leading to rod like morphology.

2.2 Self-assembly of Nanoparticles for Coatings.

Self-assembly is typically associated with thermodynamic equilibrium, where the organized structures being characterized as the minimum free energy state. Directed self-assembly employs the same basic principles of self-assembly except that the assembled structures are also affected by interaction of nanoparticles to external

environment including physical confinement (e.g. substrate, structural templates, and interfacial confinement) and external fields (e.g. electric fields, gravitational fields, flow fields and magnetic fields).[18] The process may give rise to non-equilibrium structures free from the constraints of entropy maximization. On the other hand, the presence of certain restriction on the assembly surface, e.g. liquid-air interface, or solid air interface, can also decrease the diversity of the assembled structures. For example, the formation of the colloidal crystals on flat substrates induced by capillary forces almost inevitably generates crystal structure with (111) plane of the lattice parallel to the substrate due to the favored interaction between particles and the substrate surface.[27]

To control nanoparticle assembly process, it is important to control the interactions between nanoparticle themselves and nanoparticles with external environment.[1] In this section, the inter-particle interactions, and their roles in the nanoparticle coating processes will be reviewed.

2.2.1 Nanoparticle Coatings

Nanoparticles are widely used for engineering the interfacial properties between two bulk-phase materials[18, 28] for applications, including adhesion promoters,[28] optical filters,[27] anti-reflective coatings,[29] and superhydrophobic coatings (citations). They are especially attractive to large scale nanostructures on the materials interfaces. They can be conveniently coated on flat and micro-structured substrates over large areas by different coating methods,[30] including spin coating,[4] dip coating,[31] electrostatic layer-by-layer deposition,[32] and convective slot coating.[33]

In these processes, the nanoparticles are assembled via variety of inter-particle interactions which will be discussed in next session. Meanwhile, multiple forces might

be coexisting and the particle also interact with other interfacial phenomenon, e.g. liquid-air and liquid solid interface.

2.2.2 Inter-particle Interactions

The theory of Derjaguin, Landau, Verway, and Overbeek (DLVO)[34] considered both electrostatic repulsion and van-der-Waals interaction to understand colloidal interactions. If sufficient screening is present to lower the electrostatic repulsion, where the energy barrier between the primary and secondary energy minimum in DLVO energy potential below a few k_BT, rapid aggregation of the nanoparticles will occur. In real material systems, the interactions governing colloidal particle assembly can be much broader. An understanding of other colloidal interactions (e.g. steric interaction, depletion interaction, and hydrophobic interaction) and meanwhile interaction between particles and other surface are necessary to evaluate and design colloidal particle assembly system.[34]

Electrostatic Forces. Surface charge of particles can be generated due to the partial dissociation of surface functional groups. For oxide nanoparticles, surface charge can be generated from the dissolution of hydroxyl groups or the reaction of hydroxyl groups with other surface modification reactants.[34] For polymer nanoparticles, the ionization surface group can be formed due to oxidization of the hydrocarbon chains, or through the polymerization of monomers with charged function groups.[35, 36] Those nanoparticles that are not naturally charged can be latter functionalized by surfactants and/or adsorbed polymers to generate sufficient repulsion against intrinsic attraction between particles. The length scales of the electrostatic repulsion dictated by the electro-double layer formed around the colloidal particles with a dimensionless constant, k^{-1} "Debye Screened Length".[37] As the electro-double layer is easily tuned by changing the pH, ionic strength, and/or type of electrolyte. Changing the solution

conditions for adjusting the electrostatic repulsion can provide a powerful way of controlling nanoparticle assemblies.[4, 10, 11, 35-46] This in fact is a technique that has not been as fully exploited, in particular for particles with dimension comparable to the k^{-1}. On the other hand, the particles can also interact with other charged surfaces (e.g. substrates, assembly-templates, and macromolecules).[47] In general, the same charge induces repulsion of particles, while the opposite charge of the surface can induce deposition and aggregation of the particles.

Capillary Forces. Attractive capillary forces can be generated from surface tension induced forces from curved menisci bridging two adhering particles during evaporation, condensation, and other processes.[48] Such forces have been used to assemble ordered 2 dimensional and 3 dimensional colloidal crystals on substrates.[27, 49, 50] It has been shown that capillary forces can also induce assembly of anisotropic particles to induce anisotropic interaction forming distinctive morphology of the assembly. Such forces are also present in a variety of coating techniques, which can cause compaction of nanoparticles on the coating surfaces, e.g. convective dip/slot coating, and spray coating.

Solvation/hydrophobic Interaction and Depletion Forces. Solvation/hydrophobic forces arise when solvent molecules interact with the nanoparticle surfaces in either favored or non-favored manners.[34] When such interaction occurs, the interface can generate either attraction or repulsion upon reorientation of the solvent molecules near the nanoparticle surface (favored solvent generate repulsion force, and non-favored solvent generate attraction forces).[34] Depletion forces is a force related to the multi-body interaction with in the suspension, where the attraction can be induced to the reduction of the total entropy of the system, e.g. in system mixture of nanoparticles, solvent, and free polymers. In order for the polymer to get highest degree of freedom

that lower the total free energy, the particles can become aggregated or deposited to the substrates.[34]

van der Waals forces. van der Waals forces originated from interactions of dipoles, quadrapoles, and higher multipoles interaction are common between all molecules and particles.[6, 34, 51] Hamaker integrated these forces to allow the model applied to the macroscopic bodies. In his work, it was assumed that London interactions for multiple oscillators could be summed pairwise, suggesting that the van der Waals forces can be considered as long range inter-particle forces with magnitude depending on the dielectric nature of the particle materials and their surrounding media.[34] The Van der Waals forces between identical materials are always attractive. But they can also be repulsive between dissimilar materials in a third (usually liquid) medium. Normally, the uncoated, nanoparticles of metals, metal oxides, ceramic materials, and chalcogenides have strong van der Waals forces due to significant dissimilarity of dielectric nature to the surrounding solvent environments. Without sources of repulsive interaction, aggregation can occur and lead to fusion or coalescence. On the other hand, materials with very similar dielectric response, i.e. materials with similar refractive indices in UV-Vis range, have negligible Van-der-Waals interactions.[36, 37, 43]

2.3 Templated Assembly of Nanoparticles

The templates are referred as surface-modified substrates in 1 dimensional, 2 dimensional, and 3 dimensional, containing active sites, which can selectively induce nanoparticle deposition or provide confining effects to trap the nanoparticles.[18] the template is considered as scaffold for particles to be arranged onto. They may or may not have morphologies complementary to that of the particles.[1] In fact, there are large variety of materials can be templates to direct the assembly process for interaction with nanoparticles, such as single molecules (e.g. DNA),[52] carbon nanotubes,[53]

44

lithographic micropatterns[54-57]), block copolymers[58], and assemblies of surfactant molecules.[59]

Generally, the templates can be categorized into hard and soft ones. Soft templates are materials that have long-range interactions with the nanoparticles, and the templates can be deformed/affected by the interactions with nanoparticles.[18] soft templates are typically formed by assemblies of small molecules, linear polymers and copolymers, and biomolecules. In contrast, the forces required to deform the hard templates are much stronger compared to the inter-particle interactions, therefore the templates define the final structure of the particle assembly. materials such as carbon nanotubes and lithographic patterns are considered as hard templates.[18]

2.4 Creating Super-non-wetting Surface

2.4.1 Super-non-wetting Effects

The lotus leaf is known to possess excellent water repellency or superhydrophobicity with water contact angle 150° or greater with very small contact angle hysteresis ($<10^o$).[60] Namib desert beetles, on the other hand, has patchy surface chemistry on its surface.[61] These examples from nature illustrates wetting phenomena should be governed not only by surface chemistry alone, but also surface morphology and wettability contrast.

For a liquid droplet sitting on a flat surface, the theoretical equilibrium shape of the droplet is defined by balancing of the surface tension the solid-liquid-air interface. Based on this concept, Thomas Young derived a force-balance equation to predict the equilibrium contact angle θ (or Young's contact angle) of a droplet on an ideal homogeneous rigid surface, known as Young's equation:[48]

$$\cos \theta_Y = \frac{\gamma_{SG} - \gamma_{SL}}{\gamma_{LG}} \qquad (2.1)$$

where γ_{LG} is the interfacial energy of liquid-gas, γ_{SG} is the interfacial energy of solid-gas, and γ_{SL} is the interfacial energy of solid-liquid. Hydrophobicity and hydrophilicity of the surface is defined as $\theta_Y < 90°$ for hydrophilic surface, and $\theta_Y > 90°$ for hydrophobic surface. In certain case, liquid can completely wet the surface ($\theta_E = 0°$) on a surface, when $\gamma_{SG} - \gamma_{SL} > \gamma_{LG}$. On the contrary, for surface with the lowest surface tension groups, i.e. fluorocarbon, water has the highest equilibrium contact angle, ~ 120°.

on chemically heterogeneous surfaces and/or rough surfaces much more diverse wetting properties can be observed. The wetting phenomena are often interpreted by more complex models, including Wenzel, Cassie-Baxter, Hemi-wicking states, and metastable states in-between.[62]
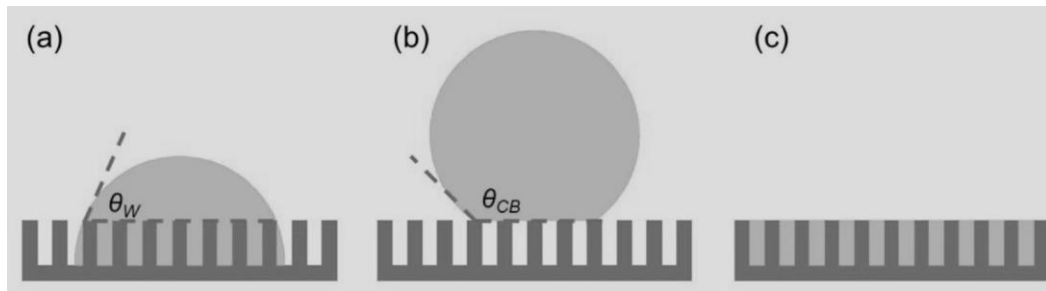
Figure 2.3. Wetting states: (a) Wenzel state, (b) Cassie-Baxter state, (c) Hemi-wicking state.

The effect of surface roughness to the wetting behavior was first hypothesized by Wenzel in 1936.[63] He explained the roughness effects from an increased interfacial energy gained/removed from the solid surface due to increased contact area between

the solid and liquid. If the material is hydrophilic ($\theta_Y < 90°$), the apparent contact angle should decrease with the increase of roughness. Vice versa, the apparent contact angle on a rough and hydrophobic surface should increase. Wenzel defined a surface roughness ratio r as the ratio of apparent solid-liquid contact area to the projected area. The apparent contact angle in Wenzel model (θ_W) thus becomes (Fig. 2.3 a)

$$\cos \theta_W = r \cos \theta_Y \qquad (2.2)$$

Later, Cassie and Baxter considered the droplets sitting on a composite interface involving a linear average of surface energy from the chemical heterogeneity on surface.[48] If the fraction of the total surface area of each distinctive chemistry (with equilibrium contact angle θ_{En}) to the total projected area is denoted as f_n, the apparent contact angle in Cassie-Baxter model is given by

$$\cos \theta_C = \sum_n f_n \cos \theta_{En} \qquad (2.3)$$

For a binary system consisting of solid (f_1, θ_{E1}) and air (f_2, θ_{E2}), where $\theta_{E2}=180°$. The contact angle is simplified as

$$\cos \theta_C = f_1 \cos \theta_{E_1} + f_1 - 1 \qquad (2.4)$$

For simplicity, the superhydrophobic state is often explained by the formation of either Cassie-Baxter or Wenzel state, since the hydrophobicity can be significantly increased by either roughness effects or composite interface with air. In the Hemi-wicking phase, the liquid can imbibe into a highly rough surface, much like water get imbibed into cotton cloth. Here, it is very similar to Cassie-Baxter state described earlier, yet now the composite interface is composed of liquid to the imbibed liquids and liquid to the

solid, and the contact angle should approach zero degree due to high affinity of the liquid to itself.

While the above models are based on equilibrium states, on real surface the shape of liquid drops can never reach equilibrium, due to pinning of the contact line upon deposition of the liquid. There exists a wetting hysteresis upon the history of liquid drop deposition. Therefore, dynamical contact angles, advancing contact angle, θ_{adv}, and receding contact angle, θ_{rec} are better representatives to the actual wetting behaviors on a real surface. Here, θ_{adv} refers to the maximum contact angle that the solid-liquid-gas triple phase contact line withstand before the contact line propagates. θ_{rec} is defined as the minimum contact angle that the triple phase contact line withstands before the contact line recedes. The difference between the θ_{adv} and θ_{rec} is referred as the contact angle hysteresis, $\Delta\theta$. Such hysteresis can result in the adhering of liquid drop to the surface, and thus the liquid drop need to have a finite tilting angle to roll off from a tilted surface. The sliding angle, α, is related to both size and contact angle hysteresis of the surface

$$\sin\alpha = \frac{2R\gamma_{LG}(\cos\theta_R - \cos\theta_A)}{\rho g V} \quad (2.5)$$

Where R is the contact radius of the droplet; ρ is the liquid density; g is the gravitational acceleration, V is the droplet volume. Since the contact angle hysteresis on superhydrophobic/superoleophobic coating is very small, the liquid can slide at a very small sliding angle. Meanwhile, given a certain tilting angle of the surface, the critical volume of the liquid drop adhering to the surface is much smaller compared to normal surfaces.

When low surface tension liquid makes a contact with the rough surface, it is more preferable to enter Wenzel state due to the lower interfacial energy compared to the Cassie-Baxter state. Here, the Wenzel state of the liquid can cause significantly enhanced adhesion to the solid surface, the low surface tension liquid can be detrimental to the super-non-wetting effects. In order to achieve stable Cassie-Baxter state, an "re-entrant structure" is preferred so that the energy barrier between the Cassie and Wenzel state can be enhanced.

2.4.2 Super-non-Wetting on Nanoparticle Coatings

The fabrication of surfaces with enhanced liquid repellency have many promising applications,[64-67] including self-cleaning, enhanced interfacial heat transfer via condensation, reduced underwater dragging forces, anti-icing, and anti-corrosion effects. Previously, to realize the Cassie-Baxter state of wetting, different techniques have been used to introduce surface roughness,[30, 65, 68] e.g. etching, lithography, micro-phase separation, templating, and direct laser sintering. However, most of these techniques are limited to small fabrication area and/or high cost of time and energy to fabricate them. Assemblies of nanoparticles provide a promising method to scalable manufacturing super-non-wetting surfaces at a low cost.

To enhance the water repellency, dual-scale micro- and nano-roughness are often desired. They can be created by methods, including layer-by-layer deposition, dip-coating, slot coatings, and spray coatings,[30, 65, 68] via control of the coating sequence, choice of solvent, nanoparticle concentration, and solvent evaporation speed.[30, 65, 68] Most of the previous research uses inorganic nanoparticles (e.g. TiO_2, and SiO_2) with spherical shapes due to simplicity of the synthesis and abundance of the materials. ZnO nanoparticles are used for coating because of their light responsive wetting behaviors.[69, 70] Particles from rare earth oxides (e.g., Ceria, CeO_2) are used

due to their intrinsic hydrophobic nature, and thus tolerate harsh environments encountered during the applications (e.g. temperature > 1000°C).[71, 72]
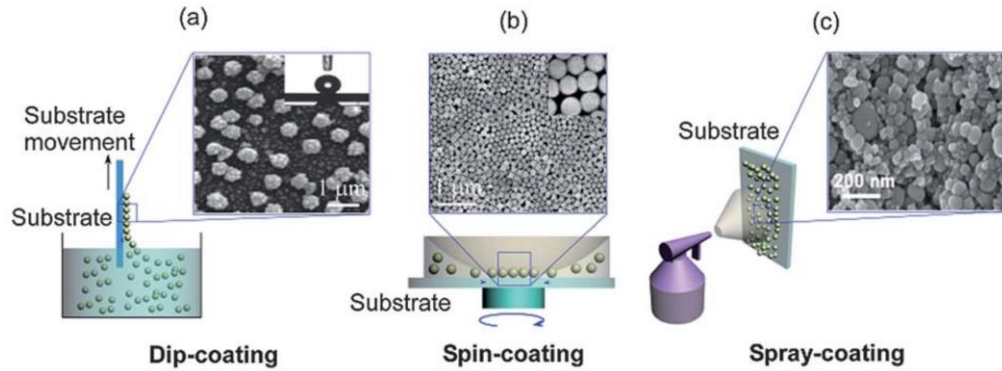
Figure 2.4. Schematics illustration of different coating techniques for generating superhydrophobic nanoparticle coatings: (a) dip-coating, (b) spin-coating, and (c) spray-coating.[65]

Nanoparticles with non-spherical shape requires more complex procedures to synthesize, and thus are not widely exploited in literature.[8] However, they offer new opportunities to create ultrathin yet hierarchically rough surfaces due to their unique morphologies. It will be highly desired to develop scalable methods for synthesis of nanoparticles (e.g. via microwave synthesis) and assembly of the nanoparticles on the substrate in a continuous fashion (e.g. via roll-to-roll process).

2.5 References

1. Lee, Y.S., *Unified Approach to Self-Assembly*, in *Self-Assembly and Nanotechnology*. 2007, John Wiley & Sons, Inc. p. 1-19.

2. Mihi, A., M. Ocaña, and H. Míguez, *Oriented Colloidal-Crystal Thin Films by Spin-Coating Microspheres Dispersed in Volatile Media*. Advanced Materials, 2006. **18**(17): p. 2244-2249.

3. Jiang, P., et al., *Two-dimensional nonclose-packed colloidal crystals formed by spincoating*. Applied Physics Letters, 2006. **89**(1): p. 011908.

4. Jiang, P. and M.J. McFarland, *Large-Scale Fabrication of Wafer-Size Colloidal Crystals, Macroporous Polymers and Nanocomposites by Spin-Coating*. Journal of the American Chemical Society, 2004. **126**(42): p. 13778-13786.

5. Yang, H. and P. Jiang, *Large-Scale Colloidal Self-Assembly by Doctor Blade Coating*. Langmuir, 2010. **26**(16): p. 13173-13182.

6. Frenkel, D., *Colloidal crystals: Plenty of room at the top*. Nat Mater, 2006. **5**(2): p. 85-86.

7. Yu, J.-S., et al., *Fabrication of Ordered Uniform Porous Carbon Networks and Their Application to a Catalyst Supporter*. Journal of the American Chemical Society, 2002. **124**(32): p. 9382-9383.

8. Jeong, S., et al., *Fast and Scalable Printing of Large Area Monolayer Nanoparticles for Nanotexturing Applications*. Nano Letters, 2010. **10**(8): p. 2989-2994.

9. Hwang, H., S.-H. Kim, and S.-M. Yang, *Microfluidic fabrication of SERS-active microspheres for molecular detection*. Lab on a Chip, 2011. **11**(1): p. 87-92.

10.   Bharti, B., G.H. Findenegg, and O.D. Velev, *Co-Assembly of Oppositely Charged Particles into Linear Clusters and Chains of Controllable Length.* Sci. Rep., 2012. **2**.

11.   Kim, S.-H., et al., *Osmotic-pressure-controlled concentration of colloidal particles in thin-shelled capsules.* Nat Commun, 2014. **5**.

12.   Stöber, W., A. Fink, and E. Bohn, *Controlled growth of monodisperse silica spheres in the micron size range.* Journal of Colloid and Interface Science, 1968. **26**(1): p. 62-69.

13.   Fernández-García, M. and J.A. Rodriguez, *Metal Oxide Nanoparticles*, in *Encyclopedia of Inorganic and Bioinorganic Chemistry*. 2011, John Wiley & Sons, Ltd.

14.   Mody, V.V., et al., *Introduction to metallic nanoparticles.* Journal of Pharmacy and Bioallied Sciences, 2010. **2**(4): p. 282-289.

15.   Bangal, M., et al., *Semiconductor Nanoparticles.* Hyperfine Interactions, 2005. **160**(1): p. 81-94.

16.   Rao, C.N.R., P.J. Thomas, and G.U. Kulkarni, *Nanocrystals:: Synthesis, Properties and Applications*. 2007: Springer Berlin Heidelberg.

17.   Cho, J.-H. and D.H. Gracias, *Self-assembly of lithographically patterned nanoparticles.* Nano letters, 2009. **9**(12): p. 4049-4052.

18.   Grzelczak, M., et al., *Directed Self-Assembly of Nanoparticles.* ACS Nano, 2010. **4**(7): p. 3591-3605.

19.   Bogush, G.H., M.A. Tracy, and C.F. Zukoski Iv, *Preparation of monodisperse silica particles: Control of size and mass fraction.* Journal of Non-Crystalline Solids, 1988. **104**(1): p. 95-106.

20.   Rahman, I.A. and V. Padavettan, *Synthesis of Silica Nanoparticles by Sol-Gel: Size-Dependent Properties, Surface Modification, and Applications in Silica-Polymer Nanocomposites—A Review.* Journal of Nanomaterials, 2012. **2012**: p. 15.

21.   Van Blaaderen, A., J. Van Geest, and A. Vrij, *Monodisperse colloidal silica spheres from tetraalkoxysilanes: Particle formation and growth mechanism.* Journal of Colloid and Interface Science, 1992. **154**(2): p. 481-501.

22.   Yokoi, T., et al., *Periodic Arrangement of Silica Nanospheres Assisted by Amino Acids.* Journal of the American Chemical Society, 2006. **128**(42): p. 13664-13665.

23.   Yokoi, T., et al., *Mechanism of Formation of Uniform-Sized Silica Nanospheres Catalyzed by Basic Amino Acids.* Chemistry of Materials, 2009. **21**(15): p. 3719-3729.

24.   Snyder, M.A., et al., *Silica Nanoparticle Crystals and Ordered Coatings Using Lys-Sil and a Novel Coating Device.* Langmuir, 2007. **23**(20): p. 9924-9928.

25.   Kuijk, A., A. van Blaaderen, and A. Imhof, *Synthesis of Monodisperse, Rodlike Silica Colloids with Tunable Aspect Ratio.* Journal of the American Chemical Society, 2011. **133**(8): p. 2346-2349.

26.   Wang, J., et al., *Preparation of Anisotropic Silica Nanoparticles via Controlled Assembly of Presynthesized Spherical Seeds.* Langmuir, 2010. **26**(23): p. 18491-18498.

27.   Jiang, P., et al., *Single-Crystal Colloidal Multilayers of Controlled Thickness.* Chemistry of Materials, 1999. **11**(8): p. 2132-2140.

28.   Rose, S., et al., *Nanoparticle solutions as adhesives for gels and biological*

tissues. Nature, 2014. **505**(7483): p. 382-385.

29. Raut, H.K., et al., *Anti-reflective coatings: A critical, in-depth review.* Energy & Environmental Science, 2011. **4**(10): p. 3779-3804.

30. Bellanger, H., et al., *Chemical and Physical Pathways for the Preparation of Superoleophobic Surfaces and Related Wetting Theories.* Chemical Reviews, 2014. **114**(5): p. 2694-2716.

31. Atchison, N., et al., *Silica-Nanoparticle Coatings by Adsorption from Lysine– Silica-Nanoparticle Sols on Inorganic and Biological Surfaces.* Angewandte Chemie International Edition, 2011. **50**(7): p. 1617-1621.

32. Shimomura, H., et al., *Layer-by-Layer-Assembled High-Performance Broadband Antireflection Coatings.* ACS Applied Materials & Interfaces, 2010. **2**(3): p. 813-820.

33. Prevo, B.G., D.M. Kuncicky, and O.D. Velev, *Engineered deposition of coatings from nano- and micro-particles: A brief review of convective assembly at high volume fraction.* Colloids and Surfaces A: Physicochemical and Engineering Aspects, 2007. **311**(1–3): p. 2-10.

34. Israelachvili, J.N., *Intermolecular and Surface Forces*. 2010: Elsevier Science.

35. Royall, C.P., M.E. Leunissen, and A.v. Blaaderen, *A new colloidal model system to study long-range interactions quantitatively in real space.* Journal of Physics: Condensed Matter, 2003. **15**(48): p. S3581.

36. Leunissen, M.E., et al., *Ionic colloidal crystals of oppositely charged particles.* Nature, 2005. **437**(7056): p. 235-240.

37. Yethiraj, A. and A. van Blaaderen, *A colloidal model system with an interaction tunable from hard sphere to soft and dipolar.* Nature, 2003. **421**(6922): p. 513-

517.

38.   Wan, Q., et al., *Light curable dental composites designed with colloidal crystal reinforcement.* Dental Materials, 2008. **24**(12): p. 1694-1701.

39.   Demirörs, A.F., et al., *Directed Self-Assembly of Colloidal Dumbbells with an Electric Field.* Langmuir, 2010. **26**(18): p. 14466-14471.

40.   Hsu, M.F., E.R. Dufresne, and D.A. Weitz, *Charge Stabilization in Nonpolar Solvents.* Langmuir, 2005. **21**(11): p. 4881-4887.

41.   Liu, B., et al., *Switching plastic crystals of colloidal rods with electric fields.* Nat Commun, 2014. **5**.

42.   Bowen, W.R. and A.O. Sharif, *Long-range electrostatic attraction between like-charge spheres in a charged pore.* Nature, 1998. **393**(6686): p. 663-665.

43.   Irvine, W.T.M., V. Vitelli, and P.M. Chaikin, *Pleats in crystals on curved surfaces.* Nature, 2010. **468**(7326): p. 947-951.

44.   Hynninen, A.-P. and M. Dijkstra, *Phase diagrams of hard-core repulsive Yukawa particles.* Physical Review E, 2003. **68**(2): p. 021407.

45.   Leunissen, M.E., et al., *Electrostatics at the oil–water interface, stability, and order in emulsions and colloids.* Proceedings of the National Academy of Sciences, 2007. **104**(8): p. 2585-2590.

46.   Wu, Y.L., et al., *Melting and crystallization of colloidal hard-sphere suspensions under shear.* Proceedings of the National Academy of Sciences, 2009. **106**(26): p. 10564-10569.

47.   Israelachvili, J.N., *Chapter 13 - Van der Waals Forces between Particles and Surfaces*, in *Intermolecular and Surface Forces (Third Edition)*, J.N.

Israelachvili, Editor. 2011, Academic Press: San Diego. p. 253-289.

48.   Mittal, K.L., *Contact Angle, Wettability and Adhesion*. 2006: Taylor & Francis.

49.   Blanco, A., et al., *Large-scale synthesis of a silicon photonic crystal with a complete three-dimensional bandgap near 1.5 micrometres.* Nature, 2000. **405**(6785): p. 437-440.

50.   Vlasov, Y.A., et al., *On-chip natural assembly of silicon photonic bandgap crystals.* Nature, 2001. **414**(6861): p. 289-293.

51.   Min, Y., et al., *The role of interparticle and external forces in nanoparticle assembly.* Nat Mater, 2008. **7**(7): p. 527-538.

52.   Li, K., et al., *DNA-Directed Assembly of Gold Nanohalo for Quantitative Plasmonic Imaging of Single-Particle Catalysis.* Journal of the American Chemical Society, 2015. **137**(13): p. 4292-4295.

53.   Han, L., et al., *A Direct Route toward Assembly of Nanoparticle−Carbon Nanotube Composite Materials.* Langmuir, 2004. **20**(14): p. 6019-6025.

54.   Pinedo Rivera, T., et al., *Assisted convective-capillary force assembly of gold colloids in a microfluidic cell: Plasmonic properties of deterministic nanostructures.* Journal of Vacuum Science & Technology B, 2008. **26**(6): p. 2513-2519.

55.   Lim, J.-M., et al., *Fabrication of One-Dimensional Colloidal Assemblies from Electrospun Nanofibers.* Langmuir, 2006. **22**(8): p. 3445-3449.

56.   Malaquin, L., et al., *Controlled Particle Placement through Convective and Capillary Assembly.* Langmuir, 2007. **23**(23): p. 11513-11521.

57.   Moon, J.H., et al., *Fabrication of Ordered Macroporous Cylinders by Colloidal*

Templating in Microcapillaries. Langmuir, 2004. **20**(5): p. 2033-2035.

58.   Chang, T.-H., et al., *Directed self-assembly of block copolymer films on atomically-thin graphene chemical patterns.* Scientific Reports, 2016. **6**: p. 31407.

59.   Jensen, G.V., et al., *Direct Observation of the Formation of Surfactant Micelles under Nonisothermal Conditions by Synchrotron SAXS.* Journal of the American Chemical Society, 2013. **135**(19): p. 7214-7222.

60.   Yu, S., Z. Guo, and W. Liu, *Biomimetic transparent and superhydrophobic coatings: from nature and beyond nature.* Chemical Communications, 2015. **51**(10): p. 1775-1794.

61.   Malik, F.T., et al., *Nature's moisture harvesters: a comparative review.* Bioinspiration & Biomimetics, 2014. **9**(3): p. 031002.

62.   Quéré, D., *Wetting and Roughness.* Annual Review of Materials Research, 2008. **38**(1): p. 71-99.

63.   Wenzel, R.N., *RESISTANCE OF SOLID SURFACES TO WETTING BY WATER.* Industrial & Engineering Chemistry, 1936. **28**(8): p. 988-994.

64.   Samaha, M.A., H.V. Tafreshi, and M. Gad-el-Hak, *Superhydrophobic surfaces: From the lotus leaf to the submarine.* Comptes Rendus Mécanique, 2012. **340**(1–2): p. 18-34.

65.   Rahmawan, Y., L. Xu, and S. Yang, *Self-assembly of nanostructures towards transparent, superhydrophobic surfaces.* Journal of Materials Chemistry A, 2013. **1**(9): p. 2955-2969.

66.   Shin, S., et al., *Bio-Inspired Extreme Wetting Surfaces for Biomedical Applications.* Materials, 2016. **9**(2): p. 116.

67.   Bhushan, B., Y.C. Jung, and K. Koch, *Micro-, nano- and hierarchical structures for superhydrophobicity, self-cleaning and low adhesion.* Philosophical Transactions of the Royal Society A: Mathematical,

Physical and Engineering Sciences, 2009. **367**(1894): p. 1631-1672.

68.   Teisala, H., M. Tuominen, and J. Kuusipalo, *Superhydrophobic Coatings on Cellulose-Based Materials: Fabrication, Properties, and Applications.* Advanced Materials Interfaces, 2014. **1**(1): p. n/a-n/a.

69.   Kwak, G., et al., *Superhydrophobic ZnO Nanowire Surface: Chemical Modification and Effects of UV Irradiation.* The Journal of Physical Chemistry C, 2009. **113**(28): p. 12085-12089.

70.   Wu, J., et al., *A Brief Review on Bioinspired ZnO Superhydrophobic Surfaces: Theory, Synthesis, and Applications.* Advances in Materials Science and Engineering, 2013. **2013**: p. 10.

71.   Azimi, G., et al., *Hydrophobicity of rare-earth oxide ceramics.* Nat Mater, 2013. **12**(4): p. 315-320.

72.   Li, J., et al., *Facile fabrication of superhydrophobic ZnO nanoparticle surfaces with erasable and rewritable wettability.* Applied Surface Science, 2012. **258**(22): p. 8585-8589.

Chapter 3: Capillarity Induced Instability in Responsive Hydrogel Membranes with Periodic Hole Array

Adapted from X. Zhu, **G. Wu**, R. Dong, C.-M. Chen and S. Yang, *Soft Matter*, 2012, 8

3.0 Introduction

Periodic structures in nano- or micro-scale are of interest for a wide range of applications, including photonic[1] and phononic[2, 3] crystals, structural colors,[4] memory and logic layouts,[5, 6] and tunable hydrophobic surfaces.[7] In these applications, a small change of structural details will lead to dramatic alteration of the physical properties. It will be attractive if we can change the form (size, shape, symmetry, and filling fraction) of the periodic structures in an affine manner, so called pattern transformation, using an external stimulus.

In two-dimensional (2D) periodic structures from elastomers [e.g. poly(dimethylsiloxane) (PDMS)] and elasto-plastic materials (e.g. SU-8), we and others have demonstrated that pattern transformation can be triggered by compressive stress generated by mechanical compression,[8, 9] solvent swelling,[10, 11] and polymerization[12] over multiple length scales. For example, when swollen in an organic solvent, the elastic PDMS membrane consisting of micron-sized circular holes in a square array buckles to a diamond plate pattern of elliptical slits (width of 100 nm or smaller) with the neighboring units perpendicular to each other.[10] Recently, Willshaw *et al*. reported pattern transformation in two- (2D) plus one-dimensional (1D) soft solids.[13] The spontaneous pattern transformation in periodic structures is attractive for potential applications, including tunable photonics,[10] phononics,[9, 11] and negative Poisson's ratio materials.[14]

In the case of swelling-induced pattern transformation, the deformed elastomeric PDMS membrane would snap back immediately to the original shape upon solvent drying,[10, 15] whereas the transformed pattern in plasticized SU-8 membrane can be locked upon evaporation off the solvent due to the increased glass transition temperature (T_g) of the film.[11, 12, 16] The deformed SU-8 pattern can be recovered to the original shape by reswelling in a good solvent.[11] The ability to capture the transformed pattern allows us to take advantage of the deformed states for photonic/phononic switching without continuous input of external stimulus. It also offers opportunities to study the transit states of transformed patterns to elucidate the instability mechanism.

Hydrogels are a type of polymer gels that have a high affinity with water. Water molecules can diffuse in and out of the mesh between the polymer chains and swell the network. The mesh size can be varied by the crosslinking density and the affinity between the polymer chains and water, leading to different swelling ratios. They can be tailored to be responsive to external stimuli, such as solvent, pH, temperature and electric field. Among them, poly(2-hydroxyethyl methacrylate) (PHEMA) based hydrogels are of particular interest here due to their high mechanical strength, optical transparency and stability in water, which are important to tune the pattern deformation and recovery in an aqueous environment. They have been widely used in biomedical applications, such as contact lenses and tissue scaffold.[17] Recently microstructured PHEMA gels have been fabricated to study water transportation in humidity sensitive microvascular channels,[18] to create ultrathin whitening materials[19], and to study the wrinkling and creasing formation.[20, 21] Compared to a typical hydrogel system (e.g. polyacrylamide), PHEMA does not swell much in water: for PHEMA gels crosslinked with 1 wt% ethylene glycol dimethacrylate (EGDMA), the equilibrium

linear expansion values (α_e) is 1.5.[20] It will be intriguing to see whether the swollen PHEMA membrane can undergo pattern transformation. Another unique feature of PHEMA based gels is that the rubbery (water swollen) PHEMA gels become glassy when drying off water, much like the behavior observed in swollen SU-8 film. Thus, it will allow us to lock the deformed pattern and investigate the instability mechanism.

Here, we fabricated a series of PHEMA based hydrogel membranes, including PHEMA and poly(hydroxyethyl methacrylate-*co-N*-isopropylacrylamide) (PHEMA-*co*-PNIPAAm), with micron-sized cylindrical holes (1 μm diameter, 4 μm height and 2 μm pitch) in a square lattice. The membranes were swollen in water, followed by drying off in air. It was found that the pure PHEMA membrane first underwent breathing mode instability, that is, the holes slightly reduced size but retained the circular shape when exposed to deionized (DI) water. However, upon drying, the square array of circular holes buckled into a diamond plate pattern, that is neighboring elliptical slits were arranged mutually perpendicular to each other, suggesting that capillary force might play a critical role to induce pattern transformation. To confirm this, we compared the capillary pressure with the critical buckling tension, which is proportional to the shear modulus at that state. When the deformed dry film was re-exposed to water, the original square array of circular holes was recovered. We then introduced themoresponsive PNIPAAm, which had a lower critical solution temperature (LCST) of 32 ºC, in PHEMA to manipulate the elasticity of the film, thus, the critical buckling tension vs. capillary pressure. Dried below LCST at 25 °C, the pores in PHEMA-*co*-PNIPAAm membrane were deformed in the same fashion as those in PHEMA membrane, but remained unchanged if dried above LCST at 40 °C. This is because that above LCST the polymer gel dehydrated and thus had much higher modulus, preventing the film from buckling. Along the pattern transformation, we observed dramatic change of

optical property in the PHEMA membrane, from highly reflective to transparent, which could potentially be useful as an environmentally responsive window.

3.1 Experimental

Fabrication of epoxy pillar array. Epoxy pillar array (diameter $D = 1$ μm, pitch $P = 2$ μm, and depth $H = 4$ μm) in a square lattice was used as the template to fabricate PHEMA based membranes. They are fabricated via replica molding from the silicon master following the procedure reported earlier.[22]

Preparation of PHEMA precursor. The precursor was prepared following a modified procedure from the literature.[23] In a typical procedure, 2.5 mL of HEMA (Fig. 3.1) was mixed with photoinitiator, 75 μL Darocur 1173 (Ciba Specialty Chemicals Inc.) in a 20 mL glass vial and exposed to UV light (97435 Oriel Flood Exposure Source, Newport Corp.) to obtain a partially polymerized precursor solution. In order to ensure the homogeneity of photopolymerization, the UV exposure was carried out in multi-steps: 1000 mJ/cm^2 twice, 100 mJ/cm^2 twice and 50 mJ/cm^2 six times, totaling 2500 mJ/cm^2. Between every two exposures, the sample was homogenized. Last, an additional 50 μL Darocur 1173 and 25 μL ethylene glycol dimethacrylate (EGDMA, Alfa Aesar) were added to prepare the molding solution.

62
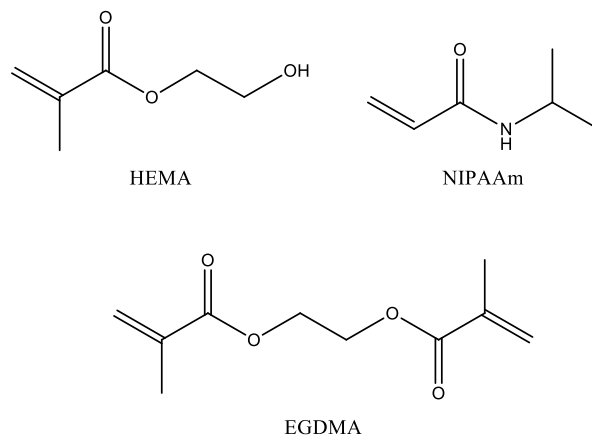
Fig. 3.1 The chemical structures of monomers, HEMA and NIPAAm, and crosslinker, EGDMA.

Preparation of PHEMA-*co*-PNIPPAAm precursor. In a typical procedure, 1.5g NIPAAm was dissolved in 1.5mL HEMA, followed by mixing with 75 µL Darocur 1173. The mixture was partially polymerized using the same procedure as that for PHEMA precursor. After thoroughly homogenizing the mixture, additional 50 µL Darocur 1173 and 25 µL EGDMA were added to prepare the molding solution.

Replica molding of hydrogel membrane (Fig. 3.2). The glass substrates were rinsed with acetone, followed by oxygen plasma (Harrick Expanded Plasma Cleaner & PlasmaFlo™) for 1 h. These glass slides were then treated with 3-(trimethoxysilyl)propylmethacrylate silane (Sigma-Aldrich) via vapor deposition in a vacuum chamber for 2 h as an adhesion promoter. The surface of epoxy pillar master was passivated with (tridecafluoro-1, 1, 2, 2-tetrahydroctyl)trichlorosilane (Gelest, Inc.) as release agent via vapor deposition in a dessicator for ~ 1 h. A 10 µL hydrogel precursor solution was cast onto the silanized epoxy pillar array pattern, and then the treated glass substrate was placed over the precursor as the flat confining surface. After exposing to UV light at a dosage 1000 mJ/cm^2, the hydrogel membrane was separated from the epoxy template.
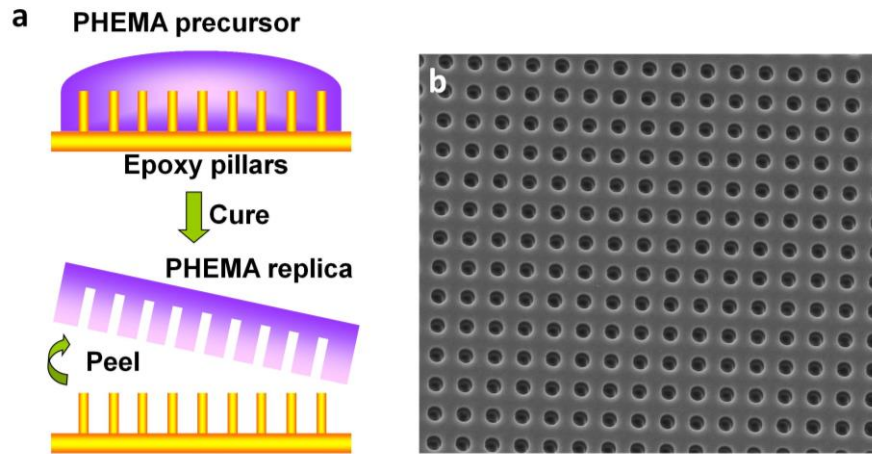
Fig. 3.2 (a) Schematic illustration of replica molding of PHEMA membrane from epoxy pillars. (b) SEM images of PHEMA membrane with hole diameter $D = 1$ μm, pitch $P = 2$ μm, and depth $H = 4$ μm.

Characterization. Scanning electron microscopy (SEM) images were taken by FEI Strata DB235 Focused Ion Beam in high vacuum mode with acceleration voltage of 5kV. Surface topography of the PHEMA-*co*-PNIPAAm dried at 25 °C and 40 °C was imaged by a DI Dimension 3000 Atomic Force Microscope (AFM) in tapping mode, and the raw images were imported to open source software, Gwyddion, for post-processing. The optical images were taken from an Olympus BX61 motorized microscope. The water contact angles of PHEMA at room temperature (25 °C) and PHEMA-*co*-PNIPAAm at different temperatures (25 °C and 40 °C) were measured from a goniometer (ramé-hart Model 200) equipped with an environmental chamber. The transparency of the hydrogel membrane was measured by UV-Vis spectrometer (Varian Cary 5000 UV-visible-NIR Spectrometer).

Modulus measurement of PHEMA and PHEMA-*co*-PNIPAAm films by AFM. The moduli of PHEMA at room temperature (25 °C) and PHEMA-*co*-PNIPAAm at

different temperatures (25 °C and 40 °C) were measured by AFM (Agilent 5500 with Lakeshore 325 temperature controller) in a liquid cell. Each sample was measured at least three times from different regions. The conical shaped tips were utilized and the samples were equilibrated in water at respective temperatures for at least 0.5 h. The force curves measured by AFM can be expressed as:[24]

$$z - z_0 = a - a_0 + \sqrt{\frac{\pi k (a - a_0)}{2E(1 - v^2)\tan\theta}} \qquad (3.1)$$

where E is the Young's modulus of the film, z and z_0 are the piezo displacement and the zero displacement, respectively. a and a_0 are the tip deflection and the zero deflection, respectively, v is the Poisson ratio, θ and k are the half cone angle and the spring constant of the AFM tip, respectively.

Eq. 3.1 shows a linear relationship between (z-a) and (a-a_0)$^{1/2}$. Therefore, the Young's modulus E can be determined from the slope m of the curve (z-a) vs. (a-a_0)$^{1/2}$ as:[19]

3.2 Results and Discussion

Previously, we and others have reported swelling-induced pattern transformation in PDMS[10] and SU-8[11] membranes. When the generated osmotic pressure is built above the critical buckling stress, the circular pores deform and snap shut to relieve the stress. Motivated by these studies, we are interested in exploring how porous membranes open and close pores in response to changes in environmental factors, such as moisture and temperature, and whether it is possible to lock the deformed structure after removing the external stimulus.

Here, we report the study of pattern transformation behaviors from a model polymer gel system, PHEMA with micropores arranged in a square lattice. PHEMA

was chosen because of its high mechanical strength, optical transparency and stability in water. It could be further tailored to be temperature and pH responsive by introducing temperature responsive PNIPAAm and pH responsive poly(acrylic acid).[23] We note that, however, the swelling ratio of PHEMA gels in DI water, ~150%, is considerably smaller than that from a typical hydrogels, such as poly(acrylamide) in water. When the PHEMA membrane (Fig. 3.3 a) was immersed in DI water, it was found that the pore size was reduced but the pores remained circular (Fig. 3.3 b). When water evaporated, however, the square lattice of cylindrical holes collapsed abruptly and bifurcated into a diamond plate pattern with neighboring closed holes mutually perpendicular to each other (Fig. 3.3 c), the same as that appeared in swollen PDMS membrane.[10] When the water was completely evaporated, the diamond plate pattern was locked. The latter can be explained by transition of PHEMA gel from rubbery (in water) to glassy (in dry state), accompanied by the increase of T_g from ~ 4 ^{o}C up to ~ 105 ^{o}C.[20, 21] When re-exposed to DI water, the hydrogel membrane became rubbery again and the transformed pattern was recovered back to the original circular holes. The pattern transformation and recovery processes could be repeated many times.
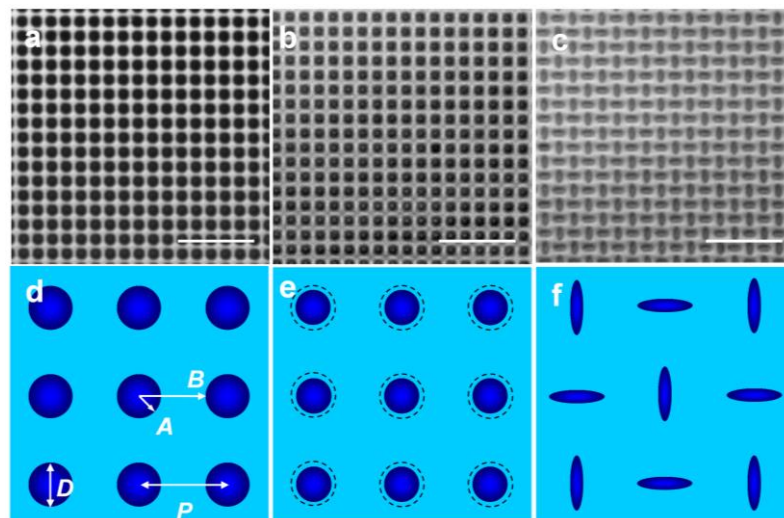
Fig. 3.3 Instability of PHEMA membranes with a square lattice of holes, diameter D = 1 μm, pitch P = 2 μm, and depth H = 4 μm. (a-c) Optical images of PHEMA membranes: (a) pristine state, (b) swollen in DI water (i.e. breathing state), and (c) deformed to diamond plate pattern after water evaporation (i.e. buckling state). Scale bars: 10 μm. (d-f) Corresponding schematic illustration of (a-c).

Although the morphology of the deformed PHEMA membrane appeared the same as that of the swollen PDMS membranes, the forces responsible to pattern transformation in two membranes were completely different. Formation of diamond plate pattern in PHEMA membrane occurred during water evaporation, suggesting that capillary force should play a critical role to induce pattern transformation, possibly assisted by the lowered modulus of PHEMA membrane upon swelling by water.

To estimate the critical tension (σ_{cr}) for pattern transformation, we adopted the model proposed by Cai *et al*.[25] Inspired by the observation of osmosis in an artificial tree made of PHEMA gels at different humidity,[18] Cai *et al*. have theoretically studied the deformation of a void (cylindrical and spherical) in an elastomer.[25] In their model, the void is filled with liquid water, while the elastomer is surrounded by unsaturated air. The diffusion of water molecules from inside the void to outside induces tension that competes against the elastic energy of the elastomeric wall. They suggest three modes of deformation, including breathing, buckling and creasing, depending on the magnitude of tension imposed to the void and the wall thickness. In breathing mode, the void size becomes smaller in the breathing state but retains the shape. When the tension increases above a critical value, the cylindrical void changes shape, by buckling if the wall is thin or by creasing if the wall is thick. The critical tension is dependent on *B*/*A*, where *A* and *B* are inner and outer radii of the cylindrical

void, and the shear modulus, G.

Our experimental observation from PHEMA membrane in water clearly indicated that swelling induced breathing mode instability. However, osmotic pressure generated by swelling was not sufficient to induce buckling or creasing. In our system, we only observed buckling not creasing.

The holes in PHEMA membrane always buckles at the thinnest bridge, due to the lower energy barrier for the buckling along those directions. Therefore, the buckling threshold of the holes in the hydrogel membrane is considered to be close to the cylindrical void with ratio of $B/A = (2P\text{-}D)/D = 3$ (see Figure 3.3 d for the definition of A and B in our system). According to Fig. 11 in Ref. [25], the critical tension for buckling is $\sigma_{cr}^{bk} \cong 0.98G$, and $\sigma_{cr}^{cs} \cong 1.05G$ for creasing at $B/A=3$. Since $\sigma_{cr}^{cs} > \sigma_{cr}^{bk}$, the cylindrical holes should collapse by buckling first, which corroborates with our observation.

During the drying process, water evaporation creates a liquid vapor meniscus in the holes (Fig. 3.4). This induces a hydrostatic tension in the liquid, which is balanced by an axial compression on the swollen hydrogel wall. Then the hole shrinks and more water is fed to the menisci, where it is evaporated.
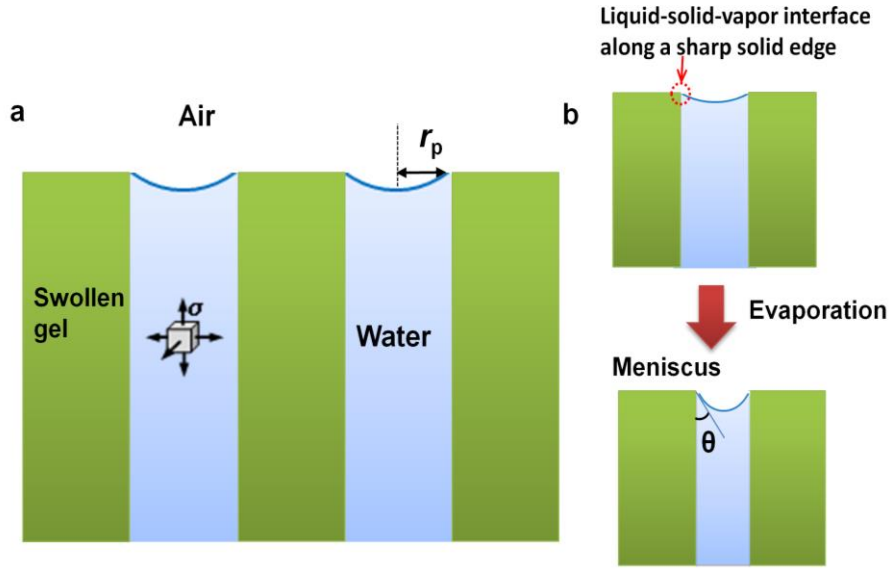
Fig. 3.4 (a) Illustration of capillary force exerted to swollen PHEMA membrane. (b) The liquid vapor meniscus becomes shaper when water evaporates.

For a cylindrical hole, the hydrostatic tension (i.e. capillary pressure) is

$$S = \frac{2g_{\mathrm{LV}}\cos q}{r_p} \qquad (3.2)$$

where γ_{LV} is the liquid-vapor interfacial energy (i.e. the surface tension) ($\gamma_{\mathrm{water}} = 0.072$ J/m^2 at 25 °C, and 0.069 J/m^2 at 40 °C),[26] θ is the water contact angle at the water/hydrogel interface, and r_{p} is the hole radius.

The equilibrium meniscus radius r_{m} at any instance is given by the compressive stress that the swollen gel can support. Here, θ is undetermined along a sharp solid edge. Higher compression states of the hydrogel leads to a higher hydrostatic tension in the liquid. Therefore, the menisci become sharper and sharper (i.e. the meniscus radius r_{m} become smaller) when contraction increases. This keeps a gel shrinking until r_{m} reaches r_{p} if the hole does not collapse. Beyond this critical point of drying, capillarity can no

longer increase the compressive stresses on hydrogel.

When water evaporates through the micron-sized holes, the swollen hydrogel network will partially lose water, hence, increasing the gel modulus. However, since the mesh size in hydrogel network is typically in the range of 1 to 10 nm, the equilibrium vapor pressure above a meniscus is significantly lower than that in the micron-sized holes, allowing the latter more capacity to hold water. Here, for simplicity, we assume that hydrogel is almost fully swollen and its modulus is close to a constant before water evaporates out of the micron holes.

By comparing the hydrostatic tension σ with the buckling critical tension $\sigma_{cr}^{bk} = 0.98G$, we can obtain the prerequisite to buckle a hole as

$$\cos\theta = \frac{0.98r_p}{2\gamma_{LV}}G \leq 1 \qquad (3.3)$$

Therefore, the shear modulus must obey

$$G \leq \frac{2\gamma_{LV}}{0.98r_p} \qquad (3.4)$$

At the critical point of $\sigma = \sigma_{cr}^{bk}$, the mechanical instability switches from the breathing mode to buckling, and the radius of the cylindrical hole reduces to $r_p \cong 0.65A = 0.325$ μm according to Fig. 10 in Ref. [25]. Accordingly, $G \leq 452$ kPa at 25 °C and $G \leq 433$ kPa at 40 °C, respectively, for buckling.

For the water-swollen PHEMA film, G is ~ 134.4±23.3 kPa, and thus σ_{cr}^{bk} ~ 131.7±22.8 kPa. This G value can meet the prerequisite condition, and the buckling occurred at $\theta = 57.4\pm2.6°$ according to Eq. 5, close the static contact angle on PHEMA

surface, 61.1±0.6° (averaged over six measurements). Therefore, the capillary pressure exerted on PHEMA film can provide sufficient tension to buckle the cylindrical holes. In Cai *et al.*'s model, buckling of a single void is considered. In an array of holes, such as ours, once one hole is deformed, it will stretch or compress its neighbors, and the pattern transformation propagates from the nucleation site, and finally the whole film is buckled into diamond plate pattern.

So far, we have shown that capillary force plays a key role to induce pattern transformation in PHEMA membranes while the lowered shear modulus by water swelling (from ~ 1.8 GPa in the dry state to ~ 134.4 kPa in water swollen state) assists the buckling by lowering the critical stress. To further support the conclusion, we copolymerized temperature responsive PNIPAAm with PHEMA. The PNIPAAm gel is known to have the lower critical solution temperature (LCST) near ~ 32 $^{\circ}$C, above which the polymer network collapses out of water.[27] Along the line, there is temperature dependent wettability and mechanical properties.[28] When increasing the temperature from 25 $^{\circ}$C to 40 $^{\circ}$C, the measured shear modulus G of swollen PHEMA-*co*-PNIPAAm gels increased from ~ 82.8±25.3 kPa to ~ 366.1±108.4 kPa, and hence the buckling critical tension σ_{cr}^{bk} ($\cong 0.98G$) raised from 81.1±24.8 kPa to 358.8±106.2 kPa. The G value of the film at 25 $^{\circ}$C is much lower than the upper limit value for capillarity induced buckling, 452 kPa. The hole would buckle at $\theta = 63.7°$ according to Eq. 5, which is larger than the static water contact angle of PHEMA-*co*-PNIPAAm, 46.0±3.3°. As seen in Fig. 3.5, when evaporating water from PHEMA-*co*-PNIPAAm membrane at 25 °C, a typical diamond plate pattern was observed (Fig. 3.5a-b). However, when dried at 40°C, the holes remained circular (Fig. 3.5c-d), suggesting that the compressive stress was insufficient to buckle the hydrogel holes above LCST. As shown earlier, at 40 $^{\circ}$C, the shear modulus of PHEMA-*co*-PNIPAAm gel was increased

to 366.1±108.4 kPa. The static water contact angle was also increased to 70.0±3.9°. The *G* value is smaller than the upper threshold modulus for capillarity induced buckling, 433 kPa calculated from Eq. 6. The discrepancy might be due to 1) non-negligible modulus enhancement caused by the dehydration of hydrogel network above LCST upon water evaporation, and 2) errors in modulus measurement. Below LCST, polymer chains form hydrogen bonding with water molecules, thus, are in stretched configuration. Above LCST, polymer chains form intramolecular hydrogen bonding, thus, they become globular and precipitate out of water. It is anticipated that the hydrogel network will dehydrate much faster above LCST, leading to significant enhancement in modulus during the drying process in comparison to that at room temperature. Since the modulus reported here were measured by AFM in a liquid cell, followed by data fitting, the AFM tip shape (here, conical), fitting model, and the sample equilibration time at the desired temperature could greatly affect the accuracy of the reported modulus data. Nevertheless, we show that by varying the environmental temperature of the responsive hydrogel film, we can tune the modulus and hydrophilicity/hydrophobicity, which in turn affects the film instability.
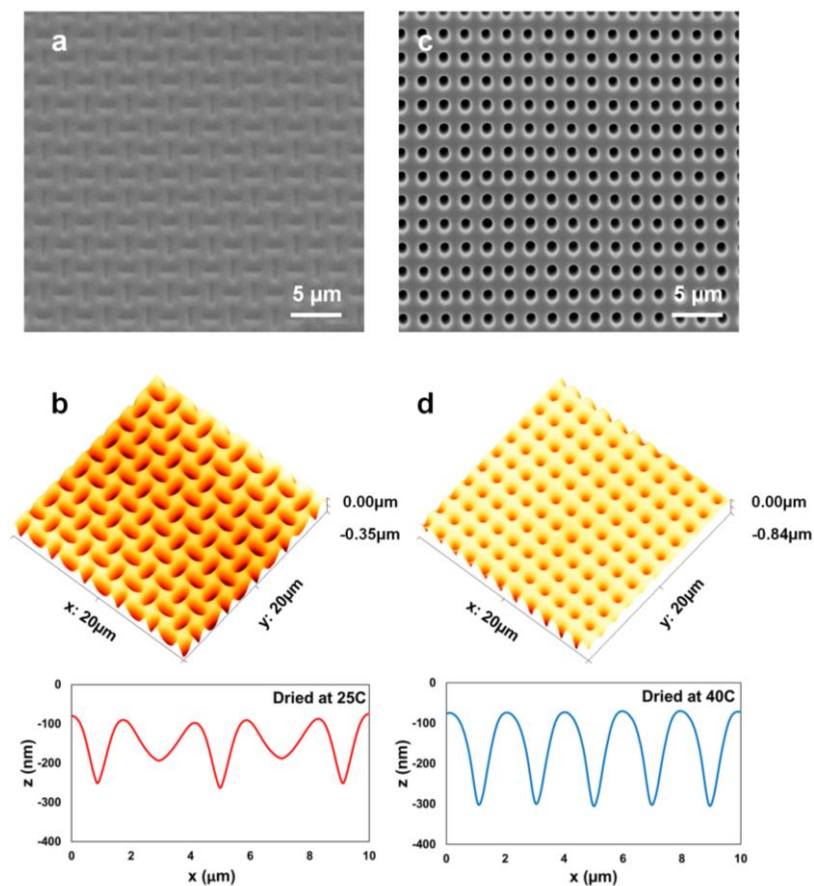
Fig. 3.5 SEM (a, c) and AFM images (b, d) of PHEMA-*co*-PNIPAAm membranes dried at different temperatures. (a) and (b) 25°C. (c) and (d) 40°C. (b) and (d) Top: surface topography. Bottom: line profile analysis. Since the AFM cantilever tip did not touch the bottom of the hydrogel membrane, the line profile does not reflect the actual depth of the pattern.

Finally, we illustrate a potential application of pattern transformation of PHEMA membrane with periodic micron-sized holes as a new type of smart window. PHEMA itself is highly transparent and has been widely used in hydrogel contact lenses. However, the periodic array of micropores in PHEMA membrane led to strong scattering of light at the air-solid interface. Thus, the transmittance of the film was dramatically decreased to ~ 30 % in the visible region (Fig. 3.6a). When buckled, the

73

transformed film became highly transparent again (~ 80% transmittance) because the air holes were mostly shut, thus, minimizing the scattering at the air-film interface. As a proof-of-concept, we placed "Penn" logo beneath the PHEMA membrane and visualize the logo before and after the pattern transformation (Fig. 3.6b). As seen in Fig. 3.6a, "Penn" can be clearly seen through the PHEMA film with diamond plate pattern while the refraction from 2D structure in the pristine film make it difficult to visualize the "Penn" logo.
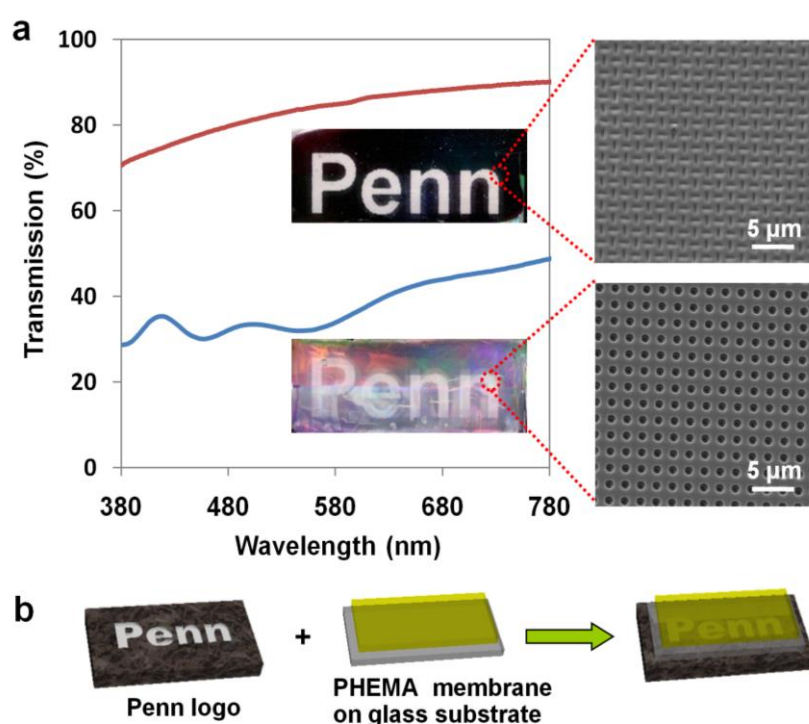
Fig. 3.6 (a) UV-Vis spectra of the pristine PHEMA and transformed diamond plate patterns averaged over four samples, each at two different spots. Insets: optical photography of the "Penn" letter viewed through the original and transformed films, and the corresponding SEM images. (b) Schematic illustration of sample preparation for visualization of the "Penn" letter through PHEMA membrane on a glass substrate.

3.3 Conclusion

We studied the instability in PHEMA and PHEMA-*co*-PNIPAAm hydrogel membranes

with a square lattice of micron-sized cylindrical holes. When exposed to water, the PHEMA membrane underwent breathing mode instability with smaller void size but circular shape. As water evaporation proceeded, the cylindrical holes were deformed into elliptical slits, and the square lattice bifurcated into a diamond plate pattern with neighboring slits perpendicular to each other. When it was re-exposed to DI-water, the buckled holes recovered to the original cylindrical shape. The deformation and recovery cycle could be repeated many times. Our analysis of the critical tension of buckling suggests that the capillary pressure played an important role in buckling the pores while the PHEMA membrane became rubbery after swelling in water. When copolymerizing thermo-responsive PNIPAAm with PHEMA gel, pattern transformation only occurred when drying the film below the LCST. Further, we demonstrated that the deformed PHEMA membrane had significantly enhanced transparency due to much reduced hole-size (up to 20 times smaller) upon pattern transformation. We believe that the presented understanding of the pattern transformation and recovery in hydrogel membranes can be applied to many other material systems or lattice symmetries (e.g. triangular lattice) to design smart materials and devices.

3.4 References

1.   Joannopoulos, J.D., et al., *Photonic crystals*. 2nd ed. 2008: Princeton University Press.

2.   Gorishnyy, T., et al., *Hypersonic phononic crystals.* Phys. Rev. Lett., 2005. **94**(11): p. 115501.

3.   Jang, J.H., et al., *Combining Pattern Instability and Shape-Memory Hysteresis for Phononic Switching.* Nano Lett., 2009. **9**(5): p. 2113-2119.

4.   Kinoshita, S. and S. Yoshioka, *Structural colors in nature: The role of regularity and irregularity in the structure.* Chem. Phys. Chem., 2005. **6**(8): p. 1442-1459.

5.   Tan, S.G., et al., *Magnetoelectric spin-FET for memory, logic, and amplifier applications.* Journal of Superconductivity, 2005. **18**(3): p. 357-365.

6.   Lewis, E.R., et al., *Fast domain wall motion in magnetic comb structures.* Nat. Mater., 2010. **9**(12): p. 980-983.

7.   Parker, A.R. and C.R. Lawrence, *Water capture by a desert beetle.* Nature, 2001. **414**(6859): p. 33-34.

8.   Mullin, T., et al., *Pattern transformation triggered by deformation.* Physical Review Letters, 2007. **99**(8): p. 084301.

9.   Bertoldi, K. and M.C. Boyce, *Mechanically triggered transformations of phononic band gaps in periodic elastomeric structures.* Phys. Rev. B, 2008. **77**(5): p. 052105.

10.   Zhu, X.L., et al., *Two-Dimensional Photonic Crystals with Anisotropic Unit Cells Imprinted from Poly(dimethylsiloxane) Membranes Under Elastic Deformation.* Appl. Phys. Lett., 2008. **93**(16): p. 161911.

11.   Jang, J.-H., et al., *Combining Pattern Instability and Shape-Memory Hysteresis for Phononic Switching.* Nano Lett., 2009. **9**(5): p. 2113-2119.

12.   Singamaneni, S., et al., *Instabilities and Pattern Transformation in Periodic, Porous Elastoplastic Solid Coatings.* ACS Appl. Mater. Interfaces, 2009. **1**(1): p. 42-47.

13.   Willshaw, S. and T. Mullin, *Pattern switching in two and three-dimensional soft solids.* Soft Matter, 2012. **8**(6): p. 1747-1750.

14.   Bertoldi, K., et al., *Negative Poisson's Ratio Behavior Induced by an Elastic Instability.* Adv. Mater., 2010. **22**(3): p. 361-366.

15.   Zhang, Y., et al., *One-step nanoscale assembly of complex structures via harnessing of elastic instability.* Nano Lett., 2008. **8**(4): p. 1192-1196.

16.   Singamaneni, S., et al., *Bifurcated Mechanical Behavior of Deformed Periodic Porous Solids.* Adv. Funct. Mater., 2009. **19**(9): p. 1426-1436.

17.   Peppas, N.A., et al., *Hydrogels in biology and medicine: From molecular principles to bionanotechnology.* Adv. Mater., 2006. **18**(11): p. 1345-1360.

18.   Wheeler, T.D. and A.D. Stroock, *The transpiration of water at negative pressures in a synthetic tree.* Nature, 2008. **455**(7210): p. 208-212.

19.   Chandra, D., et al., *Biomimetic Ultrathin Whitening by Capillary-Force-Induced Random Clustering of Hydrogel Micropillar Arrays.* ACS Appl. Mater. Interfaces, 2009. **1**(8): p. 1698-1704.

20.   Guvendiren, M., J.A. Burdick, and S. Yang, *Solvent induced transition from wrinkles to creases in thin film gels with depth-wise crosslinking gradients.* Soft Matter, 2010. **6**(22): p. 5795-5801.

21. Guvendiren, M., S. Yang, and J.A. Burdick, *Swelling-Induced surface patterns in hydrogels with gradient crosslinking density.* Adv. Funct. Mater., 2009. **19**(19): p. 3038-3045.

22. Zhang, Y., et al., *Replica molding of high-aspect-ratio polymeric nanopillar arrays with high fidelity.* Langmuir, 2006. **22**(20): p. 8595-8601.

23. Chandra, D., J.A. Taylor, and S. Yang, *Replica molding of high-aspect-ratio (sub-)micron hydrogel pillar arrays and their stability in air and solvents.* Soft Matter, 2008. **4**(5): p. 979-984.

24. Domke, J. and M. Radmacher, *Measuring the elastic properties of thin polymer films with the atomic force microscope.* Langmuir, 1998. **14**(12): p. 3320-3325.

25. Cai, S.Q., et al., *Osmotic collapse of a void in an elastomer: breathing, buckling and creasing.* Soft Matter, 2010. **6**(22): p. 5770-5777.

26. Speight, J.G., ed. *Lange's handbook of chemistry*. 16th ed. 2005, McGraw-Hill. 1661-1665.

27. Rubinstein, M. and R.H. Colby, *Polymer Physics*. 2003: Oxford University Press, USA.

28. Cheng, X.H., et al., *Surface chemical and mechanical properties of plasma-polymerized N-isopropylacrylamide.* Langmuir, 2005. **21**(17): p. 7833-7841.

Chapter 4: Buckling, Symmetry Breaking, and Creasing in Periodically Micro-Structured Hydrogel Membranes

4.0 Introduction

Soft materials that can reconfigure the shape and structural symmetry in response to external stimuli are of great interest for potential applications in miniaturized devices,[1-3] micro-actuation,[3-6] optical manipulation,[7, 8] microfluidic devices,[9] and drug delivery[10]. It also presents scientific and engineering challenges to the designs of soft materials with reversible, fast, and controllable deformation.

Mechanical instabilities in soft materials, often accompanying with large deformation and dramatic shape change in response to relatively small external perturbations, provide opportunities for designing reconfigurable structures with dramatic change of physical properties. Specifically, we and others have demonstrated spontaneous pattern transformation in periodic porous structures triggered by swelling, drying, polymerization and mechanical compression together with shape memory effect over multiple length scales,[11-24] The resulting photonic[25, 26] and phononic[24] bandgap properties, and mechanical behaviors (e.g. negative Poisson's ratio effect[17, 21]) are significantly altered due to the change of lattice symmetry, pore size or shape, and the volume filling fraction.

Among different approaches to induce instabilities in periodic porous structures, swelling induced buckling[13, 15, 16, 24] is of particular interest because of its simplicity, reversibility and versatility to generate variety of reconfigurable structures in different material systems from sub-micron to millimeter scales. It is known that choice of solvent and elasticity of the polymer membrane together with geometric features of the pattern (e.g. pore size, spacing and symmetry) will determine the volume

change, and the buckling behavior of the membrane, and thus, control the emergent patterns at equilibrium. So far, most studies reported in literature focus on achieving a single equilibrium state of the buckled structure by choosing a solvent with desired solvent - polymer network interaction parameter. However, many materials could be swollen to a large extent and meanwhile the swelling ratio can be fine-tuned continuously, for example, by changing pH or temperature of the environment. As a result, questions rise whether the morphology of the deformed soft membrane can be varied continuously by fine-tune the swelling ratio of the polymer network. More specifically, how the swelling induced pattern transformation occurs, and whether the transformed pattern can be amplified and evolved into new and more complex morphologies.

As a three-dimensional (3D) hydrophilic network of polymers, the responsive hydrogel offers a unique system to study swelling induced pattern transformation and morphology evolution. The swelling ratio and the equilibrium state of hydrogel pattern is a result of balancing the osmotic pressure generated from expansion and the elasticity of the polymer network, which can be tailored by the chemistry and composition of the hydrogel networks, as well as external stimuli, including choice of solvent,[2] pH,[27] temperature,[28] and light.[29] Poly(N-isopropyl acrylamide) (PNIPAAm) hydrogel has a lower critical solution temperature (LCST)[30] at ~32°C. Below LCST, the gel is swollen, and above LCST, the gel becomes collapsed out of water. When incorporating acid groups [e.g. carboxylic groups from poly(acrylic acid) (PAA)] in the PNIPAAm network, the swelling ratio could be fine-tuned by controlling both temperature and pH. Such bi-responsive hydrogel networks have been shown to have a wide range of tunable swelling ratio (by up to 20 folds increase from the collapsed state to the fully swollen state).[31] Another important factor that we are considering is the response rate of the volume changes. Since the characteristic rate of volume change is inversely

80

proportional to the square of the linear size of the gel,[32] the gel with small size (i.e. microstructured hydrogel membrane) is preferred due to the improved response rate.Here, we report the swelling-induced buckling instability and the corresponding post-buckling behaviors in pH and temperature dual-responsive hydrogel membranes of micron sized pores in a square array. The membrane was fabricated from poly(2-hydroxyethyl methacrylate-*co*-N-isopropylacrylamide-*co*-acrylic acid) (PHEMA-*co*-PNIPAAm-*co*-PAA) (43.7:40.8:14.5 mol%). We first studied the morphology change of the hydrogel membranes at different pH values at room temperature. The bulk hydrogel swelled ~1.61 to 9.18 times of its dried volume when increasing pH from 2 to 7. Within this regime, we observed four distinctive morphologies of the hydrogel membrane, including breathing mode of the membrane having circular pore arrays, buckled pore arrays of alternating mutually orthogonal ellipses, twisted snap-shut pores to form "S" shaped slits, and creases formed at local regions that perturbed the 2D periodicity of the hydrogel membrane. Using 3D confocal imaging, we followed the pattern evolution process as pH increased. We observed a symmetry breaking transition occurred between the buckled state (pH 4, achiral) and the twisted state (pH 5, chiral), where the later exhibited a mixed distribution of right- and left-handed chiral structures at pH 5. Further increase of the swelling ratio at pH 7 resulted in compression of the adjacent swollen hydrogel domains, leading to the formation of cusps randomly in the film. Finally, we demonstrated reversibly switching of the hydrogel membrane from the twisted state to the original circular hole array by increasing the temperature above the LCST of PNIPAAm.

4.1 Experimental

Sample preparation. Polydimethylsiloxane (PDMS, SYLGARD® 184 SILICONE ELASTOMER KIT) pillar array (diameter $D = 10$ μm, pitch $P = 15$ μm, and depth $H = 20$ μm) in a square lattice was used as the template to fabricate PHEMA-*co*-PNIPAAm-

co-PAA membranes (molar ratio, PHEMA/PNIPAAm/PAA= 43.7/40.8/14.5) by replica molding following the procedure reported earlier.[13]

For the hydrogel precursor, 1 g NIPAAm (Sigma-Aldrich) was dissolved in 1 mL 2-hydroxyethyl methacrylate (HEMA) (Sigma-Aldrich), followed by mixing with 30 µL Darocur 1173 (Ciba) and 200 µL acrylic acid (AA, Sigma-Aldrich). The mixture was then exposed to UV light (365 nm, 97435 Oriel Flood Exposure Source, Newport Corp.) to obtain a partially polymerized precursor solution. In order to ensure the homogeneity of photopolymerization, the UV exposure was carried out in small amount, 200 mJ/cm^2, for three times. After thoroughly homogenizing the mixture, additional 20 µL Darocur 1173 and 40 µL ethylene glycol dimethacrylate (EGDMA , Sigma-Aldrich) were added to prepare the molding solution.

The glass substrates were rinsed with acetone, followed by oxygen plasma (Harrick Expanded Plasma Cleaner & PlasmaFlo™) for 1 h. These glass slides were then treated with 3-(trimethoxysilyl)propylmethacrylate silane (Sigma-Aldrich) via vapor deposition in a vacuum chamber for 2 h as an adhesion promoter. 5 µL hydrogel precursor solution was cast onto the silanized glass substrate, and then the PDMS mold was placed on top to allow the precursor solution filling into the PDMS mold by capillarity. After exposed to UV light at a dosage, 1J/cm^2, the PDMS mold was peeled off from the hydrogel membrane.

Characterization. The hydrogel precursor in the same formulation as that used to fabricate the hydrogel membranes was infiltrated into a plastic tube with diameter of 2 mm. After exposing to the UV irradiation of 1 J/cm^2, the plastic tube was strip off and the solidified hydrogel was cut into small pieces (~ 5 mm length). These hydrogel rods were immersed into large amount of DI water for three days to remove the unreacted monomers and non-crosslinked oligomers, and then into the pH buffer solutions of different pH values: 2, 3, 4, 4.3, 4.7, 5, 5.3, 5.7, 6.4, and 7. After swelling for another

three days to ensure the hydrogel rods reaching the equilibrium states, the weight (W_s) was recorded. The hydrogel rods were then dried in an oven at 65 $^{\circ}$C for three days to obtain their dry weight (W_d). The mass swelling ratio was calculated as $Q_M = \dfrac{W_s}{W_d}$. The volumetric swelling ratio of the hydrogel was obtained as $Q_V = \dfrac{(Q_M - 1)\rho_P}{\rho_W} + 1$, where ρ_P is the density of polymer network, and ρ_W is the density of water. Since the value of ρ_P is difficult to be directly measured, we estimated $\rho_P = 1.1998$, based on the average density of the monomers and the crosslinkers used in the hydrogel network, assuming there was only minor volume change during the polymerization process.

In a similar manner, we tested the thermal responsiveness of the hydrogel. In this case, the hydrogel rods were placed into pH 4, 5, and 6 buffer solutions to reach equilibrium, and then placed into a water bath with controlled temperature of 20, 25, 30, 35, 40, and 45 $^{\circ}$C, respectively. At each temperature, the hydrogel rods were equilibrated for at least 2 days, and the weight was measured. The mass and the volumetric swelling ratio were calculated using above equations.

Observation of the Morphology Change of the Hydrogel Membrane at Different pH and Temperature. To investigate the swelling induced buckling instability and the corresponding post-buckling behaviors, the hydrogel membranes were immersed into the buffer solutions of different pH values overnight before taking images under the optical microscope (Olympus BX61 motorized microscope). For recording the transformation process, the samples were covered with cover glasses with small amount of buffer solution trapped underneath, and were heated on a small hotplate (Mettler Toledo FP82HT Hotstage), which was fitted into the microscope, from 20 to 45 $^{\circ}$C at a temperature gradient of 10 $^{\circ}$C/min. To image the equilibrium morphologies of the hydrogel membranes at 20, 30 and 40 $^{\circ}$C, the samples were heated in a water bath under

microscope (Warner Instrument Corporation, Micro-Incubation System), which has a feedback loop that controlled the water temperature inside with accuracy of ± 1 $^\circ$C. In this case, the hydrogel membrane was equilibrated until there was no obvious structural change, before images were taken.

Imaging of the Hydrogel Membranes. To directly observe the structural change of hydrogel membranes at different pH values and temperatures, we copolymerized a small portion (0.05 wt%) of rhodamine-B (RB, Aldrich) attached HEMA monomers into the hydrogel network, allowing for the direct imaging using the confocal microscopy. The attachment of RB to the HEMA monomers was based on the esterification reaction between the carboxylic (–COOH) groups on RB and the hydroxyl (–OH) groups on HEMA following the similar reactions reported in the literature.[28] In brief, 1 g RB (2.26 mmol), 1ml HEMA (8.24 mmol), 0.512 g dicyclohexylcarbodiimide (DCC, 2.49 mmol), and 0.304 g 4-dimethylaminopyridine (DMAP, 2.49 mmol) were dissolved in 50 ml dichloromethane. The reaction mixture was stirred at room temperature overnight for reaction to complete. After the insoluble salts formed during the reaction was removed by infiltration, the product was concentrated and further purified by silica gel column chromatography using ethyl acetate/isopropanol mixture.

The morphologies of the fluorescence labeled samples were captured under a laser scanning confocal microscope (Leica SP5 Spectral Imaging Confocal) with a 20X water immersing lens (HCX APO L20x/1.00W; working distance = 2 mm). The green laser of 543 nm wavelength was used to excite the fluorescence of the RB. The images taken by the microscope was then post-processed by using commercial software (Volocity 6.2.1).

The 3-D reconstruction was obtained by proceeding depth profile in z-scans with a step distance of 0.45 µm by confocal microscopy. The 3D model was then

reconstructed using the visualization package in the software (Volocity 6.2.1). The 3-D reconstruction of individual hydrogel domain was obtained by cropping the corresponding volume from the 3-D reconstruction of the hydrogel membranes.

The hydrogel membranes in the dry state were imaged using scanning electron microscopy (SEM) by FEI Strata DB235 Focused Ion Beam in high vacuum mode with acceleration voltage of 5kV.

4.2 Results and Discussion

We are interested in swelling-induced reconfigurations of the hydrogel membranes, specifically, how the deformed patterns evolve in response to the change of swelling ratio triggered by the external stimuli, such as pH and temperature. PHEMA based hydrogels were chosen in our experiments because of the high mechanical strength in the dry state, which allows for faithful replica molding of micron sized features, and mechanical stability in water, which is crucial for studies that require large degree of swelling without losing the integrity of the membrane structures. However, pure PHEMA hydrogel does not swell much in water: the equilibrium linear expansion (α_e) is ~1.5 using 1 wt% ethyleneglycol dimethacrylate (EGDMA) as crosslinker, and the degree of swelling is not tunable in response to any external stimuli.[33] Previously, we fabricated the PHEMA and PHEMA-*co*-PNIPAAm membranes (pore diameter $D = 1$ μm, pitch $P = 2$ μm, and depth $H = 4$ μm) in a square lattice. During swelling, the hydrogel membrane underwent a "breathing" mode deformation, where the pore size shrank somewhat but remaining circular shape.[20] Pattern transformation occurred during drying driven by capillary forces. Here, PAA was introduced to the thermoresponsive PHEMA-*co*-PNIPAAm network to increase the swellability of the hydrogel due to the hydrophilic nature of PAA in basic or neutral environment and make the network pH responsive. The porous hydrogel membranes with periodic

85

circular holes were fabricated by replica molding of the hydrogel precursor composed of HEMA, AA, and NIPAAm as monomers, EGDMA as crosslinker in a molar ratio of HEMA/NIPAAm/AA/EGDMA = 43.7:40.8:14.5:1 from a PDMS mold (Fig. 4.1 a-b), following the procedure described in literature.[34]
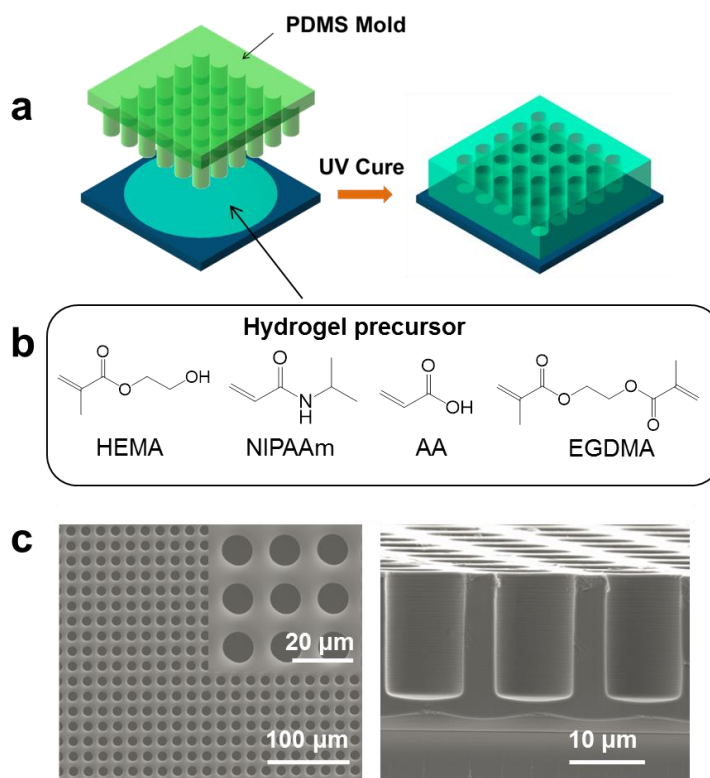
Figure 4.1 (a) Schematic illustration of the fabrication of hydrogel membrane by replica molding. (b) Chemical structures of the hydrogel precursors composed of monomers, including HEMA, NIPAAm, AA, and crosslinker, EGDMA. (c) SEM images of fabricated hydrogel membrane. Left: top view. Right: cross-sectional view.

When placed in water, the hydrogel swelled and the degree of swelling depended on both pH and temperature. We first characterized the volumetric swelling ratio, Q_V (see definition in Experimental Section) of the bulk hydrogel from pH 2 to 7 at room temperature (Fig. 4.2 a). The volume of the hydrogel increased with the increase of the

pH value in the buffer solution due to the enhanced degree of ionization of PAA at more basic environment. At pH 2, which was well below the pKa (~ 4.7) of PAA, the acid groups remained fully protonated; the polymer network was relatively hydrophobic due to the low ionization of the acid groups, and the formation of the hydrogen bonding between the protonated acid groups and the PNIPAAm. Thus, the swelling ratio was 1.61. Near the pKa of PAA in the range of pH from 4.5 to 5.5, there was a sharp volume change of the hydrogel, which was attributed to the large degree of ionization change of the weak acid groups. The swelling ratio Q_V = 9.18 was obtained at pH 7, when most of the acid groups became dissociated. Further increase of pH did not affect the swelling ratio due to the saturated ionization of carboxylic acid groups. Therefore, the hydrogel swelling behaviors were not further investigated at pH > 7.

In a similar manner, we characterized the thermal responsiveness of the hydrogel from 20 ℃ to 45 ℃ at pH 4, 5, and 6, respectively (Fig. 4.2 b). We observed a temperature dependent swelling similar to that from the random copolymers of PNIPAAm and PAA.[31] At pH 6 (> pKa of the PAA), LCST behavior of PNIPAAm in the copolymer network disappeared because the ionized PAA components generated sufficient hydrophilicity to overcome the aggregation of the hydrophobic PNIPAAm chains when heated above LCST.[35] On the other hand, at pH 4 (<pKa of the PAA), we found that the hydrogel networks exhibited low swelling capability even at 20 ℃, due to the low ionization of the acid groups. As a result, here we focused on the thermal switching behavior of the hydrogel at pH value near the pKa of the PAA, (i.e. pH 5), where good swelling capability at low temperature (Q_V = 5 at 20 ℃) and a clear transition to the collapsed state at high temperature (Q_V = 1.5 at 45 ℃) can be simultaneously achieved. It is worth noting that the swelling transition in our hydrogel

network was broad (spanned from 25 ºC to 40 ºC), which might be attributed to the interruption of the hydrogen bonding due to the randomly copolymerized PNIPAAm with PHEMA and PAA.[31] However, we consider this broad transition beneficial, since it can offer a broad temperature window for actuating the hydrogel swelling in response to the temperature change, and thus allowing for fine-tuning of the morphologies of the hydrogel membranes via changing the temperature.
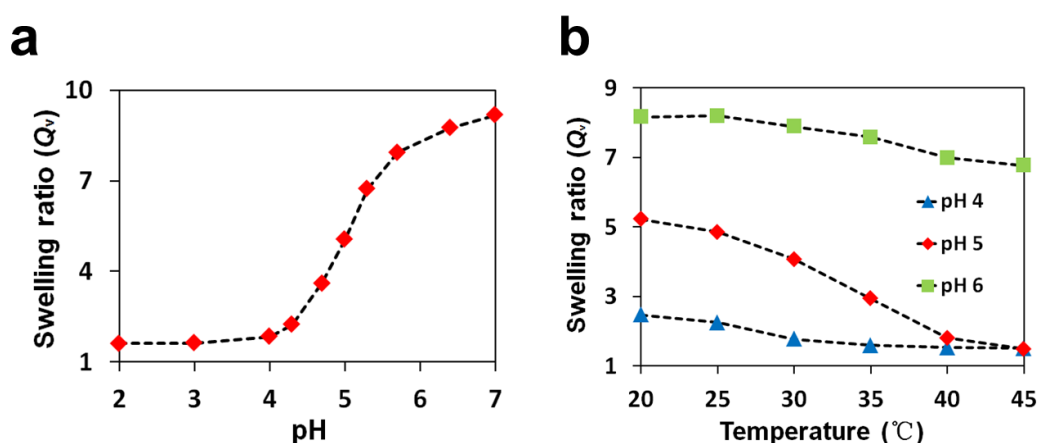
Figure 4.2 (a) The volumetric swelling ratio of the poly(2-hydroxyethyl methacrylate-*co*-*N*-isopropylacrylamide-*co*-acrylic acid) (44: 41: 15 mol%) bulk hydrogel in buffer solutions of different pH values at room temperature. (b) The volumetric swelling ratio of the hydrogel vs. the temperature at pH 4, 5, and 6, respectively.

The hydrogel membrane was first swollen in the pH 2 buffer solution, where the hydrogel exhibited the lowest degree of swelling (Q_V =1.61). As shown in Fig. 4.3 a, the pores remained circular after swelling, illustrating as "breathing" mode instability.[36] In a sharp contrast, when the swelling ratio was increased to 1.84 at pH 4, the circular pores in a square array were compressed and buckled into elliptical shape with long axis mutually orthogonal to each other; the transformation was observed

through the entire sample (~ 1cm^2). At a unit cell level of the buckled hydrogel membrane, the pattern transformation can be related to the rotations of the hydrogel domains in clockwise and counterclockwise directions, and the bending of the interconnected joints[37] as indicated on the magnified optical images (Fig. 4.3 b). We also looked at the overall deformation of the individual hydrogel domain during the transition via 3-D confocal microscopy. An obvious torsional deflection occurred, noticed as the helical edges on the hydrogel domains during the transition to the buckled state (Fig. 4.3 b).
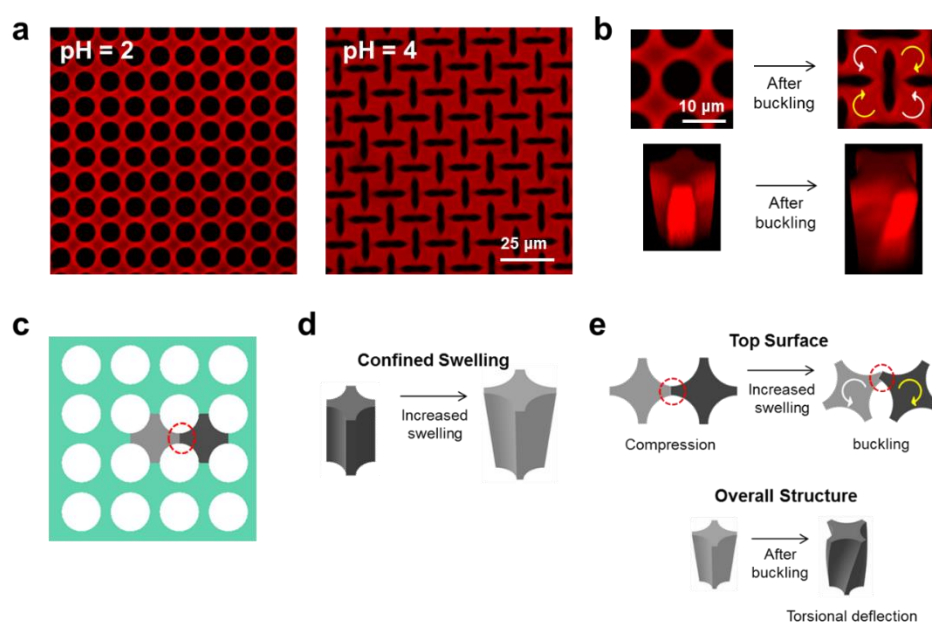
Figure 4.3 (a) Fluorescent images of the hydrogel membranes after immersed and equilibrated in pH 2 and pH 4 buffer solutions. (b) Fluorescent images of a single unit cell of the square lattice, showing detailed structural reconfiguration occurred during the pattern transformation process. (c-e) Illustration of the buckling instabilities in the hydrogel membrane. (c) Hydrogel domains and interconnected joints. (d) 3D view of confined swelling of an individual hydrogel domain. (e) Structural change of the

adjacent hydrogel domain. The yellow and the white arrows indicate the rotation directions of each domain.

We believe that high swelling induced compression at the joints between neighboring hydrogel domains triggered such dramatic deformation of the hydrogel membrane. As seen in Fig. 4.3 c, in a square lattice, the hydrogel domains diagonally bridge four neighboring holes (Fig 4.3 c). The two adjacent domains are connected by a thin joint (indicated by the red dashed circle). An isolated individual hydrogel domain undergoes confined swelling, where the bottom of the domain is restricted by the rigid substrate, while the top expands freely in x, y, and z directions (Fig. 4.3 d). In the case of swelling the hydrogel membrane, the hydrogel domains are interconnected. Therefore, the lateral expansion of the top layer becomes restricted by its neighbors, leading to a compressive force exerted to the joints and the pores (Fig. 4.3 e). At a low degree of swelling (pH 2), the compressive stress generated at the joint is small compared to the critical buckling threshold, thus, pores shrink slightly, but remain circular.[20] When compressive stress generated by osmotic pressure is increased above the buckling threshold (e.g. at pH 4), the joints are buckled, and the corresponding rotation of the hydrogel domains is triggered simultaneously (Fig. 4.3 c). Once one pore is buckled, the joints connecting the swollen hydrogel domains also contribute to the uniform spreading of the buckling instabilities, where the neighboring joints were bent accordingly, resulting in pattern transformation of the entire porous membrane, similar to what we previously observed when swelling of the PDMS membrane in toluene, where the square array of circular pores are buckled into a diamond-plate structure with mutually perpendicular slits.[13] Due to the strong confinement of the hydrogel on the substrate (the bottom of the hydrogel domains

cannot rotate), the rotational deformation on the top cannot propagate vertically through the hydrogel domain. Therefore, a gradual torsional deformation occurs to accommodate the rotational misalignment between the top and bottom surfaces.

As we further immersed the hydrogel membrane to the buffer solution of higher pH, pH 5 (Q_V=5.05), we observed a secondary structural reconfiguration process, which ended up with a state of collapsed pores twisted into "S" shape (Fig. 4.4 a). It is worth noting that this transition involved a symmetry breaking process, where the final structure of the hydrogel membrane has either right or left handedness (see insets in Fig. 4.4 a). At the phase boundary of these regimes (shown as yellow dashed line), the rotational directions of hydrogel domains were not well-defined due to the competition from the regimes of opposite handedness.

To understand the morphological transition and why the hydrogel underwent a symmetry breaking, we took a closer look at the hydrogel membrane at pH 4.3 (Fig. 4.4 b), an intermediate state (Q_V=2.24) between the buckled state at pH 4 and twisted state at pH 5. Here, the deformation to the hydrogel membrane was accentuated (Fig. 4.4 c), which cause the circular pores being largely compressed to form an "8" shape, whereas the joints in the opposite side of the pore start to touch against each other (shown in the inset of Fig. 4.4 b). Further swelling intensified the compression at the touching joints, and triggered a symmetry breaking process at pH 5, as we shown in the unit cell level (Fig. 4.4 d). During this symmetry breaking process, the increased swelling of the hydrogel membrane was compensated by rotating all the hydrogel domains in the same direction (indicated by the solid arrows). By having such reorientation of the surface structure, the two touching joints were able to slide against each other (see the white dashed arrows), which relieved the compression forces between the touching joints. We also noticed that there were two possibilities of

symmetry breaking process: clockwise or counterclockwise rotations, which explained the coexisting of both right- and left-handed chirality of the features. Meanwhile, symmetry breaking could start from different nucleation sites and propagate, leading to the formation of phase boundaries where two independently evolved regimes of opposite handedness met with each other.
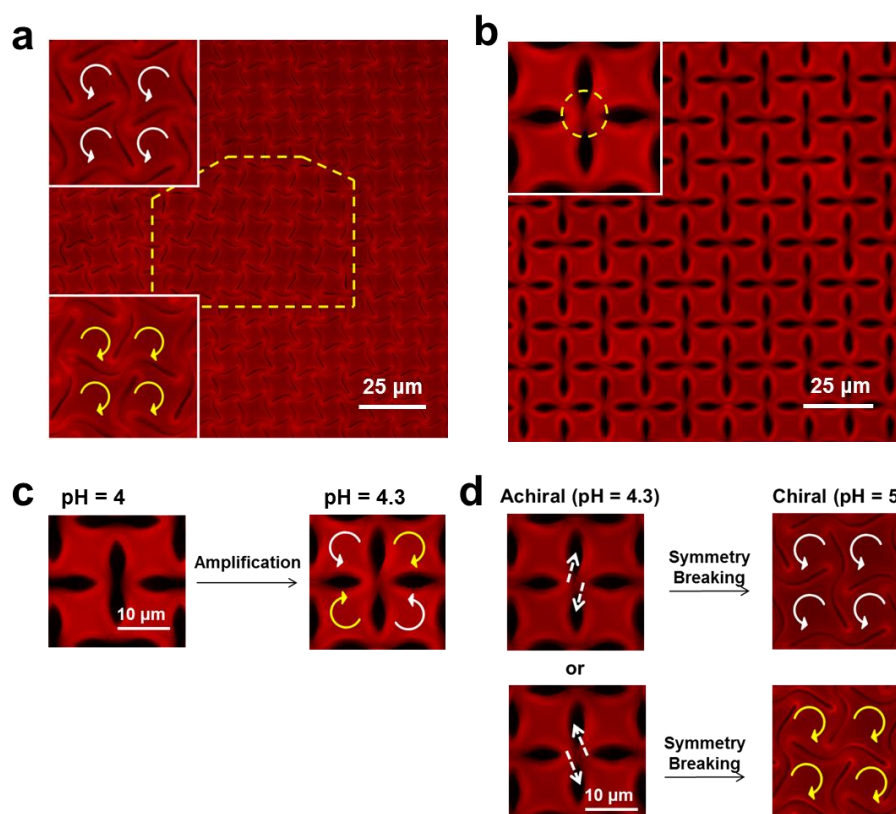
Figure 4.4 Fluorescent images of the hydrogel membranes at different deformed states. (a) The hydrogel membrane at the twisted state. Insets: showing the left- and right-handed chirality. The yellow dashed line indicates the boundary between regimes of deformed hydrogel membrane with opposite handedness. (b) The hydrogel membrane at pH 4.3, an intermediate state between the buckled and twisted states. Inset: higher magnification image revealing that the deformation of the pores led to the joints at opposite side of the pores touching against each other due to increased compression. (c) Amplification process at unit cell level of the buckled hydrogel membrane between

hydrogel membranes immersed in pH 4 to pH 4.3. (d) Symmetry breaking process at unit cell level of the buckled hydrogel membrane from achiral (pH 4.3) to chiral (pH 5). The white and yellow arrows indicate the rotation directions of the hydrogel domains, and the dashed arrows indicate the sliding directions of the joints during the transition.

The symmetry breaking process in the cellular solid has been recently reported by Kang *et al*.[24] In their experiment, by triggering different modes of buckling on the surface-attached thin plates, the cellular solids were designed to be buckled and resulted in both achiral and chiral structures upon swelling the polymer pattern in a favored solvent. We believe that the symmetry breaking process reported here is significantly different from that by Kang *et al*, even though both processes involved the swelling induced buckling. The major difference is that the chirality reported by Kang *et al*. was directed by the programed buckling modes, depending on the plate aspect ratio (length/height), and the symmetry breaking occurred simultaneously with the triggering of the buckling instability. In our experiment, the buckling instabilities initially did not invoke the symmetry breaking process (circular pores was initially buckled into the achiral buckled state), yet after the hydrogel was further swollen to a larger degree, the chirality was induced in a secondary bifurcation step. Such two-step reconfiguration mechanism led to three states of distinctive pattern symmetries, which is more advanced compared to the existing pattern transformation systems that only allow for switching between the initial and buckled states. We expect that our system can be further modified to generate a defect-free reconfiguration with single handedness by limiting nucleating sites, for example, wetting the sample from a single point.[38] Moreover, since the swelling ratio of the hydrogel membrane was coupled to both of

the pH and thermal responsiveness, later we will show to erase the chirality by deswelling of the hydrogel above LCST.

When pH of the buffer solution was increased to 7, the pores were further compressed by the highly swollen hydrogel, and star-shaped patterns appeared randomly in the film (Fig. 4.5 a), similar to the creasing instability. Solvent swelling induced transition from buckling to creasing when increasing swelling ratio has been reported by us in thin film PHEMA gels confined on a rigid substrate.[33] However, we did not observe the transition from buckling to creasing instability within individual pores as suggested in simulation by Cao *et al.*[39] This can be attributed to the local defects within the gels, where crosslinking or swelling inhomogeneity is amplified in the highly swollen gel, and thus offering local energy minimum for creasing to take place in these regions.

A closer look by confocal imaging of the depth profile of the hydrogel membrane at pH 5 and pH 7 (see Fig. 4.5 b-c) showed that the hydrogel surface in the creased region was compressed by the neighboring hydrogel domains at pH 7 to make a contact in contrast to a rather uniform height at different swollen regions at pH 5, As seen in Fig. 4.5 c, the transverse expansion of the swollen layer becomes inhomogeneous at pH 7. To release the excessive compressive stress exerted from the neighboring hydrogel domains, a cusp is formed in the membrane, much like the observation of surface folds formed on a flat thin film at a large swelling ratio.[40]
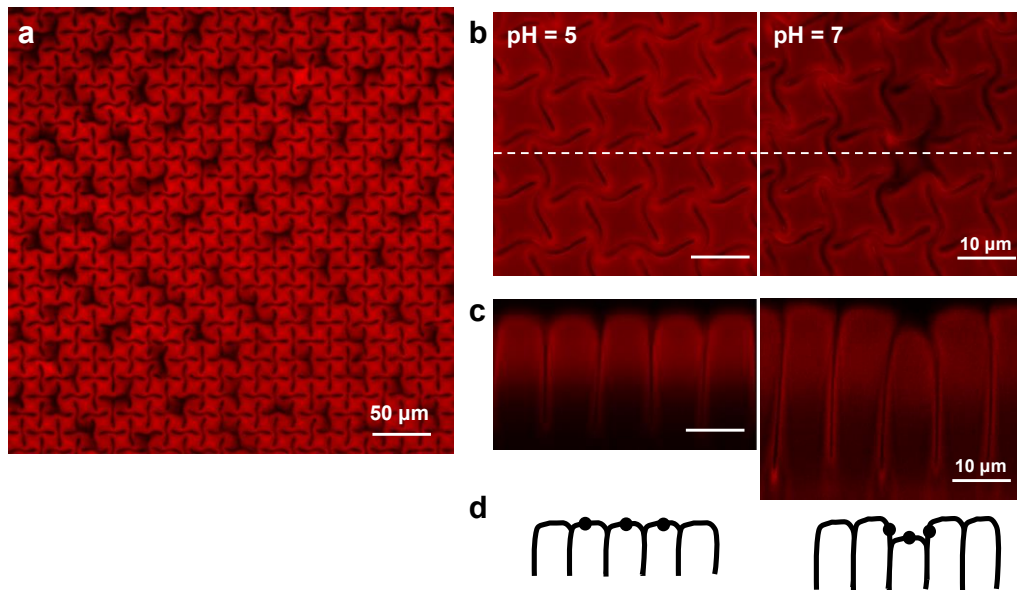
Figure 4.5 Confocal microscopy images of the hydrogel membranes visualized from different planes (a) xy plane at pH 7. (b-c) xy- (b) and xz- (c) planes at pH 5 and 7. Dotted lines in (b) correspond to the location where the cross-sectional images (viewed from xz planes) were taken, showing a cusp in the hydrogel film due to compression of the neighboring hydrogel domains. (d) Schematic illustration of creasing instability when increasing the compressive stress in the swollen hydrogel membrane. The dots on the free surface of the adjacent hydrogel domains move toward center, forming a cusp.

Finally, we demonstrated the reversible switching of the hydrogel membrane between the twisted state and circular hole arrays by applying the heating and cooling cycles between 20 °C and 45 °C at pH 5. The switching time was on the order of 10's of second due to the fast diffusion of the water and ions across the micron-sized hydrogel membrane. Since the volume of the hydrogel film could be varied continuously by temperature in a large temperature window, we were able to dynamically tune the pore size, shape, and geometry. As seen in Figure 4.6 a, the hydrogel membranes

95

equilibrated at different temperatures exhibited distinctive morphologies, including the chiral twisted structure (40 ^{o}C), diamond-plate structure (30 ^{o}C), and the original circular pore array (20 ^{o}C). Moreover, we showed that the thermal response of the hydrogel membrane persisted at least 10 heating and cooling cycles, while the pattern transformation behavior did not alter after multiple cycles, indicating that the temperature triggered switching of hydrogel membranes is quite robust. In comparison, the hydrogel membrane swollen at pH 5 at room temperature (the twisted structure) could not be fully recovered to the circular pore array when immersed in a pH 2 buffer solution even after the membrane was equilibrated for more than a week. Instead, the membrane was partially recovered to the diamond-plate structure. We suspect that there may be two reasons contributed to the non-fully recovery of the membrane by the deswelling at a lower pH: 1) the fast dehydration upon immersing into the pH 2 buffer caused the hydrogel network collapse dramatically, which might be responsible for kinetically trapping the deformed state of the hydrogel membrane due to the strong interaction between polymer chains at the collapsed state, e.g. hydrogen bonding, and hydrophobic interactions; and 2) a hysteresis commonly observed in the pH responsive hydrogels, since PAA based gels have different swelling and deswelling curves, depending on the pH value and pH gradient.[41, 42] Here, the hydrogel membrane might not be able reach the same equilibrium state when deswelling from pH 5 to pH 2 as it was initially transferred from DI water to the pH 2 buffer solution.
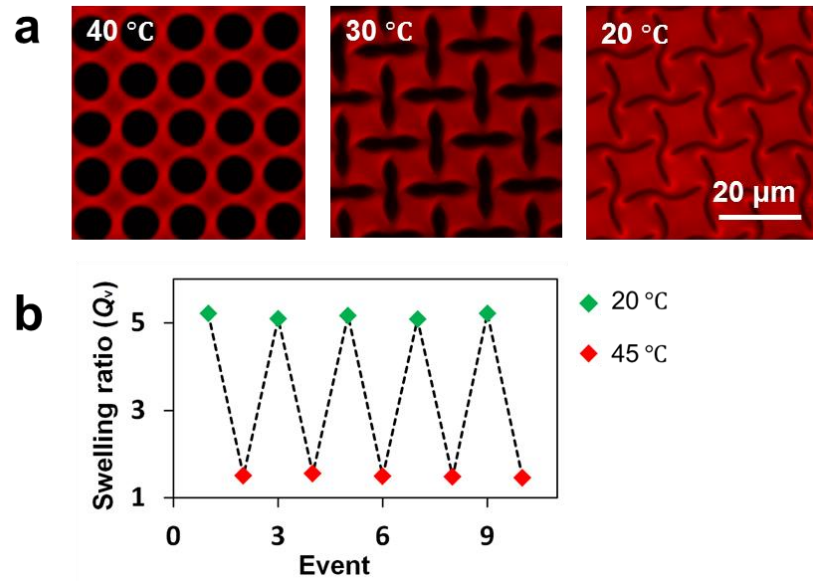
Figure 4.6 (a) Fluorescent images showing the morphologies of the hydrogel membranes equilibrate at 40 ℃, 30 ℃, and 20 ℃, respectively, in pH 5 buffer solutions. (b) The volumetric swelling ratio of the hydrogel measured at 10 heating and cooling cycles between 20 ℃ and 45 ℃.

4.3 Conclusions

In this report, we investigated swelling-induced pattern transformation and various morphologies from pH and temperature responsive hydrogel membrane. We showed that pattern transformation can be triggered and evolved into different reconfiguration states by controlling the swelling ratio of the hydrogel. At pH2, the hydrogel membrane underwent breathing mode instability, then became buckled into diamond-plate structure with mutually perpendicular ellipses at pH 4. When further increasing pH and swelling ratio, we observed a symmetric breaking transition from pH 4.3 to pH 5, where the achiral buckled state of hydrogel membrane was transformed into a chiral twisted state, along with the compaction of the hydrogel domains within the 2-D space. Such a spontaneous generation of chirality in the absence of a chiral induction has profound

97

impact for the understanding the origin of single chirality found in nature, and could lead to potential applications including optical devices, sensors, drug delivery, and advanced structural components. At an even higher degree of swelling, the hydrogel membrane fully occupied the 2D space, the excessive swelling of the hydrogel was found accommodated by forming local cavity on the hydrogel surface, similar to the initiation process of creasing instability on the flat hydrogel surface at large swelling. Finally, we demonstrated the temperature-dependent reversible switching of the hydrogel membrane among chiral twisted state, buckled state, and circular state. The study demonstrated here using the responsive hydrogel membrane with tunable swelling ratio as a model system to dynamically control the pore size and shape, pattern geometry, and chirality of periodic achiral structures in response to environment stimuli will offer new insights to the design of the next generation reconfigurable structures. Meanwhile, since the entire transformation process is driven by the tunable swelling ratio of the hydrogel, we expect such switching process can be obtained by a rich category of external stimuli (e.g. light, electric field, and biomolecules) that involve volume phase transition of the materials.

4.4 References

1. He, X., et al., *Synthetic homeostatic materials with chemo-mechano-chemical self-regulation.* Nature, 2012. **487**(7406): p. 214-218.

2. Sidorenko, A., et al., *Reversible Switching of Hydrogel-Actuated Nanostructures into Complex Micropatterns.* Science, 2007. **315**(5811): p. 487-490.

3. van Oosten, C.L., C.W.M. Bastiaansen, and D.J. Broer, *Printed artificial cilia from liquid-crystal network actuators modularly driven by light.* Nat Mater, 2009. **8**(8): p. 677-682.

4. Glazer, P.J., et al., *Multi-Stimuli Responsive Hydrogel Cilia.* Adv. Funct. Mater., 2013: p. n/a-n/a.

5. le Digabel, J., et al., *Magnetic micropillars as a tool to govern substrate deformations.* Lab Chip, 2011. **11**(15): p. 2630-2636.

6. Wu, Z.L., et al., *Three-dimensional shape transformations of hydrogel sheets induced by small-scale modulation of internal stresses.* Nat Commun, 2013. **4**: p. 1586.

7. Dong, L., et al., *Adaptive liquid microlenses activated by stimuli-responsive hydrogels.* Nature, 2006. **442**(7102): p. 551-554.

8. Shimamoto, N., et al., *Nanopattern Fabrication of Gold on Hydrogels and Application to Tunable Photonic Crystal.* Adv. Mater., 2012. **24**(38): p. 5243-5248.

9. Beebe, D.J., et al., *Functional hydrogel structures for autonomous flow control inside microfluidic channels.* Nature, 2000. **404**(6778): p. 588-590.

10. Ehrick, J.D., et al., *Genetically engineered protein in hydrogels tailors stimuli-responsive characteristics.* Nat. Mater., 2005. **4**(4): p. 298-302.

11. Mullin, T., et al., *Pattern Transformation Triggered by Deformation.* Phys. Rev. Lett., 2007. **99**(8): p. 084301.

12. Bertoldi, K., et al., *Mechanics of deformation-triggered pattern transformations and superelastic behavior in periodic elastomeric structures.* J. Mech. Phys. Solids, 2008. **56**(8): p. 2642-2668.

13. Zhang, Y., et al., *One-Step Nanoscale Assembly of Complex Structures via Harnessing of an Elastic Instability.* Nano Lett., 2008. **8**(4): p. 1192-1196.

14. Singamaneni, S., et al., *Instabilities and Pattern Transformation in Periodic, Porous Elastoplastic Solid Coatings.* ACS Appl. Mater. Interf., 2008. **1**(1): p. 42-47.

15. Jang, J.-H., et al., *Combining Pattern Instability and Shape-Memory Hysteresis for Phononic Switching.* Nano Lett., 2009. **9**(5): p. 2113-2119.

16. Singamaneni, S., et al., *Bifurcated Mechanical Behavior of Deformed Periodic Porous Solids.* Adv. Funct. Mater., 2009. **19**(9): p. 1426-1436.

17. Bertoldi, K., et al., *Negative Poisson's Ratio Behavior Induced by an Elastic Instability.* Adv. Mater., 2010. **22**(3): p. 361-366.

18. Goencue, F., et al., *Deformation induced pattern transformation in a soft granular crystal.* Soft Matter, 2011. **7**(6): p. 2321-2324.

19. Li, J., et al., *Switching periodic membranes via pattern transformation and shape memory effect.* Soft Matter, 2012. **8**(40): p. 10322-10328.

20. Zhu, X., et al., *Capillarity induced instability in responsive hydrogel membranes*

with periodic hole array. Soft Matter, 2012. **8**(31): p. 8088-8093.

21.   Overvelde, J.T.B., S. Shan, and K. Bertoldi, *Compaction Through Buckling in 2D Periodic, Soft and Porous Structures: Effect of Pore Shape.* Adv. Mater., 2012. **24**(17): p. 2337-2342.

22.   Shim, J., et al., *Buckling-induced encapsulation of structured elastic shells under pressure.* Proc. Nat. Acad. Sci. U. S. A., 2012. **109**: p. 5978-5983.

23.   Willshaw, S. and T. Mullin, *Pattern switching in two and three-dimensional soft solids.* Soft Matter, 2012. **8**(6): p. 1747-1750.

24.   Kang, S.H., et al., *Buckling-Induced Reversible Symmetry Breaking and Amplification of Chirality Using Supported Cellular Structures.* Adv. Mater., 2013: p. doi: 10.1002/adma.201300617.

25.   Zhu, X.L., et al., *Two-Dimensional Photonic Crystals with Anisotropic Unit Cells Imprinted from Poly(dimethylsiloxane) Membranes Under Elastic Deformation.* Appl. Phys. Lett., 2008. **93**(16): p. 161911.

26.   Krishnan, D. and H.T. Johnson, *Optical properties of two-dimensional polymer photonic crystals after deformation-induced pattern transformations.* J. Mech. Phys. Solids, 2009. **57**(9): p. 1500-1513.

27.   Liu, D., et al., *Single-composition three-dimensionally morphing hydrogels.* Soft Matter, 2013. **9**(2): p. 588-596.

28.   Kim, J., J. Yoon, and R.C. Hayward, *Dynamic display of biomolecular patterns through an elastic creasing instability of stimuli-responsive hydrogels.* Nat. Mater., 2010. **9**(2): p. 159-164.

29.   Yoon, J., et al., *Local Switching of Chemical Patterns through Light-Triggered Unfolding of Creased Hydrogel Surfaces.* Angew. Chem. Inter. Ed., 2012.

51(29): p. 7146-7149.

30.   Heskins, M. and J.E. Guillet, *Solution Properties of Poly(N-isopropylacrylamide).* Journal of Macromolecular Science: Part A - Chemistry, 1968. **2**(8): p. 1441-1455.

31.   Yu, H. and D.W. Grainger, *Thermo-sensitive swelling behavior in crosslinked N-isopropylacrylamide networks: Cationic, anionic, and ampholytic hydrogels.* Journal of Applied Polymer Science, 1993. **49**(9): p. 1553-1563.

32.   Tanaka, T. and D.J. Fillmore, *Kinetics of swelling of gels.* The Journal of Chemical Physics, 1979. **70**(3): p. 1214-1218.

33.   Guvendiren, M., J.A. Burdick, and S. Yang, *Solvent induced transition from wrinkles to creases in thin film gels with depth-wise crosslinking gradients.* Soft Matter, 2010. **6**(22): p. 5795-5801.

34.   Chandra, D., J.A. Taylor, and S. Yang, *Replica molding of high-aspect-ratio (sub-)micron hydrogel pillar arrays and their stability in air and solvents.* Soft Matter, 2008. **4**(5): p. 979-984.

35.   Chen, G.H. and A.S. Hoffman, *GRAFT-COPOLYMERS THAT EXHIBIT TEMPERATURE-INDUCED PHASE-TRANSITIONS OVER A WIDE-RANGE OF PH.* Nature, 1995. **373**(6509): p. 49-52.

36.   Cai, S., et al., *Osmotic collapse of a void in an elastomer: breathing, buckling and creasing.* Soft Matter, 2010. **6**(22): p. 5770-5777.

37.   Mullin, T., et al., *Pattern Transformation Triggered by Deformation.* Physical Review Letters, 2007. **99**(8): p. 084301.

38.   Kang, S.H., et al., *Buckling-Induced Reversible Symmetry Breaking and Amplification of Chirality Using Supported Cellular Structures.* Advanced

Materials, 2013: p. n/a-n/a.

39.   Cai, S.Q., et al., *Creasing instability of elastomer films.* Soft Matter, 2012. **8**(5): p. 1301-1304.

40.   Trujillo, V., J. Kim, and R.C. Hayward, *Creasing instability of surface-attached hydrogels.* Soft Matter, 2008. **4**(3): p. 564-569.

41.   Suzuki, A. and H. Suzuki, *Hysteretic behavior and irreversibility of polymer gels by pH change.* J. Chem. Phys., 1995. **103**(11): p. 4706-4710.

42.   Richter, A., et al., *Characterization of a microgravimetric sensor based on pH sensitive hydrogels.* Sens. Actuator B-Chem., 2004. **99**(2-3): p. 579-585.

Chapter 5: Buckling into Single-handed Chiral Structures from pH-sensitive Hydrogel Membranes

Adapted from (Cao, B.[*]; **Wu, G.**[*]); Xia, Y.; Yang, S., *Extreme Mechanics Letters* **2016,** *7.*

[*]Equally contributed.

5.0 Introduction

Mechanical instabilities in soft materials, precipitated by dewetting,[1] swelling,[2] crumpling,[3, 4] wrinkling,[5] and buckling,[6] often accompanied with large deformation and shape change in response to relatively small external perturbations, providing new opportunities to design reconfigurable materials with dramatic change of physical properties. Recently, we and others have demonstrated spontaneous pattern transformation in periodic porous membranes triggered by swelling, drying, polymerization and mechanical compression together with shape memory effect over multiple length scales,[7-20] The resulting photonic[21, 22] and phononic[20] bandgap properties, and mechanical behaviors (e.g. negative Poisson's ratio[13, 17]) are significantly altered due to the simultaneous change of lattice symmetry, pore size or shape, and the volume filling fraction.

It is known that choice of solvent and elasticity of the polymer together with geometric features of the pattern (e.g. pore size, spacing and symmetry) will determine the volume change, and the buckling behavior of the membrane, and thus, control the emergent patterns. As a three-dimensional (3D) hydrophilic network of polymers, hydrogel offers a unique system to study swelling induced pattern transformation and morphology evolution: the degree of swelling can be fine-tuned, and the structural evolution upon swelling can be visualized upon swelling at different environment. Recently, we report the swelling-induced buckling instability and the corresponding

post-buckling behaviors in the pH and temperature dual-responsive poly(2-hydroxyethyl methacrylate-*co*-*N*-isopropylacrylamide-*co*-acrylic acid) (PHEMA-*co*-PNIPAAm-*co*-PAA) hydrogel membranes of micron sized pores in a square array.[23] When pH was increased from 2 to 7, we observed four distinctive morphologies, including breathing mode of the membrane having circular pore arrays, buckled pore arrays of alternating mutually orthogonal ellipses, twisted snap-shut pores to form "S" shaped slits, and cavitation formation at local regions that perturbed the 2D periodicity of the hydrogel membrane. Importantly, we observed a symmetry breaking transition between the buckled state (pH 4, achiral) and the twisted state (pH 5, chiral), where the latter exhibited mixed domains of right- and left-handed (RH and LH) chiral structures with random phase boundaries. Little is known about buckling induced, chiral symmetry breaking mechanism.

Such a spontaneous generation of chirality in the absence of a chiral induction could have a profound impact on the understanding of the origin of single chirality found in nature, such as sea shells, pine tree cones and sunflower seeds,[24, 25] which is often driven by the instability and packing constrain within a limited space. Meanwhile, chirality is of interests for applications including optical devices, sensors, medicine, and advanced structural components. The immediate question is whether we can control the pattern transformation to create single-handed chirality over the entire film. Previously, we have demonstrated that the pattern evolution process of hydrogel membrane upon swelling can be directly visualized by immersing the pH responsive hydrogel membrane within buffer solution having different pH values. It provides a unique system to investigate the pattern evolution and symmetry breaking mechanism on hydrogel membrane.

Here, we investigated how small bias to the initial square arrays of periodic structures affect the overall chiral transformation of the hydrogel membrane. This is known as a process closer to structural reconfiguration in the nature environment, where the initial structures can be imperfect or distorted. In our model system, the bias was introduced from pre-stretched with 5% strain to PDMS pillar arrays with initial square arrays pillars at different directions against its lattice axis (i.e. angle against the y-axis of the lattice of 15°, 30°, 45°, 60°, 75°, see Fig. 1). After replica molding to the hydrogel precursor, we obtained oblique lattice of micro-pore arrays on pH sensitive poly(2-hydroxyethyl methacrylate)-*co*-poly(acrylic acid) (PHEMA-*co*-PAA) hydrogel membrane to investigate the structural evolution upon swelling. After immersing the hydrogel membrane in buffer solution at pH values of pH 3, 4.7 and 6, three states on swollen hydrogel membrane can be visualized: buckled state – pH 3, transition state – at pH 4.7, and chiral twisted state at pH 6. We demonstrated that even such a small bias to the initial porous structure can significantly affect the tendency of the symmetry breaking process offering controlled single chirality after entering fully swollen state of the hydrogel. With LH structures in the pre-stretching angle smaller than 45° (15°, 30°) membranes, where transformed pattern is predominated with counterclockwise rotation of the hydrogel structures. Meanwhile, the RH structures was observed from hydrogel membrane obtained from replicating PDMS pillars at pre-stretching angle larger than 45° (60°, 75°), where the hydrogel structures were rotated clockwise during the symmetry-breaking. The discovery here can potentially inspire the understanding of spontaneous single chiral structures formation, and applications such as chiral separation and biomolecular devices.

5.1 Experimental

Fabrication of hydrogel membranes. The hydrogel membranes were replica molded from a original/pre-stretched poly(dimethylsiloxane) (PDMS) mold following the procedure in literature.[26] To prepare the hydrogel precursor, 200 μL acrylic acid (AA, Sigma-Aldrich), 2 mL 2-hydroxyethyl methacrylate (HEMA, Sigma-Aldrich) (HEMA /AA = 78/14 mol/mol), and 30 μL of Darocur 1173 (Ciba Specialty Chemicals) as a photoinitiator were mixed in a vial and ultrasonicated for 30 min. The mixture was then exposed to UV light (365 nm, 97435 Oriel Flood Exposure Source, Newport Corp.) three times at a dosage of 200 mJ/cm^2 each time. Next, an additional 20 μL Darocur 1173 and 40 μL ethylene glycol dimethacrylate (EGDMA, Sigma-Aldrich) as a crosslinker were added into the mixture to form the hydrogel precursor for molding. The PDMS mold consisting of a square arrayed micropillars (diameter =10 μm, pitch = 15 μm, and height = 20 μm) was fabricated by replicating the epoxy master from Sylgard 184 kit from Dow Corning (prepolymer: crosslinker = 10: 1 wt/wt) and cured at 65 ^{o}C for 4h. Glass slides used as substrates were rinsed by acetone, followed by oxygen plasma (Harrick Expanded Plasma Cleaner & Plasma-Flo^{TM}) for 30-40 min. They were then treated by 3-(trimethoxysilyl) propyl methacrylate (TMS, Sigma-Aldrich) *via* vapor deposition for at least 2h in a vacuum chamber to increase the adhesion between the substrate and the hydrogel membrane. 10 μL of the aforementioned hydrogel precursor was cast on a treated glass slide, and then a PDMS mold was placed on the top of it. Slight force was applied on the PDMS mold to make sure it had close contact with the precursor. The hydrogel precursor infiltrated into the PDMS mold by capillarity, followed by UV curing at a dosage of 2 J/cm^2. Finally, the hydrogel membrane was obtained after peeling off the PDMS mold.

To introduce bias of pore arrangement in the hydrogel membranes, the PDMS molds were pre-stretched with a strain of 5% at various angles (θ, 15°, 30°, 45°, 60°, 75°), denoted as θ_{15}, θ_{30}, θ_{45}, θ_{60}, θ_{75}, respectively, before replica molded into hydrogel membranes (see Fig. 5.1). Thus, the square array of porous membrane (non-stretched) is slightly distorted to oblique arrays while the pore shape remained circular due to the small strain applied to the pillar arrays. For replica molding of pre-stretched pillar to the hydrogel membrane, 10 µL hydrogel precursor was spread over the PDMS mold, and then another TMS silane treated glass slide was placed on top of the hydrogel precursor, followed by 2 J/cm^2 UV exposure to cure the hydrogel precursor.
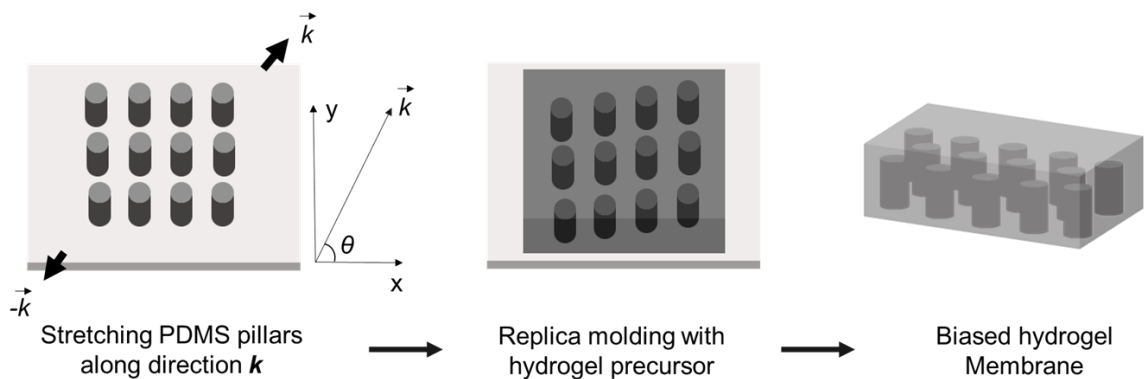
Fig. 5.1 Schematic illustration of replicating hydrogel membrane from stretched PDMS pillars

Characterization. The swelling ratio of PHEMA-*co*-PAA hydrogel at different pH was measured from a hexagonal pillar (side=30 µm, pitch=60 µm, and height=150 µm) scratched off from the substrate, followed by swelling in different pH solutions (2, 3, 4, 4.3, 4.7, 5, 5.3, 5.7, 6, 6.4, 6.7). The diagonal length (L_d) of the hexagon was measured under an optical microscope (Olympus BX61 motorized microscope) before and after swelling of 2 min. The volumetric swelling ratio was calculated as $Q_v =$

$(L_d/L_s)^3$, where L_s is the diagonal length of the hexagon post after swelling (see Fig. 5.2).
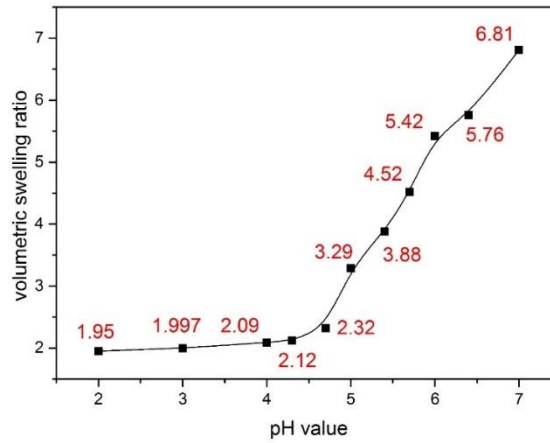
Fig. 5.2 Volumetric hydrogel swelling ratio as a function of pH.

To better observe the pattern transformation of the hydrogel membranes at different pH under the optical microscope, rhodamine B (RB, Sigma-Aldrich) was introduced in the hydrogel membranes to enable observation under fluorescent microscopy offering higher contrast compared to regular optical microscopy. Before observing the shape reconfiguration, the hydrogel membranes were first immersed in DI water overnight to remove the uncrosslinked monomers. The hydrogel membranes were taken out and 0.05 wt % of rhodamine-B aqueous solution was dropped onto the membranes and kept for 2h. The dyed samples were rinsed by DI water before dropping into buffer solutions with different pH values. In addition to optical images, scanning electron microscopy (SEM, FEI Quanta FEG ESEM and FEI Strata DB235) was utilized to image hydrogel membranes in the dry state.

5.2 Results and discussion

Since the emergent pattern is determined by the original structures, to control structural evolution on hydrogel membrane to reach twisted state having controlled chirality, we decided to break the symmetry of the original hydrogel membrane. To do so, we molded hydrogel membranes from pre-stretched PDMS molds at an angle of 15º, 30º, 45º, 60º, 75º, respectively, while keeping the strain small, 5% (see experimental section and Fig. 5.1). The square array of micro-pillars was dislocated into oblique lattices (Fig. 5.3 a) with lattice parameters shown in Fig. 5.3 b. We note that as the application of a small strain to the PDMS pillar structure, the deformation mainly distributed across the bulk layer of PDMS underneath the micro-pillars arrays, and thus shape of the pillar still remains circular. When the distorted pillar arrays were replicated to hydrogel membrane, we thus obtained the reverse structures of distorted pillar arrays. As an example, in Fig. 5.3 c-e, we show the SEM images of the hydrogel porous membrane from PDMS pillar arrays without stretching, stretching at θ_{75}, and stretching at θ_{15} respectively.

θ (°)	15	30	45	60	75
a (μm) ± 0.1	16.3	15.7	15.9	15.3	15.2
b (μm) ± 0.1	15.2	15.3	15.9	15.7	16.3
Φ (°) ± 0.1	87.1	86.1	84.5	84.3	84.0
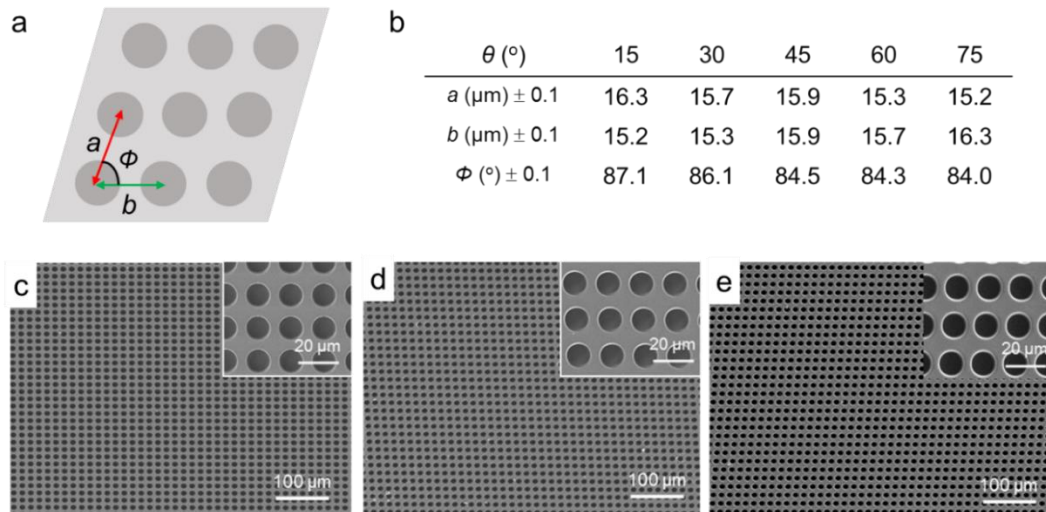
Fig. 5.3 (a) Schematic illustrating the oblique arrays of hydrogel micro-pores generated from replica molding from a pre-stretched PDMS pillar arrays. (b) Table shows the

lattice parameters in oblique arrays of micro-pores measured from hydrogel membrane replicated from pre-stretched PDMS pillar arrays. (c-e) SEM images of hydrogel membrane of square arrays, and oblique arrays of micro-pores at θ_{15} and θ_{75} respectively.

Previously, on PHEMA-*co*-PNIPAAm-*co*-PAA hydrogel membranes with square arrays of circular pores, we observed that amplification of buckled hydrogel membrane leads to the transition from an achiral buckled state to a chiral twisted state driven by the compaction of the hydrogel domains within confined space as swelling ratio of the hydrogel membrane is increased. Here, we first demonstrated the same structural evolution on the PHEMA-*co*-PAA hydrogel membrane with square arrays of micro-pores as pH increase from 3 to 6.4 (Fig. 5.4 a). Since the degree of swelling can be tuned through immersing the hydrogel membrane in to buffer solution with different pH, we also captured the intermediate state during the transition by immersing the hydrogel membrane at pH 5.3. Here, we observed that the deformation to the hydrogel membrane was first accentuated during transition, which caused the circular pores being largely compressed to form an "8" shape, where the joints in the opposite side of the pore started to touch against each other. Further swelling intensified the compression at the touching joints, and triggered symmetry breaking at pH 6.4, as shown at the unit cell level. During this symmetry breaking process, the increased swelling of the hydrogel membrane was compensated by rotating all the hydrogel domains in the same direction (indicated by the solid arrows, Fig. 5.4 a). By having such reorientation of the surface structure, the two touching joints were able to slide against each other, which relieved the compression forces between the touching joints. However, there were two possibilities of the symmetry breaking process: clockwise or

counterclockwise rotations, which explained the coexistence of both RH and LH chirality of the features. Meanwhile, symmetry breaking could start from different nucleation sites and propagate, leading to the formation of phase boundaries (dashed line in Fig. 5.4 a, pH 6.4) where two independently evolved regimes of opposite handedness met with each other.

However, for slightly biased hydrogel membranes, the touching inter-pore ligament during transition were dislocated relative to each other due to the pre-applied strain field across the hydrogel membrane. Fig. 5.4 (b-d) show three distinctive scenarios of how the pre-stretching can affect the symmetry breaking of the structural evolution of the hydrogel membrane. In the first case, when the pre-stretching angle is less than 45°, the off-set between the two inter-pore ligaments in the vertical slits (see orange arrows in Fig. 5.4 b at pH 5.3) was found predominant over the off-set between the two inter-pore ligaments in the horizontal slides (see orange arrows in Fig. 5.4 b at pH 5.3). As the sliding between two touching joints occurred upon further swelling, the counterclockwise rotation of the hydrogel domains became preferred due to the higher elastic energy barrier prohibited the clockwise rotation of the hydrogel domains during the transformation, due to the offset between two ligaments in the vertical slits. In the second scenario, when the pre-stretching angle is greater than 45°, we observed that the off-set between the two inter-pore ligaments in the horizontal slits became predominant, which thus favored the opposite rotation of the hydrogel domains (i.e. clockwise rotation). In the third scenario, when the pre-stretching angle is equal to 45°, almost the same magnitude of the off-set was observed on the horizontal and vertical slits (see orange arrows in the Fig. 5.4 d). As a result, despite of the pre-stretching, there was no preference for the further rotation of the hydrogel domains. However, compared to the non-stretched samples, we did not observe two separated phases of hydrogel domain

rotation, while each individual hydrogel domains seemed to be distort randomly (see Fig. 5.4 d at pH 6.4). This is possibly due to the existing of significant energy barriers to reach the twisted states with either clockwise or counterclockwise rotations of the hydrogel domains.
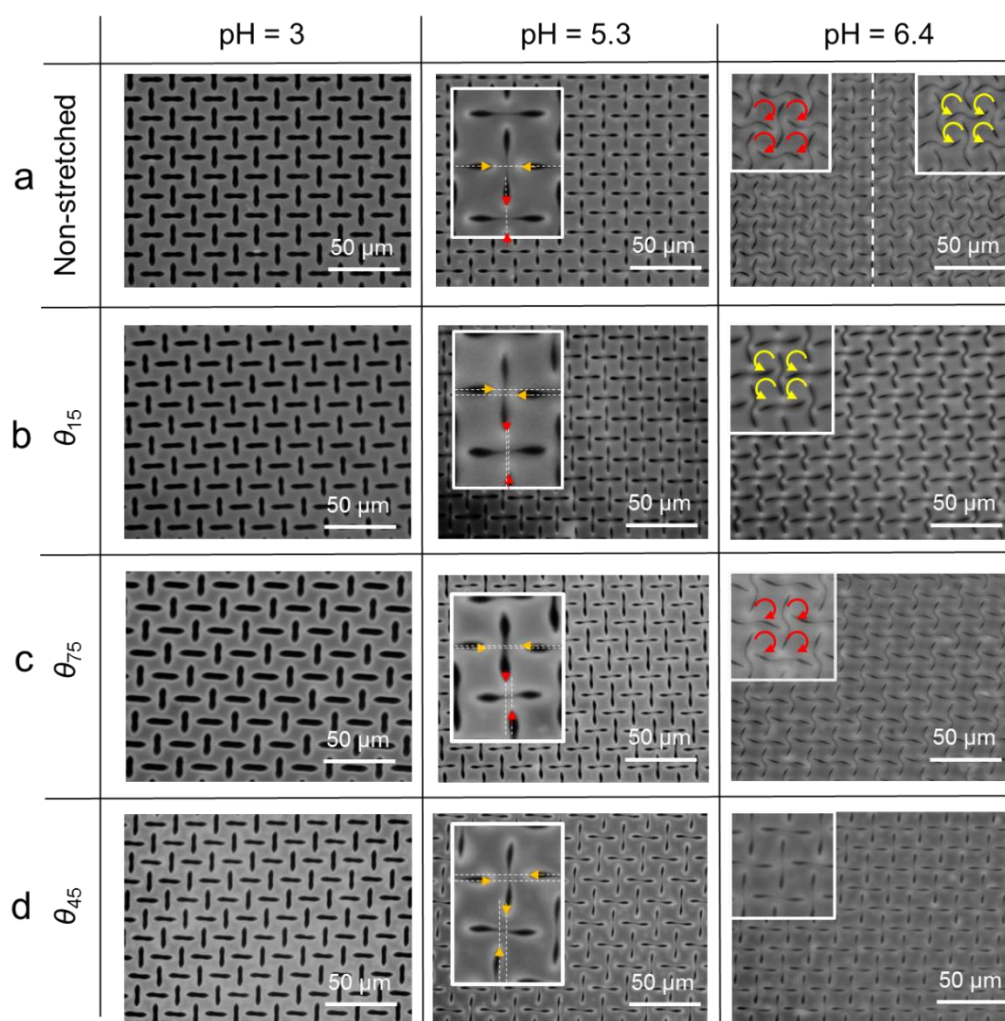
Fig. 5.4 Structural evolution of micro-pore arrays with square arrays, and oblique arrays formed by stretching the PDMS pillar arrays at different angles (i.e. 15°, 75°, and 45°). The structural evolution can be visualized by swelling at different pH values: pH 3 – buckled state, pH – 5.3 transition state, and pH 6.4 – twisted state.

To further demonstrate the induced preference of the hydrogel domain rotation driven by the biased arrangement of the micro-pore arrays leads to the single chirality

of the hydrogel membrane in the twisted state. We sampled randomly over 500 hundred hydrogel domains on each sample to evaluate the overall chirality of the sample. In Fig. 5.5, we shows the fraction of enantiomeric excess (E) on samples (i.e. absolute difference between the mole fraction of each enantiomer), including both square arrays of pore, and oblique arrays of pores (i.e. θ_{15}, θ_{30}, θ_{45}, θ_{60}, and θ_{75}). It is clear that once there is a preference of rotation induced from the biased arrangement of pore arrays, the single chirality can be achieved (i.e. $E > 95\%$). It is also worth noting that since the initial buckling process and the symmetry breaking process (i.e. post-buckling deformation) on the hydrogel membrane are associated to two separated process, the defects generated during the buckling of the hydrogel membrane (i.e. phase boundaries) has negligible effects to the single chirality formation on the hydrogel membrane. As shown in Fig 5.6 a-b, on both sides of the buckling induced phase boundary, the single handedness of the twisted state was maintained. The only exceptions here are the hydrogel domains near the buckling induced phase boundary (labelled with red dashed rectangles), where the irregular deformations typically occurred during the initial buckling of the hydrogel membrane.
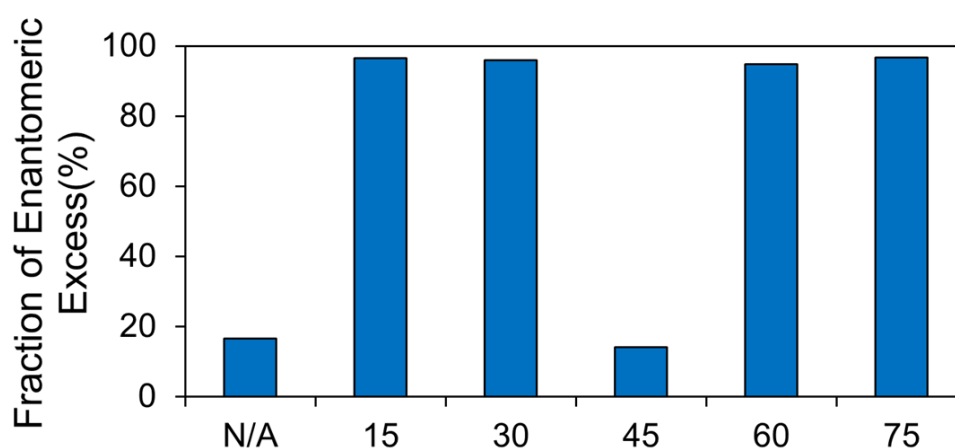
Fig. 5.5 Diagram of fraction of enantiomeric excess at square arrays of micro-pores and oblique arrays of micro-pores.
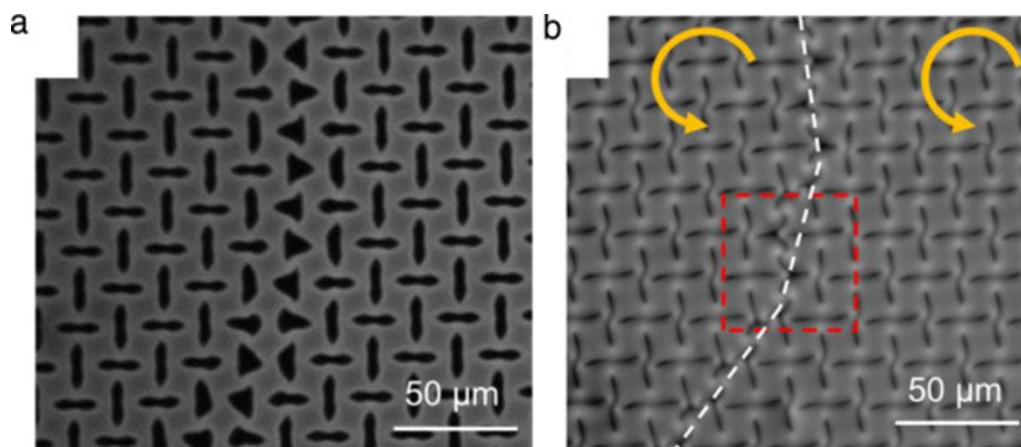
Fig. 5.6 Optical microscopy images of the pre-stretched hydrogel membrane at θ_{15}. (a) At pH 3, and (b) at pH 6.4. After further increasing the swelling ratio, irregular deformation occurs near the defects (i.e. phase boundary) formed during the initial buckling of the hydrogel membrane (surrounded by the red box). The orange arrows indicate the counterclockwise rotation of the hydrogel domains at both sides of the boundaries.

5.3 Conclusion

In summary, we investigated how small bias to the initial square arrays of periodic structures affect the overall chiral transformation of the hydrogel membrane. The distortion to the arrangement of the square arrays of micro-pores was achieved by replicating a pre-stretched PDMS pillar with 5% strain at different stretching angles (i.e. angle between stretching direction and the y-axis of the lattice, $\theta = 15^o$, 30°, 45°, 60°, 75°). In this case, we observed that the chirality of the post-buckling structures at the twisted state was strongly affected by the small bias due to the preference of hydrogel domain rotation during transition from buckled state to the twisted state. The

selectivity of the handedness of the chiral structures were determined by the pre-stretching angles. The hydrogel domains on the membrane with the stretching angle smaller than 45º (i.e. 15º, 30º) had the tendency to rotate counterclockwise, forming the LH structure in twisted state. While the membranes replicated from PDMS mold with the stretching angle larger than 45º (i.e. 60º, 75º) would rotate in the opposite direction and transformed to the RH shape. Meanwhile, without preferences of rotations of the hydrogel domains, single handedness was not observed in the twisted state of the hydrogel membrane. For non-biased square arrays of micro-pores, RH and LH phases with approximately 50/50 composition was observed. For oblique arrays of pores having 45º stretching angle, the individual hydrogel domains were found to be distorted randomly, rather than forming separated phases. This paper provides a robust method to generate high percentage single chiral structures by introducing diminutive strain distribution difference during hydrogel membrane fabrication, which offers insights to the origin of the single chiral structures in nature on mechanical perspective. Furthermore, the easily fabricated membranes with single chirality has the potential application in nano/micro- fabrication with twisted chiral structures that potentially benefits fields including chiral molecule separation/sensing, polarized optical devices, and chiral mechanical metamaterials.

5.4 References

1.   Herminghaus, S., et al., *Spinodal dewetting in liquid crystal and liquid metal films.* Science, 1998. **282**(5390): p. 916-919.

2.   Tanaka, T., et al., *Mechanical Instability of Gels at the Phase-Transition.* Nature, 1987. **325**(6107): p. 796-798.

3.   Lobkovsky, A., et al., *SCALING PROPERTIES OF STRETCHING RIDGES IN A CRUMPLED ELASTIC SHEET.* Science, 1995. **270**(5241): p. 1482-1485.

4.   Trujillo, V., J. Kim, and R.C. Hayward, *Creasing instability of surface-attached hydrogels.* Soft Matter, 2008. **4**(3): p. 564 - 569.

5.   Cerda, E., K. Ravi-Chandar, and L. Mahadevan, *Thin films - Wrinkling of an elastic sheet under tension.* Nature, 2002. **419**(6907): p. 579-580.

6.   Roman, B. and A. Pocheau, *Buckling cascade of thin plates: Forms, constraints and similarity.* Europhys. Lett., 1999. **46**(5): p. 602-608.

7.   Mullin, T., et al., *Pattern transformation triggered by deformation.* Phys. Rev. Lett., 2007. **99**(8): p. 084301.

8.   Bertoldi, K., et al., *Mechanics of deformation-triggered pattern transformations and superelastic behavior in periodic elastomeric structures.* J. Mech. Phys. Solids, 2008. **56**(8): p. 2642-2668.

9.   Zhang, Y., et al., *One-Step Nanoscale Assembly of Complex Structures via Harnessing of an Elastic Instability.* Nano Lett., 2008. **8**(4): p. 1192-1196.

10.   Singamaneni, S., et al., *Instabilities and Pattern Transformation in Periodic, Porous Elastoplastic Solid Coatings.* ACS Appl. Mater. Interf., 2008. **1**(1): p. 42-47.

11. Jang, J.-H., et al., *Combining Pattern Instability and Shape-Memory Hysteresis for Phononic Switching.* Nano Lett., 2009. **9**(5): p. 2113-2119.

12. Singamaneni, S., et al., *Bifurcated Mechanical Behavior of Deformed Periodic Porous Solids.* Adv. Funct. Mater., 2009. **19**(9): p. 1426-1436.

13. Bertoldi, K., et al., *Negative Poisson's Ratio Behavior Induced by an Elastic Instability.* Adv. Mater., 2010. **22**(3): p. 361-366.

14. Goencue, F., et al., *Deformation induced pattern transformation in a soft granular crystal.* Soft Matter, 2011. **7**(6): p. 2321-2324.

15. Li, J., et al., *Switching periodic membranes via pattern transformation and shape memory effect.* Soft Matter, 2012. **8**(40): p. 10322-10328.

16. Zhu, X., et al., *Capillarity induced instability in responsive hydrogel membranes with periodic hole array.* Soft Matter, 2012. **8**(31): p. 8088-8093.

17. Overvelde, J.T.B., S. Shan, and K. Bertoldi, *Compaction Through Buckling in 2D Periodic, Soft and Porous Structures: Effect of Pore Shape.* Adv. Mater., 2012. **24**(17): p. 2337-2342.

18. Shim, J., et al., *Buckling-induced encapsulation of structured elastic shells under pressure.* Proc. Nat. Acad. Sci. U. S. A., 2012. **109**: p. 5978-5983.

19. Willshaw, S. and T. Mullin, *Pattern switching in two and three-dimensional soft solids.* Soft Matter, 2012. **8**(6): p. 1747-1750.

20. Kang, S.H., et al., *Buckling-Induced Reversible Symmetry Breaking and Amplification of Chirality Using Supported Cellular Structures.* Adv. Mater., 2013: p. doi: 10.1002/adma.201300617.

21. Zhu, X.L., et al., *Two-Dimensional Photonic Crystals with Anisotropic Unit*

Cells Imprinted from Poly(dimethylsiloxane) Membranes Under Elastic Deformation. Appl. Phys. Lett., 2008. **93**(16): p. 161911.

22.   Krishnan, D. and H.T. Johnson, *Optical properties of two-dimensional polymer photonic crystals after deformation-induced pattern transformations.* J. Mech. Phys. Solids, 2009. **57**(9): p. 1500-1513.

23.   Wu, G., Y. Xia, and S. Yang, *Buckling, symmetry breaking, and cavitation in periodically micro-structured hydrogel membranes.* Soft Matter, 2013: p. http://dx.doi.org/10.1039/C3SM51640G.

24.   Fratzl, P. and F.G. Barth, *Biomaterial systems for mechanosensing and actuation.* Nature, 2009. **462**(7272): p. 442-448.

25.   Dawson, C., J.F.V. Vincent, and A.-M. Rocca, *How pine cones open.* Nature, 1997. **390**(6661): p. 668-668.

26.   Chandra, D., J.A. Taylor, and S. Yang, *Replica molding of high-aspect-ratio (sub-)micron hydrogel pillar arrays and their stability in air and solvents.* Soft Matter, 2008. **4**(5): p. 979-984.

Chapter 6: Directing the Deformation Paths of Soft Metamaterials with Prescribed Asymmetric Units

Adapted from **Wu, G.**; Cho, Y.; Choi, I.-S.; Ge, D.; Li, J.; Han, H. N.; Lubensky, T.; Yang, S., *Adv. Mater.* **2015,** *27* (17)

6.0 Introduction

Metamaterials are artificially engineered materials whose physical properties are functions of the structural parameters of the underlying periodic microstructures, including shape, geometry, size, orientation, and arrangement. Soft metamaterials with reconfigurable microstructures in response to external stimuli are thus of great interest for their switching behavior with potential applications, including miniaturized devices,[1-3] micro-actuation,[3-6] optical manipulation,[7, 8] microfluidic devices,[9] and drug delivery.[10] However, deformation, if not controlled, could lead to failure that can interfere with the performance of devices.

Recently, we and others have explored buckling instabilities of soft membranes with periodic hole arrays, where the bending of the inter-pore ligaments triggers homogeneous and reversible pattern transformations.[11-26] The transformation occurs at a broad range of length scales ranging from submicron[14, 16, 19, 20] to centimeter scale,[11, 21, 26] and offers a unique mechanism to induce significant change of the physical properties of the metamaterials, including photonic[27, 28] and phononic[24] bandgaps, mechanical properties (e.g. negative Poisson's ratio),[17, 21] and symmetry breaking[24, 25] arising from simultaneous alterations of lattice symmetry, pore size and shape, and volume filling fraction. Meanwhile, there has been significant effort in theoretical understandings of mechanical behaviors of periodic structures with respect to geometry, including rectangular,[29-35] chiral honeycomb,[36-38] and triangular

structures,[39-42] via rotation of the basic units.

Despite these advances, challenges remain. For example, mechanical instability accompanied with compression of the periodically porous structures often leads to sudden structural change, and thus change of mechanical properties, above the critical buckling threshold. The deformation path of a porous structure is often limited to the one with the lowest elastic energy increment (i.e. the buckling mode with the lowest eigenvalue), whereas those with higher eigenvalues are not readily accessible.[26] Further, unwanted structural defects (e.g. anti-phase boundaries) originated from inhomogenity introduced during the fabrication or uneven external loading, are often produced during the deformation process. Therefore, controllability over the entire structure during deformation needs to be investigated, in particular, to direct the deformation paths and prevent mechanical instabilities and/or possible structural defects.

Here, we chose kagome lattices with triangular structure units as the model system to address the above issues. Among various two-dimensional (2D) lattices that undergo periodic collapse mechanisms, the kagome lattices (also referred as trihexagonal tiling) and related lattices offer many desirable transport and elastic properties, heat-dissipation characteristics, and large photonic bandgaps.[43-48] The twisted kagome and related lattices exhibit isotropic elasticity with a vanishing bulk modulus.[39] More importantly, kagome lattices of N lattice sites can have an order of $N^{1/2}$ "floppy" modes of lattice distortion under free boundary conditions, that is, they have $N^{1/2}$ modes of low-energy deformations of the structures via rotation of neighboring "rigid" structural units (here triangles) against each other without distorting the triangles. Correspondingly, kagome lattices could exhibit maximal negative Poisson's ratio -1.[49] Therefore, kagome lattices offer an ideal model to investigate how to control the deformation path upon expansion and contraction, and the production of large

deformations in response to relatively small external perturbations – a highly attractive feature for applications of mechanical metamaterials.

6.1 Experiments

Sample Fabrication. The soft porous structures (lattice size) were fabricated from silicone rubber (Elite® Double 32, Zhermack) through replica-molding from acrylonitrile butadiene styrene (ABS) templates fabricated by 3D printing (Objet30 Photopolymer Printer). A very thin layer of Teflon oil (DuPont) was cast onto the template as a lubricant layer for the mold releasing. The dimensions of the fabricated cellular structures were found close to the designed cellular structures (with error less than 5% for the finest features). Thickness of all three samples was measured to be 5.3 mm. On the top and bottom of the samples we intentionally left beam-like silicone pieces with 6 mm width, allowing us to apply more uniform uniaxial compression to the structures.

Finite-element simulations. The general purposed implicit finite-element (FE) code, ABAQUS/Standard, was used to analyze kagome structures with different ligament shape. Plane strain conditions were assumed throughout the analyses. ABAQUS element type CPE3 with an average characteristic length of 0.4 mm was used. For the symmetric non-twisted kagome structure, a buckling analysis was performed first to determine the collapsing mode, followed by a post-buckling analysis with 0.5% of geometrical imperfection. For the asymmetric pre-twisted structures, the buckling analysis was omitted since the deterministic ligaments in the structures effectively suppress the buckling instability. Yeoh hyperelastic model was used as a constitutive relation, of which strain energy density is expressed as follows:

$$W_{Yeoh} = \sum_{i=1}^{3} \left\{ C_{i0}(I_1 - 3)^i + \frac{(J-1)^{2i}}{D_i} \right\}$$

where $I_1=\text{tr}\{\text{dev}(F^TF)\}$, $J=\det(F)$, and F is the deformation gradient. Here, we used $C_{10}=240$ kPa, $C_{20}=0$, $C_{30}=3.5$ kPa, and $D_1=D_2=D_3=3.8$ GPa^{-1} to capture the mechanical behavior of silicone rubber used in the experiments.

Uniaxial Compression Test. Uniaxial compression tests were performed using an Instron machine (Instron Model 5564, with a 2 kN load cell) under displacement control (10 mm/min). During the test the specimens were placed between two closely fit acrylic plates (5 mm thick) with spacing of 6 mm to eliminate out-of-plane buckling. Chalk was lightly dusted on the surfaces of the specimen to help reduce friction. A third acrylic plate clamped to the load cell was then inserted between the two parallel acrylic plates and provide uniform displacement to the top of the specimen. The load to displacement curve measured from uniaxial compression test was then transferred into stress vs. strain curve based on the measured dimensions of the cellular solid structure. With same approach, the uniaxial compression tests were also applied to samples without top and bottom silicone rubber beams to demonstrate the possibility of reaching fully compacted state upon uniaxial compression.

In order to analyze the in-situ evolution of the micro-structure during uniaxial compression, the deformation of the lattices was recorded using a high resolution Canon 60D camera which was set to take the images for every 3s. This corresponds to capturing the microstructure reconfiguration at a normal displacement of 0.5 mm per image.

6.2 Results and Discussion

Guided by finite-element (FE) modeling, we designed and fabricated periodic, porous membrane structures with asymmetric ligaments in kagome lattices prescribed with a pre-twisting angle. These designs not only prevented buckling instabilities but also

offered deterministic pattern transformations guided by the asymmetric inter-pore ligaments. We investigated the mechanical response and structural evolution of these soft metamaterials upon mechanical compression both numerically and experimentally. We found that structural reconfiguration behaviors were strongly affected by the asymmetric nature of the inter-pore ligaments, which in turn determined the attractive features of these soft metamaterials systems. Specifically, we could fine-tune the pathway of the structural change, the deformation mode, structural stiffness, and the achievable negative Poisson's ratio by prescribing the pore units with designated pre-twisting angles.

Prototypes of the kagome lattices were designed according to their geometric models, including rotating rigid units and hinge-jointed vertices. Two simple collapsing mechanisms are investigated (Figure 6.1A): Mode I, in which the triangular units rotates against every hingesand deformation is locally isostropic, and Mode II, the triangular units rotates against 2/3 of the hinges, producing a pattern of alternately tilted distorted hexagonal pores. Both collapsing mechanisms can be characterized by a single angle α specifying the direction of kagome triangles relative to the x-axis; $\alpha = (120° - \theta)/2$ where θ is the angle between two edges of interconnected triangular units (see Figure 6.1A). In both cases, as α increases from 0° (full extension) to 60° (full compaction), the lattice contracts in all directions by a factor of $\cos\alpha$, and the area of the lattice decreases by a factor of $\cos^2\alpha$, and thus the total area becomes 0.25 of the original area at full compaction ($\alpha = 60°$). This compaction is considerably higher than that of rotating square (theoretical value, 0.5) and, therefore, allows for wider design space in tunable soft metamaterials.

By replacing the hinges using thin polymer ligaments and the triangular units with bulk polymers, we create a series of kagome lattice based porous structures with

and without pre-twisting (see Figure 6.1B). The beauty of this system is that the thin polymer ligaments have very low bending stiffness, M, compared to that of the triangular units, which is defined by $M = EC\kappa t^3$. Here, E is the elastic modulus, C is the geometric constant, κ is the curvature, and t is the width, which varies from w (at hinge) to L (at the triangular edge; see Figure 6.1B). Therefore, highly localized bending deformation is trigged at the ligaments, leading to pattern transformation via rotation of the ligaments. This implies that the designed characteristics of the ligaments will directly affect the overall mechanical behavior of the porous structures. Specifically, the relative bending stiffness of the ligaments can be tuned by the ratio L/w, and the pre-twisting angle α (see Figure 1A), which controls the nature of the ligaments: $\alpha = 0°$ for perfect symmetric ligaments, and $\alpha > 0°$ for asymmetric ligaments.
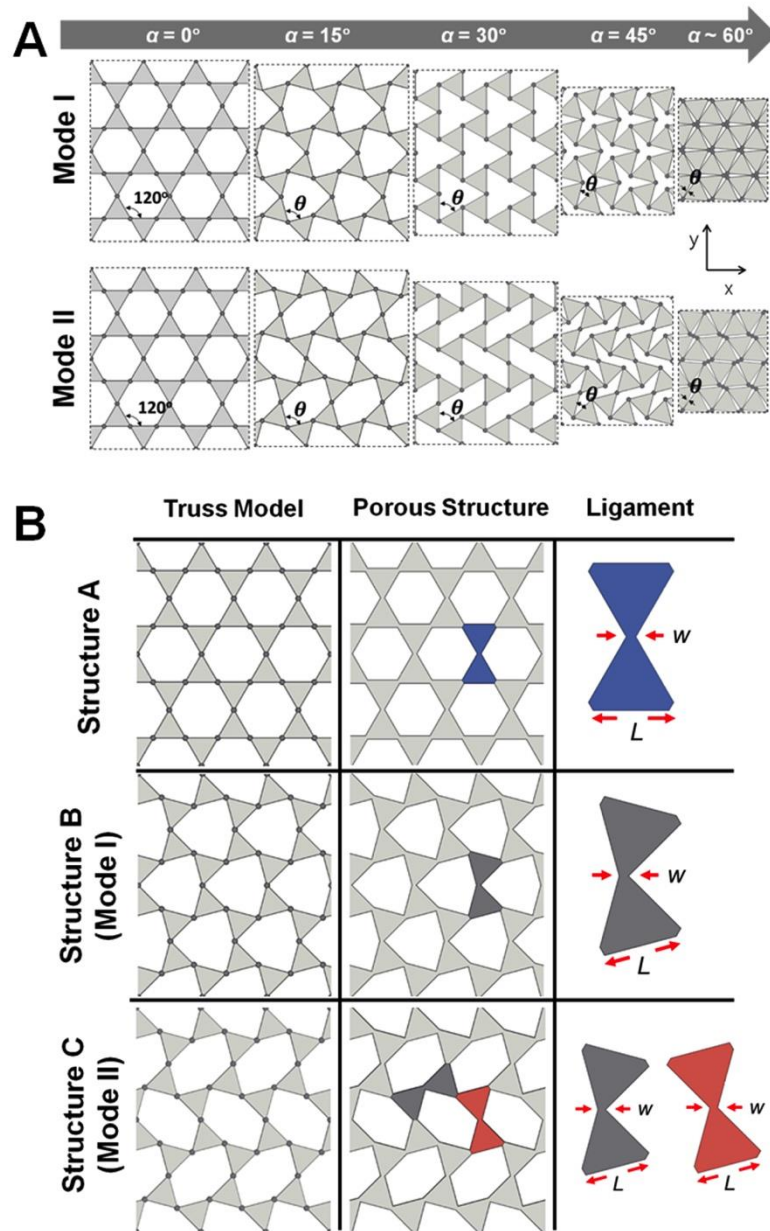
Figure 6.1 (A) Schematics showing the geometric model of kagome lattice and the corresponding two collapsing modes. With increasing the twisting angle α from 0o to 60o degrees, the lattice reaches full compaction. The twisting angle α is defined by (120°-θ)/2. (B) Schematics illustration of three types of soft porous structures (Structure A, B, and C) based on the periodic truss model of kagome lattices and the corresponding inter-pore ligaments with twisting angle, α, of 15° degree.

First, we focus on how the symmetry of the ligaments affects the overall mechanical response of the kagome lattices. We fixed the $L/w = 8$ ($L = 6$ mm, and $w = 0.75$ mm in both experiments and simulation), and created a porous structure from the non-twisted kagome lattice ($\alpha = 0°$, structure A), and two types of pre-twisted ($\alpha = 15°$) kagome lattices, including structure B with all ligaments pre-twisted, and structure C with only 2/3 of ligaments pre-twisted. The latter two represent the collapsing modes I and II, respectively (see Figure 6.1B). It is worth noting that this process is similar to that in the re-entrant foam structures, where the pre-applied compressive strain forces the foam ribs to bend inward. Here, through the introduction of the pre-twisted thin polymer ligaments, we essentially created two sets of 2D re-entrant structures from the kagome lattice with biaxial shrinkage of $2L(\cos\alpha\text{-}1)/(2L+w)$ in both x and y directions. As shown in Figure 1B, at the same pre-twisting angle for collapsing modes I and II, both structures B and C have the same shaped asymmetric ligaments (shown as the dark grey blocks in Figure 6.1B), but their composition and arrangement in 2D are quite different. In experiments, a small pre-twisting angle (i.e. $\alpha = 15°$) was introduced in the original lattice such that the sample would experience minimal biaxial shrinkage (~3.2%). Compared to structure A, the reduction of the porosity for structures B and C is only ~1.8% (from 66.4% to 64.6% at $L/w = 8$). Such small difference in porosity generally does not lead to a significant change in the mechanical behavior of the overall structure.[17] However, it is sufficient to guide the bending direction of the ligaments, thus, inhibiting buckling in structures B and C. In structure A, at the buckling threshold each ligament has one independent choice of the bending direction because of the symmetric nature of the ligaments. In fact, in the previously reported deformation of periodic porous structures,[11, 15, 16, 20, 21, 25] all require (a) a buckling threshold to initiate bending, (b) consequently, a sudden change of structure above the buckling

threshold, and (c) lack of control on the bending direction of the individual ligament. For structure A, the non-deterministic bending led to incomplete compaction, especially under an inhomogeneous load (see Figure 6.2A). In comparison, the pre-twisted kagome lattices (structures B and C) showed deterministic bending of ligaments even under an inhomogeneous load (Figure 6.2B and 2C), and the porous membranes were completely closed.
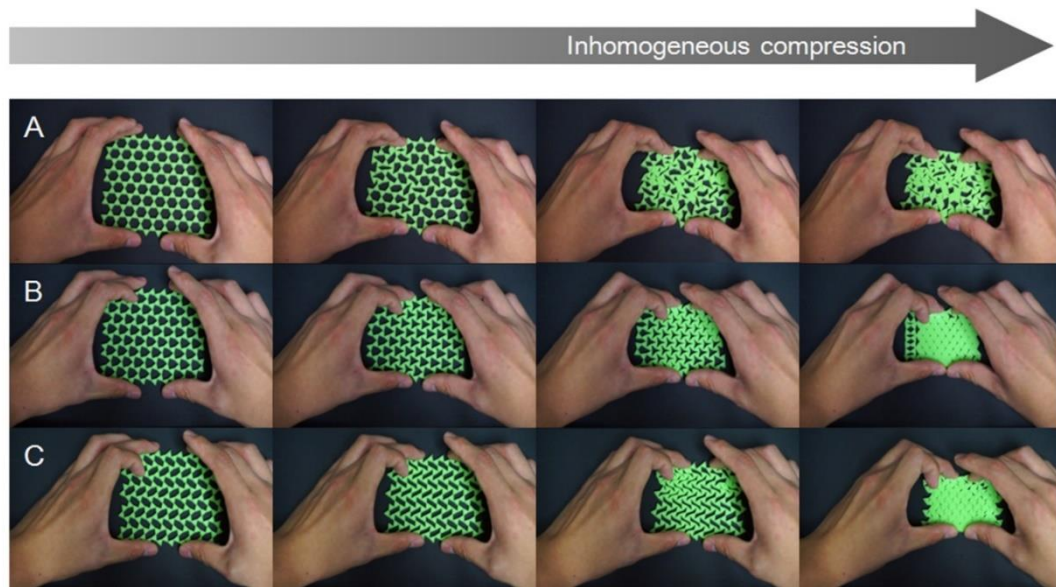
Figure 6.2 Biaxial compression experiments for structure A, B, and C. (A) Non-twisted kagome lattice with symmetric ligaments. Under inhomogeneous loading by hand, each ligament is bent randomly, producing topological defects throughout the structure. (B) and (C) Pre-twisted kagome lattices with asymmetric ligaments. Each ligament is bent according to prescribed pre-twisting regardless of the inhomogeneous loading, producing close-packed compaction.

To support our design, we built physical and numerical models of all three cellular solid structures consisting of 8 x 10 hexagonal or slightly deformed hexagonal voids (See Figure 6.3). The soft porous structures were fabricated from silicone rubber

through replica-molding of templates fabricated by 3D printing. On the top and bottom of the samples we intentionally left beam-like layers of silicone with 6 mm width (see Figure 6.3), allowing for uniform compression. Uniaxial compression tests were performed by sandwiching the rubber sheet between two acrylic plates and a third acrylic plate was clamped to a load cell. The overall deformation process and mechanical behaviors were simulated using the general purposed implicit FE code, ABAQUS/Standard, for interpretation of the mechanical deformation to the porous structures. In simulation, plane strain condition was used, and the behavior of the silicone rubber was captured using the Yeoh hyperelastic model.[38] The uniaxial compression tests were simulated by imposing vertical displacements at the top surface while keeping vertical movement on the bottom surface fixed. Along the horizontal direction, the structure could move freely.
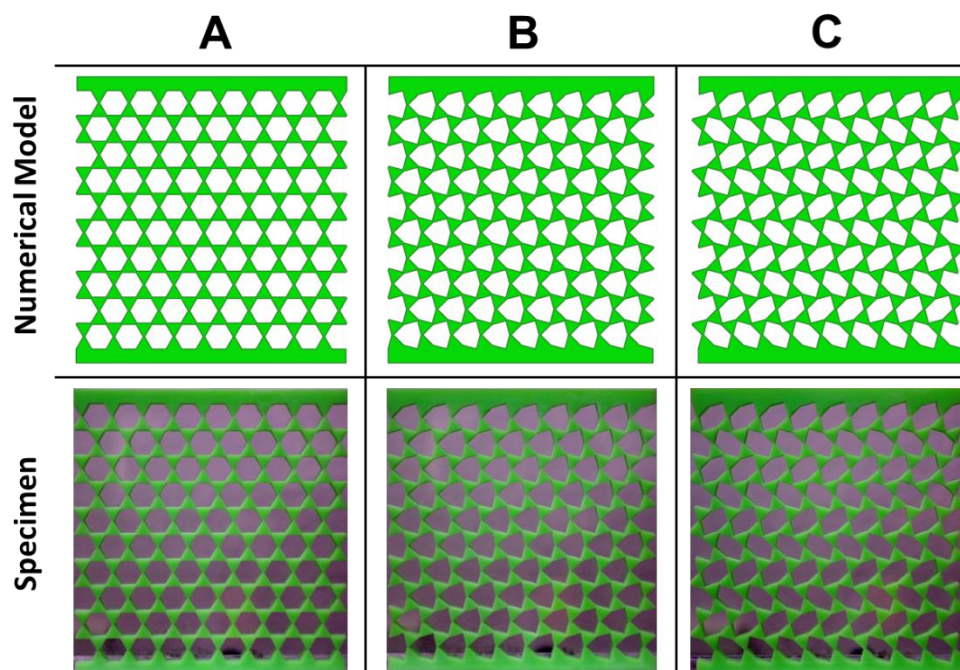
Figure 6.3 Numerical models input into FE simulation, and the corresponding cellular solids fabricated from replica molding of the silicone rubber.

Representative experimental images taken during the compression test were compared with simulation shown in Figure 6.4 at different nominal strains ($\varepsilon_y = 0$, 0.02, 0.04, 0.1, and 0.16). Here, ε_y is defined by $(H_0-H)/H_0$, where H_0 is the initial height of the structure and H is the height after compression. We focused on structural change at the central region of the samples, where the boundary effect was minimized. In all three cases, the experimental results showed excellent agreement with FE simulation, which captured mechanical response of the cellular solids to the nominal strain up to 16%.
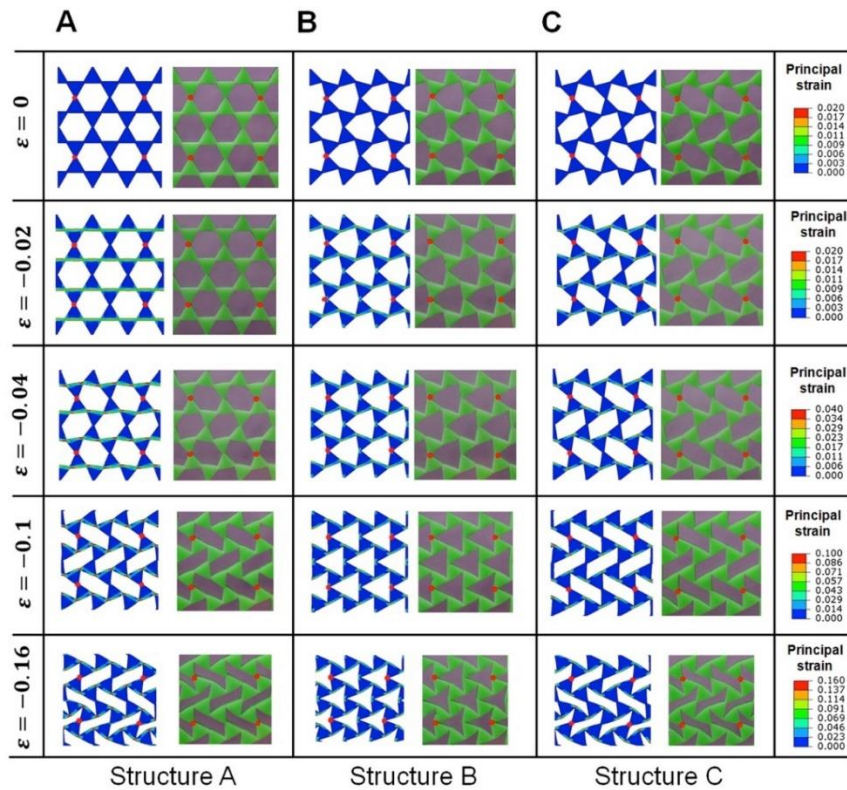
Figure 6.4 Numerical (left) and experimental (right) images of the deformation processes of three kagome-based lattices. (A) Non-twisted, (B) twisted (Mode I) , and (C) twisted (Mode II) structures. The twisted (collapsing) modes are defined in Figure 1. B and C have the same pre-twisting angle, α =15°, but different amounts of pre-

twisted ligament (100% for B, and ~67% for C). The principal strain shown in the legend represents the maximum principal strain.

During uniaxial compression, structure A with symmetric ligaments experienced buckling instability, that is an abrupt transition of the porous structure to an array of sheared hexagons above the critical strain $\varepsilon_c \sim 0.033$. The triggered buckling modes resembled the collapsing mode II in periodic truss model. After the buckling of the inter-pore ligaments, the deformation to the periodic porous structure was accommodated by further rotation of the triangular units and bending of the inter-pore ligaments. In comparison, an unevenly distributed strain level across the asymmetric ligaments in structures B and C were found even at a very small loading (e.g. $\varepsilon = -0.02$, see Figures 6.4B and 6.4C), thus, they bent immediately at the onset of the loading without experiencing any buckling instability. The microstructures evolved smoothly and strictly followed the collapsing modes prescribed by the asymmetric ligament structures. Specifically, we achieved a distinctive deformation path in structure B, where all of the inter-pore ligaments were bent simultaneously during the pattern transformation process. Such a deformation path is not achievable in normal compression of non-twisted kagome lattice because it has much higher eigenvalue than the one in structure A or C.[26] Our results suggest that it is possible to access a much richer range of deformation paths by introducing asymmetric ligaments to the cellular solid structures or mixing structures, for example, B and C with different portions and at different locations within the specimen as demonstrated in our earlier work.[35] As a result, different mechanical responses during compression will be obtained.

A more quantitative investigation was carried out by comparing experimental results with FE simulation following the evolution of the stress and Poisson's ratio vs. the applied nominal strain. For structure A, we observed a typical stress-strain behavior for the buckling induced pattern transformation process,[21] including a linear elastic regime, a stress plateau, and eventually a non-linear curve-up region (see Figure 6.5A). The departure from linearity is an indication of structural buckling and corresponds to the process of abrupt transition of the lattice geometry into sheared hexagons. The densification of the periodic porous structure at high compressive strain causes the curve-up in the stress-strain curve. For structures B and C, however, there was no clear transition from the linear elastic regime to a plateau regime; the stress - strain curves were smooth with a slope gradually decreased before reaching the densification (see Figure 6.5A). This observation is consistent with the smooth evolution of the microstructure during compression.
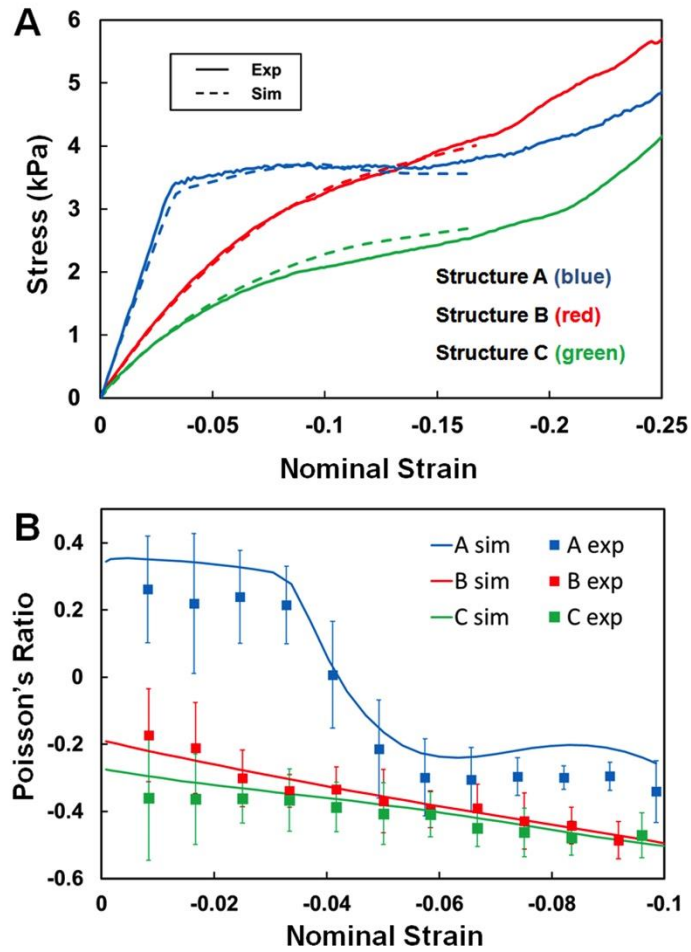
Figure 6.5 (A) The stress - strain relationship obtained from uniaxial compression and FE simulation of structures A, B, and C. (B) Macroscopic Poisson's ratio ν as a function of the nominal strain.

Noticeably, the three structures studied here showed very different flexibility. Structure A required the highest energy (proportional to the area under the stress-strain curve in Figure 6.5A) to reach a nominal strain of -0.1. This suggests that the presence of the pre-twisted ligament reduces the energy cost required for compacting the soft porous structures, a much desired property in designing foldable devices. Meanwhile, structure C was found to be more flexible than structure B. This difference in flexibility

again is the direct result of different deformation paths of microstructures: deformation of structure B was accommodated by bending of every ligament, while only 2/3 of the ligaments in structure C were bent (see Figure 4). It was also found that the ratio between the integration of measured stress over strain from $\varepsilon = 0$ to -0.1 for structures B and C was also ~3/2. Therefore, on average the energy consumed in bending each ligament in structure B and C are approximately the same. This observation implies that the mechanical responses of the soft porous structures are not only related to the bending of the inter-pore ligaments, but also their arrangement.

It is well known that rotating rectangular or triangular units possess negative Poisson's ratio (or so-called auxetic behavior).[49] Figure 6.5B shows the average Poisson's ratio (ν) with respect to the applied nominal strain. ν is calculated from the ratio of the nominal strains in the horizontal edge to that in the vertical edge in the rectangular regions surrounded by four red dots (see Figures 4, Figure 6 and details in Support Information). It is clear that the introduction of the asymmetric ligaments to the cellular solid greatly affects the evolution of the Poisson's ratio during deformation. Structure A initially had a positive ν. Similar to the report in literature on square arrays of circular pores,[17] the dramatic pattern transformation induced by the buckling of the inter-pore ligaments led to a monotonic decrease of ν as function of nominal strain and eventually became negative. Structures B and C were, however, strikingly different from A. They had negative Poisson's ratio from the start (~ -0.2 for structure B, and ~ -0.3 for structure C), which underwent mild decays and leveled at values ~ -0.5 to -0.6 at a higher nominal strain. As a result, the negative Poisson's ratios achieved by structures B and C (with asymmetric ligaments) are considered as ready-to-use properties, This is distinctly different from structure A and other 2D porous structures

reported in literature,[17, 21] where a significant pre-strain is often required (normally ~ 5% to 10%) to achieve the negative Poisson's ratio.
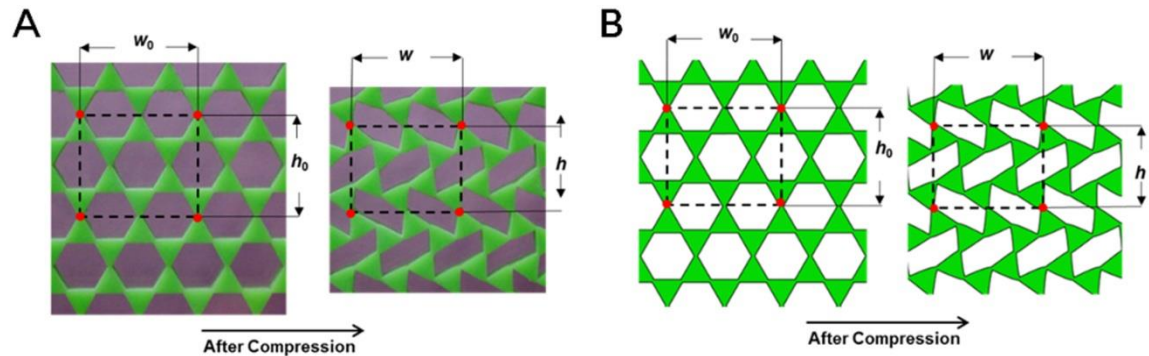
Figure 6.6 Illustration of how to calculate the Poisson's ratio of the cellular structures in a rectangular unit area. (A) Physical and (B) numerical models.

We note that Grima and Evans have theoretically investigated mechanical behaviors of kagome lattices extensively,[40] providing a full description of the mechanical properties including Poisson's ratio and elastic moduli. The study, however, is derived from an idealized kagome structure where triangles are rigid and zero-width hinges have finite bending stiffness, resulting in Poisson's ratio of -1 regardless of the pre-twisting angle. This is different from our experimental and FE simulation results. We believe the discrepancy is originated from the non-ideal nature of the experimental system, where the triangle units are made of deformable silicone rubber and the hinges between them have a finite width. For structure A, the bending deformation of the ligaments and rotation of the triangles that mimic the collapsing path of kagome lattice are not triggered until reaching the buckling threshold of the entire structure. Therefore, the Poisson's ratio of structure A is positive at the beginning of the deformation, and thus exhibits the largest deviation from the ideal collapsing mechanisms.

To better exploit the utility of the pre-twisting angle, we performed simulation on the soft porous structures based on the collapsing modes I and II with different pre-twisting angles (15°, 30°, and 45°, see Figures 6.7A and 6.7D). As shown in Figures 6.7B, 6.7C, 6.7E, and 6.7F, the mechanical response of the soft metamaterials, including flexibility and auxetic behavior, can be dynamically tuned simply by varying the pre-twisting angle. A large negative and stable value of Poisson's ratio is achieved from structures with a pre-twisting angle of 45°. These results are in sharp contrast to the theoretical study of ideal kagome lattices reported in literature,[40] where the Poisson's ratio is kept constant, -1, irrespective of the twisting angle. By combining structures of different types of pre-twisted ligaments in various arrangements, we can fine-tune the range of negative Poisson's ratio and thus flexibility of the entire film and/or at local positions.
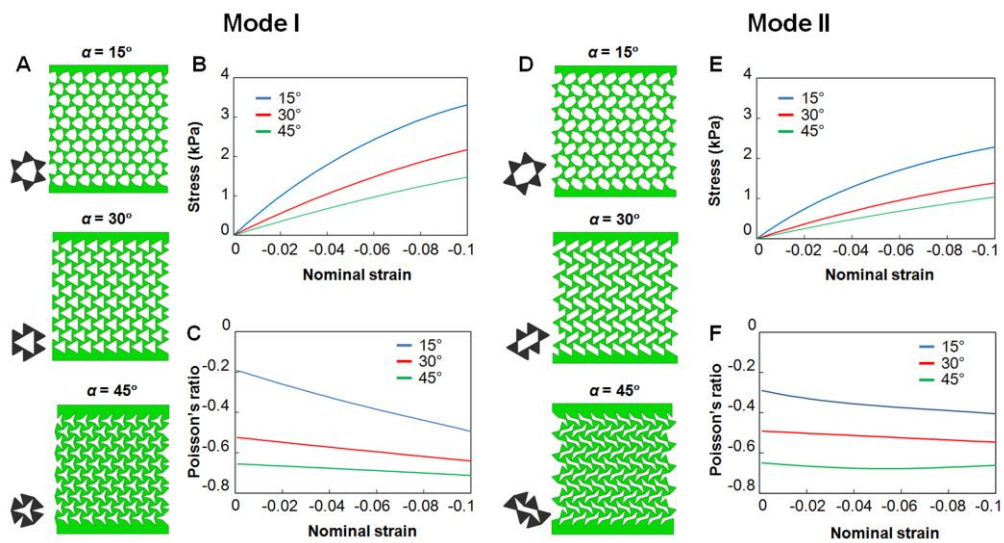
Figure 6.7 FE simulation of pre-twisted kagome lattices with different pre-twisting angles under uniaxial compression. (A-C) Mode I (structure B). (D-F) Mode II (structure C). (A, D) The original non-deformed structures for modeling. (B, E) Stress - strain relationship. (C, F) The corresponding evolution of the Poisson's ratio.

6.3 Conclusion

In summary, we studied the collapsing modes of pre-twisted kagome lattices with prescribed asymmetric ligaments in different arrangements. We successfully avoided the buckling instability, allowing for smooth and homogenous structural reconfiguration in a deterministic fashion. The mechanical responses of the designed metamaterials, including stress-strain behaviors and the resulting negative Poisson's ratios, were strongly affected by the symmetry of the ligaments and their arrangement. Here, we suggest a new and important design concept in soft metamaterials, that is, the introduction of asymmetric ligaments to the periodic porous structures. It will allow for exquisite control of the compaction path of the porous structures, thus reaching much richer range of transformed patterns and their corresponding physical properties. The knowledge presented here will also provide critical insights to design foldable or deployable devices by precisely control of the materials stiffness and mechanical response in 2D and 3D sheets.

6.4 References

1.   He, X., et al., *Synthetic homeostatic materials with chemo-mechano-chemical self-regulation.* Nature, 2012. **487**(7406): p. 214-218.

2.   Sidorenko, A., et al., *Reversible Switching of Hydrogel-Actuated Nanostructures into Complex Micropatterns.* Science, 2007. **315**(5811): p. 487-490.

3.   van Oosten, C.L., C.W.M. Bastiaansen, and D.J. Broer, *Printed artificial cilia from liquid-crystal network actuators modularly driven by light.* Nat Mater, 2009. **8**(8): p. 677-682.

4.   Glazer, P.J., et al., *Multi-Stimuli Responsive Hydrogel Cilia.* Adv. Funct. Mater., 2013: p. n/a-n/a.

5.   le Digabel, J., et al., *Magnetic micropillars as a tool to govern substrate deformations.* Lab Chip, 2011. **11**(15): p. 2630-2636.

6.   Wu, Z.L., et al., *Three-dimensional shape transformations of hydrogel sheets induced by small-scale modulation of internal stresses.* Nat Commun, 2013. **4**: p. 1586.

7.   Dong, L., et al., *Adaptive liquid microlenses activated by stimuli-responsive hydrogels.* Nature, 2006. **442**(7102): p. 551-554.

8.   Shimamoto, N., et al., *Nanopattern Fabrication of Gold on Hydrogels and Application to Tunable Photonic Crystal.* Adv. Mater., 2012. **24**(38): p. 5243-5248.

9.   Beebe, D.J., et al., *Functional hydrogel structures for autonomous flow control inside microfluidic channels.* Nature, 2000. **404**(6778): p. 588-590.

10. Ehrick, J.D., et al., *Genetically engineered protein in hydrogels tailors stimuli-responsive characteristics.* Nat. Mater., 2005. **4**(4): p. 298-302.

11. Mullin, T., et al., *Pattern transformation triggered by deformation.* Phys. Rev. Lett., 2007. **99**(8): p. 084301.

12. Bertoldi, K., et al., *Mechanics of deformation-triggered pattern transformations and superelastic behavior in periodic elastomeric structures.* J. Mech. Phys. Solids, 2008. **56**(8): p. 2642-2668.

13. Zhang, Y., et al., *One-Step Nanoscale Assembly of Complex Structures via Harnessing of an Elastic Instability.* Nano Lett., 2008. **8**(4): p. 1192-1196.

14. Singamaneni, S., et al., *Instabilities and Pattern Transformation in Periodic, Porous Elastoplastic Solid Coatings.* ACS Appl. Mater. Interf., 2008. **1**(1): p. 42-47.

15. Jang, J.-H., et al., *Combining Pattern Instability and Shape-Memory Hysteresis for Phononic Switching.* Nano Lett., 2009. **9**(5): p. 2113-2119.

16. Singamaneni, S., et al., *Bifurcated Mechanical Behavior of Deformed Periodic Porous Solids.* Adv. Funct. Mater., 2009. **19**(9): p. 1426-1436.

17. Bertoldi, K., et al., *Negative Poisson's Ratio Behavior Induced by an Elastic Instability.* Adv. Mater., 2010. **22**(3): p. 361-366.

18. Goencue, F., et al., *Deformation induced pattern transformation in a soft granular crystal.* Soft Matter, 2011. **7**(6): p. 2321-2324.

19. Li, J., et al., *Switching periodic membranes via pattern transformation and shape memory effect.* Soft Matter, 2012. **8**(40): p. 10322-10328.

20. Zhu, X., et al., *Capillarity induced instability in responsive hydrogel membranes*

with periodic hole array. Soft Matter, 2012. **8**(31): p. 8088-8093.

21.   Overvelde, J.T.B., S. Shan, and K. Bertoldi, *Compaction Through Buckling in 2D Periodic, Soft and Porous Structures: Effect of Pore Shape.* Adv. Mater., 2012. **24**(17): p. 2337-2342.

22.   Shim, J., et al., *Buckling-induced encapsulation of structured elastic shells under pressure.* Proc. Nat. Acad. Sci. U. S. A., 2012. **109**: p. 5978-5983.

23.   Willshaw, S. and T. Mullin, *Pattern switching in two and three-dimensional soft solids.* Soft Matter, 2012. **8**(6): p. 1747-1750.

24.   Kang, S.H., et al., *Buckling-Induced Reversible Symmetry Breaking and Amplification of Chirality Using Supported Cellular Structures.* Adv. Mater., 2013: p. doi: 10.1002/adma.201300617.

25.   Wu, G., Y. Xia, and S. Yang, *Buckling, symmetry breaking, and cavitation in periodically micro-structured hydrogel membranes.* Soft Matter, 2014. **10**(9): p. 1392-1399.

26.   Shan, S., et al., *Harnessing Multiple Folding Mechanisms in Soft Periodic Structures for Tunable Control of Elastic Waves.* Advanced Functional Materials, 2014. **24**(31): p. 4935-4942.

27.   Zhu, X.L., et al., *Two-Dimensional Photonic Crystals with Anisotropic Unit Cells Imprinted from Poly(dimethylsiloxane) Membranes Under Elastic Deformation.* Appl. Phys. Lett., 2008. **93**(16): p. 161911.

28.   Krishnan, D. and H.T. Johnson, *Optical properties of two-dimensional polymer photonic crystals after deformation-induced pattern transformations.* J. Mech. Phys. Solids, 2009. **57**(9): p. 1500-1513.

29.   Grima, J.N. and K.E. Evans, *Auxetic behavior from rotating squares.* J. Mater.

Sci. Lett., 2000. **19**(17): p. 1563-1565.

30. Grima, J.N., et al., *Do zeolites have negative Poisson's ratios?* Adv. Mater., 2000. **12**(24): p. 1912.

31. Ishibashi, Y. and M. Iwata, *A microscopic model of a negative Poisson's ratio in some crystals.* J. Phys. Soc. Jpn., 2000. **69**(8): p. 2702-2703.

32. Vasiliev, A.A., et al., *Elastic properties of a two-dimensional model of crystals containing particles with rotational degrees of freedom.* Phys. Rev. B, 2002. **65**(9): p. 7.

33. Grima, J.N., A. Alderson, and K.E. Evans, *Negative Poisson's ratio from rotating rectangles.* Comp. Methods Sci. Technol. , 2004. **10**(2): p. 137-145.

34. Taylor, M., et al., *Low Porosity Metallic Periodic Structures with Negative Poisson's Ratio.* Adv. Mater., 2014. **26**(15): p. 2365-2370.

35. Cho, Y., et al., *Engineering the shape and structure of materials by fractal cut.* Proc. Natl. Acad. Sci. U. S. A., 2014. **111**(49): p. 17390-17395.

36. Lakes, R., *DEFORMATION MECHANISMS IN NEGATIVE POISSON RATIO MATERIALS - STRUCTURAL ASPECTS.* J. Mater. Sci., 1991. **26**(9): p. 2287-2292.

37. Prall, D. and R.S. Lakes, *Properties of a chiral honeycomb with a Poisson's ratio of -1.* Int. J. Mech. Sci., 1997. **39**(3): p. 305-&.

38. Alderson, A., et al., *Elastic constants of 3-, 4-and 6-connected chiral and anti-chiral honeycombs subject to uniaxial in-plane loading.* Compos. Sci. Technol., 2010. **70**(7): p. 1042-1048.

39. Sun, K., et al., *Surface phonons, elastic response, and conformal invariance in*

twisted kagome lattices. Proc. Natl. Acad. Sci. U.S.A., 2012. **109**(31): p. 12369–12374.

40.   Grima, J.N. and K.E. Evans, *Auxetic behavior from rotating triangles.* J. Mater. Sci., 2006. **41**(10): p. 3193-3196.

41.   Mitschke, H., et al., *Symmetry detection of auxetic behaviour in 2D frameworks.* EPL (Europhysics Letters), 2013. **102**(6): p. 66005.

42.   Kane, C.L. and T.C. Lubensky, *Topological boundary modes in isostatic lattices.* Nat. Phys., 2014. **10**(1): p. 39-45.

43.   Hyun, S. and S. Torquato, *Optimal and Manufacturable Two-dimensional, Kagomé-like Cellular Solids.* J. Mater. Res., 2002. **17**(01): p. 137-144.

44.   Hutchinson, R.G. and N.A. Fleck, *Microarchitectured cellular solids – the hunt for statically determinate periodic trusses.* ZAMM, 2005. **85**(9): p. 607-617.

45.   Dyogtyev, A.V., I.A. Sukhoivanov, and R.M. De La Rue, *Photonic band-gap maps for different two dimensionally periodic photonic crystal structures.* J. Appl. Phys., 2010. **107**(1): p. -.

46.   Jang, D., et al., *Fabrication and deformation of three-dimensional hollow ceramic nanostructures.* Nat Mater, 2013. **12**(10): p. 893-898.

47.   Russell, P., *Photonic Crystal Fibers.* Science, 2003. **299**(5605): p. 358-362.

48.   Tantikom, K., Y. Suwa, and T. Aizawa, *In-Plane Compression Response of Regularly Cell-Structured Materials.* MATERIALS TRANSACTIONS, 2004. **45**(2): p. 509-515.

49.   Grima, J.N., A. Alderson, and K.E. Evans, *Auxetic behaviour from, rotating rigid units.* Phys. Status Solidi B-Basic Solid State Phys., 2005. **242**(3): p. 561

Chapter 7: Ultrathin, Superhydrophobic Coatings Assembled from Chained Nanoparticles

Adapted from manuscript **G. Wu**, D. Ge, Y. Zhao, S. Yang, "Robust Water Repellency on Ultra-thin (sub-100 nm) Nanoparticle Film"

7.0 Introduction

There has been tremendous effort to create superhydrophobic surfaces with water contact angle (WCA) greater than 150º and contact angle hysteresis (i.e. difference between the advancing and receding contact angle, CAH) <10º, which are of interests for a wide range of applications, including self-cleaning,[1] anti-(bio)fouling,[2] anti-corrosion,[3] anti-ice and anti-frost,[4] drag reduction,[5] and enhanced heat transfer.[6] The mechanism of superhydrophobicity is often explained by the Cassie–Baxter (CB) model, where air is trapped in the grooves between the rough hydrophobic textures, reducing the area fraction of the solid/liquid (liquid/air) interface.[7] As a result, water droplets can roll-off from the surface easily.

Top-down techniques such as photolithography and nanoimprint lithography have been used to create nanostructures with superhydrophobicity.[8] However, these techniques rely on expensive instrument and the fabricated structures are often limited to a small area. To produce large-area and scalable coatings, nanoparticle assemblies are often used since they are inexpensive and versatile to apply to a wide range of substrates, and compatible with many existing coating techniques.[9] Previously, we and others have demonstrated superhydrophobic surfaces from assemblies of spherical nanoparticles via techniques, including layer-by-layer deposition,[10] hierarchical assembly,[11] spin-coating,[12] and spray coating.[13, 14] However, to achieve optimized superhydrophobicity, it often requires nanostructures with large surface

roughness or high aspect ratios such that it minimizes the contact between the liquid and solid,[15] which has been difficult to achieve on nanoparticle coating surfaces due to the spherical nature of the nanoparticles.[10] Further, once wetted, e.g. under high impact pressure, the grooves between nanoparticles are filled with water, and the high aspect ratio structures make it difficult for water to dewet from such surfaces and recover the superhydrophobicity. Thus, it imposes the question whether we can develop a new coating system from nanoparticle assemblies with large asperity yet thin enough to achieve and maintain water repellency on the coating surfaces.

Here, we self-assembled a new form of nanoparticles that are chained together and highly wiggly, much like placing "nano-caltrops" onto the substrate with part of the chain pointing towards the interface, thus minimizing the contact between liquid and the nanotexutre. The silica nanoparticles are chained together using L-arginine according to literature.[16] By controlling the destabilizing effects of the seed particles, chained nanoparticles (CNPs) of different length were synthesized. To create ultrathin films and to study the surface wetting behaviors as a function of nanoparticle morphology, we deposited a monolayer of CNPs on the substrate via charge induced adsorption, followed by chemical vapor deposition (CVD) of fluorosilane to passivate CNP surface. We then characterized the static WCA and dynamic WCA, including advancing (θ_{adv}) and receding (θ_{rec}) WCAs. It was found that the WCA underwent significant increase when the chain length was increased, while the CAH decreased significantly. To further quantify the interaction between water and the coating surfaces, we convert the contact angle measurement into two adhesion factors, that is normal and shear adhesion factors, which are dimensionless parameters proportional to the forces required to vertically detach the water droplet and shear the water droplet on the coating surface, respectively.[17] Compared to the spherical particle (SP) coating, the normal

144

and shear adhesion factors of the long CNP (L-CNP) coatings decreased by 10 times and up to 50 times, respectively. This significantly decreased liquid adhesion can be attributed to the large asperities formed by the highly wiggly nature of the CNPs as confirmed by atomic force microscopy (AFM) characterization of the coating surface morphology.

7.1 Experiments

Synthesis of CNPs and SPs. The CNPs were synthesized based on controlled aggregation of seed particles during growth step in the presence of amino acids. Here, we modified the procedure reported in literature[16]. In brief, to synthesize silica nanoparticle seeds (~20 nm diameter), 0.0566 g L-arginine was dissolved in 40.45 g deionized (DI) water in a 125 mL glass flask at room temperature. After heating the solution to 60 $^\circ$C, 4.2g tetraethoxy silane (TEOS) was added to the L-arginine aqueous solution. The solution was maintained at 60 $\pm$ 0.5 $^\circ$C with constant stirring for 24 h to complete the reaction. Homogeneous spherical silica seeds were characterized using dynamic light scattering (DLS) with a hydrodynamic diameter of 20 $\pm$ 2 nm. The subsequent growing step determines the final morphology of the CNPs. In this case, we followed the literature to vary the concentration of the seed particles and L-arginine to control the chain length, which is summarized in Table 7.1. In brief, CNPs/SPs were synthesized by a seeded growth reaction: x g L-arginine was dissolved in y g water together with 64 g ethanol and z g aqueous suspension of spherical silica seeds (2 wt%) (see Table 7.1 for the values of x, y and z). Subsequently, 1.0 g TEOS was added at 60 $\pm$ 0.5 $^\circ$C. After 24 h, the obtained CNPs were centrifuged at 8000 rpm for 30 min (EPPENDORF Centrifuge 5804 R) and re-dispersed in DI water aided by sonication for 1h.

Table 7.1 Reaction conditions to synthesize CNPs and SPs

Sample	x (g)	y (g)	z (g)
SPs	0.1	10	6
S-CNPs*	0.259	12	4
I-CNPs*	0.259	10	6
L-CNPs*	0.259	8	8

*: S-CNP, I-CNP, and L-CNP indicate short, intermediate, and long chain-like particles respectively.

Surface Functionalization of Substrates with Amino Groups. The Si wafers or glass slides were pre-cleaned by sonication in acetone for 15 min, followed by rinsing with isopropanol, and dried by air gun. The substrates were oxygen plasma treated (30 W, 0.2 Torr, Harrick plasma cleaner PDC-001) for 30 min. The freshly oxidized Si wafers or glass sides were then treated with (3-Aminopropyl)trimethoxysilane (APTMS) immediately by chemical vapor deposition (CVD) within a vacuum desiccator for 15 min to generate amino groups on surface. The excess APTMS was removed by rinsing with ethanol for 15 s, and then water for 5 min, followed by drying with compressed air. The coated substrate was then heated to 100 ℃ for 30 min and stored in a desiccator before use. The thickness of APTMS deposited on the substrate was measured as 1.2 ± 0.3 nm by ellipsometer (Woodland VASE), assuming APTMS has the same optical properties as SiO_2.

Nanoparticle Deposition and Hydrophobilization. APTMS-silanized Si wafers were immersed in a well-dispersed aqueous solution of nanoparticles (0.05 wt %) at pH 6 for

2h. After coating, the substrate was rinsed in DI water twice to remove the loosely adsorbed particles. The pH value of the suspension was adjusted by adding 0.1 mM NaOH or 0.1 mM HCl and monitored with a pH meter (Oakton Waterproof pHTestr 30). To generate coating with monolayer of nanoparticles, the coating process is performed under minimized ionic strength: no ionic species were added except for small amount of NaOH/HCl to adjust the pH of the suspension. The substrate was then dried and subsequently treated with oxygen plasma (30 W, 0.2 Torr) for 30 min to introduce hydroxyl groups on nanoparticle surface. The freshly samples were passivated in a vacuum desiccator containing 100 μL perfluorosilane [(tridecafluoro-1,1,2,2-tetrahydrooctyl)trichlorosilane, Gelest, Inc.] on a separate plastic bowl for vapor deposition for 30 min. After perfluorosilane treatment, the coated substrate was heated to 65 °C for 10 min to chemically react the hydroxyl groups on perfluorosilane and hydroxyl groups on nanoparticles. The substrate was rinsed in acetone and water subsequently to remove the excess perfluorosilane on the surface.

Characterization. The morphology of the nanoparticle films was imaged by scanning electron microscopy (SEM, FEI Strata DB235 FIB). The hydrodynamic diameters and zeta potential of the particles was measured using Zetasizer Nano S (Malvern Instruments) from diluted particle suspension (0.05 wt. %) at pH 6. The surface topography of the samples was measured by AFM (Bruker Icon, Digital Instruments) with a Si_3N_4 cantilever in the tapping mode.

Static and dynamic CAs were measured using Ramé-Hart standard automated goniometer (model 200) using the sessile drop method. The static WCA was measured from a 5 μL water droplet. Advancing and receding contact angles from water and water/ethanol mixtures were measured by automatically adding and removing water from the substrate at a rate of 0.125 μL/s. All CA values were averaged over three

different spots on each sample. For roll-off angle measurements, the substrate was placed on a custom-designed stage attached with a protractor, and a 10 μL water droplet was used.

7.2 Results and Discussion

Synthesis of the CNPs from the spherical seeds involves two steps ([Fig. 7.1 (a)]: controlled assembly of spherical seeds in the presence of L-Argine in water/ethanol mixture, and the growth of SiO_2 layer over the assembled seed particles. The length of the chains is controlled by varying the concentrations of L-Arginine, water, ethanol, and seed particles, respectively, and the amount of TEOS added during the growth step determines the particle diameter.[16] Representative SEM images of the synthesized nanoparticles are shown in Fig. 7.1 (b-e), and the other characteristics are summarized in Table 7.2. Compared to SEM results, a similar increase of hydrodynamic diameter was observed from DLS measurements (Table 7.2, typically peaked at ~50 - 150 nm), indicating a well-dispersed form of the nanoparticles in the aqueous solutions regardless of their forms. The suspension was also found highly stable over time: the intensity and peak wavelength from the DLS measurements barely shifted after the solutions were stored for a few months in the centrifuge tubes.
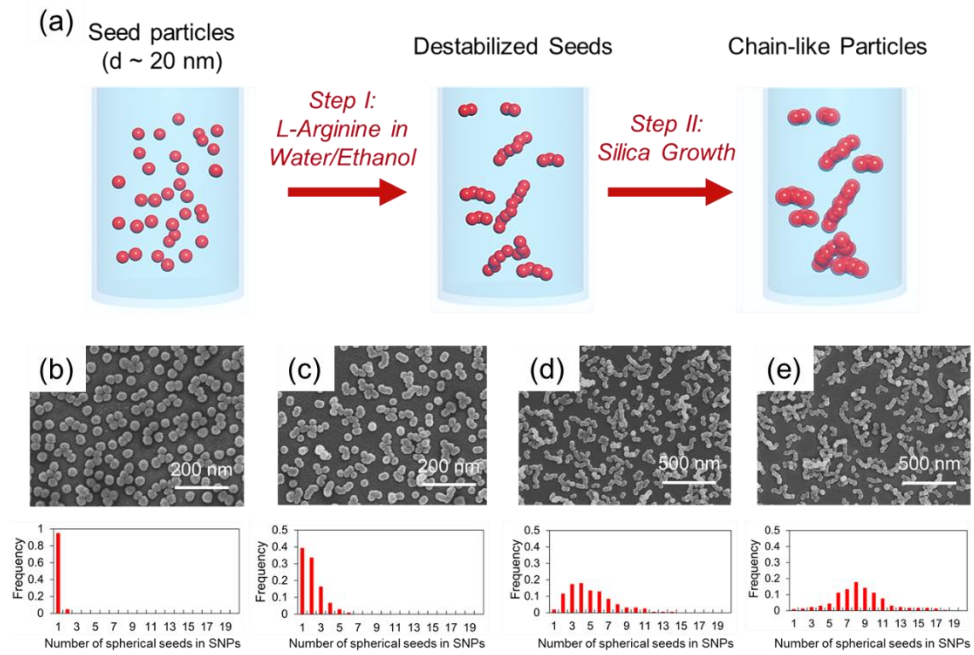
Figure 7.1 (a) Schematics of the CNP synthesis. (b-e) SEM images of the synthesized CNPs and SPs used in the coatings. Histogram below each SEM image shows the distribution of the number of silica seed particles that constitute each set of CNPs or SPs. (b) SPs. (c) S-CNPs. (d) I-CNPs. (e) L-CNPs.

149

Table 7.2. Summary of the characteristics of nanoparticles used in the coatings

Sample	D_h (nm)	Zeta Potential (mV)	diameter (nm)
SPs	60	-40 ± 2	43 ± 3
S-CNPs	89	-42 ± 2	50 ± 3
I-CNPs	128	-45 ± 2	47 ± 3
L-CNPs	144	-48 ± 2	44 ± 3

By controlling the stability of the seed particles during the growth step through controlling the solvent composition and L-arginine concentration; partially aggregated seeds particles during the growth step led to formation of anisotropic CNPs with tunable chain length, denoted as S-CNPs, I-CNPs, and L-CNPs for short, intermediate, and long CNPs, respectively.[16] When the aggregation state of the nanoparticle is low, nanoparticles have morphology close to peanut shape (see S-CNPs in Fig. 7.1c). As the growth condition becomes favorable to form highly aggregated particles, I-CNPs and L-CNPs with highly wiggly morphology and broad chain length distribution are formed (see Fig. 7.1 (d-e)). Here, the diameter of the CNPs was tuned to be ~ 43-50 nm, similar to that of SPs (Table. 7.2) so that we could compare the wetting properties of the coatings as a function of the chain length.

To create an ultrathin coating, we used charge induced adsorption of nanoparticles in aqueous solution [Fig. 7.2 (a)], where the electrostatic repulsion between particles led to self-limiting deposition to form a monolayer of nanoparticles on the substrate,

while the asperity of the coating was determined by the chain length. Since the nanoparticles had negative zeta-potentials at pH 6, we coated the substrate with aminosilane, which are known to exhibit positive charges.[18] The coated surface was passivated by perfluorosilane (~1-2 nm thick, confirmed by ellipsometry) of to achieve hydrophobic surface chemistry.
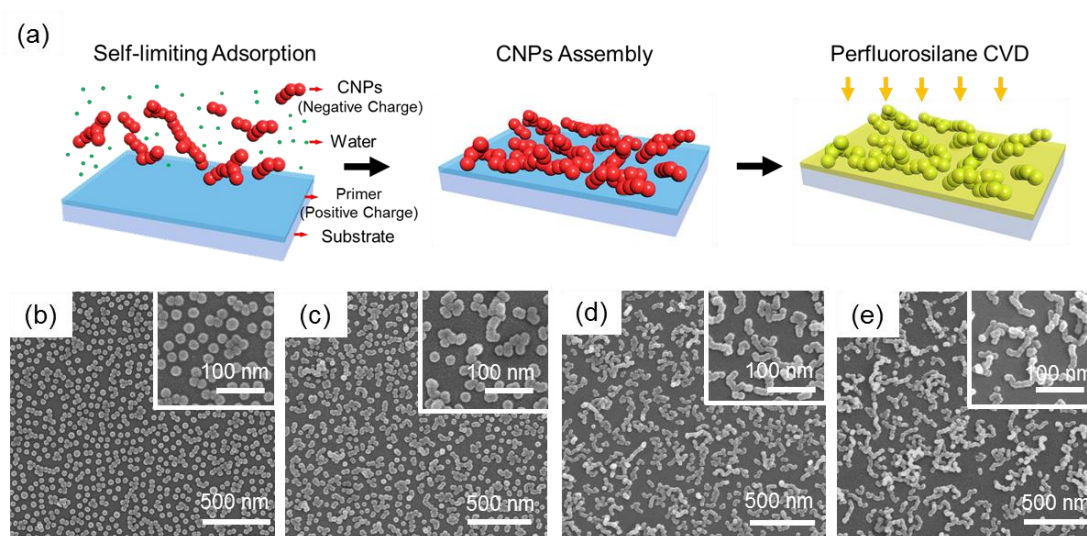
Figure 7.2. (a) Schematics of the nanoparticle deposition by charge induced adsorption. (b-e) SEM images of coatings formed by charge induced adsorption of SPs and CNPs of different length for 120 min in 0.05 wt % of nanoparticle suspension at pH 6.

Upon saturation in the aqueous solutions for 120 min, four different types of nanoparticles, including SPs, S-CNPs, I-CNPs, and L-CNPs, as seen in Fig. 7.2 (a), offered similar coverage of nanoparticles on the substrates: SNPs – $43 \pm 2\%$, S-CNPs – $41 \pm 4\%$, I-CNPs – $42 \pm 4\%$, and L-CNPs – $43 \pm 4\%$. However, their WCA and CAH were drastically different [Fig. 7.3 (a)]. All four coatings exhibit improved water mobility and repellency compared to the flat glass surface treated with perfluorosilane (WCA = $110 \pm 1°$, and CAH = $30 \pm 2°$). Superhydrophobicity was achieved when the

151

length of the CNPs was increased to xxx [Fig. 7.3 (a)]. WCAs of 141 ± 2° and 143 ± 1° were obtained from SNP and S-CNP coatings, respectively, whereas the CAH remained large, 26 ± 2° and 24 ± 2° for coatings from the assemblies of SNPs and S-CNPs, respectively). Supporting this, we observed that water droplets could not rebound after dropping them from a 2 cm height. In contrast, the WCA approached 170° and CAH decreased to 3 ± 1° and $<1^o$, respectively on coatings assembled from I-CNPs and L-CNPs. As shown in Fig. 7.3 (c), the water droplets could rebound after hitting the surface from a 2 cm height.
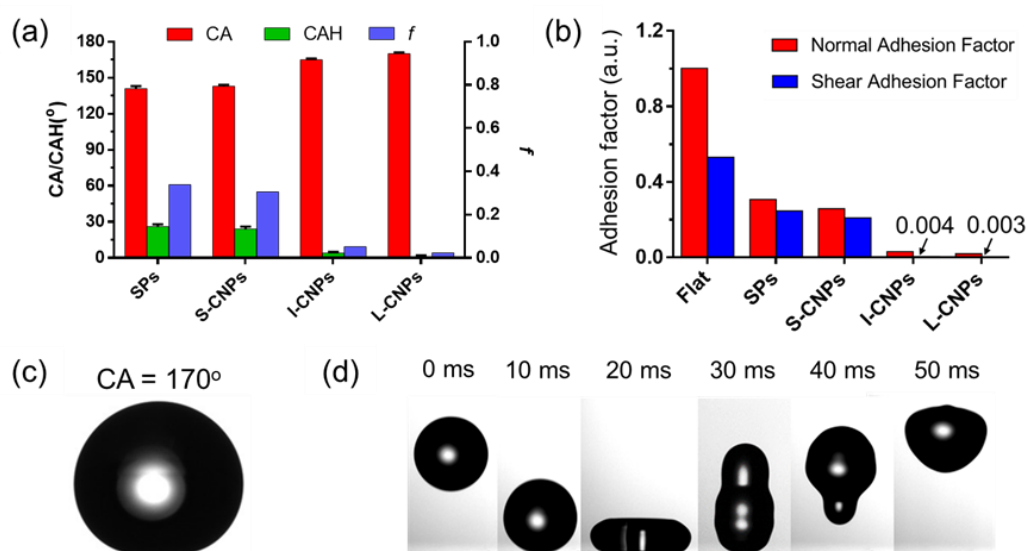
Figure 7.3 (a) WCA, CAH, and filling fraction (*f*) of solid on the composite surface from coatings assembled from different nanoparticles. *f* is estimated by Eq. 7.1. (b) Adhesion factors obtained from Eq. 7.2 and 7.3 on different coating surfaces. (c-d) Optical images of the 5 μL water droplet sitting on the L-CNP coating surface (c), and rebound of 6 μL water droplet from a 2 cm height (d).

According to the Cassie-Baxter model,[7] the enhanced water repellency (high CA and low CAH) seen on I-CNP and L-CNP coatings should be attributed to the small

fraction of solid surface in contact with water, while the surface coverage and thickness of the coating was kept the same:

$$\cos \theta = -1 + f(\cos \theta_0 + 1) \qquad\qquad (7.1)$$

where θ is the apparent CA on the coating surface, f is the area fraction of the solid in contact with liquid, and θ_0 is the equilibrium CA or Young's CA on a flat surface. We estimated the value f of nanoparticle coatings from the apparent WCAs (see Fig. 7.2 (f)): f of coatings assembled from I-CNPs and L-CNPs was very small, 2.3 % and 5%, respectively, in sharp contrast to ~ 34 % and 31 % from SNP and S-CNP coatings.

To better understanding the implication of the improved water repellency to the solid-liquid interaction, we convert the CA results into normal and shear adhesion factors (see Fig. 7.3 (b)),, which are dimensionless parameters proportional to the forces required to vertically detach and shear the water droplets from the coating surface, respectively[17]

$$\text{Normal adhesion factor: } x = 1 + \cos \theta_{rec} \qquad (7.2)$$

$$\text{Shear adhesion factor: } y = \cos \theta_{adv} - \cos \theta_{rec} \qquad (7.3)$$

Here, the flat surface is the glass slide treated with perfluorosilane. As seen in Fig. 3b, water adhesion to NP coatings decreased significantly due to the formation of the composite interfaces. It is noted that as the chain length of the CNPs reached a threshold, the water adhesion dropped dramatically, and became almost vanished on the L-CNPs. When compared to the adhesion parameters of the SP coating, the shear adhesion of water on the L-CNP coating surface decreased by ~50 times, and normal adhesion decreased by ~10 times. Compared to those of the flat substrate coated with fluorosilane,

both adhesion factors on L-CNP coating decreased by more than 100 times. These results are consistent with the significantly reduced f estimated from Eq. 7.1 [see Fig. 7.3 (a)], where the decreased adhesion is associated to the reduced contact between liquid and solid.[19]

Since the wetting behaviors are highly dependent on the nanotexture of the coating, we imaged the surface topography of the coatings using AFM. to make sure the AFM images in the scanned area can represent the overall coating morphology, for each sample, five 2.5 µm by 2.5 µm scans were taken at different locations. root mean square surface roughness (R_{RMS}) and average coating thickness were calculated and compared from different locations for each sample to ensure that the scanned area represented the overall surface topography of the entire coatings.
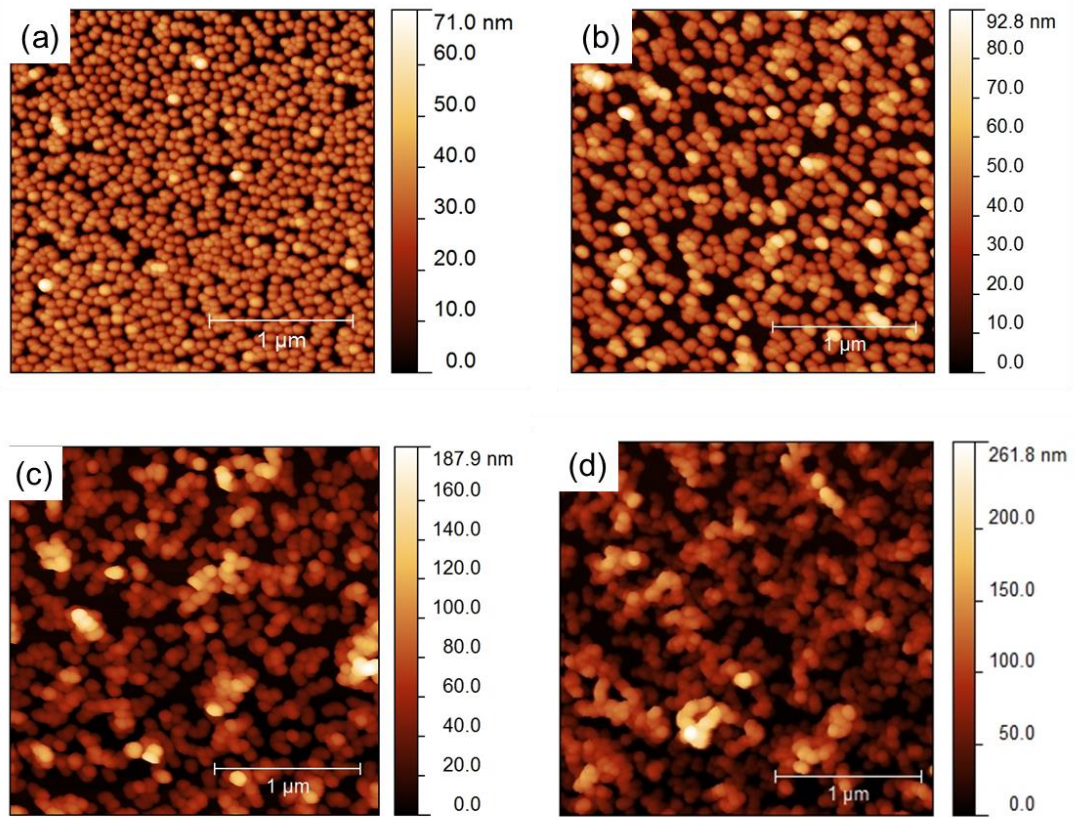
Figure 7.4 Representative AFM images of the coatings assembled from different nanoparticles: (a) SPs, (B) S-CNPs, (C) I-CNPs, and (D) L-CNPs.

As seen in Fig. 7.5, when the chain length of the nanoparticles increased, both R_{RMS} and the average nanoparticle thickness (h) was also increased given similar coverage of the particles to the substrates. Here, the average thickness of the coating increased from 22 ± 3 nm (on SP coating) to 48 ± 5 nm (on L-CNP coating), and the R_{RMS} increases from 11 ± 1 nm (on SP coating) to 36 ± 3 nm (on L-CNP coating).
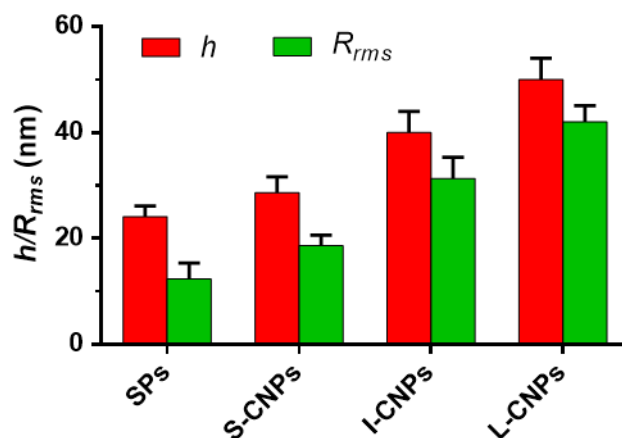
Figure 7.5 The average coating thickness (h) and R_{RMS} from different nanoparticle coating surfaces. The error bars indicate the standard deviation of the tested results scanned from five locations on the samples.

Previously, a few studies have proposed that the reduced contact area to nano-roughness can be achieved by introducing large nano-asperities with the radius of curvature on the order of 10's of nm.[8, 20] Here, we believe that the improved water repellency should be explained by a smaller number of contacted asperities on the coating surface when increasing chain length and thus chain flexibility of CNPs. When SPs are coated on a substrate, due to charge induced adsorption, the height of the nanoparticle coating is rather small, no more than their diameter as confirmed by AFM scan and illustrated by schematics (Fig. 7.6 a and c), therefore, water can easily impregnate into the air pockets between nanoparticles. For CNPs, they are flexible and wiggly. Therefore, they do not lay flat on surface. As seen in Fig. 7.6 b and d, the height of L-CNPs is spiked due to their wiggly morphology, much larger than the diameter of the nanoparticles, creating two-tiered roughness, which not only increases surface

156

roughness to enhance water repellency but also makes it more difficult for water to impregnate the grooves between CNPs.
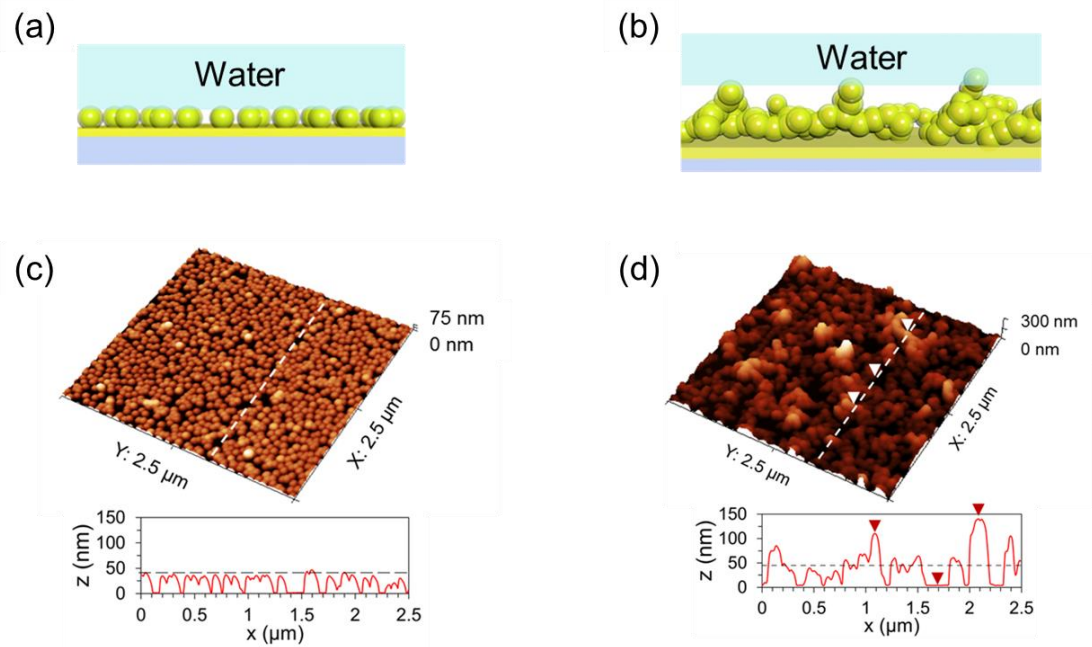
Figure 7.6 (a-b) Schematics showing the wetting mechanism on spherical particles vs. wiggly CNPs. (c-d) AFM image and line profile taken from SP coatings vs. L-CNP coatings. The grey dashed lines indicate the diameter of the nanoparticles.

It is important to note that the unique two-tier morphology of L-CNP coating is ultrathin, less than 100 nm. Therefore, the coating is not only superhydrophobic but highly transparent (see Fig. 7.7). As previously, we discovered, for rough surface to be transparent, the surface roughness need to be smaller than 100 nm, beyond that surface roughness, the coatings typically have reduced optical transparency due to Mie scattering.[21] In our system, the transmittance of L-CNP coating in the visible to near infrared (NIR) regions was found slightly higher than that of the bare glass (Fig. 7.7), which is attributed to the effects reduction of Fresnel reflection on the coating surface

due to the intermediate refractive index obtained on the coated nanoparticles.[22] In Fig. 7.7 (a), the optical transparency of the coating at normal incidence is shown; and in Fig. 7.7 (b), the average transparency of the coating and bare glass between wavelength 400 nm and 800 nm is shown. In both cases, the coated glass slide is more transparent than non-coated one. Maintaining high optical transparency on SH surface can be very beneficial for applications, including water proof optical instrumentation, solar cell panel, goggles, and vehicle windshields.
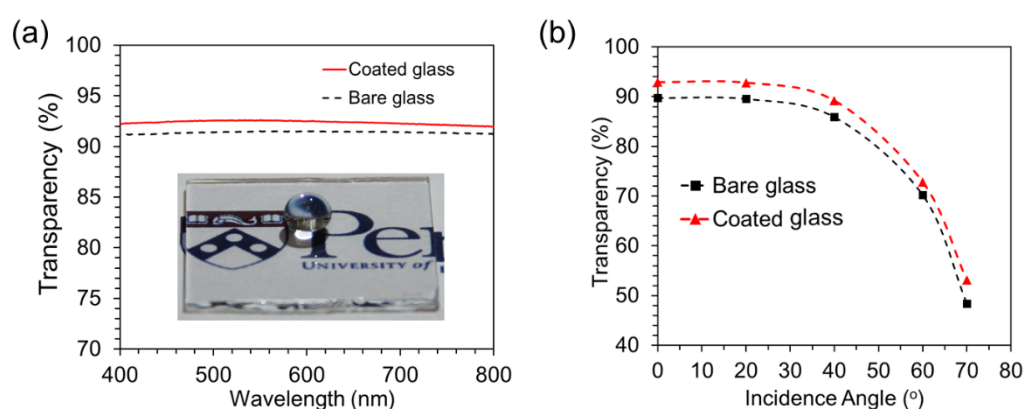
Figure 7.7 Transmittance of the glass coated with L-CNPs vs. bare glasses at normal incidence (a) and at different incidence angles (b) in the wavelength from 400 nm to 800 nm.

7.3 Conclusion

We successfully created ultrathin superhydrophobic coating with high transparency in the visible regions from charge-induced assembly of chained silica nanoparticles. both SEM and AFM images showed that nanostructures obtained from CNP coatings had high nano-asperity due to the highly wiggly nature of CNPs, thus minimizing the contact between water and the coating surface. While surface coated with I-CNPs and L-CNPs were superhydrophobic, those from SPs and S-CNPs at the same surface

158

coverage had WCA of ~140° and ~170° respectively. Using Cassie-Baxter equation, we estimated the solid area filling fraction from the nanoparticle coatings, decrease from ~34% on SP coating to 2.3% on L-CNP coating. Accordingly, we observed ~50 times reduction on shear adhesion parameter and 10 times reduction of normal adhesion parameter from L-CNP coatings compared to those from SP coatings. Because our CNP coating was ultrathin (less than 100 nm thick), they showed anti-reflectivity and omni-transparency in the visible to NIR regions.

7.4 References

1. Quéré, D., *Wetting and Roughness*. Annual Review of Materials Research, 2008. **38**(1): p. 71-99.

2. Bhushan, B. and Y.C. Jung, *Natural and biomimetic artificial surfaces for superhydrophobicity, self-cleaning, low adhesion, and drag reduction*. Progress in Materials Science, 2011. **56**(1): p. 1-108.

3. Bellanger, H., et al., *Chemical and Physical Pathways for the Preparation of Superoleophobic Surfaces and Related Wetting Theories*. Chemical Reviews, 2014. **114**(5): p. 2694-2716.

4. Samaha, M.A., H.V. Tafreshi, and M. Gad-el-Hak, *Superhydrophobic surfaces: From the lotus leaf to the submarine*. Comptes Rendus Mécanique, 2012. **340**(1–2): p. 18-34.

5. McHale, G., M.I. Newton, and N.J. Shirtcliffe, *Immersed superhydrophobic surfaces: Gas exchange, slip and drag reduction properties*. Soft Matter, 2010. **6**(4): p. 714-719.

6. Kim, S. and K.J. Kim, *Dropwise Condensation Modeling Suitable for Superhydrophobic Surfaces*. Journal of Heat Transfer, 2011. **133**(8): p. 081502-081502.

7. Cassie, A.B.D. and S. Baxter, *Wettability of porous surfaces*. Transactions of the Faraday Society, 1944. **40**(0): p. 546-551.

8. Park, K.-C., et al., *Nanotextured Silica Surfaces with Robust Superhydrophobicity and Omnidirectional Broadband Supertransmissivity*. ACS Nano, 2012. **6**(5): p. 3789-3799.

9. Rahmawan, Y., L. Xu, and S. Yang, *Self-assembly of nanostructures towards*

transparent, superhydrophobic surfaces. Journal of Materials Chemistry A, 2013. **1**(9): p. 2955-2969.

10. Bravo, J., et al., *Transparent Superhydrophobic Films Based on Silica Nanoparticles.* Langmuir, 2007. **23**(13): p. 7293-7298.

11. Karunakaran, R.G., et al., *Highly Transparent Superhydrophobic Surfaces from the Coassembly of Nanoparticles (≤100 nm).* Langmuir, 2011. **27**(8): p. 4594-4602.

12. Xu, L., et al., *Transparent, Superhydrophobic Surfaces from One-Step Spin Coating of Hydrophobic Nanoparticles.* ACS Applied Materials & Interfaces, 2012. **4**(2): p. 1118-1125.

13. Campos, R., et al., *Superoleophobic Surfaces through Control of Sprayed-on Stochastic Topography.* Langmuir, 2012. **28**(25): p. 9834-9841.

14. Ogihara, H., et al., *Simple Method for Preparing Superhydrophobic Paper: Spray-Deposited Hydrophobic Silica Nanoparticle Coatings Exhibit High Water-Repellency and Transparency.* Langmuir, 2012. **28**: p. 4605.

15. Martines, E., et al., *Superhydrophobicity and Superhydrophilicity of Regular Nanopatterns.* Nano Letters, 2005. **5**(10): p. 2097-2103.

16. Wang, J., et al., *Preparation of Anisotropic Silica Nanoparticles via Controlled Assembly of Presynthesized Spherical Seeds.* Langmuir, 2010. **26**(23): p. 18491-18498.

17. Gao, L. and T.J. McCarthy, *Wetting 101°.* Langmuir, 2009. **25**(24): p. 14105-14115.

18. Zhang, F., et al., *Chemical Vapor Deposition of Three Aminosilanes on Silicon Dioxide: Surface Characterization, Stability, Effects of Silane Concentration,*

and Cyanine Dye Adsorption. Langmuir, 2010. **26**(18): p. 14648-14654.

19.   Nosonovsky, M. and B. Bhushan, *Hierarchical roughness optimization for biomimetic superhydrophobic surfaces.* Ultramicroscopy, 2007. **107**(10–11): p. 969-979.

20.   Checco, A., A. Rahman, and C.T. Black, *Robust Superhydrophobicity in Large-Area Nanostructured Surfaces Defined by Block-Copolymer Self Assembly.* Advanced Materials, 2014. **26**(6): p. 886-891.

21.   Hwang, H.S., et al., *Facile Fabrication of Transparent Superhydrophobic Surfaces by Spray Deposition.* ACS Applied Materials & Interfaces, 2011. **3**(7): p. 2179-2183.

22.   Raut, H.K., et al., *Anti-reflective coatings: A critical, in-depth review.* Energy & Environmental Science, 2011. **4**(10): p. 3779-3804.

Chapter 8: Robust Air-like Superhydrophobicity on Monolayer of Long-Chained Silica Nanoparticle Coatings

Adapted from manuscript **G. Wu**, D. Ge, Y. Zhao, S. Yang, "Robust Water Repellency on Ultra-thin (sub-100 nm) Nanoparticle Film"

8.0 Introduction

As discussed in Chapter 7, there remains a contradictory fact to enhancing the water repellency, where the surface may harm the sitting stability of liquid phase when only small portion of solid is contacted liquid phase, resulting in invasion and irreversible loss of water repellency under environments of water drop impingements,[1] hydrostatic pressure,[2] and vapor phase condensation[3, 4]. Inspired by superhydrophobicity (SH) observed on lotus leaves, which have hierarchical roughness composed of both micro- and nanostructures, it has been widely adopted in literature that both micro- and nanostructures are capable of trapping air pockets to enhance the water repellency while addition of high asperity nanoscale roughness to relatively small roughness in microscale could enhance the wetting robustness.[5] However, the existence of micro-scale surface roughness is not desired for some other aspects of coating properties[6-8], e.g. optical transparency due to strong Mia scattering from microstructures,[9] and trapping of smaller sized droplets such as condensing liquid, which are typically in the range of 1- 40 µm in contrast to mm sized rain droplets on lotus leaves. Therefore, in recent years, there has been increasing efforts to create surface with nano-roughness (preferably with size less than 100 nm) to achieve robust Cassie-Baxter non-wetting state.

Theoretically, robust non-wetting state can be achieved via, e.g. highly dense nanostructures,[10] and/or re-entrant structures.[11] it is also important to remember

that to achieve high contact angle (CA) and low contact angle hysteresis (CAH, the difference between advancing CA and receding CA), it requires minimized contact area between solid and liquid phases. In fact, lower CA and higher CAH are found for nanostructures with increased packing density and/or introduction of re-entrant tip structures due to increased solid-liquid contact area.[12] So far, to resolve these conflicting requirements, additional features, e.g. nanoscale hierarchy,[13] structure with sharp tips,[14] and optimized spacing between the nanostructures, are introduced. However, these methods also complicate the fabrication processes. Therefore, it is highly desired to develop a simple system with nanoscale structures that would allow scalable manufacturing of robust water repellency.

In Chapter 7, we investigated wetting behaviors on nano-structures formed by an ultrathin monolayer of chained nanoparticles deposited on a substrate via charge induced adsorption, followed by vapor deposition of perfluorosilane. It was found that the highly wiggly morphology of the long chain nanoparticles (L-CNPs) offers unique nanostructures with high asperity with minimized water contact with the nanostructures, leading to SH. In this Chapter, we investigated the stability of the Cassie-Baxter state on such nanostructures. We found that the nanostructures from L-CNPs were highly stable against impinging water drops at a speed up to 8 m/s and maintained SH against hydrostatic pressure up to 15-17 kPa, and condensing water droplet with diameter as small as a few micro-meters diameter. The L-CNP coatings also show improved repellency toward low surface tension liquids from ethanol/water mixtures compared to the coating from spherical particles (SPs), and the water repellency still maintains even upon condensation. We attributed the high stability of the L-CNP coating to the two-tier nanostructures formed on coating surfaces.

8.1 Experiments

Synthesis of L-CNPs. The L-CNPs were synthesized based on controlled aggregation of seed particles during growth step in presence of amino acids as described in details in Chapter 7, where we modified the procedure reported in literature[15]. In brief, to synthesize silica nanoparticle seeds (~20 nm diameter), 0.0566 g L-arginine was dissolved in 40.45g deionized (DI) water in a 125 mL glass flask at room temperature. After heating the solution to 60 °C, 4.2g tetraethoxy silane (TEOS) was added to the L-arginine aqueous solution. The reaction solution was maintained at 60 ± 0.5 °C with constant stirring rate for 24h to complete the reaction. Homogeneous spherical silica seeds were characterized using dynamic light scattering (DLS) with a hydrodynamic diameter of 20 ± 2 nm. The chained nanoparticles were synthesized by a seeded growth reaction. 0.259 g L-arginine was dissolved in 8 g water together with 64 g ethanol and 8 g spherical silica seed aqueous suspension (2 wt %). Subsequently, 1.0 g TEOS was added at temperature 60 ± 0.5 °C. After 24 h, the nanoparticles were centrifuged at 8000 rpm for 30 min (EPPENDORF Centrifuge 5804 R) and re-dispersed in DI water aided by sonication for 1h.

Surface Functionalization of Silicon/Glass Substrates with Amino groups. The Si wafers/glass slides were pre-cleaned by sonication in acetone for 15 min, followed by rinsing with isopropanol, and dried by air gun. The substrates were oxygen plasma treated (30 W, 0.2 Torr, Harrick plasma cleaner PDC-001) for 30 min. The freshly oxidized Si wafers/glass sides were then treated with (3-Aminopropyl)trimethoxysilane (APTMS) immediately by chemical vapor deposition (CVD) within a vacuum desiccator for 15 min to generate amino groups on surface. The excessive APTMS was removed by rinsing with ethanol for 15 s, and then water for 5 min, followed by drying with compressed air. The coated substrate was then heated to 120 °C for 30 min and

stored in desiccator before further use. A 1.2 ± 0.3 nm layer thickness was measured by Ellipsometry (Woodland VASE), assuming APTMS has the same optical properties as SiO_2.

L-CNP and Spherical Particle Deposition and Hydrophobilization. APTMS-silanized Si wafers were immersed in a well-dispersed aqueous solution of L-CNP particles at 0.05 wt. % at pH 6 for different amount from time (from 1 min to 4 h). After coating, the substrate was rinsed twice in DI water to remove loosely adsorbed particles. The pH value of the suspension was adjusted by adding 0.1 mM NaOH or 0.1 mM HCl and monitored with pH meter (Oakton Waterproof pHTestr 30). In all of the experiments, the coating process was performed under minimized ionic strength: no ionic species were added except for small amount of NaOH/HCl to adjust the pH of the suspension. For coating the spherical particles, similar approach is applied to the spherical particle suspension with concentration of 0.01 wt.% at pH 6 with coating time from 30 min. The substrate was then dried and subsequently treated with oxygen plasma (30 W, 0.2 Torr) for 30 min to introduce surface hydroxyl groups and placed in a vacuum desiccator containing 100 μL perfluorosilane [(tridecafluoro-1,1,2,2-tetrahydrooctyl)trichlorosilane, Gelest, Inc.] on a separate plastic bowl for vapor deposition for 30 min. After perfluorosilane treatment, the coated substrate was heated up to 65 °C for 10 min to encourage chemical reactions between perfluorosilane and hydroxyl groups on nanoparticles. The substrate was rinsed in acetone and water subsequently to remove the excessive perfluorosilane on the surface.

Characterization. The morphologies of the L-CNP coatings were imaged with an FEI Strata DB235 FIB scanning electron microscopy (SEM). The surface topography of the samples was measured from a Bruker Icon atomic force microscope (AFM) from

166

Digital Instruments with a Si_3N_4 cantilever in tapping mode. Static and dynamic water contact angles (CA) were measured using a model 200 Ramé-Hart standard automated goniometer with sessile drop method. The static CA was measured from a 5 μL water droplets. Advancing and receding water contact angles (CA_{adv} and CA_{rec}) were measured by automatically adding and removing water from the substrate with addition/removal rate of 0.125 μL/s respectively. All CA values were averaged over five different spots on each sample. High speed movies for impinging drop experiments were taken with a high-speed camera (Phantom Ultra-high speed) with frame rate and exposure time at 1000 fps and 1 ms respectively.

Water condensation behaviors on L-CNPs were imaged using an FEI Quanta 200 field emission gun (FEG) environmental scanning electron microscope (ESEM) at 30 kV voltage, following the method by Rykaczewski *et al.*[16] In brief, the chamber was first vacuumed to 1 Torr, and the Peltier was cooled to -12 ^{o}C. After the temperature was stabilized, the pressure was gradually increased to ~4.5 Torr to enable the continuous condensation on the coating surface. During this step, the temperature of Peltier gradually increased to ~-2.2 ^{o}C due to the heat released during the condensation. The sample was tilted at 75-85° and imaged at a scan rate of 1 picture frame/s to avoid heating and surface damage by the electron beam.

8.2 Results and Discussion

8.2.1 Surface Coating and Characterization
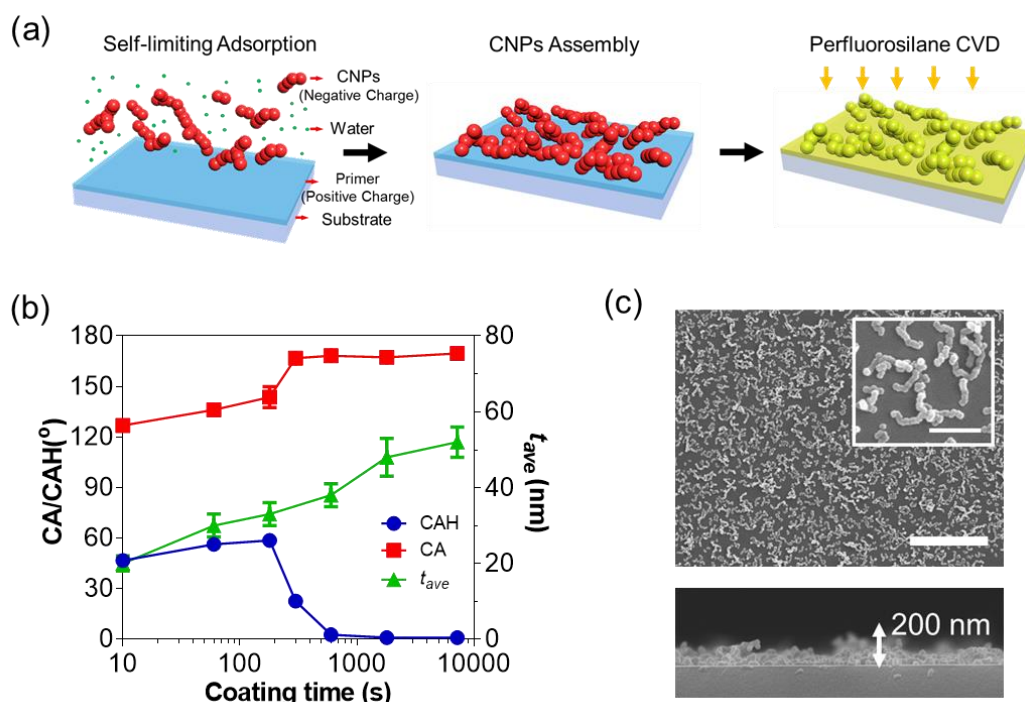
Figure 8.1 (a) Schematics showing the deposition of nanoparticles via the charge induced adsorption. (b) WCA, CAH, and average thickness of the coating at different deposition time of the CNPs, where the CA start to reach 170° and CAH reach ~1° as the average coating thickness approaching 50 nm. (c) Top/side-view SEM images of the coating formed from immersing APTMS functionalized glass in 0.05 wt % L-CNP particle aqueous suspension at pH = 6 for 30 min.

In Fig. 8.1 (b), WCA, CAH, and average thickness of the coating surface was plotted against the coating time for L-CNPs. It was observed that as the coating thickness reached ~50 nm, the coating began to exhibit extreme water repellency with WCA ~ 170° and CAH < 1°. Fig. 8.1 (c) shows formation of a monolayer of L-CNPs after 30 min deposition, at which points the coating coverage reached saturation and

168

extreme water repellency was observed. Such behavior was found to be attributed to the large nanostructure asperities formed from highly wiggly morphology of L-CNPs. Here, we focus on study of the stability of Cassie-Baxter state of the coating prepared from 30 min immersion time vs. hydrodynamic pressure, hydrostatic pressure, low surface tension liquids, and water condensation.

8.2.2 Robustness of Cassie-Baxter State against Hydrostatic and Hydrodynamic Pressure

The robustness of Cassie-Baxter state of wetting on the two-tier nanostructures as we discovered in chapter 7 were first investigated in study against hydrodynamic pressure and hydrostatic pressure. For water drop impacts, Bartolo *et al*.[17] and Reyssat *et al*.[1] demonstrated that increasing the velocity beyond a critical value will cause water droplet pinned on SH surfaces. Particularly, the kinetic energy of the water drop can overcome the energy barrier between the suspended Cassie-Baxter state and the pinned Wenzel state, which is defined by the anti-wetting capillary pressure of the smallest length-scale structure present on the surface.[18] The external pressure generated from the impacting water droplet is characterized by two scales of the pressures,[19] known as P_{HW}, and P_D defined by:

$$P_{WH} \sim k\rho c v \quad (8.1)$$

$$P_B \sim 0.5\rho v^2 \quad (8.2)$$

where ρ is the density of water, c is the speed of sound in water, and v is the impact velocity, and k is a pre-factor on the order 0.2 depending on surface topology of the superhydrophobic surface. Here, P_{HW} is associated to the events of shock wave (*i.e.*, water hammer effect) generated within the initial impact zone. P_D is associated to the Bernoulli pressure during spreading of the liquid over the SH surface.

P_{HW} can be as large as a few MPa due to the water hammer effects, and thus it can easily induce local impregnation of water on most SH surfaces. So far, only a few specific SH structures have been reported to completely repel high speed impinging (i.e. speed ~ a few meter per second[1, 10, 13, 18, 20]) water drops, including hierarchical surface texture composed both micro- and nano-textures to alleviate the hydrodynamic pressure (i.e. up to a few MPa) as water droplets impinging along the micro-roughness,[5] or high aspect ratio surface roughness with extremely small spacing (<10 nm) to provide robust water repellency (high anti-wetting pressure) against water drop speed up to 10 m/s.[18]

To investigate the robustness of our coating, we performed water impingement on L-CNPs coatings from water droplets with different volume (5 µL to 25 µL) from different heights (0.2 m to 6 m). It is noted that it is very difficult to impinge the small water drops to the relative small area of the sample surface from a large height, *e.g.* 6 m, whereas the terminal speed is significantly smaller than that of the larger water drops.[21] Therefore, we chose to data from relatively large water drops with an initial volume of 25 µL with a diameter of ~3.6 mm to represent the studies (see Table 8.1). Two characteristic pressures associated to the water drop impingements are tabulated in Table 8.1, according to Eq. 8.1 and 8.2.

Table 8.1 Summary of water droplet (initial volume of 25 μL) impingement experiments

Height (m)	Speed (m/s)	P_{WH} (MPa)	P_B (kPa)	Completely Repel
0.5	~3	~0.9	~4.5	Yes
1	~4.5	~1.3	~10	Yes
3	~7[21]	~2.1	~24	Yes
6	~8[21]	~2.4	~32	Yes

For water droplets impinged from heights of 0.5 m and 1 m, the dynamic process is recorded by a high-speed camera and the speed is measured based on recorded frames. The process of the surface to completely repel the water droplet can be identified as splash and fully recoil of the impinging water drop from the surface. For water droplets impinged from heights of 3 m and 6 m, we were not able to capture the water impingement dynamics using the camera setup in the room given the height. However, we carefully examined the samples afterwards whether any liquid was sticky to the coating surface and the speed of water droplet was estimated using the method reported in literature.[21] Interestingly, we did not observe any water pinning effect from impinging water at a speed up to ~ 8 m/s, which was approaching the terminal speed of the water droplet tested in the experiments or the speed of rain in a storm.
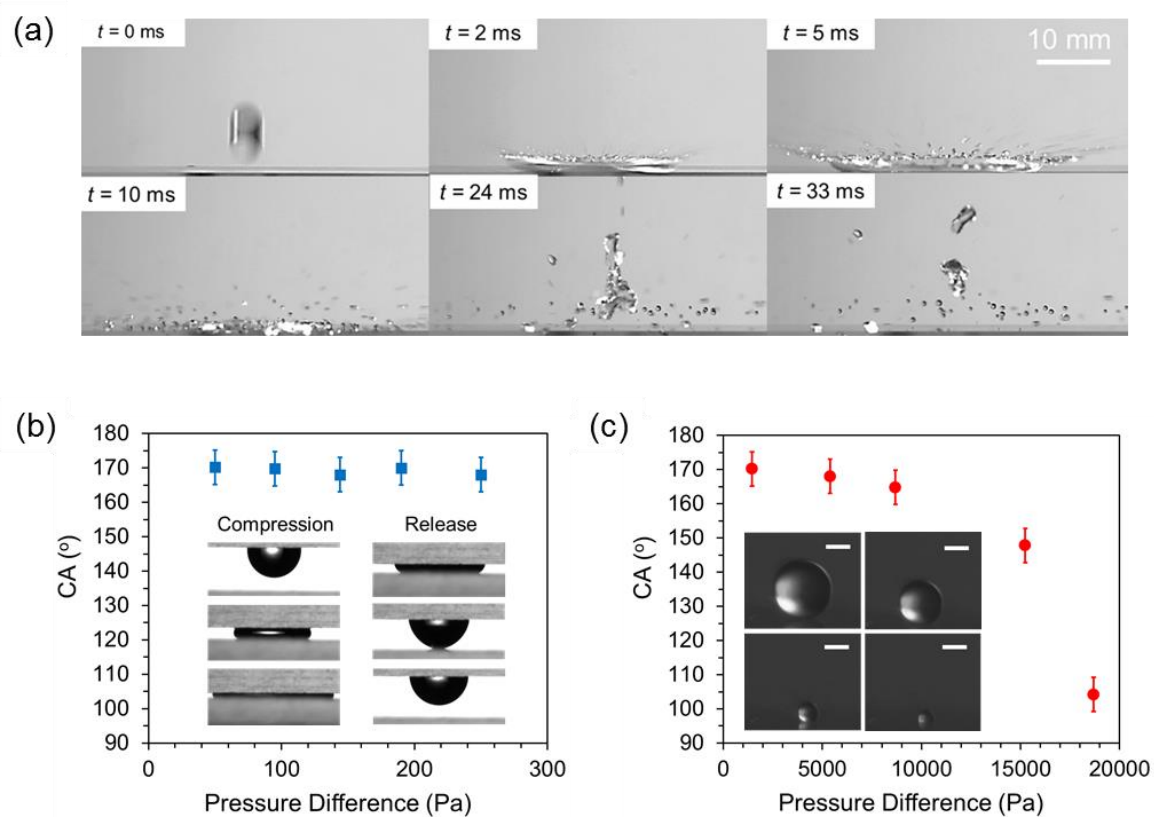
Figure 8.2 (a) Sequential video frames of a ~25 μL water droplet impacting the L-CNP coated glass surface at a speed of ~ 4.5 m/s. (b) CAs during compression and release of the L-CNP coated surface to a perfluorosilane treated flat substrate. Inset: Optical images taken during the compression and release process. (c) CA of evaporating small water drops on the L-CNP coating surface vs. the internal Laplace pressure against the composite interface. Inset: pictures of the evaporating water micro-droplet. Scale bar: 20 μm.

To quantify the robustness of the superhydrophobic NP coatings, we performed two experiments by applying hydrostatic pressure following the literature,[2] including (a) compression experiments by squeezing water droplets between two surfaces, and (b) evaporating small water droplets on the coating surface. In Fig. 8.2 (b), we show

compression of a 5 μL water droplet between the SH surface and a flat hydrophobic surface treated with perfluorosilane up to a small separation (~0.15 mm). The applied pressure to the composite interface was deduced using the Laplace equation:

$$\Delta P = \gamma(\cos\theta_b + \cos\theta_t)/x, \text{for } x \ll R \quad (8.3)$$

where γ is the water-vapor surface tension, θ_b and θ_t are the contact angles at the bottom and top surfaces upon compression, respectively, and R is the radius of the water drop. For each ΔP, we measured the receding WCAs on the L-CNP coating surface as we relax the bottom plate. During the relaxation, we did not observe any water droplet stuck to the L-CNP coating and the receding contact angle of the water droplet maintained above 165°, confirming that Cassie-Baxter state was maintained. To reach even higher hydrostatic pressures, small water drops were deposited to the surface using a water spray bottle with initial radii of ~ 30 to 50 μm. At this length scale, the gravitational force becomes negligible, and the internal pressure, ΔP, applied to the composite interface is given by the Laplace equation $\Delta P = 2\gamma/R$. As water drops evaporate, hydrodynamic pressure applied to the composite interface is increased due to the shrunk drop size. To capture the dynamic process of evaporation, we took the side-view images from water drop under the optical microscope. As seen in Fig 8.2 (c), the water droplet remained nearly spherical until its radius reached ~ 7 μm. To compare the Cassie-Baxter state stability of our coatings with existing literature during droplet evaporation, we investigated the relationship between CA of the water drop and the internal Laplace pressure due to the shrunk drop size. For the evaporating water drop as shown in Fig. 8.2 (c), CA decreased to ~ 150° when the internal pressure reached ~15kPa and to ~105° at a pressure of 17 kPa. These results suggest that a maximum sustainable pressure difference of the composite interface can be in the range ~ 15-17

kPa. We monitored evaporation of multiple water drops on our coating surface, the critical pressure that the composite interface sustains was found varied slightly from ~15 kPa to 20 kPa. The small difference could be attributed to the local variation of the nanoparticle coating when the contact-line dimension is comparable to the dimension of spacing between the nano-asperities. In comparison, on other superhydrophobic surfaces (e.g. micro-structures, artificial hierarchical structures, and lotus leaf), significant drop of WCA occurs at much smaller internal pressures, ranging from ~200 Pa to 2kPa.[22-25]

8.2.3 Wetting Behavior of the Coating Against Low Surface Tension Liquids

While superhydrophobic surface can repel small droplet size water, it may not repel liquids with lower surface tensions, which can then impregnate the grooves between nanotextures. Therefore, wetting by low surface tension liquid To further confirm that our coatings have two-tiered nanoroughness, we prepared low surface tension liquid from ethanol /water mixture with different mixing ratios (up to 25 wt% ethanol) and the surface tension was reduced from 72.8 (pure water) to 36.0 mN/m at room temperature.[26] In Fig. 8.3 (a) and (c), we show the CA_{adv}, CA_{rec}, and CAH for wetting of ethanol/water mixtures on both SPs and L-CNP coatings. The coating assembled from L-CNPs is resistant to low surface tension liquids. We hypothesized that WCA underwent a two-step transition as a result of the variation of nano-asperities created by the wiggly chains [see Fig. 8.3 (b)]. When ethanol concentration was less than 5 wt.%, CA_{adv} was found greater than 160º, indicating a full Cassie state, where liquid remain contact with locally protruded asperities. Drops in this region experienced only a very weak decrease in apparent WCA and slightly increase of CAH. as ethanol concentration continued to increase, the CAH increased sharply at two distinct critical concentrations, each we believe indicated a wetting transition. After passing the first

critical ethanol concentration, 5 wt. %, the CAH increased from < 7° to 22° as the ethanol concentration was increased to 7.5 wt. %. From 7.5 to 15 wt. % ethanol concentration, we observed that the liquid remained un-pinned across the sample despite of increased CAH, suggesting that some regions remained dry. After passing the second critical concentration of 15 wt. %, it became extremely difficult to recede the liquid droplets as they were pinned to the coating surface, suggesting a fully wetted surface. In this case, a full transition from Cassie-Baxter to Wenzel state occured at surface tension ~40 mN/m for L-CNPs, and ~55 mN/m for SPs coating, which indicates improvement of the Cassie-Baxter state stability upon low surface tension liquids.
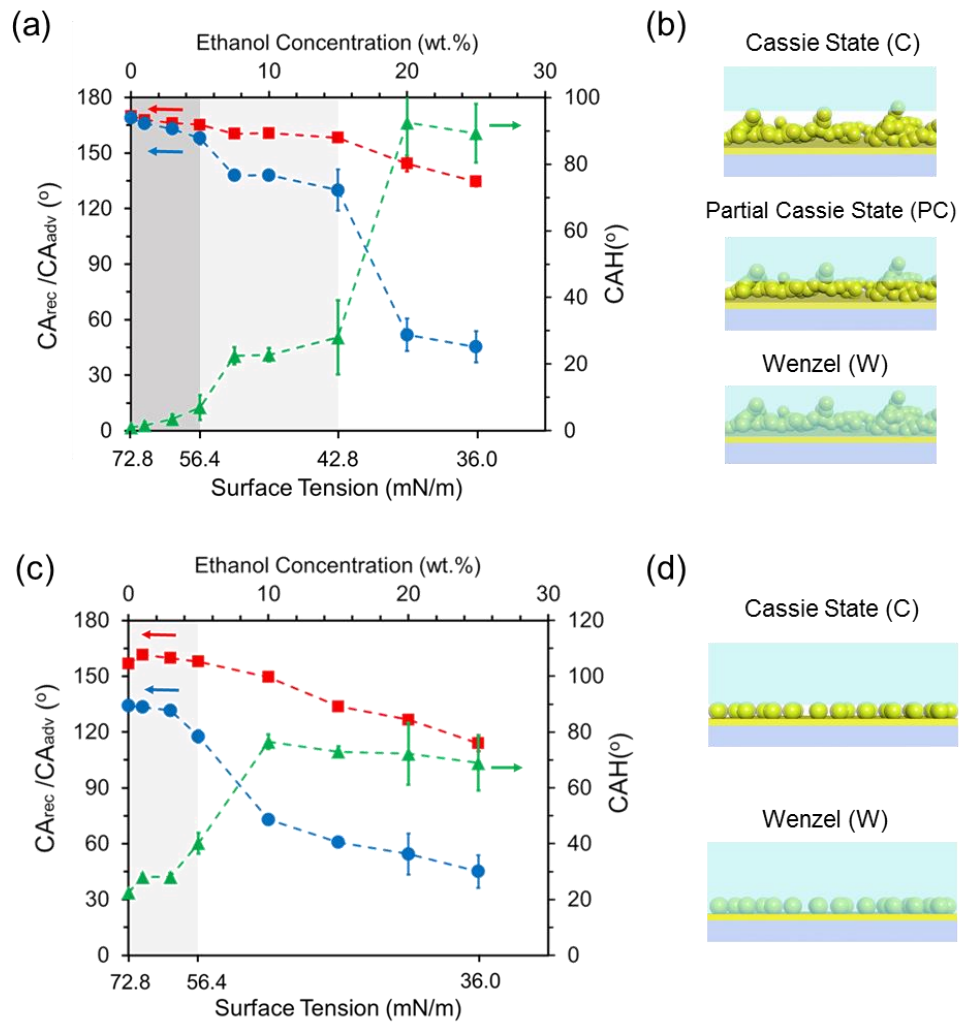
Figure 8.3 (a) The CA_{adv}, CA_{rec}, and CAH of the mixed ethanol/water on the coating surface prepared from L-CNPs as function of ethanol concentration and the corresponding liquid surface tension. Three different wetting states are evident from the sharp wetting transitions at 5 wt. % and 15 wt. % and are denoted as the full Cassie-Baxter, partial Cassie-Baxter, and Wenzel regimes. (b) schematic illustration of the proposed wetting mechanisms on L-CNP coated surface. (c) The CA_{adv}, CA_{rec}, and CAH of the deposited drop on the coating surface prepared from SPs as function of ethanol concentration and the corresponding liquid surface tension. Here, only a single wetting transitions was observed at ~5 wt. % ethanol concentration. (d) Schematic illustration of the proposed wetting mechanism on SP coated surface.

8.2.4 Wetting Behaviors Against Water Condensation

Another challenge to maintain SH is attributed to the small water droplets. Cassie-Baxter SH observed on the lotus leaf comes from raindrops (from a few hundred μm to a few mm) impacting the leaf surface; raindrops are much larger than the typical length scales of the surface patterns. The water droplet size condensed from the atmosphere, however, is much smaller (~ 1 to 40 μm). Therefore, they can be readily formed within the grooves of the rough surface, resulting in the loss of the SH.[4] On the other hand, maintaining SH on surface during water condensation is of great interests to water harvesting,[27] heat transfer,[28-30] and dehumidification.[31]

Here, we performed condensation experiments on L-CNP coated surface discovered in chapter 7 within an enclosed chamber to investigate its water repellency under condensation conditions. In experiments, the temperature and humidity of the chamber, measured by a thermo-hygrometer mounted inside the chamber, was maintained at $\sim 22\,°C \pm 1$ and $\sim 70 \pm 1\%$, respectively. The temperature of the substrates was kept at $\sim 7 \pm 1\,°C$, as measured by a thermocouple attached to the cooling module. The critical drop size before the water drop roll-off from the surface was used to evaluate the water repellency during condensation. Compared to a flat substrate treated with perfluorosilane ($CA_{adv} = 113 \pm 1°$, and $CA_{rec} = 98 \pm 2°$), the condensed water drops on L-CNP coated surface could be easily swept away by the gravitational force during the entire condensation process up to 6 h [see Fig. 8.4 (b)]: on L-CNP coated surface the water drops were removed at an average radius, $R_S = 0.3 \pm 0.05$ mm, compared to that on the flat surface of $R_S = 1.6 \pm 0.1$ mm. The mobility of water droplets is determined by the competition between the retention force, F_r, due to the wetting hysteresis on the coating surface and the gravitational force, F_g, of the water drop. The gravitational force for a water droplet on a vertical surface is given by $F_g = \rho g V$, where

V is the drop volume, ρ is the density of water, g is the gravitational acceleration. The smaller size of the water drop departing from the coating surface indicates a smaller F_g is required to overcome the F_r from the L-CNP coating surface. It is clear that L-CNPs surface is much more mobile compared to a flat hydrophobic surface. Quantitatively, the retention force due to CAH that resists mobility of water is given by[32]

$$F_r = 2r_c\sigma(\cos\theta_{rec} - \cos\theta_{adv}) \quad (8.4)$$

where γ is the surface tension of water, r_c is the radius of contact line (considered as circular), θ_{adv} and θ_{rec} are the CA_{adv} and CA_{rec} respectively on the surface. Then, assuming the water drop has an approximate shape of spherical cap with contact equal to $\theta = \frac{\theta_{adv} + \theta_{rec}}{2}$ (that is often found true on hydrophobic low contact angle hysteresis surface), the gravitational force on the drop can be expressed as following:[33]

$$F_g = \frac{\pi}{3}R_S^3(2 + \cos\theta)(1 - \cos\theta)^2 \quad (8.5)$$

Thus, R_S, which is the critical radius of water drop removed by gravidty can be estimated based on the measured θ_{adv} and θ_{rec} by balancing the F_r and F_g:[7]

$$R_S = \left(\frac{6\sigma \sin\theta(\cos\theta_{rec} - \cos\theta_{adv})}{\pi\rho g(2 + \cos\theta)(1 - \cos\theta)^2}\right)^{\frac{1}{2}} \quad (8.6)$$

R_S from experimental measurements were compared to the predicted values using Eq. (8.6). As seen in Fig. 8.4 (c), on a flat hydrophobic surface the experimentally obtained R_S is in good agreement with the predicted critical size range . For L-CNP coatings, the observed R_s can only be reached when the SH surface has high CA and low CAH, e.g. at $\theta_{adv} = 165^o$, $\theta_{rec} = 160^o$, which gives a predicted R_s of 0.3 mm. Therefore, our coating

178

surfaces can maintain very high water repellency/mobility even with respect to vapor phase condensation. the observed R_s, however, is bigger than the values predicted by using the θ_{adv} and θ_{rec} measured from sessile drop method (i.e. $\theta_{adv} = 170^o$, $\theta_{rec} = 169^o$, and $R_s = 0.05$ mm), suggesting the mobility of water droplets did decrease. Meanwhile, any small change of the external condition such as humidity, and temperature could affect the measured water contact angles and condensed water droplet size. We note that the small R_s was maintained after up to 6 h of continuous condensation, and thus our coating is highly robust against long-term exposure to saturated humidity environments [Fig. 8.4 (c)].
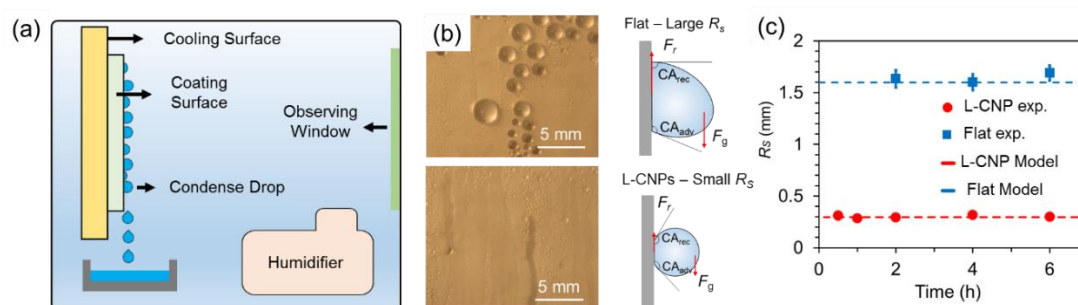
Figure 8.4 (a) Schematics of the water condensation testing chamber. (b) Optical images for water condensed on the L-CNP coating surface and flat perfluorosilane coated substrate at different time, maintaining significantly small drop size on the coating surface. (c) The experimentally measured R_s of water drop rolling-off from the surface vs. the value R_s through balancing the F_r and F_g, using $CA_{adv} = 113 \pm 1^o$, and $CA_{rec} = 98 \pm 2^o$ on a flat perfluorosilane treated surface and L-CNP coating, $CA_{adv} = 165^o$, $CA_{adv} = 160^o$.

During the condensation, we also observed other mechanism of liquid departure from the coating surface, e.g. jumping water drops due to coalesce from condensed micro-

drops, which is also an indication of maintained high water repellency upon water condensation.(citation) To investigate the detailed mechanism of how L-CNP coating can repel condensing liquid, we directly observed nucleation and condensation phenomena under environmental SEM (ESEM). Condensing SH has been reported on nanotextured SH surfaces, including nanowire/nanotube arrays, nanopillar arrays, etched copper oxide surface[16, 30, 34]). In our experiments, we observed that on L-CNP coating surface the water drops initially nucleated within the surface roughness had a relatively low CA; yet, the surface roughness could confine the propagation of the contact line during the growth of the micro-droplets [Fig. 8.5 (a)]. Thus, these micro-drops can reach CA >165° when the radius was greater than 3 μm. As the condensation proceeds, the coalesced the micro-drops released themselves from the initially pinned areas by formation of a new larger drop [Fig. 8.5 (b)] which explains the maintained high mobility of these water drops on the L-CNP coated surface.
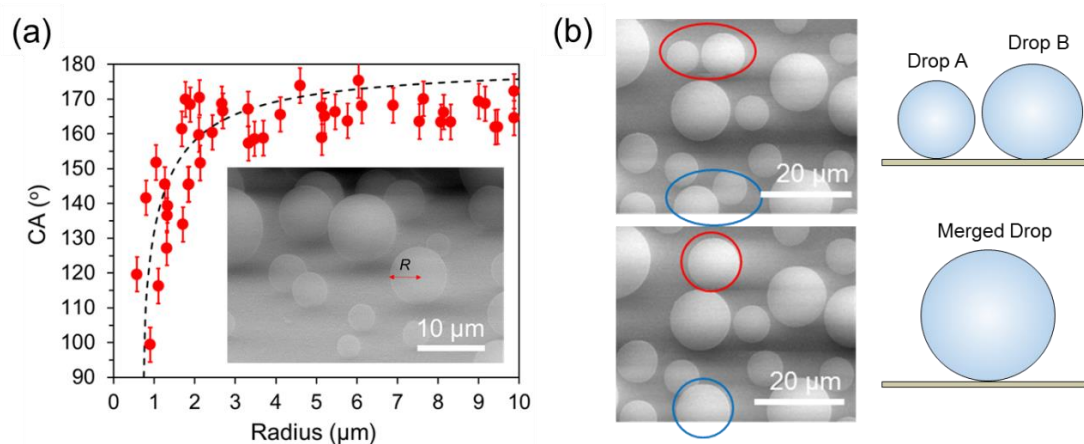
Figure 8.5. Water condensation on L-CNP coating observed in ESEM. (a) Water contact angle vs. the radius of the condensing water droplets. Inset: SEM images of the condensing water droplets. (b) SEM images of coalescence of micro-drops on the coating surface (Left). Right: schematic illustration of water coalescence as seen in Left. The circles show the water drops before and after merging.

8.3 Conclusion

By creating a coating from charge induced deposition of L-CNP particles, we demonstrated generation of optimized water repellency on the coating surfaces. Through investigating SH properties in both dynamic and static conditions, we confirmed that even at constraint of extreme low coating thickness, by using L-CNP with highly wiggly morphology, it is possible to achieve extreme water repellency (CA ~ 170°, and CAH < 1°). More importantly, the coating resist significantly lower surface tension liquids compared to pure water (up to 15 wt.% ethanol water mixture with surface tension ~42.8 mN/m). The Cassie-Baxter state on the nanoparticle coating is also extremely stable against high speed water drop impingement (speed up to 8 m/s), which is attributed to its unique two-tier morphology. Further, we observed that the water repellency was maintained under condensation, where the coating surface can repel nucleated water microdroplets.

8.4 Reference

1. Bartolo, D., et al., *Bouncing or sticky droplets: Impalement transitions on superhydrophobic micropatterned surfaces.* EPL (Europhysics Letters), 2006. **74**(2): p. 299.

2. Lafuma, A. and D. Quere, *Superhydrophobic states.* Nat Mater, 2003. **2**(7): p. 457-460.

3. Enright, R., et al., *Condensation on Superhydrophobic Surfaces: The Role of Local Energy Barriers and Structure Length Scale.* Langmuir, 2012. **28**(40): p. 14424-14432.

4. Cheng, Y.-T. and D.E. Rodak, *Is the lotus leaf superhydrophobic?* Applied Physics Letters, 2005. **86**(14): p. -.

5. McCarthy, M., et al., *Biotemplated hierarchical surfaces and the role of dual length scales on the repellency of impacting droplets.* Applied Physics Letters, 2012. **100**(26): p. -.

6. Xu, L., et al., *Transparent, Superhydrophobic Surfaces from One-Step Spin Coating of Hydrophobic Nanoparticles.* ACS Applied Materials & Interfaces, 2012. **4**(2): p. 1118-1125.

7. Kim, S. and K.J. Kim, *Dropwise Condensation Modeling Suitable for Superhydrophobic Surfaces.* Journal of Heat Transfer, 2011. **133**(8): p. 081502-081502.

8. Miljkovic, N., R. Enright, and E.N. Wang, *Effect of Droplet Morphology on Growth Dynamics and Heat Transfer during Condensation on Superhydrophobic Nanostructured Surfaces.* ACS Nano, 2012. **6**(2): p. 1776-1785.

9.   Hwang, H.S., et al., *Facile Fabrication of Transparent Superhydrophobic Surfaces by Spray Deposition.* ACS Applied Materials & Interfaces, 2011. **3**(7): p. 2179-2183.

10.   Park, K.-C., et al., *Nanotextured Silica Surfaces with Robust Superhydrophobicity and Omnidirectional Broadband Supertransmissivity.* ACS Nano, 2012. **6**(5): p. 3789-3799.

11.   Ellinas, K., et al., *Superamphiphobic Polymeric Surfaces Sustaining Ultrahigh Impact Pressures of Aqueous High- and Low-Surface-Tension Mixtures, Tested with Laser-Induced Forward Transfer of Drops.* Advanced Materials, 2015. **27**(13): p. 2231-2235.

12.   Tuteja, A., et al., *Robust omniphobic surfaces.* Proceedings of the National Academy of Sciences, 2008.

13.   Shieh, J., et al., *Robust Airlike Superhydrophobic Surfaces.* Advanced Materials, 2010. **22**(5): p. 597-601.

14.   Martines, E., et al., *Superhydrophobicity and Superhydrophilicity of Regular Nanopatterns.* Nano Letters, 2005. **5**(10): p. 2097-2103.

15.   Wang, J., et al., *Preparation of Anisotropic Silica Nanoparticles via Controlled Assembly of Presynthesized Spherical Seeds.* Langmuir, 2010. **26**(23): p. 18491-18498.

16.   Rykaczewski, K., *Microdroplet Growth Mechanism during Water Condensation on Superhydrophobic Surfaces.* Langmuir, 2012. **28**(20): p. 7720-7729.

17.   Reyssat, M., et al., *Bouncing transitions on microtextured materials.* Europhys. Lett., 2006. **74**(2): p. 306-312.

18.   Checco, A., A. Rahman, and C.T. Black, *Robust Superhydrophobicity in Large-*

Area *Nanostructured Surfaces Defined by Block-Copolymer Self Assembly.* Advanced Materials, 2014. **26**(6): p. 886-891.

19.   Deng, T., et al., *Nonwetting of impinging droplets on textured surfaces.* Applied Physics Letters, 2009. **94**(13): p. -.

20.   Amrei, M.M. and H.V. Tafreshi, *Effects of Hydrostatic Pressure on Wetted Area of Submerged Superhydrophobic Granular Coatings.* Colloids and Surfaces A: Physicochemical and Engineering Aspects, (0).

21.   van Boxel, J.H. *Numerical model for the fall speed of rain drops in a rain fall simulator.* in *Workshop on wind and water erosion.* 1997.

22.   Tuvshindorj, U., et al., *Robust Cassie State of Wetting in Transparent Superhydrophobic Coatings.* ACS Applied Materials & Interfaces, 2014. **6**(12): p. 9680-9688.

23.   Reyssat, M., J.M. Yeomans, and D. Quéré, *Impalement of fakir drops.* EPL (Europhysics Letters), 2008. **81**(2): p. 26006.

24.   Chen, X., et al., *Evaporation of Droplets on Superhydrophobic Surfaces: Surface Roughness and Small Droplet Size Effects.* Physical Review Letters, 2012. **109**(11): p. 116101.

25.   Cha, T.-G., et al., *Nanoscale Patterning of Microtextured Surfaces to Control Superhydrophobic Robustness.* Langmuir, 2010. **26**(11): p. 8319-8326.

26.   Boreyko, J.B., et al., *Wetting and Dewetting Transitions on Hierarchical Superhydrophobic Surfaces.* Langmuir, 2011. **27**(12): p. 7502-7509.

27.   Feng, J., et al., *Why Condensate Drops Can Spontaneously Move Away on Some Superhydrophobic Surfaces but Not on Others.* ACS Applied Materials & Interfaces, 2012. **4**(12): p. 6618-6625.

28.   Hou, Y., et al., *Recurrent Filmwise and Dropwise Condensation on a Beetle Mimetic Surface.* ACS Nano, 2014. **9**(1): p. 71-81.

29.   Miljkovic, N., et al., *Electric-Field-Enhanced Condensation on Superhydrophobic Nanostructured Surfaces.* ACS Nano, 2013. **7**(12): p. 11043-11054.

30.   Enright, R., et al., *Condensation on Superhydrophobic Copper Oxide Nanostructures.* Journal of Heat Transfer, 2013. **135**(9): p. 091304-091304.

31.   Parker, A.R. and C.R. Lawrence, *Water capture by a desert beetle.* Nature, 2001. **414**(6859): p. 33-34.

32.   Kim, H.-Y., H.J. Lee, and B.H. Kang, *Sliding of Liquid Drops Down an Inclined Solid Surface.* Journal of Colloid and Interface Science, 2002. **247**(2): p. 372-380.

33.   Quéré, D., M.-J. Azzopardi, and L. Delattre, *Drops at Rest on a Tilted Plane.* Langmuir, 1998. **14**(8): p. 2213-2216.

34.   Rykaczewski, K., et al., *How nanorough is rough enough to make a surface superhydrophobic during water condensation?* Soft Matter, 2012. **8**(33): p. 8786-8794.

Chapter 9: Confined Assemblies of Colloidal Particles with Soft, Repulsive Interactions

Adapted from manuscript **G. Wu**, H. Cho, D. A. Wood and A. D. Dinsmore, S. Yang,

"Confined Assemblies of Colloidal Particles with Soft, Repulsive Interactions"

9.0 Introduction

Spherical colloidal particles with isotropic interactions pack into phases with high coordination numbers, including face entered cubic (fcc) and body centered cubic (bcc) structures, to maximize the entropy.[1] Under physical confinement, however, interfacial forces, structural frustration, and symmetry breaking can play more dominant roles in determining the organization of colloidal particles in a template. As a model system, colloidal assemblies in cylindrical confinement have drawn considerable interests in the soft matter community. Based on the hard sphere packing model in cylindrical channels, researchers have shown both experimentally[2-15] and theoretically.[16-21] that the colloidal particles can pack into a wide variety of morphologies (*e.g.* zigzag, helical, zipper-like wire structures) and chirality depending on the ratio of pore diameter vs. particle diameter,[17, 18] the competing interactions, and boundary effects.[12] The spontaneous formation of spirals or so-called phyllotaxis indeed is commonly seen in biological systems[16], including plants (*e.g.* sunflower seeds and leaves, and pine cones),[22] DNA and protein assemblies,[23] collagen fibrils,[19] microfilaments of actin, and molecular microtubules.[24] It has been hypothesized that the phyllotacy allows sunflower seeds and leaves to avoid self-shading problem for more efficient sunlight harvesting. Confinement of water molecules in non-polar pores, *e.g.* carbon nanotube (CNTs), offers significant insights of biological functions such as gating and proton flow.[25] Study of packing and

orientation of molecules such as fullerene C_{60} in CNTs sheds light on molecular forces and molecular motions in nano-confinement.[26]

Nevertheless, the short-range hard sphere models commonly used in literature cannot capture some of the more complex structures in molecular assemblies and biological systems, where long-range repulsion, or soft interactions, are more common. The ability to control the soft interactions will in turn allow us to explore a diverse range of phase behaviors and manipulating them using a small external perturbation. However, direct and *in situ* observation, and thus interpretation, of the phases of living systems at atomic and molecular levels is challenging. Therefore, assemblies of soft colloids at the (sub)micron scale will offer an ideal analogy to reveal the inter-atomic and intermolecular interactions.

Here, we prepare soft colloids from charged silica nanoparticles (NPs, ~500 nm in diameter) dispersed in photocrosslinkable monomers of similar refractive index, and study the the colloidal packing morphologies in microchannels as a result of soft interactions with fixed dimension (diameter, 1.8 μm, and height, 8 μm). Our system can be crosslinked to lock the assembled colloids within the resulting micropillars for latter direct imaging by techniques such as scanning electron microscopy (SEM) with nanometer resolution, which is unmatched by conventional optical microscopy techniques that are commonly used to observe colloidal suspensions. We also directly image the assemblies in the third dimension using focused ion beam (FIB) to cut the samples in different directions for SEM imaging. In bulk, due to electrostatic double layer forces, the NPs form a random hexagonal close-packed (*rhcp*) structure at as low as 7.5 vol% of colloids in monomers. The varied concentration of particles in the bulk does not vary packing symmetry, yet the lattice constant decreases for packing more particles. As opposed to bulk phase assembly, a rich variety of assembly morphologies

are observed in microchannels when varying the particle volume fraction in monomers from 15 to 40 vol%, which are in good agreement with molecular dynamics simulation results accounting for the electrostatic interactions. Unlike the hard sphere model systems where the confined structures are determined by the diameter ratio of microchannels to colloidal particles, we find that local concentration of the colloidal particles within the cylindrical confinement play a critical role to the evolution of the assembled structures.

9.1 Experiments

Silica NP/EPTPA Suspensions. Monodispersed silica NP powder (500 nm in diameter，with real size 495 ± 20 nm determined by SEM) were purchased from Alfa Aesar. To enhance the electrostatic repulsion between the particles, we activated the surface silanol groups, render NP surface weakly charged negatively, by hydrolyzing the particle surface in 0.1 M HCl overnight, followed by centrifugation twice in water and re-dispersing the particles in ethanol (Thermo Fisher Scientific Inc.). The silica NPs were ready for use after evaporating ethanol in an oven at 65 $^{\circ}$C overnight.

Monomer, trimethylolpropane ethoxylate triacrylate (ETPTA, Aldrich) was washed with deionized (DI) water repeatedly to remove ionic species until the conductivity became less than 1 μS/cm (measured by Oakton ECTestr 11 dual-range, pin-style pocket conductivity tester). To disperse silica particles in ETPTA, the pelletized silica powder was added into ETPTA, followed by agitation using ultra-sonication until a homogeneous suspension was obtained. Then, 3 v/w% of photoinitiator, Darocur 1173 (Aldrich), was added to the suspension. The volume fraction of the suspension is defined as $f = \frac{V_{silica}}{V_{silica} + V_{ETPTA}}$, where V_{silica} is the volume

of the silica particles (= mass x density, 2.04 g/cm^3[27]), and V_{ETPTA} is the volume of the monomers.

Assembly of Silica NPs. Before infiltration into the porous membrane, the silica NP/ETPTA suspension was agitated with vortex and sonication 15 min. Poly(dimethylsiloxane) (PDMS) microporous membrane was replicated from the silicon master with a square array of micropillars (diameter of 1.8 μm and height of 8 μm). 10 μL of silica NP suspension was dropped on top of the PDMS membrane to infiltrate the suspension via capillary force. After 1 min, the excessive amount of suspension remained on PDMS membrane was removed using a razor blade. The suspension in PDMS membrane was cured at 365 nm at a dosage of 2 J/cm^2 (UV light source from Newport Inc.) in a nitrogen chamber. To extract the cured suspension from the PDMS membrane, additional 20 μL of ETPTA with 3 v/w% of Darocur 1173 was cast on top of the PDMS, which was then covered with a clean glass slide and cured at 365 nm at a dosage of 2 J/cm^2. After peeling off the PDMS mold, we obtained the micropillar arrays of assembled nanoparticles embedded within the ETPTA matrix. To reveal the silica NP assembly morphology within the cylindrical confinement, the micropillars were subjected to oxygen plasma (Gatan Plasma System) at a power of 30 W for 12-20 min, giving an etching rate of ~25 nm/min for the crosslinked ETPTA.

Characterization of the Bulk Silica Particle Suspensions. To observe the assembly of the silica particle suspension in bulk, the suspension was first infiltrated into a rectangular glass capillary with cross-section dimension of 0.1 mm x 2 mm. The suspension was UV cured at a dosage of 2 J/cm^2, and the cured composite was taken out by breaking the glass capillary. Oxygen plasma etching of 2 min was applied to have a clear view of colloidal particle assembly along to the capillary wall. To image

the cross-section, the sample was immersed in liquid nitrogen and fractured for observation in SEM.

Characterization of the Assembled Particles in Micropillars. The micro-pillars packed with silica particles were cut off from the substrate using a razor blade for observation under SEM (FIB Strata, voltage of 5kV). To confirm the packing within each micropillar, we tilted the sample stage to have a side view. For internal structure of the packed particles, the micro-pillars were cut into half by focused ion beam (FIB) at 30 kV acceleration voltage and a current of 400 pA.

9.2 Results and Discussion

9.2.1 Observation and Characterization of the Suspension

Long-range interactions between colloidal particles can be realized through their electrostatic repulsion. Derjaguin-Landau-Verwey-Overbeek (DLVO) theory describes the contribution of electrical double layer repulsion and van der Waals (vdW) attraction to stabilize the charged particles dispersion.[28] The decay of the potential in the electrical double layer is governed by the Debye screening length (k^{-1}), which is dependent on ionic concentration c and dielectric constant of the dispersion, ε. For monovalent salt such as NaCl in electrolyte,

$$k^{-1} = \left(\frac{2e^2c}{\varepsilon\varepsilon_0 k_B T}\right)^{1/2} \qquad (9.1)$$

Where e is the charge of the electron and ε_0 is the permittivity of vacuum. Therefore, to create a system with long-range electrostatic repulsion, first, vdW attraction should be minimized by matching the refractive indices of suspension medium and dispersed particles in visible wavelength.[28, 29] Second, the concentration of electrolyte in dispersion should be very low such that k^{-1} can reach the same order of magnitude of

190

the size of colloidal particles.[30] Additionally, to direct image the assembled structures, it will be desirable to lock the structures in the dispersion without altering them. Here, we dispersed silica NPs in trifunctional monomers (ETPTA), which can be photocrosslinked almost instantaneously after UV exposure to lock the assembled particle structure.[31, 32] Meanwhile, in visible wavelength ETPTA has a refractive index ($n = 1.47$) comparable to silica ($n = 1.45$), thus, effectively reducing vdW attraction between the particles. Here, interparticle interactions is dominated by electrostatic repulsion from partially dissociated silanol groups on the particle surfaces.[33, 34] After repetitively washing the monomers with DI water, k^{-1} in our system could be ~ 100 nm, allowing for study of packing of soft colloids within the cylindrical micro-confinement.

DLVO theory combines van der Waals (vdW) attraction and electric double layer force. For charged particles, the double layer force is important to determine the separation distance or the Debye screening length (k^{-1}) between particles. The surface conductivity of the dispersion, σ, can be estimated as[32, 35]

$$\sigma = c\mathring{A}_0 \qquad (9.2)$$

Where c is the ionic concentration and $\mathring{A}_0$ is the limiting molar conductance. The limiting molar conductance for ETPTA can be calculated using Walden's rule[28, 35]

$$\mathring{A}_0^{water}\eta^{Water} = \mathring{A}_0^{ETPTA}\eta^{ETPTA} \qquad (9.3)$$

Where η^{Water} and η^{ETPTA} are the viscosity of water (0.0091 Pa·s) and ETPTA monomers (0.07 Pa·s) at 25 °C, respectively. With $\mathring{A}_0^{Water}$ approximated from monovalent salt (*e.g.* Na$^+$) as 50 cm^2·S/mol, $\mathring{A}_0^{ETPTA}$ = 0.71 cm^2·S/mol. Taking conductivity of ETPTA as 0.5 μS/cm, the ionic concertation c can be calculated,

assuming monovalent salt is present within the ETPTA monomers.[32, 35] Accordingly, the Debye screening length, k^{-1}, can be calculated as

$$k^{-1} = \left(\frac{2e^2c}{\varepsilon\varepsilon_0 k_B T}\right)^{1/2} \tag{9.4}$$

Where e is the charge of the electron, 1.602×10^{-19} C, ε is the dielectric constant of the dispersion, and ε_0 is the permittivity of vacuum, 8.854×10^{-12} C^2/N·m^2. Here, the dielectric constant of ETPTA, $\varepsilon_{ETPTA} \sim 3$. k^{-1} is estimated as ~ 100 nm, in agreement with the experimental observation (Fig. 9.1). Again, we assume the charged species are monovalent sodium-ion-like species. Previously, such approximation has been shown close to represent the true Debye screened length and thus has been widely used in literature.[1, 10, 29, 35, 36]

The morphology of silica NPs in bulk were obtained from NP/ ETPTA suspensions in a rectangular glass capillary (2 mm x 0.1 mm). As seen in Fig. 9.1 (a-c), at 7.5 vol % loading of silica NPs, *rhcp* structures were observed in bulk, where NPs were hexagonally packed in the x-y plane with variation of lattice constants, but randomly layered in the z direction. Despite different volume fractions up to 40 vol. %, the assembly symmetry remained as *rhcp* in bulk. In Fig. 9.1 d, we plotted the relationship of inter-particle distance (*D*) and inter-layer spacing (*h*) (see definition in Fig. 9.1 c) vs. volume fraction (*f*). The *D* and *h* predicted from *rhcp* structures are in good agreement with experimental measurement. The phase transition from amorphous to ordered structures occurred between 5 vol % (see Fig. 9.2) and 7.5 vol %, significantly smaller than ~40-44 vol % typical in the case of hard sphere packing.[12, 37]
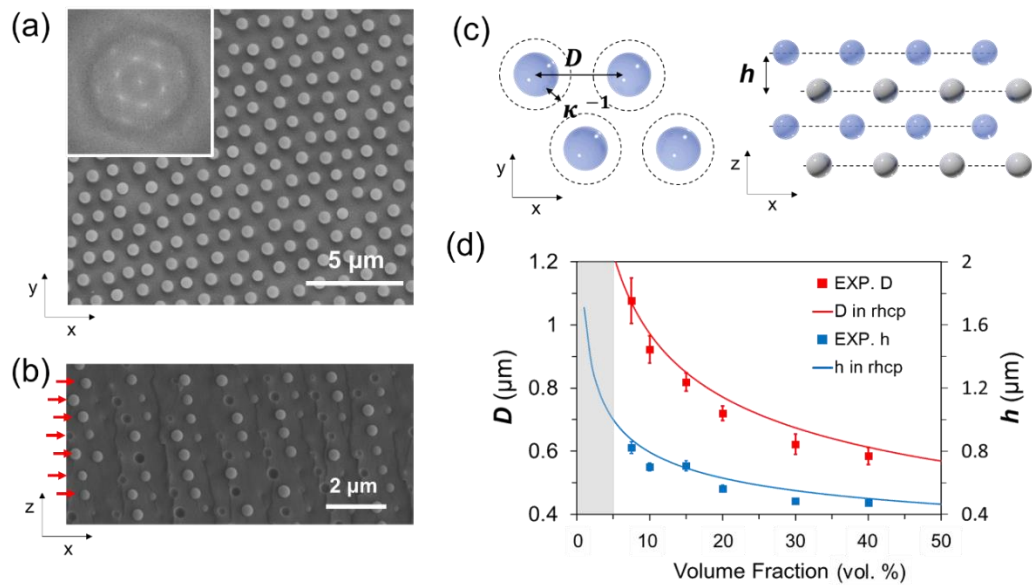
Figure 9.1 (a-b) Top-view (a) and cross-sectional view (b) SEM images of the crosslinked colloidal suspension (7.5 vol %) in bulk, showing random hexagonal close-packing (rhcp) of silica NPs. Inset in (a) is the Fourier transform of image (a), confirming hexagonal packing in the x-y plane. (c) Schematics showing the packing of the colloidal particles in the monomer suspension before UV curing. D is the inter-particle distance in the x-y plane, h is inter-plane distance. (d) Relationship of D and h vs. the bulk volume fraction of NPs. The lines indicate the ideal relationship from rhcp. The shaded region is the amorphous phase.
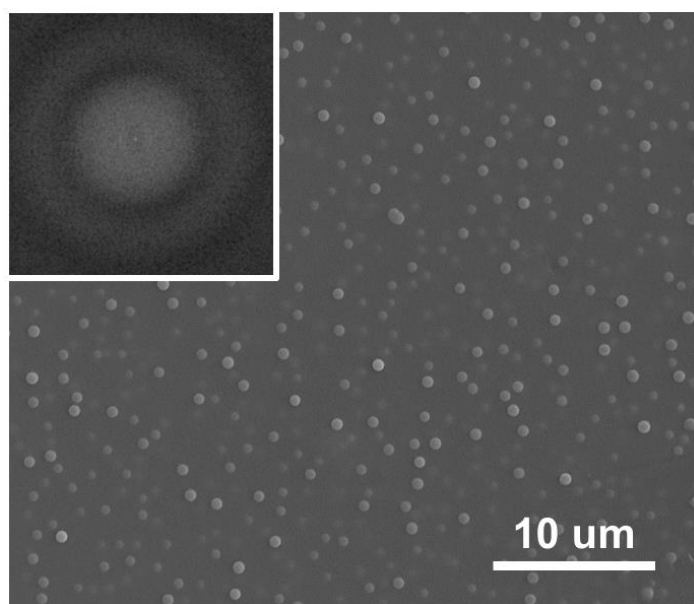
Figure 9.2 SEM image of the colloidal assembly at 5 vol % in ETPTA in amorphous phase. Inset: Fourier transform of the 2D SEM image.

9.2.2 Observation of Structures Under Confinements

The mixture was infiltrated into the PDMS porous membrane, followed by UV curing (see Fig. 9.3 a-b). To reveal the particle assembly structures within the micropillars, the polymers near surface were removed by oxygen plasma (see Fig. 9.3 c). Compared to the bulk structure, packing of soft colloids within the cylindrical confinement could be influenced by multiple factors, including inter-particle electrostatic repulsion, the boundary condition at the PDMS wall of the micro-channels, and the air/suspension interface. To demonstrate the effect of soft interactions between particles to the packing behaviors, here, we fixed the dimensions of the particle and cylindrical confinement as 495 ± 20 nm (NP diameter), 1.8 μm (cylindrical pore diameter), and 8 μm (cylindrical pore height), respectively. The only variable is the bulk volume fraction of silica NPs in ETPTA , $f = 15$ to 40 vol % with an increment of 5 vol % to investigate how particles are accommodated as the number of particles

194

entrapped in the confinement varies. Since NP/EPTPA pillars are crosslinked, we can directly image them in SEM. To better view the assembly structures along the pillar height, we cut the pillars off the substrate for examination at different tilting angles. It can be seen that the silica NPs are uniformly dispersed throughout the entire pillar structures, suggesting that the cross-linking rate is fast enough to allow us capture the packing phase of NPs in ETPTA.

Figure 9.3 (a) Schematic illustrations of the assembly process and revealing of the assembled particles within the PDMS micropore array. (b) Magnified schematics and SEM images of the structures corresponding to the box shown in (a). Scale bar: 2 μm.

For hard sphere packing, the particles are jammed within the confinement; additional particles cannot be fitted into the confinement because there is no space to explore unless increasing the diameter of the cylinder. In our system, the packing morphology is strongly affected by both the bulk and local concentrations of the suspension. As more and more particles are forced to pack into the cylindrical confinement with fixed diameter and length, the inter-particle distance is reduced but

particles remained separated due to the soft long-range repulsion (see Fig. 9.1 d and Fig. 9.4). Unlike the bulk assembly symmetry, which remained as *rhcp* for colloidal particle volume fraction above 7.5 vol %, packing morphology evolved as the volume fraction of the bulk colloidal suspension increases, which should be attributed to packing confinement. In particular, the packing morphology of the silica particles is extremely sensitive to the local concentration, *i.e.* the number of particles trapped in each pillar (*N*). Even at the same bulk particle concentration, coexistence of multiple packing structures was often observed (see Fig. 9.5). We did not investigate NP concentration above 40 vol. % since the suspension is too viscous for capillary infiltration into the micro-pores, possibly due to particle jamming and significant shear thickening effects at high volume fraction.[38]
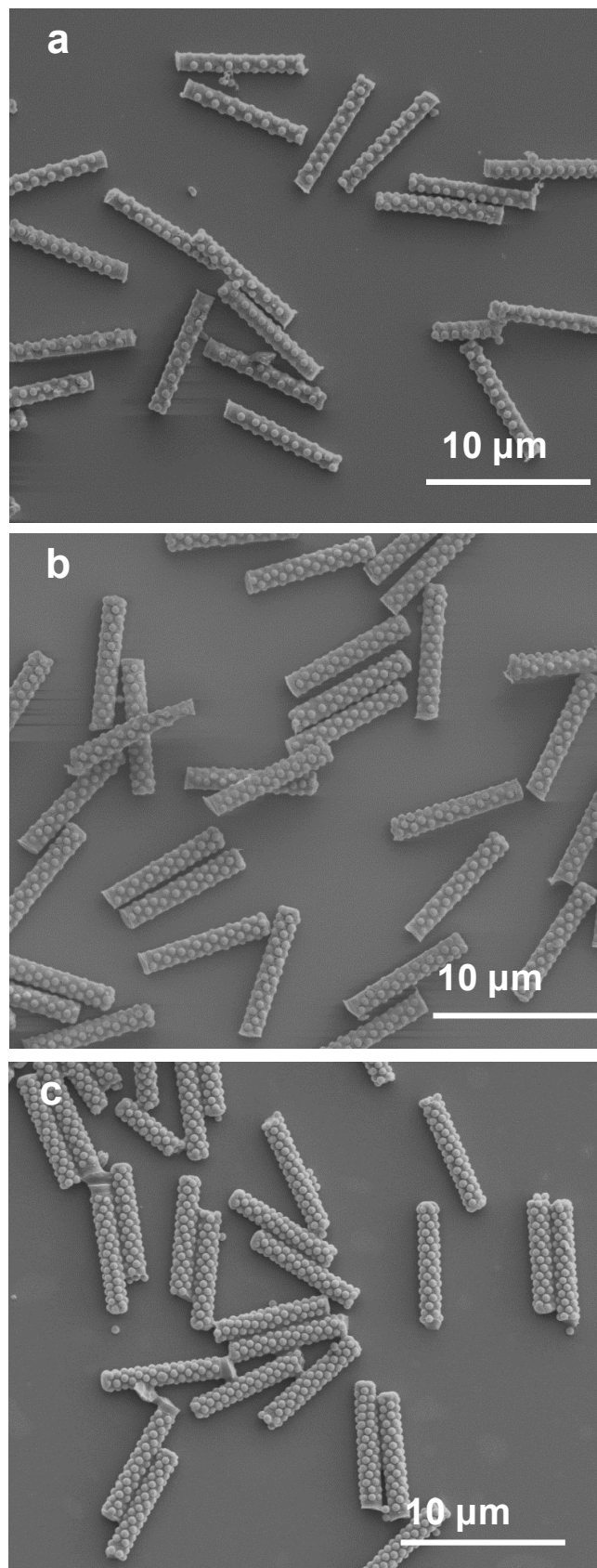
Figure 9.4 SEM images of assembled structures with increased bulk volume fraction of colloidal particle suspension at (a) 20 vol %, (b) 30 vol %, and (c) 40 vol %.
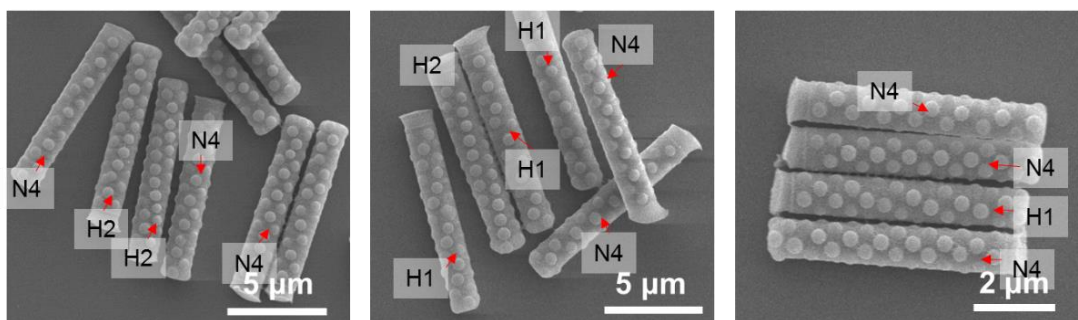
Figure 9.5 SEM images showing the coexistence of multiple phases at 25 vol % of bulk colloidal particle suspension.
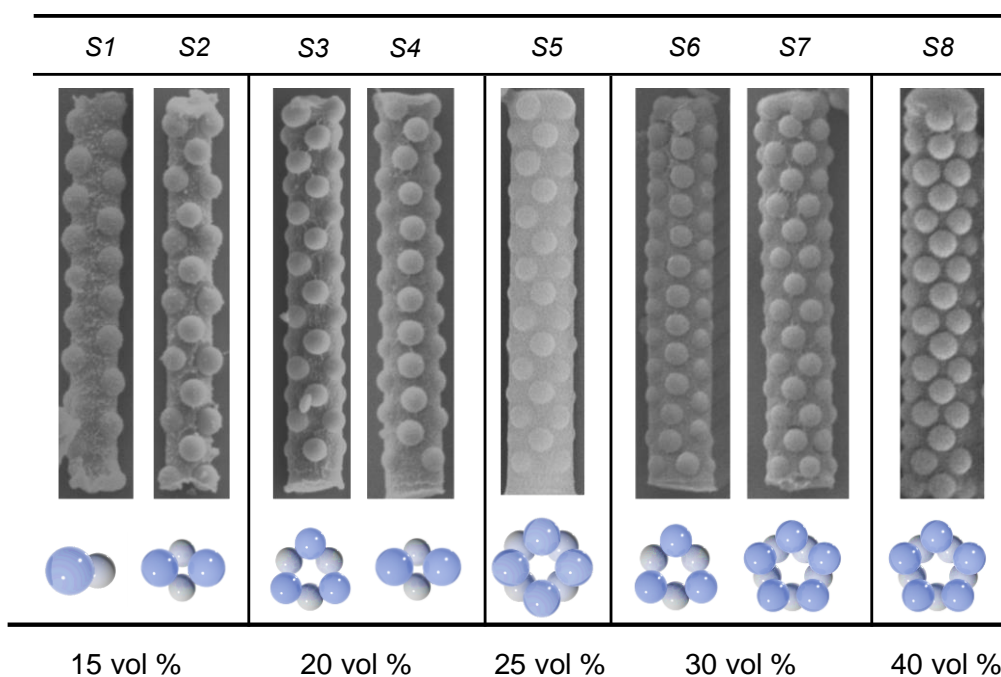
Figure 9.6 Summary of the observed dominant achiral packing phases in the micropore arrays as the bulk NP concentration increases from 15 to 40 vol%. The assembled structures are formed by staggered stacking of particle layers consisting of different number of particles. Top: SEM images. Bottom: Illustration of the morphology of two consecutive layers (represented in different colors) of particles at the outer surface of the micropillar. For phases S7 and S8, we also observed a 1-D inner column of particles.

In Fig. 9.6, we show the examples of packing structures formed by stacking layered particles in a consecutive manner. The schematics illustrate the NP assembly in each layer. As the bulk concentration is increased, the increased number of particles is accommodated by increasing either the number of layers or the number of particles per layer. For example, S2 and S4 phases have the same stacking morphology (*i.e.* staggered layers of two particles per layer), while more particles are accommodated in S4 (20 vol%) vs. S2 (15 vol%) with increased number of layers. Similar trends were observed for phases S6 (30 vol%) vs. S3 (20 vol%), and S8 (40 vol%) vs. S7 (30 vol%). As more particles are entrapped in the microporous channels, the number of particles per layer packed around the wall increased to from one in phase S1 to five for S7 and S8. The particles prefer to pack around the wall due to electrostatic repulsion from each other. However, as the packing density increases, particles move toward the center of the cylinder. As shown in Fig. 9.7, in the case of S7 phase (30 vol%), we observed packing of 5 and 6 particles per layer with the additional particle taking the center position of the pillar, leading to the formation of a one-dimensional (1D) column of silica NPs stacked in the center and a zigzag structure wrapping around the surface of the cylindrical confinement. In addition to achiral structures shown in Fig. 9.6, we also observed a variety of helices (both right and left handed) from colloidal packing in cylinders. While double and triple helices have been reported in literature from hard sphere models,[17, 19] here, we observed 3, 4, and 5 stranded helices of particles packed in each pillar (Fig. 9.8), reminding us the diverse nature of the assemblies by soft colloids.

5 particles/layer   Wrapped particle
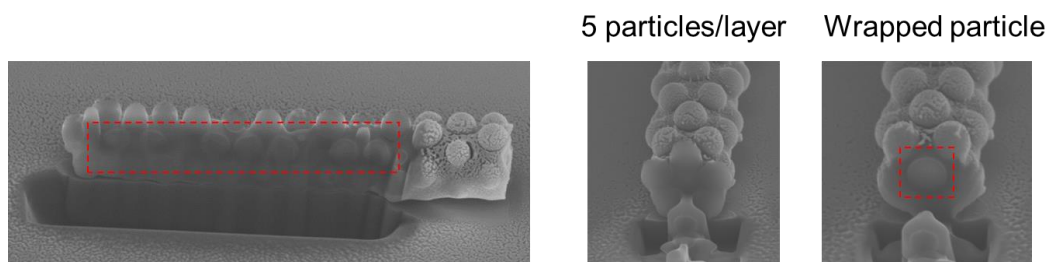
Figure 9.7 FIB cut SEM images of the colloidal assembly showing the internal structures of the packing phase S7 at 30 vol %. A 1D column of NPs packed in the center is indicated by the dashed rectangles.

H1	*H2*	*H3*
25 vol %		40 vol %
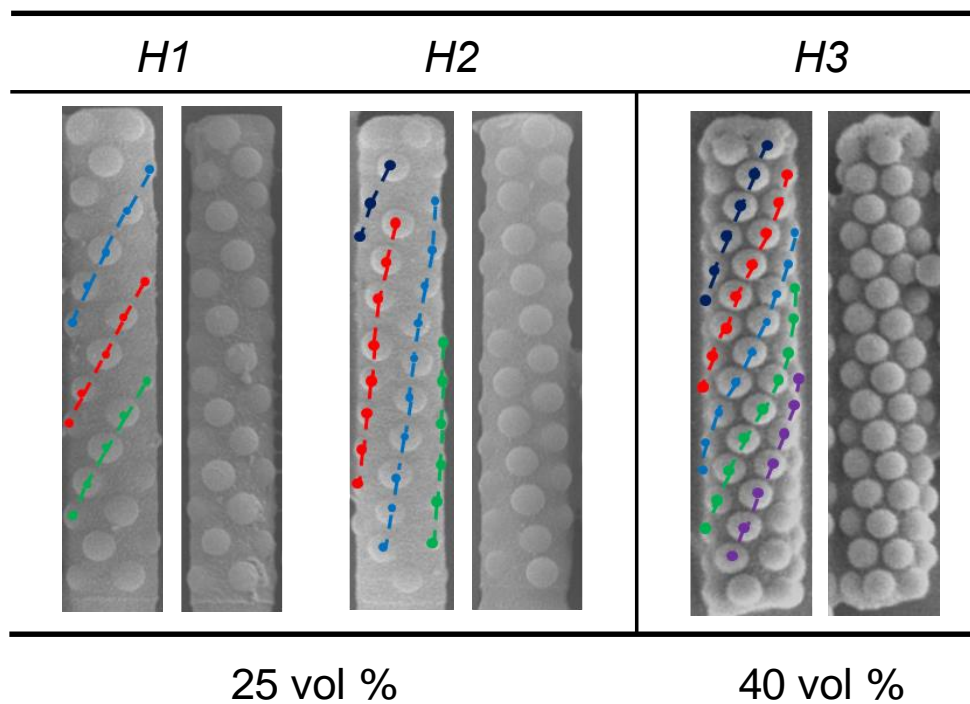
Figure 9.8 SEM images of different helical structures from NP assembly in the micropore arrays with multiple helical strands of particles labeled in different colored dots connected by dashed lines.

9.2.3 Comparison to Theoretical Modeling

Clearly, the strong electrostatic repulsion between silica particles is the main driving force to the particle assemblies since in all the observed phases there remains significant spacing between particles. To better understand the long-range electrostatic repulsion in our system, we compared the experimental observations with the theoretical predictions by Oğuz et al. [20] on helicity of charged particles assembled in a cylindrical tube with Yukawa pair-potential, a commonly used potential to describe the electrical double layer between colloids. In their studies, the assembled phases are predicted based on two dimensionless parameters, that is reduced line density $\eta = Na/L$, and reduced inverse screening length $\lambda = \kappa a$, where N is the number of particles confined in a cylinder of length L. Here, a is the radius of the cylinder with surface intercept the center of the packed spherical particles. Experimentally, a is measured from SEM images (see Table 9.1). L is 8 μm and N is the determined from number of particle per layer and total layer of particles entrapped in the pillar. Accordingly, we calculated these parameters (see Table 9.1) and compared our observation with those predicted by Oğuz et al.[20] We found great coincidence between the experiments with the phases (S1, S2, S3, and S4) with the prediction. In simulation, the particles are packed in N2 phase with zigzag stacking of one particle per layer at the lowest packing density. As the density of particles increases, the packing phase shift to staggered stacking of two particles per layer (referred as N4), then to three particles per layer (i.e. N6). It worth noting that simulation also predicts a re-entrant phase transition from N6 to N4 phase at increased packing density, leading to decreased number of particles per layer but increasing layer of particles. This was found consistent with transition observed from S3 to S4 in our experiments. Unfortunately, Oğuz et al. do not go further to predict the phases with higher packing density of particles as shown in our experiments.

To further confirm the role of long-range repulsion to the assembly behaviors in our system, we performed similar molecular dynamics (MD) simulation as Oğuz *et al*. but at higher packing densities using parameters directly obtained from the experiments. For the electrostatic repulsion between silica NPs, Yukawa potential was used with Debye screening length of 100 nm, where particles interacted with each other and the side walls of the channel via Yukawa potential, and were annealed at a temperature between 20 k_BT/ε to 0.002 k_BT/ε with ε as a parameter defined as the interaction strength between particles. The charge density ratio between the particles and the PDMS side wall was set to be 200, this number was finely tuned by imaging analysis comparing packing 1 µm particles within the same channel, where the packing structures are much simpler to analyze. For the top and bottom of the channel, the hard-wall interaction was used. By placing different numbers of colloidal particles into the cylindrical pore until reaching the steady state, we found the same packing phases as those observed experimentally, where the packing morphology was extremely sensitive to the local concentration of the particles (Fig. 9.9). Meanwhile, almost all of the phases observed experimentally can be reproduced in simulation with relatively simple Yukawa pair interaction potential. The detailed comparison is summarized in Table 9.2. Here, additional particles were found to be accommodated by forming denser zigzag layered structures wrapping around the wall while filling the internal space of the 1D channel. Two minor discrepancies are that in simulation there were slightly smaller number of particles within the cylinder compared to that observed experimentally at the same phase, and the simulation was not able to generate S6 phase. This is possibly attributed to that the boundary conditions on top and bottom of the cylindrical confinement in simulation are different from the real system. In experiments, the top was exposed to air and the bottom was PDMS. Further, the electrical double layer force in simulation was modeled as a simple pair-interaction potential between two particles and an

202

approximation of non-analytical function between particle and wall. Thus, it ignored multi-body interactions that could become significant when packing density became high and/or when the particle size was comparable with the confinement size. Previously, Bowen, *et al*.[39] have shown that within the cylindrical confinement, long-range electrostatic repulsion can be altered significantly and even become attractive with considering multi-body interactions. Nonetheless, the complexity and diversity of the current systems and consistency between experiments and theory based on the simple long-range Yukawa potential unequivocally confirms the role of long-range repulsive interactions within cylindrical confinement, which in turn lead to much richer and complex phases not seen in hard sphere systems.

Table 9.1 Comparison of experimentally observed phases with theoretical prediction by Oğuz et al.[20]

Vol %	Phase	a (nm)	N/L (μm^{-1})	λ	η	*Matching Phase from ref*[20]
15	S1	~300	~2	3	0.6	N2
	S2	~350	~3.7	3.5	1.3	N4
20	S3	~380	~5.2	3.8	2.0	N6
	S4	~400	~5	4	2.0	N4

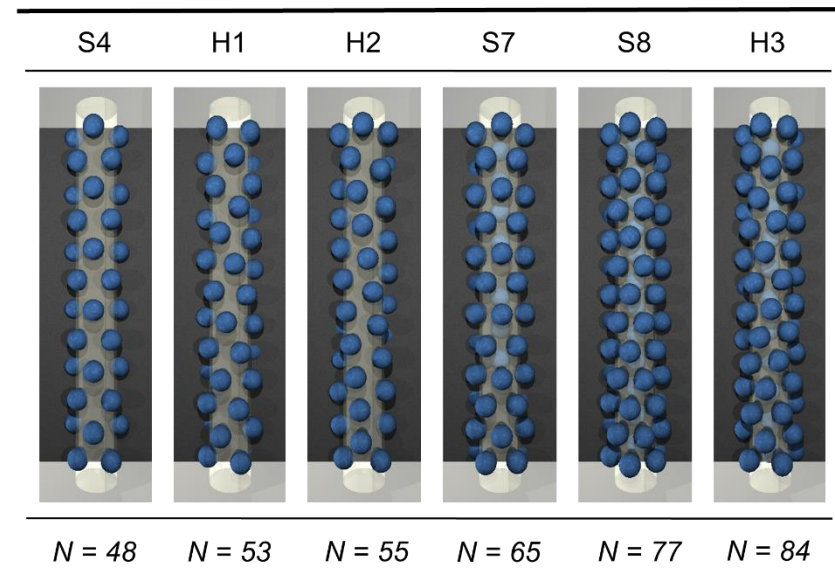| S4	H1	H2	S7	S8	H3
N = 48	*N = 53*	*N = 55*	*N = 65*	*N = 77*	*N = 84*

Figure 9.9 Simulated phases of the assembled colloids in micro-pore arrays in consistence with experiments. The phases observed from experiments (shown with symbols on top of the figure) are matched with simulated packing morphology, including S4, H1, H2, S7, S8, and H3. The number of particles used in simulation is labelled beneath the images.

Table 9.2 Summary of the structures observed in colloidal assembly in micropillar arrays in comparison with the theoretical predictions.

Vol. %	Phase	Morphology	Predicted by literature [20]	Predicted from us	Chirality
15	S1	Zigzag	Y	N/A	Achiral
	S2	Layer of 2 spheres	Y	N/A	Achiral
20	S3	Layer of 3 spheres	Y	N/A	Achiral
	S4	Layer of 2 spheres	Y	N/A	Achiral
25	H1	3-stranded helix	N/A	Y	Chiral
	H2	4-stranded helix	N/A	Y	Chiral
	S5	Layer of 4 spheres	N/A	Y	Achiral
30	S6	Layer of 3 spheres	N/A	N/A	Achiral
	S7	Layer of 5 spheres (1-D column)	N/A	Y	Achiral
40	S8	Layer of 5 spheres (1-D column)	N/A	Y	Achiral
	H3	5-stranded helix (1-D column)	N/A	Y	Chiral

9.3 Conclusions

In summary, we investigate the micro-confinement of charged silica nanoparticles dispersed in refractive index matching monomers in PDMS porous membrane. Here, the silica colloidal particles interact with each other and the pore wall via electrostatic double layer forces. Different from the hard sphere systems where the assembled morphologies are prescribed by the diameter ratio between the cylindrical confinement and the nanoparticles, here we observe a much richer variety of assemblies that are highly sensitive to both bulk and local nanoparticle concentration with fixed particle size and channel size. The experimentally observed assembly morphologies are consistent with theoretical predictions (from both literature and our calculation) based on Yukawa potential in the low packing density regime, because of the long-range repulsive interaction. The study presented here offers new insights of soft interactions in directing the colloidal assemblies in cylindrical confinement, which in turn will provide model systems to study the classical problems such as crystallization and melting, supramolecular assemblies in organic and biological systems[40], and to explore chirality and large surface area for new applications, including organic solar cells,[41] anisotropic electrical conduction,[40] proton conduction and their biological functions,[25] temperature responsive alignment and controlled release,[24] sensing,[6] catalysis, and opto-electronics.

9.4 Reference

1.   Yethiraj, A. and A. van Blaaderen, *A colloidal model system with an interaction tunable from hard sphere to soft and dipolar.* Nature, 2003. **421**(6922): p. 513-517.

2.   Yin, Y., et al., *Template-Assisted Self-Assembly: A Practical Route to Complex Aggregates of Monodispersed Colloids with Well-Defined Sizes, Shapes, and Structures.* J. Am. Chem. Soc., 2001. **123**(36): p. 8718-8729.

3.   Li, F., et al., *Synthesis of Porous Wires from Directed Assemblies of Nanospheres.* J. Am. Chem. Soc., 2003. **125**(52): p. 16166-16167.

4.   Li, F., et al., *Fabrication of Colloidal Crystals with Tubular-like Packings.* J. Am. Chem. Soc., 2005. **127**(10): p. 3268-3269.

5.   Kumacheva, E., et al., *Two-Dimensional Colloid Crystals Obtained by Coupling of Flow and Confinement.* Phys. Rev. Lett., 2003. **91**(12): p. 128301.

6.   Wu, Y., et al., *Composite mesostructures by nano-confinement.* Nat. Mater., 2004. **3**(11): p. 816-822.

7.   Moon, J.H., et al., *Fabrication of Ordered Macroporous Cylinders by Colloidal Templating in Microcapillaries.* Langmuir, 2004. **20**(5): p. 2033-2035.

8.   Moon, J.H., G.-R. Yi, and S.-M. Yang, *Fabrication of hollow colloidal crystal cylinders and their inverted polymeric replicas.* J. Coll. Interf. Sci., 2005. **287**(1): p. 173-177.

9.   Vanapalli, S.A., et al., *Fluidic Assembly and Packing of Microspheres in Confined Channels.* Langmuir, 2008. **24**(7): p. 3661-3670.

10.   Irvine, W.T.M., V. Vitelli, and P.M. Chaikin, *Pleats in crystals on curved*

surfaces. Nature, 2010. **468**(7326): p. 947-951.

11. Zerrouki, D., et al., *Chiral colloidal clusters.* Nature, 2008. **455**(7211): p. 380-382.

12. Lohr, M.A., et al., *Helical packings and phase transformations of soft spheres in cylinders.* Phys. Rev. E, 2010. **81**(4): p. 040401.

13. Pinedo Rivera, T., et al., *Assisted convective-capillary force assembly of gold colloids in a microfluidic cell: Plasmonic properties of deterministic nanostructures.* J. Vac. Sci. Technol. B, 2008. **26**(6): p. 2513-2519.

14. Ren, B., et al., *Assembly Behavior of Iron Oxide-Capped Janus Particles in a Magnetic Field.* Langmuir, 2012. **28**(2): p. 1149-1156.

15. Cong, V.T., et al., *Gold Nanoparticle Silica Nanopeapods.* J. Am. Chem. Soc., 2014. **136**(10): p. 3833-3841.

16. Erickson, R.O., *Tubular Packing of Spheres in Biological Fine Structure.* Science, 1973. **181**(4101): p. 705-716.

17. Pickett, G.T., M. Gross, and H. Okuyama, *Spontaneous Chirality in Simple Systems.* Phys. Rev. Lett., 2000. **85**(17): p. 3652-3655.

18. Mughal, A., H.K. Chan, and D. Weaire, *Phyllotactic Description of Hard Sphere Packing in Cylindrical Channels.* Phys. Rev. Lett., 2011. **106**(11): p. 115704.

19. Charvolin, J. and J.-F. Sadoc, *A Phyllotactic Approach to the Structure of Collagen Fibrils.* Biophys. Rev. Lett. , 2011. **6**(01n02): p. 13-27.

20. Oğuz, E.C., R. Messina, and H. Löwen, *Helicity in cylindrically confined Yukawa systems.* EPL, 2011. **94**(2): p. 28005.

21. Wood, D.A., C.D. Santangelo, and A.D. Dinsmore, *Self-assembly on a cylinder:*

a model system for understanding the constraint of commensurability. Soft Matter, 2013. **9**(42): p. 10016-10024.

22.   Douady, S. and Y. Couder, *Phyllotaxis as a physical self-organized growth process.* Phys. Rev. Lett., 1992. **68**(13): p. 2098-2101.

23.   Michael, T., et al., *Colloidal Crystal Wires.* Adv. Mater., 2008. **20**(58114f25-0996-fa73-9430-48a325443715).

24.   Jiang, L., et al., *Helical Colloidal Sphere Structures through Thermo-Reversible Co-Assembly with Molecular Microtubes.* Angew. Chem. Int. Ed., 2013. **52**(12): p. 3364-3368.

25.   Rasaiah, J.C., S. Garde, and G. Hummer, *Water in Nonpolar Confinement: From Nanotubes to Proteins and Beyond.* Ann. Rev. Phys. Chem., 2008. **59**(1): p. 713-740.

26.   Khlobystov, A.N., D.A. Britz, and G.A.D. Briggs, *Molecules in Carbon Nanotubes.* Acc. Chem. Res., 2005. **38**(12): p. 901-909.

27.   Bogush, G.H., M.A. Tracy, and C.F. Zukoski Iv, *Preparation of monodisperse silica particles: Control of size and mass fraction.* J. Non-Crys. Solids, 1988. **104**(1): p. 95-106.

28.   Israelachvili, J.N., *Intermolecular and Surface Forces*. 2011: Academic Press; 3 ed.

29.   Hsu, M.F., E.R. Dufresne, and D.A. Weitz, *Charge Stabilization in Nonpolar Solvents.* Langmuir, 2005. **21**(11): p. 4881-4887.

30.   Leunissen, M.E., et al., *Ionic colloidal crystals of oppositely charged particles.* Nature, 2005. **437**(7056): p. 235-240.

31.   Wan, Q., et al., *Light curable dental composites designed with colloidal crystal reinforcement.* Dent. Mater., 2008. **24**(12): p. 1694-1701.

32.   Wu, Y.L., et al., *Melting and crystallization of colloidal hard-sphere suspensions under shear.* Proc. Nat. Acad. Sci. U. S. A., 2009. **106**(26): p. 10564-10569.

33.   Kim, S.-H., et al., *Optofluidic Assembly of Colloidal Photonic Crystals with Controlled Sizes, Shapes, and Structures.* Adv. Mater., 2008. **20**(9): p. 1649-1655.

34.   Yang, H. and P. Jiang, *Large-Scale Colloidal Self-Assembly by Doctor Blade Coating.* Langmuir, 2010. **26**(16): p. 13173-13182.

35.   Royall, C.P., M.E. Leunissen, and A.v. Blaaderen, *A new colloidal model system to study long-range interactions quantitatively in real space.* J. Phys., 2003. **15**(48): p. S3581.

36.   Demirörs, A.F., et al., *Directed Self-Assembly of Colloidal Dumbbells with an Electric Field.* Langmuir, 2010. **26**(18): p. 14466-14471.

37.   Pusey, P.N. and W. van Megen, *Phase behaviour of concentrated suspensions of nearly hard colloidal spheres.* Nature, 1986. **320**(6060): p. 340-342.

38.   Mueller, S., E.W. Llewellin, and H.M. Mader, *The rheology of suspensions of solid particles.* Proceedings of the Royal Society of London A: Mathematical, Physical and Engineering Sciences, 2010. **466**(2116): p. 1201-1228.

39.   Bowen, W.R. and A.O. Sharif, *Long-range electrostatic attraction between like-charge spheres in a charged pore.* Nature, 1998. **393**(6686): p. 663-665.

40.   Jin, W., et al., *Self-assembled graphitic nanotubes with one-handed helical arrays of a chiral amphiphilic molecular graphene.* Proc. Natl. Acad. Sci. U. S.

A., 2005. **102**(31): p. 10801-10806.

41.   Hill, J.P., et al., *Self-Assembled Hexa-peri-hexabenzocoronene Graphitic Nanotube.* Science, 2004. **304**(5676): p. 1481-1483.

Chapter 10: Summary and Outlook

10.0 Summary

This thesis has covered two topics of my research. In the first topic, I investigated the pattern transformation of periodic arrays of porous membranes. In the second topic, I fabricated ultrathin superhydrophobic surface by self-assembly of chained silica nanoparticles, and designed a model system to investigate the colloidal assembly within porous channel confinements and the role of long-range repulsive interactions.

To study pattern transformation of porous membranes, I fabricated the membranes from pH and temperature responsive hydrogel materials from poly(2-hydroxyethly methacrylate) in square, oblique, and kagome lattices, and manipulate their structural reconfigurations at microscale (see Chapter 3-6). In Chapter 4, we investigated swelling induced instabilities in porous membranes with a square array of micron-sized circular holes prepared from pH and temperature dual-responsive hydrogel, poly(2-hydroxyethyl methacrylate-co-N-isopropylacrylamide-co-acrylic acid) (PHEMA-co-PNIPAAm-co-PAA). At room temperature, hydrogel swelled ~1.61 to 9 times of its dried volume when pH was increased from 2 to 7. Within this regime, we observed four distinctive morphologies of the hydrogel membrane, including "breathing" mode of the membrane having circular pore arrays, buckled pore array of alternating mutually orthogonal ellipses, twisted snap-shut pores forming "S" shaped slits, and cavitation formed at local regions that perturbed the 2D periodicity of the hydrogel membrane. Using 3D confocal imaging technique, we followed the post-buckling behaviors of the porous membranes and investigated the pattern evolution process as a function of pH. Amplification of buckling and symmetry breaking were observed between immersing the sample in buffer solutions of pH 4.0 and 5.0, respectively, leading to the transition from achiral buckled state (pH 4.0) to a chiral twisted state (pH 5.0) facilitated by the

212

compaction of the hydrogel domains within the space to completely close the pores. When further increasing pH to 7, star-shaped patterns appeared randomly in the film, where the hydrogel domain was compressed by the adjacent neighbors, thus forming a cusp or cavitation. Finally, we demonstrated reversibly switching of the hydrogel membrane from the twisted state to the original circular hole array when increasing the temperature to 45 °C, which was above the lower critical solution temperature of PNIPAAm. It raises question of whether it is possible to control the single handedness.

In Chapter 5, we investigate swelling induced pattern transformation from pH-sensitive hydrogel membranes made of poly(2-hydroxyethyl methacrylate)-co-poly(acrylic acid) (PHEMA-co-PAA) with periodic pores (10 μm in diameter, 15 μm in pitch, and 13 μm in height) in both square and oblique array. They are created by replica molding twice from a poly(dimethylsiloxane) (PDMS) mold with square arrayed pillars, which is mechanically pre-stretched at a very small strain (5%) in different angles (15°, 30°, 45°, 60°, 75°) relative to the lattice axis. Symmetry breaking occurs at pH 4.7 (swelling ratio ~2.3) from the buckled state (pH 3, achiral, swelling ratio ~ 2.0) to the twisted state (pH 6.4, chiral, swelling ratio ~5.4), leading to formation of chiral structures. While the swollen hydrogel membranes fabricated from the un-stretched PDMS mold typically show nearly 50/50 mixture of right and left handed chiral structures, predominant single handedness can be obtained from the oblique array of porous membranes, depending on the pre-stretching angle in the PDMS mold. ~ 98.2% left-handedness is obtained from the ones with low pre-stretching angles (15°, 30°) while nearly exclusive right-handedness (~ 98.3%) is obtained from the ones with large pre-stretching angles (60°, 75°).

Building upon the study of square and oblique lattices, we design twisted kagome lattices guided by finite element method (FEM) simulation. By prescribing asymmetry

213

units in silicone materials, in chapter 6, we studied the collapsing modes of pre-twisted kagome lattices with prescribed asymmetric ligaments in different arrangements. We avoided the buckling instability, allowing for smooth and homogenous structural reconfiguration in a deterministic fashion. The mechanical responses of the designed metamaterials, including stress-strain behaviors and the resulting negative Poisson's ratios, were strongly affected by the symmetry of the ligaments and their arrangement. Here, we suggest a new and important design concept in soft metamaterials, that is, the introduction of asymmetric ligaments to the periodic porous structures. It will allow for exquisite control of the compaction path of the porous structures, thus reaching much richer range of transformed patterns and their corresponding physical properties. The knowledge presented here will also provide critical insights to design foldable or deployable devices by precisely control of the materials stiffness and mechanical response in 2D and 3D sheets.

Meanwhile, I have great passion nanoparticle assemblies. In the first case, we utilized a new form of silica nanoparticles (i.e. with chain-like morphology) to generate sharp nanostructures on the coating surface that minimized the contact between liquid and solid phase, and thus improve dramatically of the water repellency on the coating surfaces. While the chain nanoparticles are deposited on a flat open surface, there are many questions about the self-assembly of soft matter in a physical confinement. I there designed colloidal suspensions as a model system to study the packing of colloidal particles within confinements. By matching experimentally, the inter-particle interactions with those used in previous theoretical study of colloidal assembly (i.e. long range electrostatic repulsion) within the confined the space. The beauty of the system is that the colloidal suspension can be cross-linked and lock the assembled structure, so that the assembled morphology can be directly observed under electron

microscope. We thus can compare assembled structure from theory and molecular dynamic simulation results from collaboration with colloidal physicists at University of Massachusetts. In this case, a good consistence has been observed between the experimental systems and theory/simulation, indicating a validated approach to study the assembly of colloids under confinements with the developed systems.

10.1 Outlook

In the study of pattern transformation, we focused on simple lattices in 2D made from single set of soft materials. In the case of kagome lattices, the experiments do not completely agree with elastic theory of Maxwell lattices since the units are not perfectly rigid. There are many questions on how lattices will deform when pore size and pore shape are not uniform, or hybrid materials, that is combination of soft and hard materials placed at different units or struts. We have begun to design the lattices with hierarchical structures using FEM. It will be interesting to realize the studies in experiments and compare the results with FEM simulation.

In the nanoparticle assemblies, we focus on maintaining stable Cassie state, which has been claimed as a major requirement of practical applications of the coatings. However, the practical applications of superhydrophobic coatings have been hampered by other requirements, e.g. mechanical durability, outdoor stability, and high fabrication costs, and how to apply the coatings in a cost-effective way without environmental concerns. However, if we think an opposite side of the problem, the knowledge of superhydrophobic effects can be applied to the fields requiring to destabilize the composite interface. One example is that in agricultural industry, the spray of water based pesticides and herbicide can be found to have a low efficiency on many plant surfaces due to the intrinsic superhydrophobic effects on the plant leaf surfaces. A chemical/physical approach in formulation of the spraying liquids, and

fundamental understanding of the wetting transition on super-non-wetting effects on these plants leave surfaces can provide significant insight to improve the efficiency of usage of pesticide/herbicide that create greener and less toxic agriculture.

Appendix I

Publication List

1. Yang. X; Ge. D; **Wu. G**; Yang. S, Production of Structural Colors with High Contrast and Wide Viewing Angles from Assemblies of Polypyrrole Black Coated Polystyrene Nanoparticles, *Applied Materials and Interfaces*

2. Y. Wu, R. Cao, **G. Wu**, Z. Chen, X. Yang and Y. Tu, From Ultratough Artificial Nacre to Elastomer: Poly (n-butyl acrylate) Grafted Graphene Oxide Nanocomposites, Composites Part A

3. B. Cao[*]; **G. Wu**[*]; Xia, Y.; Yang, S., Buckling into single-handed chiral structures from pH-sensitive hydrogel membranes. Extreme Mechanics Letters. ([*]Equally contributed to the paper)

4. Liu, C.; Liao, S.-C.; Song, J.; Mauk, M. G.; Li, X.; **Wu, G.**; Ge, D.; Greenberg, R. M.; Yang, S.; Bau, H. H., A high-efficiency superhydrophobic plasma separator. *Lab on a Chip* 2016, 16, 553-560.

5. Cho, Y; Lee, Su, Y; Ellerthorpe, L.; Feng, G.; Lin, G.; **Wu, G.**; Yin, J. and Yang, S., "Power-free mechanochromic sensors from force-recording, elasto-plastic inverse opals", *Adv. Funct. Mater*. **2015**

6. **G. Wu**, Y. Cho, I.-S. Choi, D. Ge, J. Li, H. N. Han, T. Lubensky and S. Yang, "Directing the Deformation Paths of Soft Metamaterials with Prescribed Asymmetric Units, *Advanced Materials*, 2015, 27, 2747-2752

7. D. Ge, L. Yang, **G. Wu** and S. Yang, "Spray coating of superhydrophobic and angle-independent coloured films", *Chem. Commun.*, 2014, 50, 2469-2472.

8. D. Ge, L. Yang, **G. Wu** and S. Yang, "Angle-independent colours from spray coated quasi-amorphous arrays of nanoparticles: combination of constructive interference and Rayleigh scattering", *J. Mater. Chem. C*, 2014, 2, 4395-4400.

9. **G. Wu**, Y. Xia and S. Yang, "Buckling, symmetry breaking, and cavitation in periodically micro-structured hydrogel membranes", *Soft Matter*, 2014, 10, 1392-1399.

10. K. Liu, A. Ahmed, S. Chung, K. Sugikawa, **G. Wu**, Z. Nie, R. Gordon and E. Kumacheva, "In Situ Plasmonic Counter for Polymerization of Chains of Gold Nanorods in Solution", *ACS Nano*, 2013, 7, 5901-5910.

11. M. A. Gharbi, M. Cavallaro, **G. Wu**, D. A. Beller, R. D. Kamien, S. Yang and K. J. Stebe, "Microbullet assembly: interactions of oriented dipoles in confined nematic liquid crystal", Liquid Crystals, 2013, 1-9.

12. X. Zhu, **G. Wu**, R. Dong, C.-M. Chen and S. Yang, "Capillarity induced instability in responsive hydrogel membranes with periodic hole array", *Soft Matter*, 2012, 8, 8088-8093.

13. **G. Wu**, Y. Zhao, S. Yang, "Omni-transparent and superhydrophobic coatings assembled from chain-like nanoparticles" (patent disclosure, United States Provisional Application No. 62/157,712)

Under Preparation

14. **G. Wu**, D. Ge, Y. Zhao, S. Yang, "Robust Water Repellency on Ultra-thin (sub-100 nm) Nanoparticle Film" (in preparation)

15. **G. Wu**, H. Cho, S. Yang, "Confined Assemblies of Colloidal Particles with Soft, Repulsive Interactions" (submitted)

16. D. Ge, X. Yang, **G. Wu**, S. Yang, "Tool-independent, Drop-based Assemblies of Uniform 3D Structural Colors from Bumpy Core-shell Colloidal Ink" (submitted, under review)

17. G. Lin, D. Ge, Y. Tang, Y. Xia, **G. Wu**, L. Han, S. Yang, J. Yin, "Creating reconfigurable logic gate-like metasurfaces via cutsguided buckling" (submitted, under review)

18. D. Ge, **G. Wu**, W. Hallwachs, S. Yang, "Unique and diverse whiteness on Carystoides escalantei butterfly wings" (submitted)

Appendix II

Patterned Superhydrophobic (SH) Surfaces

Heterogeneous surfaces consisting of both hydrophilic and hydrophobic regions have been shown to enhance water condensation and water harvesting. [1, 2] Charge induced adsorption of nanoparticles as shown in Chapter 7 can be used for generate surface patterned with superhydrophobic and highly hydrophilic regions (Fig. 1).
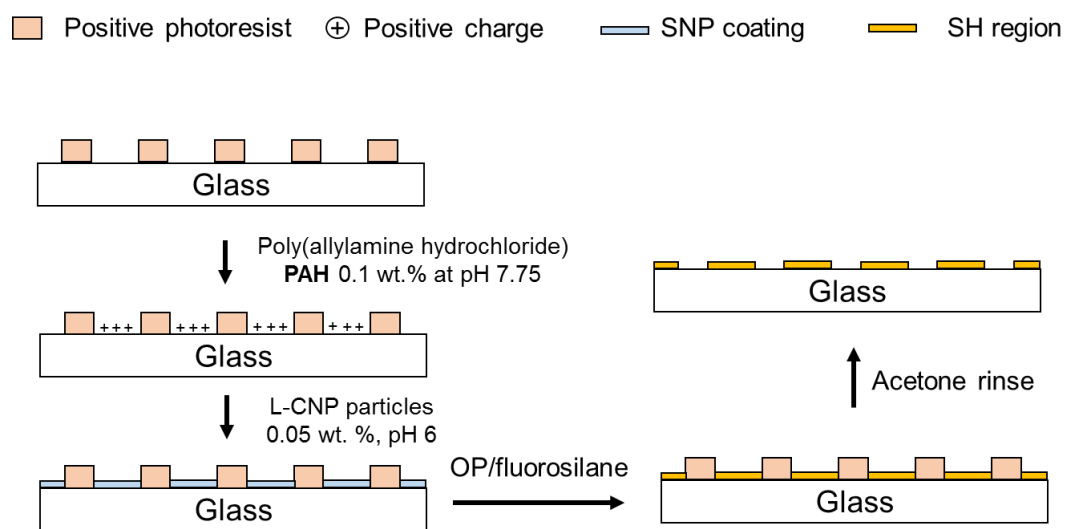

Figure 1. Schematics showing the patterning process to create a surface with superhydrophobic and hydrophilic regions.

First, the pattern was patterned by photolithography using positive photo-resist S1818 (Fig. 2 and 3). As an example, the 20 μm 1D pattern was created.
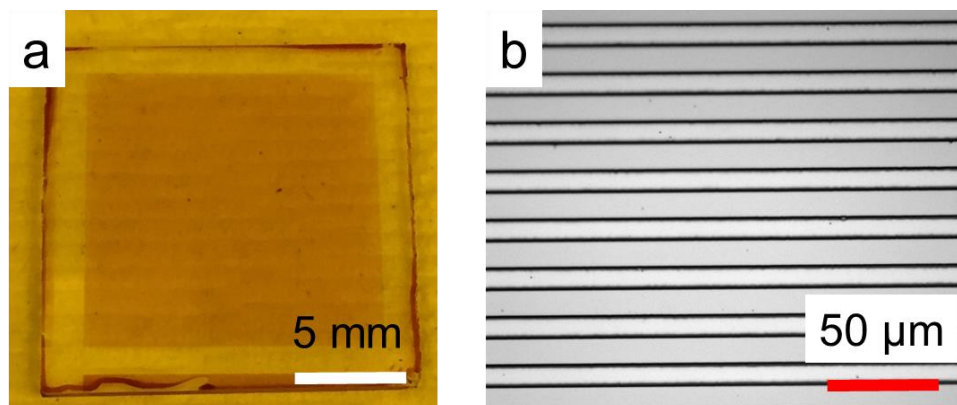
Figure 2. Stripe width 20 µm on glass.

The positive charge on the glass surface was created by immersing the sample in 0.1 wt. % aqueous solution of polyallylamine (PAH, Aldrich) at pH 7.5 for 5 min. Then, the sample was immersed L-CNP silica nanoparticle suspension (see chapter 7, 0.05 wt. % in water at pH 6) for 90 min to deposit the particles. After fluoro-silane (Gelest. 8174) treatment, the S1818 photoresist was removed by rinsing with acetone (see Fig. 4).
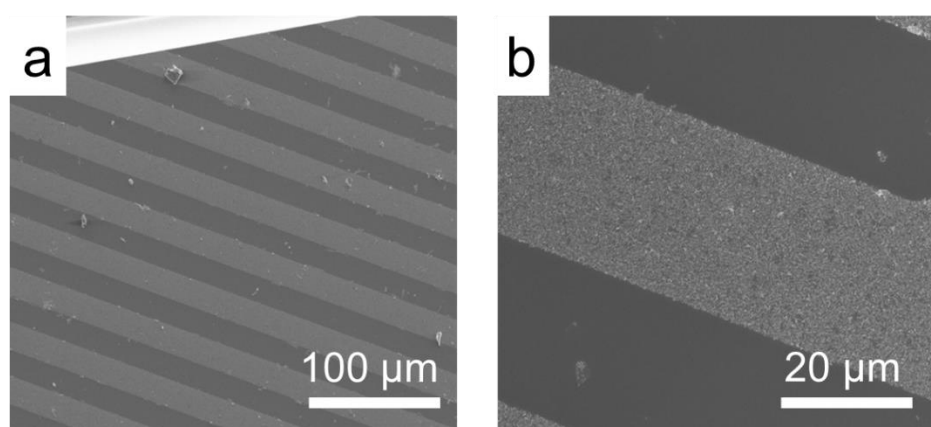
Figure 3. SEM images of the patterned SH surface. (a) low magnification, and (b) high

magnification.

Here, the nanoparticle coated area is superhydrophobic with contact angle (CA) 65°, and the flat region is mainly bare glass (CA < 10°). The patterned SH surface with 1D pattern has strong anisotropic wetting properties. The water CA parallel to the stripes is less than 90°, but the contact angle orthogonal to the stripes is ~165° (see Fig. 5).
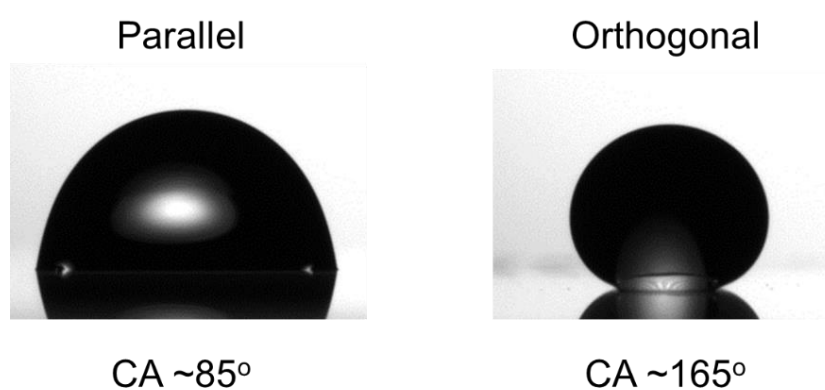
Figure 4. Water contact angles on the line patterns in the parallel and orthogonal directions.

We then performed the water condensation experiments on the patterned SH surfaces (i.e. patterned with 20 µm width of stripes and 40 µm pitch) at the environmental temperature of ~22 $^{\circ}$C, the substrate temperature of ~ 4 $^{\circ}$C, and humidity is ~ 70%. However, we did not observe anisotropic condensation behaviors as expected on the coating surface; the water droplets remained nearly circular (see Fig. 6).
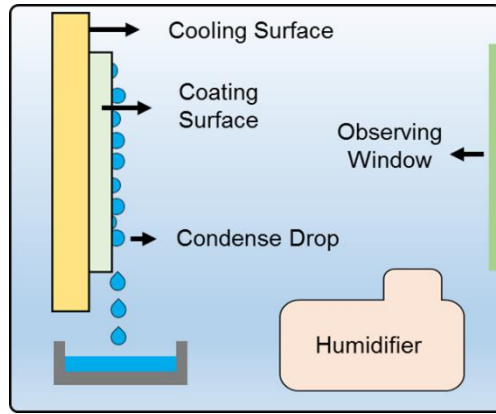
Figure 5. The setup for performing condensation experiments on the patterned SH substrates.
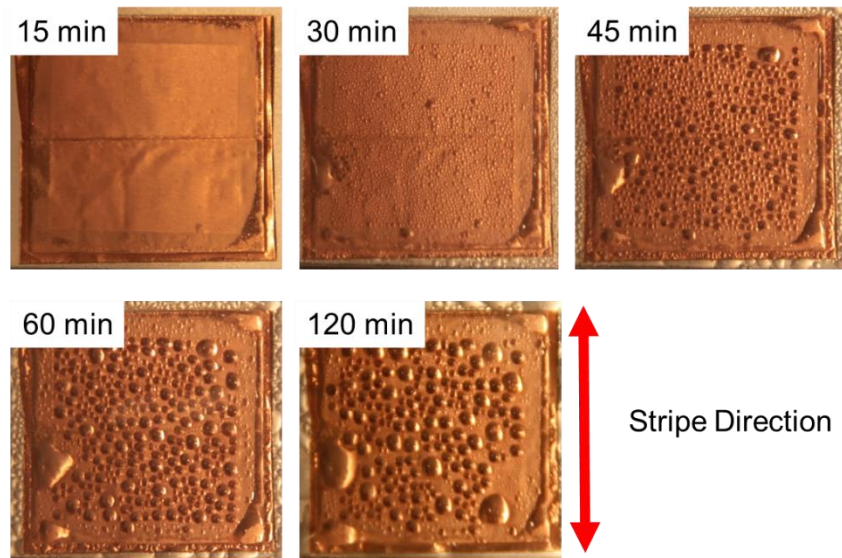
Figure 6. Optical images of water droplets condensed on the substrate with patterned SH regions (i.e. patterned with 20 μm width of stripes and 40 μm pitch) for different amount of time. The red arrow indicates the stripe direction.

Here, the absence of anisotropic condensation behavior can be attributed to the fact that the water drops are significantly larger compared to the size of micro-channels patterned with hydrophilic region. Thus, the wetting phenomenon observed became an

average effect from the multiple regions having different wettability. A potential improvement will be enlarge the width of patterned hydrophilic region.

References

1.   Gau, H., et al., *Liquid Morphologies on Structured Surfaces: From Microchannels to Microchips.* Science, 1999. **283**(5398): p. 46-49.

2.   Xia, D., L.M. Johnson, and G.P. López, *Anisotropic Wetting Surfaces with One-Dimesional and Directional Structures: Fabrication Approaches, Wetting Properties and Potential Applications.* Advanced Materials, 2012. **24**(10): p. 1287-1302.

Appendix III

Under Water Recovery of the Superhydrophobic Surfaces

When superhydrophobic (SH) surface are in contact with water containing certain soluble contaminants that lower the liquid surface tension, e.g. alcohol, and surfactants that typically encountered in our daily life. The contaminated liquids will penetrate through the barrier of the surface roughness and destroys the composite interface, [1] which thus results in irreversible loss of superhydrophobic behavior. It was also observed that even after washing those pre-wetted SH surface repetitively washed pure water, the entrapped liquid is extremely difficult to remove due to the pinning effects from the surface roughness. For example, on Neverwet ®, if the coating is first wetted by ethanol, upon following rinsing with pure water, the entrapped liquid cannot be removed and the surface was found to become hydrophilic. However, on our ultra-thin nanoparticle coating, due to the extremely low thickness (sub-50 nm thickness, 3 order of magnitude thinner compared to typical SH surface, e.g. Neverwet®, and lotus leaf), the trapped liquid can evaporate instantaneously upon contacting with air, and the coating recovers superhydrophobicity after washing.
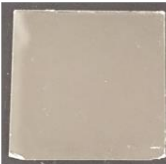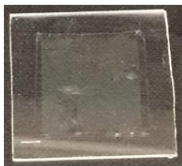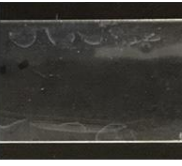
	Fluoropolymer pillars D ~ 2 um, P = 4 um, AR ~ 4	Neverwet ®	Ultra-thin NP Coating
Dry			
Wetted by Ethanol			
After Water Washing			
Water Drop on Washed Surface			
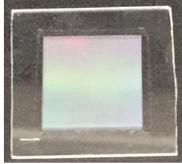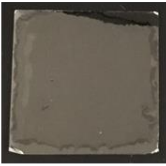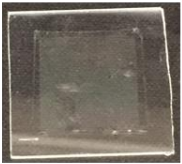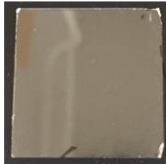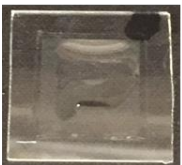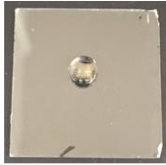
Figure 1. Pre-wetting and washing with water for different superhydrophobic surfaces.

Figure 2 shows the video frames of the rinsing process of ethanol wetted ultra-thin NP coating. In beginning, the composite interface does not exist due to wetting of ethanol into the surface roughness, which is confirmed by observation of high transparency of the coating layer in the rinsing water bath. However, after moving the coating out of the rinsing bath, the liquid dewets the surface (i.e. no liquid stay on the coating). This was found in contrast to Neverwet upon the same treatment, where surface remain wetted (i.e. a water film observed macroscopically on the coating). More importantly, after re-inserting the glass slide back into the rinsing bath, the composite interface was found recovered, observed as mirror-like appearance on the coating

surface. This observation suggests that after washing, on nano-scale the trapped liquid is completely removed, which allows regeneration of the composite interface after being wetted.
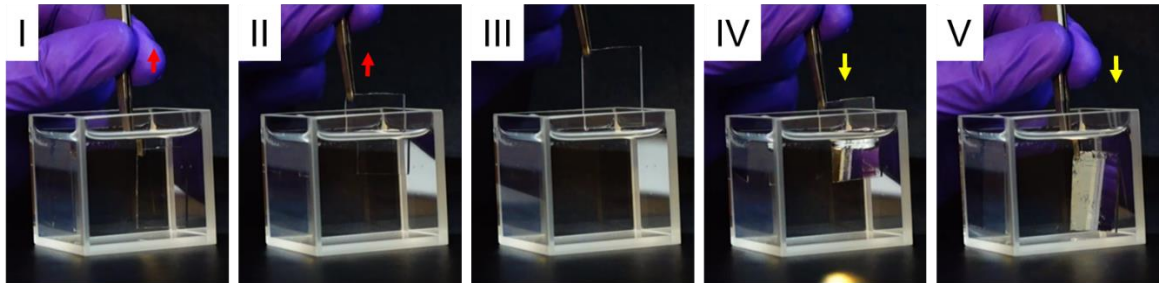

Figure 2. Rinsing and drying of the pre-wetted L-CNP superhydrophobic

References

1.   Nosonovsky, M. and B. Bhushan, *Hierarchical roughness optimization for biomimetic superhydrophobic surfaces.* Ultramicroscopy, 2007. **107**(10–11): p. 969-979.